Universidad Nacional Autónoma de México

Instituto de Energías Renovables
Instituto de Ingeniería
Escuela Nacional de Estudios Superiores-Juriquilla

# Topological impact of nano-electrodes on the structure of the electrical double layer and the differential capacitance

**T E S I S**

que para obtener el título de

Ingeniero en Energías Renovables

**P R E S E N T A**

Adrián Silva Caballero

**DIRECTOR DE TESIS**

Dr. Marcelo Lozada y Cassou

Temixco, Mor., a 30 de junio de 2020

# Topological impact of nano-electrodes on the structure of the electrical double layer and the differential capacitance

by

Adrián Silva Caballero

Thesis presented to obtain the title of
Engineer in Renewable Energies

in the

Instituto de Energías Renovables

Universidad Nacional Autónoma de México

Temixco, Mor.. June 30, 2020

**OF/IER/LIER/042/2020**
**ASUNTO:** Notificación de jurado y fecha para examen profesional mediante aula virtual.

**LIC. IVONNE RAMÍREZ WENCE**
**DIRECTORA GENERAL DE ADMINISTRACIÓN ESCOLAR**
**P r e s e n t e .**

Por medio de la presente le informo que el día martes 30 de junio de 2020, a las 10:00 hrs., mediante Aula Virtual habilitada por la Dirección General de Cómputo y de Tecnologías de Información y Comunicación de la UNAM, el **C. ADRIÁN SILVA CABALLERO,** con número de cuenta 312088772 de la Licenciatura de Ingeniería en Energías Renovables, llevará a cabo la presentación del trabajo de tesis y examen profesional titulado:

***"Topological impact of nano-electrodes on the structure of the electrical double layer and the differential capacitance"***

Debido a que el alumno ha cumplido con los requisitos que establece el Reglamento General de Exámenes, el Comité Académico de la Licenciatura de Ingeniería en Energías Renovables, le asigna el Jurado de Examen Profesional integrado por los siguientes académicos.

| | |
|---|---|
| **PRESIDENTE:** | **DR. MARIANO LÓPEZ DE HARO** |
| **VOCAL:** | **DR. VÍCTOR MANUEL ROMERO ROCHÍN** |
| **SECRETARIO:** | **DR. MARCELO LOZADA Y CASSOU** |
| **SUPLENTE:** | **DR. MIGUEL ROBLES PÉREZ** |
| **SUPLENTE:** | **DR. JESÚS MUÑIZ SORIA** |

Sin otro particular, le envío un cordial saludo.

A t e n t a m e n t e,
**"Por mi raza hablará el espíritu"**
Temixco, Mor., a 24 de junio de 2020

**Dr. Jorge Alejandro Wong Loya**
**Coordinador de la LIER**
**IER-UNAM**

JAWL´mfp.

Priv. Xochicalco s/n,
Col. Centro,
62580 Temixco, Morelos, México
T. 01 (777) 362 00 90
(52) 55 56 22 97 00

ier.unam.mx

*To my grandparents,*
*with love, and*
*admiration.*

*In human affairs of danger and delicacy successful conclusion is sharply limited by hurry. So often men trip by being in a rush. If one were properly to perform a difficult and subtle act, he should first inspect the end to be achieved and then, once he had accepted the end as desirable, he should forget it completely and concentrate solely on the means. By this method he would not be moved to false action by anxiety or hurry or fear. Very few people learn this.*

John Steinbeck

# Acknowledgments

I am most thankful to my supervisor D.Sc. Marcelo Lozada-Cassou for his advice, and comments while elaborating this piece of work. I have no doubt that his involvement positively impacted the outcome of my thesis. Also, I am grateful to his post PhD student D.Sc. Juan Montes-Pérez, who obtained the data list of the hypernetted-chain results used for this thesis, enhancing without doubt my dissertation. I specially thank both for their support and guidance when things were not running smoothly. Likewise, I thank my tutor D.Sc. Mariano López-Haro for guiding me with my supervisor and for challenging me to address the topic; without him I would not have embarked on the subject.

I am utmost grateful to the continued support, nourishment, and love of my family and friends, including those present and those left behind. I owe a most special thanks to M.Sc. Andrea Silva-Caballero, D.Sc. Cecilia I. Caballero-Miranda, D.Sc. Gilberto Silva-Romo, and Magali Nicanor-Terán for always encouraging and advocating me. I am most obliged to my classmates, specially to Sady M. García-Delgadillo, B.S.E. Luis R. Ángeles-Álvarez, and B.S.E. José M. Acosta-Hernández for all the group projects, talks, laughs, and support. I am also indebted to the National Autonomous University of Mexico, particularly to the Institute of Renewable Energies and to all the professors that formed me.

I am truly grateful to the advances in technology and to modern medicine, which gave me the chance to fight cancer and pursue this degree. I owe a sincere thanks to M.D. Roberto Peña-López, and M.D. Manuel González-Galnares since, without them, I would most likely have never been able to start and finish my Bachelor degree.

Finally, the financial support of CONACYT (Grant No. 169125) is gratefully acknowledged.

# Abstract

In this thesis we study the impact that the geometry and topology of nano-electrodes have over the structure of the electrical double layer, through the analytical solution of the linearized Poisson-Boltzmann equation, with the Stern restriction (LPBS). Both, solid and hollow electrodes are considered to be in contact with a symmetric electrolyte. *Here, we refer to the solid electrodes as solid nano-electrodes and to hollow electrodes, as nano-pores.* In particular, the LPBS is solved for different electrical charges and geometrical and/or topological parameters of the nano-electrodes, in contact with an electrolyte at different concentrations and temperatures. The differential capacitance of such system is calculated as well. While the case of large electrodes is also studied here, the emphasis is given to the nano-scale. Three different geometries of the nano-electrodes are considered: planar, cylindrical and spherical, whereas for the nano-pores we consider slits, cylindrical, and spherical shells. The three nano-pores geometries considered are topologically different among them, and with respect to the solid nano-electrodes. The three solid nano-electrodes are, of course, topologically equivalent. The charge fluid is an electrolyte modeled as punctual ions, in an uniform solvent, which is characterized by a dielectric constant. The ions' size is only considered on the interaction with electrodes (Stern correction). The dielectric constants of the nano-electrodes and nano-pores are assumed to be the same dielectric constant as that of the solvent, to avoid the image potential.

The linear Poisson-Boltzmann (LPB) equation is solved and the analytical solution of the distribution of co-ions and counter-ions (density profile), the mean electrostatic potential, the induced surface charge density, and the differential capacitance are obtained, and calculated, for different parameters of the systems. The LPB density profiles of the distinct nano-electrodes are compared against those of the hypernetted-chain/mean spherical integral equations formalism, to determine the range of their validity. Then, with the LPB, the behavior of the electrical double layer (EDL) is studied for different values of the nano-electrodes' radius and surface charge, and the molar concentration and temperature of the electrolyte. The electric potential, the induced surface charge density in the fluid, ionic concentration profiles as well the capacitance of these systems are calculated. An important dependence of these quantities with the geometry and/or topology of the nano-electrodes is found.

# Contents

# Chapter 1

# Introduction

In the development of big renewable energy projects, supercapacitors (SCs) play a relevant role. Due to the intermittence of renewable energies, such as solar and wind energy, the electric grid cannot rely on them as a base load. However, they are an excellent choice to keep up with the demand of the grid in peak hours, i.e., to work as a backup energy source. Hence, highly efficient energy storage systems are needed to stock and deliver this energy whenever the grid needs it. There are three main energy storage systems used worldwide: batteries, capacitors, and supercapacitors. Because of the technical requirements that the grid needs, that is to quickly deliver high quantities of energy in a rather short time, SCs are the best way to keep up with such demand. Other applications of SCs are in hybrid cars. They are used to boost the capabilities of batteries or fuel cells while accelerating, as well as in regenerating braking. Hence, it is seen that SCs are widely used in applications where high specific power and energy are needed, and that work with fluctuating loads, such as those used in construction cranes, and electric, aero, and medical industries. Supercapacitors, also referred as electrochemical capacitors (ECs), are divided into three main categories (electric double layer capacitors, pseudocapacitors, and hybrid capacitors) depending on the passive components in which they store energy. Electric double layer capacitors (EDLCs) store energy in the surface of an electrode-electrolyte interface. Whereas, pseudocapacitors store energy by a reversible redox reaction at its surface. Meanwhile, hybrid capacitors store energy by a combination of the two methods.

In this thesis the first results of the linear Poisson-Boltzmann equation with the Stern restriction (LPBS) [1, 2] is obtained for hollow electrodes of different topologies, and the results of the LPBS for solid electrodes is solved as well. The analytical results of the density profiles, and the differential capacitance are obtained from the solutions, among other electric parameters. The thesis is divided into five chapters. In this chapter a review of EDLCs is provided, from a quick historical background to a revision of the components used in EDLCs, and a brief compilation of the most well known theories that are used to describe the structure of the electrical double layer is given. In Chapters 2 and 3 the analytical solutions of the LPBS for solid and hollow electrodes are solved, respectively, and their density profiles are shown. Meanwhile, in Chapter 4 the mean electrostatic potential, induced surface charge density, and the differential capacitance are shown while different electrode's and electrolyte's parameters are varied. Lastly, the thesis conclusions are found in Chapter 5. Furthermore, two appendixes are included, Appendix A details the complete analytical solutions of the LPBS for solid electrodes, and in Appendix B the 'Mathematica' computer code used is added.

## 1.1 Electric double layer capacitors

A brief history of SCs is presented ahead, as well as their different components. EDLCs as other energy storage mechanism are composed of two electrodes separated by an electrolyte, these two main components will be the focus of our review. Furthermore, a short inspection of the current problems that SCs face is presented.

### 1.1.1 Historical background

The first patent known of a capacitor based on a high surface area dates back to 1957 by Becker when employed by General Electric [3, 4]. Thereupon, the first commercial EDLC was made and patented by the Standard Oil of Ohio Research Center (SOHIO) in 1961. However, due to a lack of sales, SOHIO licensed their technology to the Nippon Electric Company (NEC) in 1971 [5]. NEC developed and marketed the first commercially successful EDLC, which they named "super capacitor". Meanwhile, the Matsushita Electric Industry Co. (Panasonic) in 1978 created their own "gold capacito" [6]. From the 1980s to present time several other companies have started to produce their own electrochemical capacitors, naming them differently. Hence, after the commercial success of different EDLCs their names have started to be used as synonyms for EDLCs, such as SCs, gold capacitors, and ultra-capacitors, among others. Nowadays, the most well known EDLCs companies are Cellergy, Ioxus, Maxwell Technologies, Murata Manufacturing, Nanoramic Technologies, and NEC Tokin, among others.

### 1.1.2 Electrodes

The principle of operation of EDLCs is based on the storage and distribution of electrolyte's ions at an electrode. Hence, the amount of energy stored in the electrodes is directly proportional to the surface area of the electrode. Carbon has been utilized as a high surface area electrode material, with a specific surface area (SSA) of up to $2500\,\mathrm{m^2 g^{-1}}$, ever since the development of electrochemical capacitors began [3, 4]. Not only do carbon materials have a high surface area but they are also widely available at a low cost, and there are plenty of production technologies established for the fabrication of electrodes. The most common carbon-based electrodes are activated carbon, carbon nanotubes, and graphene electrodes, which are presented ahead.

#### 1.1.2.1 Activated Carbon

Activated carbons (ACs) are the most widely used materials for electrodes in SCs because of their high SSA, excellent chemical and thermal stability, rather good electric properties and low price [7]. ACs are produced by either thermal or chemical activation from carbon rich organic precursor materials (e.g. wood, coal, nutshell, etc.) [8, 9, 10]. Physical (thermal) activation is performed at high temperatures under an oxidizing atmosphere (e.g. $CO_2$, $H_2O$), while chemical activation is done on amorphous carbons which were previously mixed with chemicals such as alkalis, carbonates chlorides or acids (e.g.KOH, $K_2CO_3$) [9]. These activation processes result on the formation of a porous network in the bulk of the carbon; namely micropores ($< 2\,\mathrm{nm}$ in size), mesopores ($2\,\mathrm{nm}$–$50\,\mathrm{nm}$), and macropores ($> 50\,\mathrm{nm}$). Longer activation time or higher temperatures tend to larger mean pore size [11]. Depending on the activation process and the carbon precursor, the physicochemical properties widely vary, Yan *et al.* [7] list the physicochemical properties of different carbon precursors in their work. High SSA up to $3000\,\mathrm{m^2 g^{-1}}$ are achieved with a relatively small specific capacitance $< 10\,\mu\mathrm{F cm^{-2}}$, which indicates that not all pores are effective in charge accumulation [10]. Hence, despite the fact

that the SSA is an important parameter for the performance of EDLCs, the pores size distribution, pore shape and structure influence the electrochemical performance to a great extent.

#### 1.1.2.2 Carbon nanotubes

Carbon nanotubes (CNTS) have been widely study due to their unique open tubular network structures, and remarkable mechanical and electrical properties. Their open ended tunnel is beneficial for electrolyte percolation, facilitating the ion diffusion [12]. CNTs are produced by the catalytic decomposition of hydrocarbons [9]. They are divided into single-walled carbon nanotubes (SWNTs) and multi-walled carbon nanotubes (MWNTs), which are formed by different synthesis parameters. CNTs, unlike other carbon based electrodes, have mesopores that are interconnected, which allow for a continuous charge distribution that utilizes nearly all the accessible surface area [8]. Even though CNTs have a small SSA ($< 600\,\mathrm{m^2g^{-1}}$), their specific capacitance can reach up to $50.4\,\mu\mathrm{Fcm^{-2}}$ [7]. This gives the idea that if one were able to surpass this small SSA, the capacitance would follow. Coromina *et al.* [13] proved this right, they chemically activated their CNT with KOH and reached SSA of up to $3000\,\mathrm{m^2g^{-1}}$, achieving a specific capacitance of $172\,\mathrm{Fg^{-1}}$.

#### 1.1.2.3 Graphene

A remarkable electrode material is the monolayer of graphite, graphene, which can be prepared by several methods, such as mechanical exfoliation, exfoliation of graphite in organic solvents, epitaxial growth and chemical vapour deposition, and the exfoliation and reduction of chemically oxidized graphite [12]. A single layer graphene sheet is basically a two dimensional hexagonal lattice of $sp^2$ carbon atoms covalently bonded along two plane directions [14]. Graphene has outstanding properties, i.e., lightweight, high electrical and thermal conductivity, highly malleable surface charge, tenacious mechanical strength and mechanical stability [15]. These translates into a high theoretical SSA, $2630\,\mathrm{m^2g^{-1}}$ [16, 17]. If the entire SSA of graphene would be fully utilized, inhibiting the agglomeration of graphene sheets, it would achieve specific capacitance up to $550\,\mathrm{Fg^{-1}}$ [18, 8, 7]. Particularly, Chen *et al.* [19] achieved an specific capacitance of $348\,\mathrm{Fg^{-1}}$ for a partially reduced graphene oxide in an aqueous electrolyte.

### 1.1.3 Electrolytes

The performance of a SC depends not only on the electrode material but also on the selection of the electrolyte. The breakdown voltage of the electrolyte determines the cell voltage; and both energy and power density, which depend on the voltage [3]. The ideal electrolyte should have a wide voltage window, excellent electrochemical stability, high conductivity, high ionic concentration, small solvated ionic radius, low viscosity, environmental friendliness, low cost, and easy availability [10]. Accordingly, the ability of the SC to store charge relies on the accessibility of the ions, from the electrolyte, to the porous surface area of the electrode. Hence, the ion and pore size must be optimal, so both electrode and electrolyte must be picked simultaneously to enhance the capacitance [3]. Generally, the electrolytes are divided into three categories: aqueous, organic, and ionic electrolytes, they are presented and discussed below.

#### 1.1.3.1 Aqueous electrolytes

The most commonly used aqueous electrolytes are KOH, $H_2SO_4$, and $Na_2SO_4$, for alkaline, acidic, and neutral solutions [7, 20]. Aqueous electrolytes present some advantages such as low cost, non-flammability, low viscosity, and excellent safety. Furthermore, they have smaller solvated ions, higher

ionic concentration, and higher ionic conductivity (up to $1\,\mathrm{S\,cm^{-1}}$) than organic electrolytes [21, 7, 9]. Therefore, the aqueous electrolytes achieve a superior capacitance than organic electrolytes due to the higher concentration and smaller ionic radius. However, they have a limited voltage window up to 1.0 V due to the thermodynamic decomposition of water at 1.299 V, which ends up negatively impacting the energy and power density. In addition, water corrosivity must be taken into account [20].

#### 1.1.3.2 Organic electrolytes

Organic electrolytes consist in a conductive salt, e.g. tetraethylammonium tetrafluotoborate (commonly refer to $TEABF_4$), dissolved in the acetonitrile (ACN) or in propylene carbonate (PC) solvent [20, 9]. The advantage of organic electrolytes against aqueous electrolytes is the wider voltage window, as high as 2.5 V–3.0 V, giving rise to energy densities 6–9 times higher [7]. However, these advantages do not come freely since they are more expensive; and have a smaller specific capacitance, and a lower conductivity than aqueous electrolytes [20]. Moreover, there are also safety concerns due to their flammability and toxicity. In the European Union, ACN is declared highly flammable and harmful by inhalation, and in Japan its use is prohibited due to its toxicity and low flash point [20], whereas PC is far less toxic and poorly inflammable, but it has a higher viscosity, and a lower dielectric constant than ACN [22, 20]. Hence, when choosing one or the other a comprehensive analysis must be made regarding its pros and cons, when applying to EDLC, to avoid unnecessary risks while keeping a good performance.

#### 1.1.3.3 Ionic liquids

Ionic liquids (ILs) are also known as room temperature molten salts, with melting temperatures at or below room temperature [7]. They are usually made up of organic bulky cations and inorganic or organic charged localized anions, such combination contributes to a low melting point [23, 20]. ILs have attracted much attention because of their non-flammability, negligible vapour pressure, high chemical and thermal stability, and hydrophobicity [21]. Furthermore ILs have an electrochemical stability window of up to 4 V–6 V. Unfortunately, ILs present some drawbacks, such as high viscosity, low ionic conductivity and high costs [20]. Nonetheless, due to their wider voltage window and non-flammability it is expected that many future SCs electrolytes will be ILs or IL-based.

### 1.1.4 Problems to overcome

Since the use and application of EDLCs is relatively new there are some issues that need to be fixed, and probably others that still remain a mystery. These problems are presented in both theory and experiments, as well as in the commercial applications. Vatamanu and Bedrov [24] made a brief review on the molecular simulations of electrode-electrolyte interfaces, electric double layer structure, differential capacitance, and the nano-confined room temperature ionic liquids (RTILs); how they work and in which cases there is room for improvement. Whereas, Zheng et al. [25] investigated the cycling stability and aging of a famous commercial SC (Neescap, 2.7 V/10 F) under various currents and voltages. They found that the capacitance decreases with the increase of the current, and the pore structures and composition diminishes. To minimize the losses of aging components and the over- and underestimation of the electrical properties of EDLCs, works on these topics are essential. Furthermore, works in the pairing of electrodes and electrolytes, with a sustainability approach, needs to be more extensive and universal for comparison issues.

## 1.2 Theoretical models

In this section, the general principles of capacitors, the EDL theory, and of EDLCs are presented. Afterwards, some of the most well known theories that try to explain the charge storage mechanism in the EDL are outlined.

### 1.2.1 Electric double layer capacitor principles

EDLCs or SCs are devices capable of achieving higher power rates than conventional batteries. Despite the fact that EDLCs can provide hundred to thousand times higher power rates in the same volume, they are unavailable to store as much energy as batteries, between three to 30 times lower. Hence, EDLCs are suitable for applications in which power burst are needed but high energy storage capacities are not.

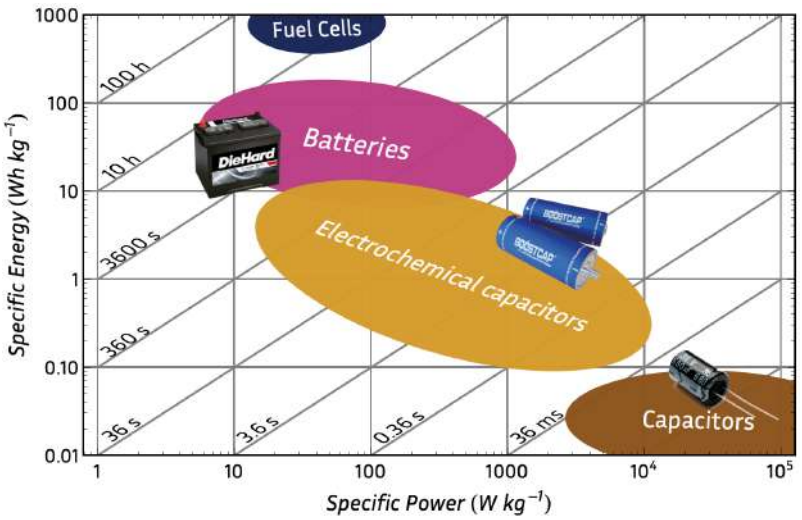


Figure 1.1: Ragone plot. Shows the available energy of an energy storage device for fixed power. Characteristic times correspond to lines with unity slopes. Data taken from Pandolfo *et al* [26].

The power output of EDLCs is lower than that of electrolytic capacitors, and the specific energy is several orders of magnitude higher. EDLCs are of interest in various electric applications because they build up the gap between electrolytic capacitors and batteries. This is graphically observed in the Ragone plot of Fig. 1.1. Fuel cells, batteries, electrochemical capacitors, and capacitors are located in the power-energy plane. Internal losses and/or leakages confine the reach of the regions [27]. Furthermore, the characteristic or charge/discharge time, which is the energy to power ratio ($E = P\,t$), is shown in the diagonal lines.

Not only can EDLCs be charged in a few seconds, but they can also be discharged in the same time. This is of great use for energy recovery systems, such as regenerative braking. In Table 1.1 a comparison between an electrolytic capacitor, an EDLC, and a battery is made.

One of the biggest advantages of EDLCs is their life cycle. They can withstand millions of cycles due to their storage mechanism, that does not involve faradaic reactions. EDLCs store charge physically at the electrode-electrolyte interaction on the electric double layer. However, the main disadvantage they affront is their low operational voltage, that needs to stay low to avoid the chemical decomposition of electrolytes, specially for aqueous-based electrolytes. In Table 1.2 a comparison is made of the main differences between batteries and EDLCs.

| Characteristics | Capacitor | EDLC | Battery |
|---|---|---|---|
| Specific energy ($Whkg^{-1}$) | $< 0.1$ | 1-10 | 10-100 |
| Specific power ($Wkg^{-1}$) | $\gg 10000$ | 500-10000 | $< 1000$ |
| Discharge time | $10^{-6}$ to $10^{-3}$ s | s to min | 0.3-3 h |
| Charge time | $10^{-6}$ to $10^{-3}$ s | s to min | 0.3-3 h |
| Coulombic efficiency (%) | $\sim 100$ | 85-98 | 70-85 |
| Cycle-life (cycles) | Infinite | $> 500000$ | $\sim 1000$ |

Table 1.1: Comparison of different electrochemical energy storage technologies. Taken from Pandolfo and Hollenkamp [28].

| Property | Battery | EDLC |
|---|---|---|
| Storage mechanism | Chemical | Physical |
| Power limitation | Reaction kinetics, mass transport | Electrolytic conductivity |
| Energy storage | High (bulk) | Limited (surface area) |
| Charge rate | Kinetically limited | High, same as discharge rate |
| Cycle life limitations | Mechanically stability, chemical reversibility | Side reactions |

Table 1.2: Comparison of properties of batteries and EDLCs. Taken from Miller and Simon [29].

An EDLC cell is made up of two electrodes with a separator in-between them, which is soaked in an electrolyte to prevent the electric contact between the electrodes. Moreover, the separator should allow the ionic charge transfer, while having a high electric resistance, high ionic conductivity, and a low thickness in order to achieve the highest performance.

As mentioned before, depending on the storage mechanism, three ECs are distinguished: EDLCs, pseudocapacitors and hybrid capacitors. The components of EDLCs are discussed in detail in Section 1.1. Meanwhile, pseudocapacitors are based on conducting polymers or metal oxide based electrodes, and sometimes in functionalized porous carbons, that combine electrostatic and pseudocapacitive charge storage mechanisms, that relies on fast redox reactions occurring on the electrode surface but not in the bulk like batteries. However, as in batteries, the redox reactions lead to mechanical changes shrinking and swelling the electrodes, giving rise to mechanical instability. Therefore, lower cycle lives are a major disadvantage of pseudocapacitors. Meanwhile, hybrid capacitors are conformed of an EDLC and a pseudocapacitor electrode, leading to an electric performance that is in between both electrochemical capacitors.

ECs are charged by applying a potential difference (voltage) across the electrodes, which causes positive and negative charges to migrate toward the surface of opposite polarity. When charged, an EC (as any capacitor) connected in a circuit will act as a voltage source for a short time. Its capacitance, $C$, which is measured in farads, F, is the ratio of electric charge on each electrode, $Q$, to the potential difference between them, $\Delta V$, so that

$$C = \frac{Q}{\Delta V} \tag{1.1}$$

Furthermore, since at a macroscopically level ECs work as regular capacitors. Their capacitance, $C$, also depends on the dielectric constant of the electrolyte, $\varepsilon_r$, the effective thickness of the double layer,

$d$ (distance between charges), and the accessible surface area, $A$,

$$C = \frac{\varepsilon_r \, \varepsilon_0 \, A}{d} \tag{1.2}$$

where $\varepsilon_0$ is the dielectric constant of vacuum.

The energy stored in an ECs is,

$$E = \frac{1}{2} C V^2 \tag{1.3}$$

where $V$ is the cell voltage. As seen in Eq. (1.3), when the voltage and/or the capacitance is increased, the energy density follows as well.

The maximum instantaneous power, $P_{max}$, that an EC is able to deliver, depends on the voltage and on the equivalent series resistance (ESR),

$$P_{max} = \frac{V^2}{4\,ESR} \tag{1.4}$$

The electric current of the EDLC is

$$I = C \frac{\mathrm{d}V}{\mathrm{d}t} \tag{1.5}$$

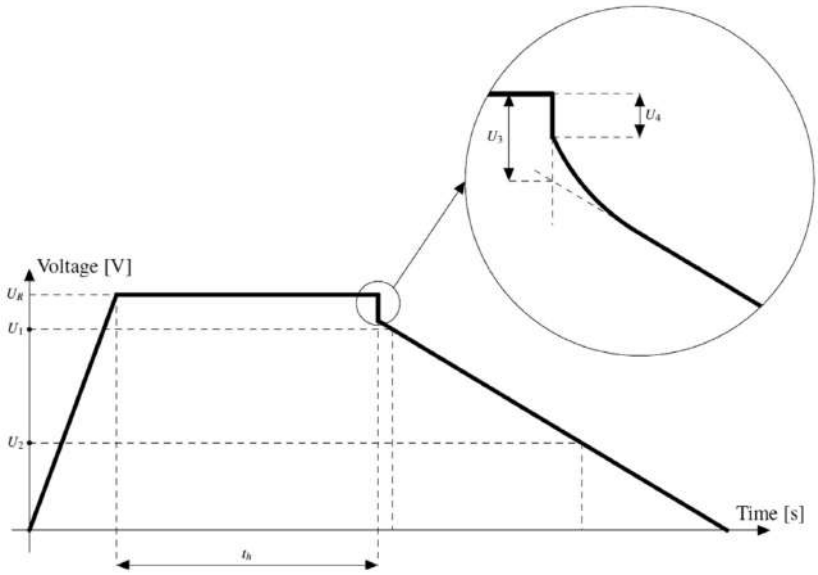


Figure 1.2: Constant current discharge EC cell test. Taken from González *et al.* [9].

The main characteristics of EDLCs are obtained from constant current tests [9]. From the capacitance calculation (integral of the area during the discharge), the ESR, and the equivalent distributed resistance (EDR), which represents the ESR and the resistance in the pores are derived. They are calculated with the notation of Fig. 1.2 as,

$$C = \frac{I_{dis} \, t_{dis}}{U_1 - U_2} \tag{1.6}$$

$$ESR = \frac{U_4}{I_{dis}} \tag{1.7}$$

$$EDR = \frac{U_3}{I_{dis}} \tag{1.8}$$

where the subscript *dis* means discharge. These electric properties and others are mainly determined by electrode materials, electrolytes, separators and current collectors.

### 1.2.2 Electric double layer theories

The interaction between a solid electrolyte and a liquid electrolyte in any surface is governed by a phenomenon called the electrical double layer. "The electrical double layer consist of a layer of electrons, a layer of adsorbed ions, and a diffuse double layer consisting of an ionic atmosphere in which ions of one sign are in defect. This atmosphere of abnormal concentrations of ions falls off rapidly as one recedes from the surface, the half-thickness of the charge density being seldom over 100 Å and usually much less. Finally, there may exist at the interface a thin layer of neutral molecules which, whether they are orientated or not, exert an influence on the thermodynamics properties of the interface (Grahame, 1947)[30]." Therefore, the double layer is the result of an uneven distribution of negative and positive ions or charges that are submerged in-between two layers.

Throughout the years there have been many models that have tried to numerically explain the behavior of the double layer. Beginning with the pioneer works of Helmholtz [31], and Gouy-Chapman [32, 33], to well founded statistical mechanical theories, such as the first principles method (FPM) and the asymptotic method (AM). These are defined and described below.

#### 1.2.2.1 Helmholtz model

The first model of the electric double layer was proposed by Helmholtz [31] in 1879. He considered the ordering of positive and negative charges in a rigid fashion on both sides of the interface, with no interactions stretching any more into the solution. He also assumed that the charge of the electrode is neutralized by the charge of the electrolyte at an atomic distance $d$ from the plane, so the dependence of the mean electrostatic potential and the surface distance is considered to be linear. The model is similar to that of a two-plate conventional electrolytic capacitor. Unfortunately, even though this is the simplest model, two principal defects are found. Firstly, the interactions that occur further from the electrode are neglected. Secondly, it does not take into consideration the dependence of the electrolyte concentration. Therefore, this model catastrophically fails to explain the electrode-electrolyte interface.

#### 1.2.2.2 Gouy-Chapman model

In contrast, the model of the diffuse layer or the Gouy[32] and Chapman[33] model, which was developed independently, considered a double layer model in which the applied potential and electrolyte concentration was taken into account. The model originates from the assumption that the charge of the electrode is not rigid and that the co-ions and counter-ions in the double layer are subject to an electric and thermal field. As a result, the counter-ions tend to accumulate on the surface and once its distribution is restored, the co-ions re-establish the homogeneity of the charge. This model is based on the Maxwell-Boltzmann distribution and on the Poisson law, hence it is commonly referred as the Poisson-Boltzmann model. However, the model fails since it does not consider the size of the ions in its formulation, regarding them as point charges, and hence, allowing them to approach excessively to the surface of the electrodes, at such degree that it is not physically possible, because of their specific size.

#### 1.2.2.3 Stern model

Stern [34] proposed a hybrid model, combining the Helmholtz model and the Gouy-Chapman model. He took into consideration the ions size by recognizing two regions of ions distributions. A rigid one, close to the electrode (also known as the compact layer of Helmholtz or the inner Helmholtz plane (IHP)); and a diffusively spread one throughout the concentration (called the diffuse layer or the outer Helmholtz plane (OHP)). Therefore, the capacitance at an electrode-electrolyte interface in

the electrical double layer, $C_{dl}$, is regarded as a two component capacitance, the compact double layer capacitance, $C_H$, and the diffuse double layer capacitance, $C_{diff}$. Hence, the conjugate of the overall double-layer capacitance is the sum of the conjugate components

$$\frac{1}{C_{dl}} = \frac{1}{C_H} + \frac{1}{C_{diff}} \tag{1.9}$$

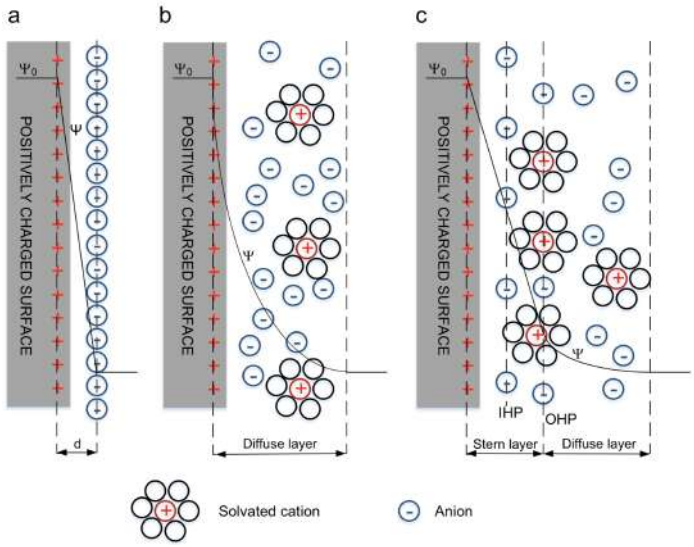


Figure 1.3: EDL models, (a) Helmholtz model, (b) Gouy-Chapman model, and (c) Stern model. Taken from González *et al.* [9].

In Fig. 1.3 the models explained above are illustrated, where $\Psi$ represents the potential, and $\Psi_0$ is the electrode potential. As we discuss later the Gouy-Chapman model, with the Stern correction is a good model for some specific systems conditions.

#### 1.2.2.4 First principles method

In the construction of statistical mechanical theories for the electrical double layer at a charged, planar interface of infinite extension, two methods, based on the well established integral equations approach, are commonly used. Both are based on generalizations of existing electrolyte theories [35, 36].

The first principles methods consists of the following steps:

(a) The system study is defined as a fluid formed by $N$ charged particles, composed by $n$ different species, immersed in a solvent of dielectric constant $\varepsilon$. So they are next to a hard, charged wall of infinite length, that is regarded as an external field.

(b) The interaction potential of the system $U_N$ is composed as

$$U_N = \sum_{i<j}^{N} U_{ij} + \sum_{i=1}^{N} U_i \tag{1.10}$$

where $U_{ij}$ is the interaction potential between particles $i$ and $j$ and $U_i$ is the interaction potential between particle $i$ and the external field.

(c) Now, following one by one all the steps employed in the derivation of a given ionic solution theory, but applying the new potential $U_N$, an electrical double layer theory is obtained.

(d) Finally, the potential $U_i$ is almost always taken as

$$U_i = -\frac{4\,\pi\,e\,z_i\,\sigma}{\varepsilon}\,x + A \tag{1.11}$$

where $e$ is the electronic charge, $z_i$ is the valence of ion $i$, $\sigma$ is the charge density on the wall, $x$ is the perpendicular distance from the ion to the wall and $A$ is an arbitrary constant which depends on the choice of the zero potential.

#### 1.2.2.5 Asymptotic method

The other method used in the derivation of the electrical double layer equations is the asymptotic method, which consists of the following steps [35]:

(a) The system of study is thought as a fluid formed by $N$ small, charged particles, of $n$ different ions species, next to a large spherical particle, which is uniformly charged on its surface. Such that the $N+1$ particles are immersed in a solvent of dielectric constant $\varepsilon$.

(b) The interaction potential is

$$U_N = \sum_{i<j}^{N+1} U_{ij} \tag{1.12}$$

where $U_{ij}$ is the interaction potential between particles $i$ and $j$

(c) Now, this electric potential $U_N$ is no different than the existing in an ionic solution. Hence, any of the ionic solution theories can be used to study this system. Although, if the sphere is sufficiently large, in principle it should be seen by the ions as a planar wall. Therefore, by taking the limit of an infinite radius and zero concentration for one of the species in a given ionic solution theory, one can obtain an electrical double layer.

#### 1.2.2.6 Integral equations

The Poisson-Boltzmann equation (PBE) for inhomogeneous charged fluids is a charge balance. Quite generally, in the soft condensed matter physics, different balance equations are solved to obtain the structure of the charged fluid (electrolyte), next to an external field of a given geometry. In this thesis we will solve the linear Poisson-Boltzmann equation, for a point ion electrolyte which is next to electrodes of different topologies and geometries. To test the validity of our results we will compare them with published integral equation solutions of the restricted primitive model (RPM) for an electrolyte, where the ionic size is considered [37, 38]. Sometimes we will also compare our results with existing Monte Carlo computer experiments.

In the RPM the particles are taken to be charged, hard spheres, with different charges. A generalization of this model is the primitive model (PM), where different ionic sizes are considered, and such that one of the species is much larger than the other two, in order to model a macroions dispersion at finite concentration [39, 40, 41, 42].

One way of calculating the structure of the ionic distribution is through the multicomponent Ornstein-Zernike (OZ) equation. The multi-component Ornstein-Zernike (OZ) equations for a homogeneous fluid of $n+1$ species are

$$h_{ij}(\mathbf{r}_{12}) = c_{ij}(\mathbf{r}_{12}) + \sum_{l=1}^{n+1} \rho_l \int_V h_{il}(\mathbf{r}_{13})\, c_{jl}(\mathbf{r}_{23})\, \mathrm{d}\mathbf{r}_3\,, \qquad \text{for} \quad i,j = 1,2,\ldots,n+1 \tag{1.13}$$

where, $\rho_l$ is the number density of species $l$, while, $h_{ij}(\mathbf{r}_{12}) \equiv g_{ij}(\mathbf{r}_{12}) - 1$ is the total correlation function, and $c_{ij}(\mathbf{r}_{12})$, is the direct correlation function, both for particles 1 and 2, of species $i$ and $j$, with position vectors $\mathbf{r}_1$ and $\mathbf{r}_2$, respectively. And, $g_{ij}(\mathbf{r}_{12})$ is the pair correlation function, also referred to as the *radial distribution function* (RDF), which gives the probability density of finding a particle 2, of species $j$, at the distance $\mathbf{r}_{12}$, from the central particle 1, of species $i$, $\quad \cdot \ni \cdot \quad \mathbf{r}_{12} = \mathbf{r}_2 - \mathbf{r}_1$. The OZ equation is a probability balance conservation condition, which also guaranties a constant chemical potential in the whole system [43]. To solve Eq. (1.13), closure relations for the direct correlation functions, $c_{ij}(\mathbf{r}_{12})$ and $c_{jl}(\mathbf{r}_{23})$, are needed. These functions are basically approximations for a quasi-particle, in the context of many-body theory [44]. Among others, two different closure approximations can be employed for $c_{ij}(\mathbf{r}_{12})$, i.e, the hypernetted-chain (HNC),

$$c_{ij}(\mathbf{r}_{12}) = h_{ij}(\mathbf{r}_{12}) + \beta\, u_{ij}(\mathbf{r}_{12}) - \ln(g_{ij}(\mathbf{r}_{12})), \tag{1.14}$$

and the mean spherical approximation (MSA),

$$c_{ij}(\mathbf{r}_{12}) = -\beta\, u_{ij}(\mathbf{r}_{12}). \tag{1.15}$$

In particular a mixture of these two closures has been successfully used in the past [45, 46, 36], i.e., with the HNC approximation in the first right hand side term of Eq. (1.13), for $|\mathbf{r}_{12}| > a_{ij}$, and the MSA in the convolution integral. In such case Eq. (1.13) is called the HNC/MSA equation. The MSA is defined as follows, $h_{ij}(\mathbf{r}_{12}) = -1$, for $|\mathbf{r}_{12}| < a_{ij}$, and $c_{ij}(\mathbf{r}_{12}) = -\beta\, u_{ij}(\mathbf{r}_{12}), \quad |\mathbf{r}_{12}| > a_{ij}$, where $a_{ij} \equiv (a_i + a_j)/2$, and $a_i$ and $a_j$ are the diameters of the particles of species $i$ and $j$, respectively.
In Eqs. (1.14) and (1.15), $\beta \equiv 1/k\,T$, being $k$ the Boltzmann constant and $T$ the absolute temperature. Meanwhile, $u_{ij}$ is the direct electrostatic potential, i.e.,

$$u_{ij}(r) = \begin{cases} \infty & r < a_{ij} \\ \frac{q_i\, q_j}{\varepsilon\, r} & r \geq a_{ij} \end{cases}, \qquad \text{with } i, j = 1, ..., n+1 \tag{1.16}$$

where $r$ is the particles' distance. Equation (1.13), together with Eqs. (1.14) and (1.15), are the HNC/MSA integral equations for a homogeneous fluid. Notice however, that the expression for $c_{jl}(\mathbf{r}_{23})$, in the convolution of Eq. (1.13), considers also the region of $|\mathbf{r}_{12}| < a_{ij}$. we will come back to this point in a few lines. For a $n+1$ species, homogeneous fluid, Eq. (1.13) become $(n+1)^2$ coupled integral equations. However, taking into account that $h_{ij}(\mathbf{r}_{12}) = h_{ji}(\mathbf{r}_{21})$, the total number of equations is reduced by $n(n+1)/2$, and we end with $(n+1)(n+2)/2$ independent, coupled, integral equations.

Now, using the fact that particles and fields are equivalent, it has been shown [35, 47, 48, 36], that many-body correlations, inhomogeneous fluids equations, can be obtained directly from equations for homogeneous fluids, by simply considering one of the species in the fluid, at zero concentration, as the source of the external field. Hence, choosing the species $(n+1)$, as the source of an external field, renaming it as $\gamma \equiv n+1$, and taking $\rho_\gamma \to 0$, Eq. (1.13) become

$$h_{ij}(\mathbf{r}_{12}) = c_{ij}(\mathbf{r}_{12}) + \sum_{l=1}^{n} \rho_l \int_V h_{il}(\mathbf{r}_{13})\, c_{jl}(\mathbf{r}_{23})\, \mathrm{d}\mathbf{r}_3 \tag{1.17}$$

with $i, j = 1, 2, \ldots, n, \gamma$, and where the summation over the convolution now runs only up to $n$, and we have $(n+1)^2 - 1$ equations. However, considering the symmetry relation $h_{ij}(\mathbf{r}_{12}) = h_{ji}(\mathbf{r}_{21})$, the total number of equations is reduced by $n(n+1)/2$, and we end with $(n+1)(n+2)/2 - 1$ independent, coupled, integral equations, of which $n(n+1)/2$ equations, correspond to the bulk, i.e., away from the external field:

$$h_{ij}(\mathbf{r}_{12}) = c_{ij}(\mathbf{r}_{12}) + \sum_{l=1}^{n} \rho_l \int_V h_{il}(\mathbf{r}_{13})\, c_{jl}(\mathbf{r}_{23})\, \mathrm{d}\mathbf{r}_3 \qquad \text{for} \quad i,j = 1,...,n \tag{1.18}$$

and $n$ equations are for the inhomogeneous part, i.e., for the fluid structure close to the external field:

$$h_{\gamma j}(\mathbf{r}_{12}) = c_{\gamma j}(\mathbf{r}_{12}) + \sum_{l=1}^{n} \rho_l \int_V h_{\gamma l}(\mathbf{r}_{13}) c_{jl}(\mathbf{r}_{23})\, \mathrm{d}\mathbf{r}_3 \qquad \text{for} \quad j = 1,...,n,\gamma \tag{1.19}$$

where it is taken into account that, at infinite dilution of the $\gamma$-species, $h_{\gamma\gamma}(\mathbf{r}_{12}) = 0$. The species $\gamma$ can be a particle/electrode of any geometry, such as a planar, cylindrical or spherical electrodes, or a slit, cylindrical or spherical pores.

If in the bulk equations, Eq. (1.18), the MSA approximation for the direct correlation function, $c_{ij}(\mathbf{r}_{21})$, is used in *both* the first term of its right hand side, and in the convolution integral, they can be analytically solved [49, 50, 51]. For this purpose, the complete definition of the MSA is needed, as defined above. This solution will give analytical expressions for $c_{li}(\mathbf{r}_{31})$.

If $c_{li}(\mathbf{r}_{31})$, inside the integral in Eq. (1.19), is taken to be given by the MSA, for which there is an analytical solution for charged fluids [51], the HNC/MSA integral equations are obtained for an homogeneous fluid of $n$-species. The use of the MSA allows to have analytical kernels in Eq. (1.19). A detailed account of the derivation of Eq. (1.19) is given in Manzanilla-Granados and Lozada-Cassou [41].

In this thesis we will compare our Poisson-Boltzmann results with this approach. Other approximations and/or combinations for $c_{ij}(\mathbf{r}_{12})$, in Eq. (1.18), are of course possible [36]. We will not discuss them here. For the inhomogeneous equations, Eq. (1.19), the HNC closure is used, for the $c_{\gamma j}(\mathbf{r}_{12})$, in the first term of its right hand side, but the MSA closure for $c_{jl}(\mathbf{r}_{23})$, in the convolution integral. Notice that the MSA direct correlation functions, $c_{jl}(\mathbf{r}_{23})$, in the convolution integral of Eq. (1.19), are obtained from Eq. (1.18), i.e., using, in Eq. (1.18), $h_{ij}(\mathbf{r}_{12}) = -1$, for $|\mathbf{r}_{12}| < a_{ij}$, and $c_{ij}(\mathbf{r}_{12}) = -\beta\, u_{ij}(\mathbf{r}_{12}), \quad |\mathbf{r}_{12}| > a_{ij}$. The total $(n+1)^2 - 1$ equations can be numerically solved with finite elements numerical methods [52, 53]. We refer to this system of coupled, non-linear integral equations, Eqs. (1.18) and (1.19), as the HNC/MSA inhomogeneous equations, for n-species next to an external field, and to Eq. (1.13), together with the HNC and MSA approximations, Eqs. (1.14) and (1.15), as the HNC/MSA homogeneous equations for $(n+1)$ species. The homogeneous and inhomogeneous HNC/MSA equations have been solved in the past for homogeneous and inhomogeneous RPM [54, 36, 55, 56] and PM [57, 58, 59] electrolyte solutions, with good agreement with computer simulations, and for inhomogeneous [60, 61], and homogeneous [39, 40] macroions solutions at finite concentration, as a model for colloidal dispersions.

As pointed out above, using the equivalence between particles and fields, one can readily obtain integral equations for inhomogeneous fluids from homogeneous fluids equations, by assuming one of the species to be at infinite dilution, and as the source of the external field. The contrary is also true, one can derive homogeneous fluids integral equations, from inhomogeneous fluids equations, by assuming the external field as just another particle of the fluid [35, 47, 48, 62, 36]. Using this second approach to derive integral equations for an homogeneous colloidal suspension, the HNC/MSA integral equations for an electrolyte next to a solid electrode or a pore of different geometries can be calculated. In this thesis we will compare our Poisson-Boltzmann solutions with HNC/MSA results from the literature.

#### 1.2.2.7 Monte Carlo methods

Monte Carlo (MC) methods are a branch of mathematics concerned with experiments on random numbers. There are of two types called probabilistic or deterministic, according to whether or not they are directly concerned with the behaviour and outcome of random processes. The simplest MC approach, for a probabilistic problem is to observe random numbers, chosen in such a way that they directly simulate the physical random processes of the original problem, and to infer the desired solution from the behavior of the random numbers. This artificial data may suit better if it is easier to amass, or if it lets us vary the statistics to an extent that our phenomenon will not permit [63].

On the other hand, the MC approach to deterministic problems is to exploit the strength of theoretical mathematics while one avoids its associated weaknesses, by replacing theory by experiment whenever the former falters. As an example, we may have a deterministic problem which can be formulated in theoretical language but it cannot be solved by theoretical means. Despite the fact that the problem has no direct association with random processes, the theory exposes its underlying structure, we may recognize that this structure or formal expressions also describe some unrelated random process, and hence it may be solved numerically by MC simulations of this concomitant probabilistic problem. This technique of solving a given problem by MC simulations of a different problem has sometimes been called sophisticated MC.

It is worth noting, that MC answers are uncertain because they arise from raw observational data consisting of random numbers but they can nevertheless be useful if we can manage to make the uncertainty fairly negligible. Although, the basic procedure of the MC method is the manipulation of random numbers, they should not be employed prodigally. Each random number is a potential source of added uncertainty in the final result, and it is useful to scrutinize each component of the MC experiment to see whether that part can or cannot be replaced by an exact theoretical analysis. Here, we will not get into any further details of the Monte Carlo method. However, we point out that this technique has been successfully tested, since long time ago, for charged homogeneous [64, 65] and inhomogeneous systems [66, 67, 46], and in particular for spherical [68, 69], and cylindrical [70, 71, 72, 73] electrodes.

Of course, the accuracy of the experiment improves significantly by increasing the statistics, i.e., by augmenting the number of particles in the simulation, while assuring the conservation of the charge electroneutrality of the system.

#### 1.2.2.8 Geometrical topology

In general, the properties of the electrode-electrolyte interface strongly depend on the geometry of the electrode, alongside other parameters of the system. This strong dependency originates from the ions' confinement due to the electrodes topology, as an open topology do not constrain the ions as a close one does. Therefore, all the electric parameters of an electrode-electrolyte interface are influenced by the electrodes' topology. In particular, the capacitance strongly depends on the shape and structure of the electrodes. This is the case of planar, cylindrical and spherical nano-electrodes, which having different geometries, nevertheless all are topologically equivalent. This is not the case of the slit, cylindrical and spherical nano-pores, all of which belong to a different topology. Here we will briefly review some concepts of geometric topology, and give a simple topological classification of the nano-electrodes studied in this thesis.

Topology (from the Greek $\tau\acute{o}\pi o\varsigma$, 'place', and $\lambda\acute{o}\gamma o\varsigma$, 'study') is a branch of mathematics, with several subbranches such as differential, algebraic, combinatorial and geometric topologies. Geometric topology must not be confused with geometry, though the two are akin to each other in many aspects. Geometry studies the geometric properties of objects, such as lines, planes, circles, cubes, cylinders, various types of curves and surfaces, and so on. In order to define a geometric property it is needed to recall the concept of congruence: Two objects $A$ and $B$ are said to be congruent to each other if there

exists a bijection $f : A \to B$ which preserves all distances in the sense that $d(x, y) = d(f(x), f(y))$ for all pairs $\{x, y\}$ of points in $A$, where $d$ is used to denote the distance between points. Such a bijection, when it exists, is called a congruence. Therefore, a geometric property is invariant under congruence, such as volume, area, and curvature. Meanwhile, in topology the 'objects', called 'topological spaces', are classified by means of homeomorphism: Let $A$, $B$ be subsets of euclidean spaces. A homeomorphism from $A$ to $B$ is a bijection $f : A \to B$ such that both $f$ and its inverse are continuous. When such $f$ exists, $A$ and $B$ are said to be homeomorphic to each other. Hence, a property or an attribute of an object, which is invariant under homeomorphisms, is topological in character [74, 75]. It is now clear that the difference between geometry and topology is wraped up to the comparison of congruence and homeomorphism. Therefore, two straight lines of lengths 1 and 2 are homeomorphic to each other but not congruent. Thus these two objects that look distinct for a geometer are the same for a topologist. Loosely speaking, stretching or shrinking does not affect the topological properties of the object although they undoubtedly change its geometric properties. However cutting or gluing (or piercing or cutting, for higher dimensions) some portions of the original object does change its topological properties, and therefore such object becomes different from the original one.

The word *homeomorphism* comes from the Greek words *όμοιος* (homoios) 'similar or same' and *μορφή* (morphē) 'shape or form', was introduced to mathematics by Henri Poincaré in 1895. Other important topological concepts are *homotopic* (from Greek *όμός*, 'same or similar' and *τόπος*, 'place'), and *genus* (latin word for origin, birth).

Two functions are said to be homotopic if one can be 'continuously deformed' into the other. In general, homeomorphism is a more basic topological equivalence than homotopy. Genus refers to the number of holes in a surface, i.e., a sphere or a bowl have no holes (genus 0), a coffee cup or a doughnut have one hole (genus 1), a pair of spectacles has two holes (genus 2), a pretzel can have three holes (genus 3), etc. To see the difference between homeomorphism and homotopy is a bit more mathematically elaborated. However, in general homotopy equivalence is a coarser relationship than homeomorphism; for example the letters 'A, R', 'D, O', and 'P, Q' are correspondingly homeomorphic, but the letters 'A, R, D, O, P, Q' are all homotopic. All these letters are genus 1, whereas, for example, the letter 'B', is genus 2, and is not homeomorphic, and not homotopic to any of the letters 'A, R, D, O, P, Q'.

Thus, in a very simple way, topology is concerned with the properties of a geometric object that are preserved under continuous deformations, such as stretching, twisting, crumpling and bending, *but not tearing or gluing*. A topological space is a set endowed with a structure, called a topology, which allows defining continuous deformation of subspaces, and, more generally, all kinds of continuity. Euclidean spaces, and, more generally, metric spaces are examples of a topological space, as any distance or metric defines a topology. The deformations that are considered in topology are homeomorphisms and homotopies. A property that is invariant under such deformations is a topological property. Basic examples of topological properties are: the dimension, which allows distinguishing between a line and a surface; compactness, which allows distinguishing between a line and a circle; connectedness, which allows distinguishing a circle from two non-intersecting circles. A topological space X is said to be disconnected if it is the union of two disjoint non-empty open sets. Otherwise, X is said to be connected.

Hence, with these definitions, clearly, the solid planar, cylindrical and spherical nano-electrodes are homeomorphic and homotopic, of genus 0, and thus, they are topologically equivalent, whereas the cylindrical nanopore, the spherical nanopore and the slit, they are all topologically different among them, and with the solid nano-electrodes. The cylindrical nanopore is genus 1, while the spherical nanopore is a 3D annulus, i.e., one sphere, within another sphere, such that the shell is a connected space, and the slit are two disconnected topological spaces.

# Chapter 2

# The single electrical double layer for solid electrodes

The interaction between a solid electrode and a liquid electrolyte in any surface is governed by a phenomenon called the electrical double layer. The EDL consists of a distribution of positive and negative charge. Next to the surface of a positively charged electrode, mainly negative charges are adsorbed, which follows by a diffusely spread distribution of positive and negative charges. This diffuse layer of ions are predominantly negative ions, until this distribution is symmetrical far enough from the plane, i.e., after the electrode's electrical field is canceled by the ionic induced charge. This EDL generates an electric potential profile, all the way from the electrode surface up to the bulk of the electrolyte solution. Therefore, the electrical double layer is the result of an uneven distribution of negative and positive ions or charges that are submerged in-between two layers, i.e., between the electrode's surface of a given charge, and the bulk solution of zero charge.

In this chapter the linearized Poisson-Boltzmann equation with the Stern restriction (LPBS) for the single electrical double layer (SEDL) is solved for solid planar, cylindrical and spherical electrodes, to obtain the co-ion and counter-ions distribution functions, i.e., the positive and negative ions reduced concentration profiles (RCP). With the RCP, the mean electrostatic potential, the surface charge density, and the differential capacitance are obtained for different system's parameters. In addition, for the solid planar electrode, the non-linearized Poisson-Boltzmann equation with the Stern restriction (nLPBS) is solved as well.

## 2.1 The single electrical double layer of a solid planar electrode

The SEDL for a solid planar electrode is obtained from the Poisson-Boltzmann equation with the Stern restriction for a plane electrode (p-PBS). Its model is shown in Fig. 2.1. The p-PBS is solved for a symmetric electrolyte by two different approaches. The linear p-PBS (p-LPBS) and non-linear p-PBS (p-nLPBS) are solved analytically, assuming a small and any potential, respectively. The analytical expressions of the mean electrostatic potentials, the charge densities, the co-ion and counter ion distribution functions, and the capacitances of the p-LPBS and p-nLPBS are found, and numerically calculated for some system's parameters.

The Poisson-Boltzmann equation (PB-eq) is given by [2, 76]

$$\nabla^2\psi(\vec{r}) = -\frac{4\,\pi\,\rho_{el}(\vec{r})}{\varepsilon} \tag{2.1}$$

where $\psi$ is the mean electrostatic potential distribution [statV], $\rho_{el}$ is the electric charge concentration given in CGS units and $\varepsilon$ is the dielectric constant of the medium. Equation (2.1) is a charge balance,

i.e., it is the differential form of the Gauss' law, where the enclosed charge, at the distance $\vec{r}$ away from the electrode, is given by the Boltzmann distribution of charge, in the canonical statistical mechanics ensemble, and gives the probability of finding the charge density at an arbitrary point, $\vec{r}$.

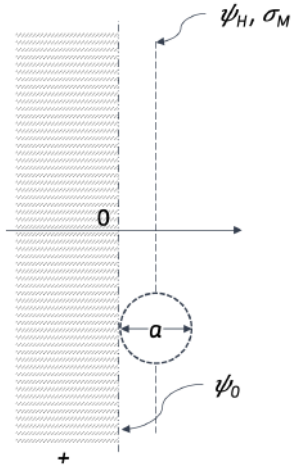


Figure 2.1: Geometry of a solid planar electrode.

### 2.1.1 The linear PB equation for the single electrical double layer of a solid planar electrode

The PB-eq can be linearized at different stages. That is, it can be linearized directly from the PB-eq at any step when solving the equation, or from the solution itself. Here, the linearization is performed on the formulation of the PB-eq.

By symmetry, the mean electrostatic potential that is formed in the interaction between an electrolyte and a planar electrode depends only on the $x$ axis. From the Stern restriction, the mean electrostatic potential is divided into two intervals $0 \leq x < \frac{a}{2}$ and $x \geq \frac{a}{2}$, as seen in Fig. 2.1. The first interval is ruled by the Laplace equation, whereas the second follows the PB-eq. Hence, the mean electrostatic potential is characterized by,

$$\nabla^2\psi(\vec{r}) = \frac{\mathrm{d}^2\psi}{\mathrm{d}x^2} = \begin{cases} 0 & \text{if } 0 \leq x < \frac{a}{2} \\ -\frac{4\,\pi\,\rho_{el}(x)}{\varepsilon} & \text{if } x \geq \frac{a}{2} \end{cases} \tag{2.2}$$

where the electric charge concentration is given by

$$\rho_{el}(x) = z\,e\,(n_+(x) - n_-(x)) \tag{2.3}$$

while $z$ is the valence of the ion, $e$ is the electron charge, and $n_+(x)$ and $n_-(x)$ are the charge concentration profiles of co-ions and counter-ions, and they are given by the Maxwell-Boltzmann distribution by,

$$\left.\begin{aligned} n_-(x) &= n\exp(z_-e\,\psi(x)/k\,T) \\ n_+(x) &= n\exp(-z_+e\,\psi(x)/k\,T) \end{aligned}\right\} \tag{2.4}$$

The Maxwell-Boltzmann distribution is used in order to take into account the thermal equilibrium of co-ions and counter-ions. By the assumption that the average concentration of co-ions and counter-ions at a given point can be calculated by the mean electrostatic potential at the same point. In order

to simplify the solution of the mean electrostatic potential, we will delimit our problem to symmetric electrolytes. Hence, $z = z_+ = z_-$, and $n\,[\mathrm{cm}^{-3}] = n_+ = n_-$ is the ions concentration away from the surface, i.e., it is the salt bulk concentration, and it is given by $n = \rho_0 \times 10^{-3}\,\mathrm{N_A}$, where $\rho_0$ is the molar concentration of the electrolyte, and $\mathrm{N_A}$ is the Avogadro number. Thus, Eq. (2.2) becomes

$$\nabla^2\psi(\vec{r}) = \frac{\mathrm{d}^2\psi}{\mathrm{d}x^2} = \begin{cases} 0 & \text{if } 0 \le x < \frac{a}{2} \\ \frac{8\,\pi\,n\,z\,e}{\varepsilon}\sinh\!\left(\frac{z\,e}{k\,T}\psi(x)\right) & \text{if } x \ge \frac{a}{2} \end{cases} \tag{2.5}$$

In Eq. (2.5), the symmetry of the system in the $y$ and $z$ coordinates has been considered in the Laplacian operator. Now, the linearization is performed by assuming that we have a mean electrostatic potential that is small enough ($z\,e\,\psi(x)/k\,T \ll 1$), such that Eq. (2.2) is almost equal to,

$$\frac{\mathrm{d}^2\psi}{\mathrm{d}x^2} = \begin{cases} 0 & \text{if } 0 \le x < \frac{a}{2} \\ \kappa^2\,\psi(x) & \text{if } x \ge \frac{a}{2} \end{cases} \tag{2.6}$$

where $\kappa$ [$\mathrm{cm}^{-1}$] is the inverse Debye length and it is given by

$$\kappa = \sqrt{\frac{8\,\pi\,\rho_0 \times 10^{-3}\,\mathrm{N_A}\,e^2\,z^2}{\varepsilon\,k\,T}} \tag{2.7}$$

The four boundary conditions needed to solve Eq. (2.5) are the same for the different solid electrodes with slight modifications, i.e.,

- The mean electrostatic potential at the surface of the electrode, $x = 0$, is equal to $\psi_0$ ($\psi(0) = \psi_0$).
- The mean electrostatic potential at the distance of maximum approach for the ions, $x = \frac{a}{2}$, is equal to $\psi_H$ ($\psi(\frac{a}{2}) = \psi_H$).
- The mean electrostatic potential at infinity is zero ($\psi(\infty) = 0$).
- From the Gauss' law we have that at the distance of maximum approach, $x = \frac{a}{2}$, the derivative of the potential against the distance is $\frac{\mathrm{d}\psi}{\mathrm{d}x} = -\frac{4\,\pi\,\sigma_M}{\varepsilon}$. Which involves that the induced surface charge density at such distance is equal to the surface charge density of the electrode ($\sigma(\frac{a}{2}) = \sigma_M$).

Solving Eq. (2.6) with these boundary conditions we find that the mean electrostatic potential is given by,

$$\psi(x) = \begin{cases} \psi_H\,\left[1 + \kappa(\frac{a}{2} - x)\right] & \text{if } 0 < x \le \frac{a}{2} \\ \psi_H\,e^{\kappa\,(\frac{a}{2} - x)} & \text{if } x \ge \frac{a}{2} \end{cases} \tag{2.8}$$

where $\psi_H$ [statV] is given by

$$\psi_H = \frac{4\,\pi\,\sigma_M}{\varepsilon\,\kappa} \tag{2.9}$$

Meanwhile, the surface charge density, at the distance $x$ from the coordinates' origin, $\sigma_P(x)$, within the Poisson-Boltzmann approximation is

$$\sigma_P(x) = -\int_x^\infty \rho_{el}(t)\,\mathrm{d}t = \frac{\varepsilon\,\kappa}{4\,\pi}\,\psi_H\,e^{\kappa\,(\frac{a}{2} - x)} \tag{2.10}$$

Whereas, for the Laplace interval, the induced surface charge density is equal to zero due to the ion's size restriction. Hence, using the relation of Eq. (2.9), the induced surface charge density is

$$\sigma_P(x) = \begin{cases} 0 & \text{if } 0 \le x < \frac{a}{2} \\ \sigma_M\,e^{\kappa\,(\frac{a}{2} - x)} & \text{if } x \ge \frac{a}{2} \end{cases} \tag{2.11}$$

Notice that $\sigma_P(x) = \varsigma_P + \int_{a/2}^{x} \rho_{el}(t)\,\mathrm{d}t$, i.e., the electrode's surface charge, $\varsigma_P$, plus the induced charge, in the surrounding electrolyte, from $t = a/2$ to $t = x$.

The co-ion and counter-ion distribution functions in the Laplace interval is equal to zero due to the ion's size restriction. Whereas, for $x \geq \frac{a}{2}$, the co-ion and counter-ion distribution functions are obtained from the mean electrostatic potential in Eq. (2.8) by

$$g_+(x) = \exp\left(-\frac{z\,e\,\psi(x)}{k\,T}\right) \tag{2.12}$$

$$g_-(x) = \exp\left(\frac{z\,e\,\psi(x)}{k\,T}\right) \tag{2.13}$$

Hence, substituting $\psi(x)$ and simplifying, we obtain

$$g_+(x) = \begin{cases} 0 & \text{if } 0 \leq x < \frac{a}{2} \\ \exp\left(-\frac{z\,e}{k\,T}\,\psi_H\,e^{\kappa\left(\frac{a}{2}-x\right)}\right) & \text{if } x \geq \frac{a}{2} \end{cases} \tag{2.14}$$

$$g_-(x) = \begin{cases} 0 & \text{if } 0 \leq x < \frac{a}{2} \\ \exp\left(\frac{z\,e}{k\,T}\,\psi_H\,e^{\kappa\left(\frac{a}{2}-x\right)}\right) & \text{if } x \geq \frac{a}{2} \end{cases} \tag{2.15}$$

The total differential capacitance is the sum of the differential capacitances in both intervals and it is given by

$$C_T = \left[\frac{4\,\pi}{\varepsilon\,\kappa}\,\left(2 + \frac{\kappa\,a}{2}\right)\right]^{-1} \tag{2.16}$$

### 2.1.2 The non-linear PB equation for the single electrical double layer of a solid planar electrode

Now, the non-linear PB-eq in Eq. (2.2), is directly solved using the boundary conditions of Section 2.1.1. As derived in Appendix A.1, the solution of the non-linear Laplace and Poisson-Boltzmann equations are,

$$\psi(x) = \begin{cases} \frac{2\,\kappa\,k\,T}{z\,e}\sinh\left(\frac{z\,e\,\psi_H}{2\,k\,T}\right)\left(\frac{a}{2} - x\right) + \psi_H & \text{if } 0 \leq x \leq \frac{a}{2} \\ \frac{2\,k\,T}{z\,e}\ln\left(\frac{\left(\exp\left(\frac{z\,e}{k\,T}\,\frac{\psi_H}{2}\right)+1\right)+\left(\exp\left(\frac{z\,e}{k\,T}\,\frac{\psi_H}{2}\right)-1\right)e^{\kappa\left(\frac{a}{2}-x\right)}}{\left(\exp\left(\frac{z\,e}{k\,T}\,\frac{\psi_H}{2}\right)+1\right)-\left(\exp\left(\frac{z\,e}{k\,T}\,\frac{\psi_H}{2}\right)-1\right)e^{\kappa\left(\frac{a}{2}-x\right)}}\right) & \text{if } x \geq \frac{a}{2} \end{cases} \tag{2.17}$$

where $\kappa$ [cm$^{-1}$] is the inverse Debye length in Eq. (2.7), and $\psi_H$ [statV] is given by

$$\psi_H = \frac{2\,k\,T}{z\,e}\sinh^{-1}\left(\frac{2\,\pi\,z\,e\,\sigma_M}{\varepsilon\,\kappa\,k\,T}\right) \tag{2.18}$$

Meanwhile, the surface charge density, at the distance $x$ from the coordinates' origin, $\sigma_P(x)$, within the Poisson-Boltzmann approximation is

$$\sigma_P(x) = -\int_x^{\infty} \rho_{el}(x)\,\mathrm{d}x = \frac{\varepsilon\,\kappa\,k\,T}{\pi\,z\,e}\,\frac{\left(\exp\left(\frac{z\,e}{k\,T}\,\psi_H\right)-1\right)\,e^{\kappa\left(\frac{a}{2}-x\right)}}{\left(\exp\left(\frac{z\,e}{k\,T}\,\frac{\psi_H}{2}\right)+1\right)^2 - \left[\left(\exp\left(\frac{z\,e}{k\,T}\,\frac{\psi_H}{2}\right)-1\right)\,e^{\kappa\left(\frac{a}{2}-x\right)}\right]^2} \tag{2.19}$$

Whereas, for the Laplace interval, the induced surface charge density is equal to zero due to the ion's size restriction of the Stern model. Hence, the induced surface charge density is

$$\sigma_P(x) = \begin{cases} 0 & \text{if } 0 \le x < \frac{a}{2} \\ \frac{\varepsilon\,\kappa\,k\,T}{\pi\,z\,e}\,\frac{\left(\exp\left(\frac{z\,e}{k\,T}\,\frac{\psi_H}{2}\right)-1\right)e^{\kappa\left(\frac{a}{2}-x\right)}}{\left(\exp\left(\frac{z\,e}{k\,T}\,\frac{\psi_H}{2}\right)+1\right)^2-\left[\left(\exp\left(\frac{z\,e}{k\,T}\,\frac{\psi_H}{2}\right)-1\right)e^{\kappa\left(\frac{a}{2}-x\right)}\right]^2} & \text{if } x \ge \frac{a}{2} \end{cases} \tag{2.20}$$

With the mean electrostatic potential given by Eq. (2.17), in the PB interval, one can easily obtain the co-ion and counter-ion distribution functions for $x \ge \frac{a}{2}$, given by Eqs. (2.12) and (2.13). Meanwhile, for the Laplace interval, the co-ion and counter-ion distribution functions are equal to zero due to the ion's size restriction. Hence, substituting $\psi(x)$ in Eqs. (2.12) and (2.13) and simplifying, we obtain

$$g_+(x) = \begin{cases} 0 & \text{if } 0 \le x < \frac{a}{2} \\ \left[\frac{\left(\exp\left(\frac{z\,e}{k\,T}\,\frac{\psi_H}{2}\right)+1\right)+\left(\exp\left(\frac{z\,e}{k\,T}\,\frac{\psi_H}{2}\right)-1\right)e^{\kappa\left(\frac{a}{2}-x\right)}}{\left(\exp\left(\frac{z\,e}{k\,T}\,\frac{\psi_H}{2}\right)+1\right)-\left(\exp\left(\frac{z\,e}{k\,T}\,\frac{\psi_H}{2}\right)-1\right)e^{\kappa\left(\frac{a}{2}-x\right)}}\right]^{-2} & \text{if } x \ge \frac{a}{2} \end{cases} \tag{2.21}$$

$$g_-(x) = \begin{cases} 0 & \text{if } 0 \le x < \frac{a}{2} \\ \left[\frac{\left(\exp\left(\frac{z\,e}{k\,T}\,\frac{\psi_H}{2}\right)+1\right)+\left(\exp\left(\frac{z\,e}{k\,T}\,\frac{\psi_H}{2}\right)-1\right)e^{\kappa\left(\frac{a}{2}-x\right)}}{\left(\exp\left(\frac{z\,e}{k\,T}\,\frac{\psi_H}{2}\right)+1\right)-\left(\exp\left(\frac{z\,e}{k\,T}\,\frac{\psi_H}{2}\right)-1\right)e^{\kappa\left(\frac{a}{2}-x\right)}}\right]^{2} & \text{if } x \ge \frac{a}{2} \end{cases} \tag{2.22}$$

While, the total differential capacitance is the sum of the differential capacitances in both intervals and it is given by

$$C_T = \left[\frac{4\,\pi}{\varepsilon\,\kappa}\,\frac{\left(2+\frac{\kappa\,a}{2}\right)}{\sqrt{1+\left(\frac{2\,\pi\,z\,e\,\sigma_M}{\varepsilon\,\kappa\,k\,T}\right)^2}}\right]^{-1} \tag{2.23}$$

## 2.2 The single electrical double layer of a solid cylindrical electrode

The Poisson-Boltzmann equation for an electrolyte next to a charged electrode of cylindrical geometry is given by

$$\nabla^2\psi(\vec{r}) = \frac{\mathrm{d}^2\psi}{\mathrm{d}r^2} + \frac{1}{r}\frac{\mathrm{d}\psi}{\mathrm{d}r} = \begin{cases} 0 & \text{if } R \le r < R+\frac{a}{2} \\ -\frac{4\,\pi\,\rho_{el}(r)}{\varepsilon} & \text{if } r \ge R+\frac{a}{2} \end{cases} \tag{2.24}$$

where $R$ is the cylinder radius, and in the Laplacian operator the symmetry of the system has been taken into account. The model of the solid cylindrical electrode is shown in Fig. 2.2. The upper part of the right-hand side of Eq. (2.24) corresponds to the Laplace equation, since due to the Stern correction, for $R \le r < R+\frac{a}{2}$, $\rho_{el}(r) = 0$, whereas for $r \ge R+\frac{a}{2}$, $\rho_{el}(r)$ gives the concentration profiles. Hence, the electrical potential of the solid cylindrical electrode is obtained by solving Eq. (2.24), for $\forall\, r \ge R+\frac{a}{2}$.

In this geometry, the expression for the linearization of Eq. (2.24) is the same as that for the linear PB-eq of a plane electrode. That is, the electric charge concentration is given by

$$\rho_{el}(r) = -\frac{2\,n\,e^2\,z^2}{k\,T}\psi(r)$$

Hence, using the definition of $\kappa$ given in Eq. (2.7), the linearized version of Eq. (2.24) becomes

$$\nabla^2\psi(\vec{r}) = \frac{\mathrm{d}^2\psi}{\mathrm{d}r^2} + \frac{1}{r}\frac{\mathrm{d}\psi}{\mathrm{d}r} = \begin{cases} 0 & \text{if } R \le r < R+\frac{a}{2} \\ \kappa^2\,\psi(r) & \text{if } r \ge R+\frac{a}{2} \end{cases} \tag{2.25}$$

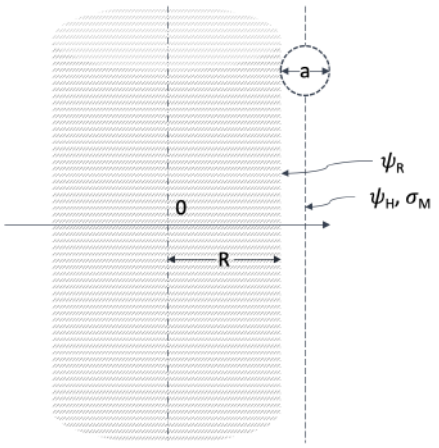


Figure 2.2: Geometry of a solid cylindrical electrode.

Now, the boundary conditions needed to solve Eq. (2.25) are equivalent to those of Section 2.1.1 with some slight modifications. That is

- The mean electrostatic potential at the surface of the electrode, $r = R$, is equal to $\psi_R$ ($\psi(R) = \psi_R$).
- The mean electrostatic potential at the distance of closest approach for the ions, $r = R + \frac{a}{2}$, is equal to $\psi_H$ ($\psi(R + \frac{a}{2}) = \psi_H$).
- The mean electrostatic potential at infinity is zero ($\psi(\infty) = 0$).
- From the Gauss' law, at the distance of closest approach ($r = R + \frac{a}{2}$), the derivative of the potential with respect to the distance is $\frac{\mathrm{d}\psi}{\mathrm{d}r} = -\frac{4\,\pi\,\sigma_M}{\varepsilon}$, i.e., the induced surface charge density at $r = R + \frac{a}{2}$ is $\sigma(R + \frac{a}{2}) \equiv \sigma_M$.

Therefore, as derived in Appendix A.2, when we solve Eq. (2.25) with these boundary conditions we find that the mean electrostatic potential is,

$$\psi(r) = \begin{cases} \psi_H \left[1 + \kappa\, \frac{K_1\left(\kappa\left(R+\frac{a}{2}\right)\right)}{K_0\left(\kappa\left(R+\frac{a}{2}\right)\right)}\, \left(R + \frac{a}{2} - r\right)\right] & \text{if } R \le r \le R + \frac{a}{2} \\ \frac{K_0(\kappa\, r)}{K_0\left(\kappa\left(R+\frac{a}{2}\right)\right)}\, \psi_H & \text{if } r \ge R + \frac{a}{2} \end{cases} \tag{2.26}$$

where $K_0$ and $K_1$ are the modified Bessel functions of second kind of zero order and first order, and $\psi_H$ [statV] is given by

$$\psi_R = \frac{4\,\pi\,\sigma_M}{\varepsilon\,\kappa} \left( \frac{K_0\left(\kappa\left(R+\frac{a}{2}\right)\right)}{K_1\left(\kappa\left(R+\frac{a}{2}\right)\right)} + \frac{\kappa\, a}{2} \right) \tag{2.27}$$

Meanwhile, the surface charge density, at the distance $r$ from the coordinates' origin, $\sigma_C(r)$, within the Poisson-Boltzmann approximation is

$$\sigma_C(r) = -\frac{1}{r} \int_r^\infty \rho_{el}(t)\, t\, \mathrm{d}t = \frac{\varepsilon\,\kappa}{4\,\pi} \frac{K_1(\kappa\, r)}{K_0\left(\kappa\left(R+\frac{a}{2}\right)\right)}\, \psi_H \tag{2.28}$$

Whereas, for the Laplace interval, the induced surface charge density is equal to zero due to the ion's size restriction. Hence, the induced surface charge density is

$$\sigma_C(r) = \begin{cases} 0 & \text{if } R \le r < R + \frac{a}{2} \\ \frac{\varepsilon\,\kappa}{4\pi}\,\frac{K_1(\kappa\,r)}{K_0\left(\kappa\left(R+\frac{a}{2}\right)\right)}\,\psi_H & \text{if } r \ge R + \frac{a}{2} \end{cases} \tag{2.29}$$

Notice that $\sigma_C(r) = \varsigma_C + \int_{a/2}^{r} \rho_{el}(t)\,\mathrm{d}t$, i.e., the electrode's surface charge, $\varsigma_C$, plus the induced charge, in the surrounding electrolyte, from $t = R + a/2$ to $t = r$.

The co-ion and counter-ion distribution functions in the Laplace interval are equal to zero, due to the ion's size restriction. However, the co-ion and counter-ion distribution functions for $r \ge R + \frac{a}{2}$ are given by Eqs. (2.12) and (2.13). Hence, with the mean electrostatic potential given in Eq. (2.26), for the PB interval, one can easily obtain the co-ion and counter-ion distribution functions

$$g_+(r) = \begin{cases} 0 & \text{if } R \le r < R + \frac{a}{2} \\ \exp\left(-\frac{z\,e}{k\,T}\,\frac{K_0(\kappa\,r)}{K_0\left(\kappa\left(R+\frac{a}{2}\right)\right)}\,\psi_H\right) & \text{if } r \ge R + \frac{a}{2} \end{cases} \tag{2.30}$$

$$g_-(r) = \begin{cases} 0 & \text{if } R \le r < R + \frac{a}{2} \\ \exp\left(\frac{z\,e}{k\,T}\,\frac{K_0(\kappa\,r)}{K_0\left(\kappa\left(R+\frac{a}{2}\right)\right)}\,\psi_H\right) & \text{if } r \ge R + \frac{a}{2} \end{cases} \tag{2.31}$$

In the meantime, the total differential capacitance is the sum of the differential capacitances in both intervals and it is given by

$$C_T = \left[\frac{4\,\pi}{\varepsilon\,\kappa}\left(\frac{2\,K_0\left(\kappa\left(R+\frac{a}{2}\right)\right)}{K_1\left(\kappa\left(R+\frac{a}{2}\right)\right)} + \frac{\kappa\,a}{2}\right)\right]^{-1} \tag{2.32}$$

## 2.3 The single electrical double layer of a solid spherical electrode

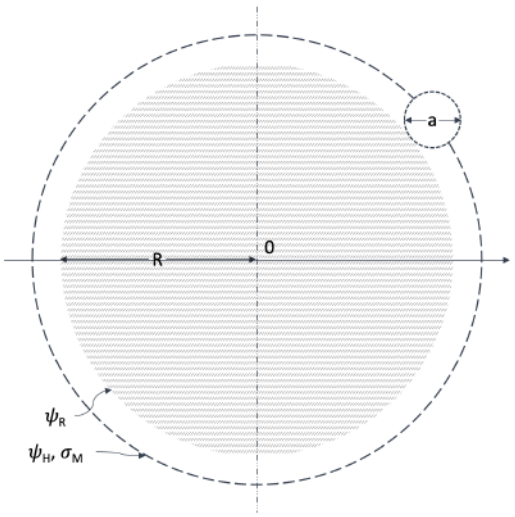


Figure 2.3: Geometry of a solid spherical electrode.

The linear Poisson-Boltzmann equation with the Stern correction for an electrode of spherical geometry (s-LPBS), shown in Fig. 2.3, is obtained from Eq. (2.1), with the Laplacian in spherical coordinates. Hence, the electric potential profile for an electrolyte around a solid spherical electrode

of radius $R$, because of the symmetry of the system, depends only on the $r$-distance to the center of the electrode. From the Stern restriction, the mean electrostatic potential is divided into two intervals, when $R \leq r < R + \frac{a}{2}$ and when $r \geq R + \frac{a}{2}$. The first interval is ruled by the Laplace equation, whereas the second follows the PB-eq. Hence the mean electrostatic potential around a spherical electrode is

$$\nabla^2 \psi(\vec{r}) = \frac{\mathrm{d}^2\psi}{\mathrm{d}r^2} + \frac{2}{r}\,\frac{\mathrm{d}\psi}{\mathrm{d}r} = \begin{cases} 0 & \text{if } R \leq r < R + \frac{a}{2} \\ -\frac{4\,\pi\,\rho_{el}(r)}{\varepsilon} & \text{if } r \geq R + \frac{a}{2} \end{cases} \tag{2.33}$$

where the electric charge concentration is the same as the c-LPBS. Hence, Eq. (2.33) is rewritten as,

$$\frac{\mathrm{d}^2\psi}{\mathrm{d}r^2} + \frac{2}{r}\,\frac{\mathrm{d}\psi}{\mathrm{d}r} = \begin{cases} 0 & \text{if } R \leq r < R + \frac{a}{2} \\ \kappa^2\,\psi(r) & \text{if } r \geq R + \frac{a}{2} \end{cases} \tag{2.34}$$

Our boundary conditions for the spherical electrode are exactly the same as those of the cylindrical electrode in Section 2.2. Therefore, as derived in Appendix A.3, the solution of Eq. (2.34) with those boundary conditions yields,

$$\psi(r) = \begin{cases} \psi_H \left[1 + \left(\kappa + \frac{1}{R+\frac{a}{2}}\right)\,\left(R + \frac{a}{2} - r\right)\right] & \text{if } R \leq r \leq R + \frac{a}{2} \\ \frac{R+\frac{a}{2}}{r}\,\psi_H\,e^{\kappa\left(R+\frac{a}{2}-r\right)} & \text{if } r \geq R + \frac{a}{2} \end{cases} \tag{2.35}$$

where $\psi_H$ [statV] is given by

$$\psi_H = \frac{4\,\pi\,\sigma_M}{\varepsilon}\left(\frac{R + \frac{a}{2}}{1 + \kappa\,\left(R + \frac{a}{2}\right)}\right) \tag{2.36}$$

Meanwhile, the surface charge density, at the distance $r$ from the coordinates' origin, $\sigma_S(r)$, within the Poisson-Boltzmann approximation is

$$\sigma_S(r) = -\frac{1}{r^2}\int_r^\infty \rho_{el}(t)\,t^2\,\mathrm{d}t = \frac{\varepsilon\,\psi_H}{4\,\pi}\left(R + \frac{a}{2}\right)\frac{(1 + \kappa\,r)}{r^2}\,e^{\kappa\left(R+\frac{a}{2}-r\right)} \tag{2.37}$$

Whereas, for the Laplace interval, the induced surface charge density is equal to zero due to the ion's size restriction. Hence, the induced surface charge density is

$$\sigma_S(r) = \begin{cases} 0 & \text{if } R \leq r < R + \frac{a}{2} \\ \frac{\varepsilon\,\psi_H}{4\pi}\left(R + \frac{a}{2}\right)\frac{(1+\kappa\,r)}{r^2}\,e^{\kappa\left(R+\frac{a}{2}-r\right)} & \text{if } r \geq R + \frac{a}{2} \end{cases} \tag{2.38}$$

Notice that $\sigma_S(r) = \varsigma_S + \int_{a/2}^{r} \rho_{el}(t)\,\mathrm{d}t$, i.e., the electrode's surface charge, $\varsigma_S$, plus the induced charge, in the surrounding electrolyte, from $t = R + a/2$ to $t = r$.

The co-ion and counter-ion distribution functions in the Laplace interval are equal to zero, due to the ion's size restriction. However, the co-ion and counter-ion distribution functions for the Poisson-Boltzmann interval are given by Eqs. (2.12) and (2.13). Hence, with the mean electrostatic potential given by Eq. (2.35), in such interval, one can easily obtain the co-ion and counter-ion distribution functions.

$$g_+(r) = \begin{cases} 0 & \text{if } R \leq r < R + \frac{a}{2} \\ \exp\left(-\frac{z\,e}{k\,T}\,\psi_H\,\frac{R+\frac{a}{2}}{r}\,e^{\kappa\left(R+\frac{a}{2}-r\right)}\right) & \text{if } r \geq R + \frac{a}{2} \end{cases} \tag{2.39}$$

$$g_-(r) = \begin{cases} 0 & \text{if } R \leq r < R + \frac{a}{2} \\ \exp\left(\frac{z\,e}{k\,T}\,\psi_H\,\frac{R+\frac{a}{2}}{r}\,e^{\kappa\left(R+\frac{a}{2}-r\right)}\right) & \text{if } r \geq R + \frac{a}{2} \end{cases} \tag{2.40}$$

In the meantime, the total differential capacitance is the sum of the differential capacitances in both intervals and it is given by

$$C_T = \left[ \frac{4\,\pi}{\varepsilon} \left( \frac{2\left(R + \frac{a}{2}\right)}{1 + \kappa\,\left(R + \frac{a}{2}\right)} + \frac{a}{2} \right) \right]^{-1} \tag{2.41}$$

## 2.4 The co-ion and counter-ion distribution functions of the single electrical double layer for different solid electrodes

In this section, results of the co-ion and counter-ion reduced concentration distribution functions for the different solid electrodes geometries are shown and discussed. Firstly, a comparison between the concentration profiles of the linear and non-linear p-PBS is made. Afterwards, a comparison of the concentration profiles obtained with the linearized Poisson-Boltzmann equation, on cylindrical (c-LPBS), spherical (s-LPBS), and planar (p-LPBS) electrodes is presented, for equal electrode's electrical field or surface charge density, which as it will be shown below are not equivalent. Lastly, the dependence of concentration profiles on the surface charge of the electrode, $\sigma_M$, and the molar concentration, $\rho_0$, and temperature, $T$, of the electrolyte, are shown and discussed for the different solid electrode's geometries, at various radius.

### 2.4.1 The concentration profiles for the linear and non-linear PBS of a solid planar electrode

The co-ion and counter-ion reduced concentration distribution functions of the p-LPBS, and the p-nLPBS are given by Eqs. (2.14) and (2.15) and Eqs. (2.21) and (2.22), respectively. It is seen from Eqs. (2.14), (2.15), (2.21) and (2.22) that the co-ion and counter-ion distribution functions depend on $\psi_H$, but from the relations between $\sigma_M$ and $\psi_H$ in Eqs. (2.9) and (2.18) we can directly vary the values of $\sigma_M$ and consequently the value of $\psi_H$. In Fig. 2.4, the concentration profiles of the linear and non-linear p-PBS, and the HNC/MSA integral equations theory of a plane electrode (p-HNC/MSA) of Lozada-Cassou *et al.* [46] are shown for different surface charges of the electrode, $\sigma_M$, and for two molar concentrations of the electrolyte.

From Fig. 2.4 it is seen that in general the p-LPBS equation is a good qualitative approximation of the p-nLPBS equation, and is even a reasonable quantitative approximation for surface charges up to $0.015\,\mathrm{C/m^2}$ and $0.05\,\mathrm{C/m^2}$ for molar concentrations of $0.01\,\mathrm{M}$ and $0.1\,\mathrm{M}$, respectively. Furthermore, it is observed that the p-nLPBS case is an excellent approximation of the p-HNC/MSA equations for all the surface charges, for both molar concentrations, as both values overlap. The approximation of the LPBS to the nLPBS case becomes better as smaller values of the surface charges of the electrode are used, regardless of the molar concentration. Whereas, the alikeness of the nLPBS case to the HNC/MSA equations is constant for all the values used of the surface charge of the electrode.

As expected, it is observed that because the plate is positively charged, in all the cases considered, the counter-ions adsorb more than the co-ions, i.e., $g_-(x) > g_+(x)$, $\forall\, x \geqq R + a/2$. This is in complete accordance with the Gauss' law, equal charges repeal each other while different ones attract each other. Furthermore, for higher values of the surface charge, $\sigma_M$, the intensity and thickness of the EDL increases. There is a clear difference between the LPBS and the nLPBS; the linear case underestimates the co-ion and overestimates the counter-ion distribution functions for the higher values of the surface charge. Nonetheless, this overestimation depends highly on the concentrations used, as for a smaller concentration than $0.001\,\mathrm{M}$, the LPBS is a good approximation of the nLPBS, for surface charges up

to $0.005\,\mathrm{C/m^2}$. Hence, for higher values of the molar concentration, a higher value of the surface charge can be used without loosing validity between the linear case and the non-linear case.

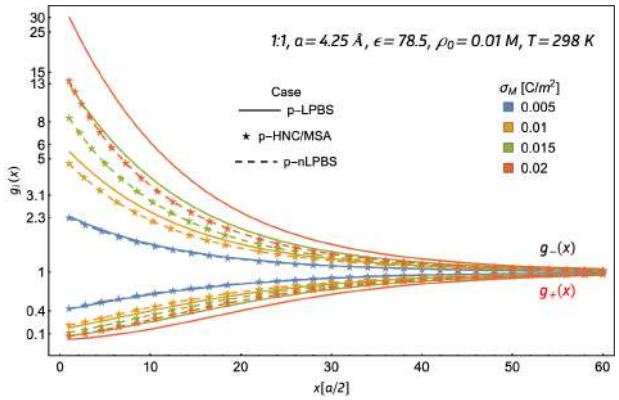


(a) The concentration profiles for $\rho_0 = 0.01\,\mathrm{M}$.

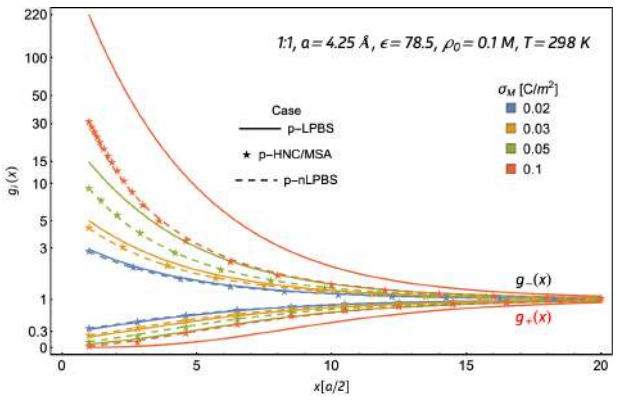


(b) The concentration profiles for $\rho_0 = 0.1\,\mathrm{M}$.

Figure 2.4: Co-ion, $g_+(x)$, and counter-ion, $g_-(x)$, distribution functions of the linear, and non-linear PBS, and those of the HNC/MSA equations of a plane electrode, for different surface charges at two molar concentrations. The p-LPB, p-nLPBS, and the p-HNC/MSA cases are represented by a solid line, a dashed line, and dotted stars, respectively.

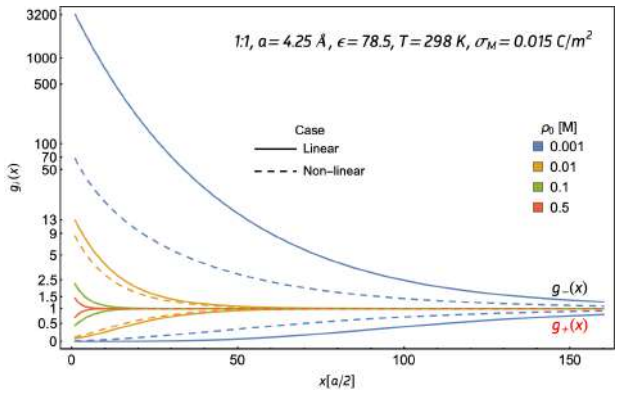


(a) The concentration profiles for $\sigma_M = 0.015\,\mathrm{C/m^2}$.

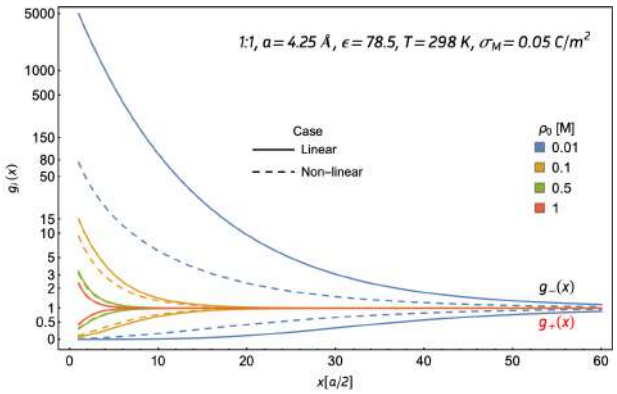


(b) The concentration profiles for $\sigma_M = 0.05\,\mathrm{C/m^2}$.

Figure 2.5: The concentration profile functions of the linear and non-linear PBS of a plane electrode for different molar concentrations, $\rho_0$, at two surface charges of the electrode. The linear and non-linear cases are represented by a solid and dashed lines, respectively.

Thus, as it is seen in Fig. 2.4, as a function of the electrode's charge, the p-LPBS equation is a good qualitative approximation of the p-nLPBS equation, for up to electrodes' surface charge densities of $0.015\,\mathrm{C/m^2}$ and $0.05\,\mathrm{C/m^2}$, at molar concentrations of $0.01\,\mathrm{M}$ and $0.1\,\mathrm{M}$. Now, in order to find the interval of validity of the p-LPBS, in terms of the molar concentrations, these surface charges are used while varying the concentration of the electrolyte. In Fig. 2.5, we compare the p-LPBS with the p-nLPBS, for various molar concentrations, and it is found that the linear case is a good approximation of the non-linear case when the molar concentrations are higher or equal than, $0.01\,\mathrm{M}$ and $0.1\,\mathrm{M}$, for plate's surface charge densities of $0.015\,\mathrm{C/m^2}$ and $0.05\,\mathrm{C/m^2}$, respectively. Hence, an interesting tendency is observed, our linear solution can withstand higher surface charges for higher molar concentrations, without loosing validity against the non-linear solution of the PBS. Moreover, it

is seen that the EDL intensity and thickness drastically decrease as the molar concentration increases, which is the exact opposite as what one would naively expect. However, this can be easily explained when one remembers the concept of molar concentration. The molar concentration represents the amount of solutes per litre of solution, so if the molarity increases, the amount of solutes increases as well. Therefore, if the molar concentration increases there is a higher proportion between counter-ions and co-ions, which corresponds to a higher competition between them, so the intensity and thickness of the EDL decrease.

In Fig. 2.4, a comparison between the LPBS, nLPBS, and the HNC/MSA for a plane electrode is made at molar concentrations of 0.01 M and 0.1 M. It was found that the LPBS case is a good approximation of the nLPBS case for surface charges up to $0.015\,\mathrm{C/m^2}$ and $0.05\,\mathrm{C/m^2}$, respectively, and that concurrently the nLPB case is a good approximation of the HNC/MSA, in such interval. Furthermore, Lozada-Cassou *et al.* [46, 77, 73, 78] found that the nLPBS model is a valid model for the SEDL on a plane electrode up to molar concentrations not higher than 0.5 M. This is because our nLPBS model despite taking into account the ion's size at the surface, it does not take it in regards for the interactions between ions. Therefore, for low molar concentrations, the interaction between ions is rare and consequently almost negligible. Whereas, for high molar concentrations, beyond 0.5 M, the interactions between ions are common and cannot be neglected without jeopardizing the validity of the results.

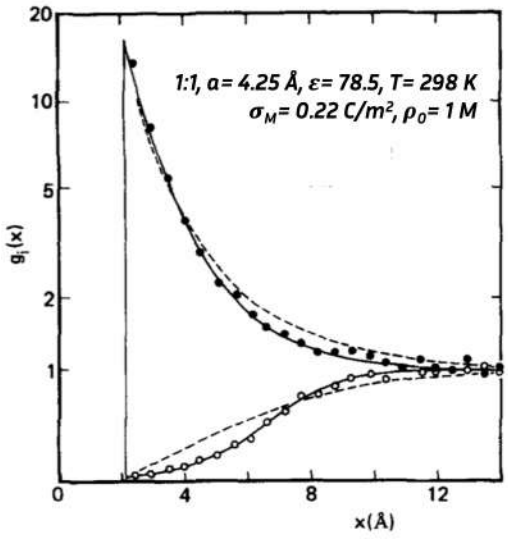


Figure 2.6: Reduced concentration profiles for a monovalent electrolyte of a planar electrode. The dots are the MC results of Torrie and Valleau [67] and the broken and solid curves the nLPBS and HNC/MSA results of Lozada-Cassou *et al.* [46]. "Reprinted" adapted with permission from Lozada-Cassou *et al.* [46].

Figure 2.6 shows the concentration profiles, for a molar concentration of 1 M, of the nLPBS, HNC/MSA [46], and the Monte Carlo (MC) results of Torrie and Valleau [67] for a monovalent electrolyte. From Fig. 2.6, it is seen that the nLPBS model is not a good fit of the Monte Carlo results for such a molar concentration. The MC results show an oscillation of the concentration profiles, due to the interaction between ions, which the nLPBS model is unable to detect due to the flaws on its formulation, whereas, the HNC/MSA equations closely follow the behavior of the MC results. Therefore, as the HNC/MSA is able to predict the MC results for high molar concentrations, for lower values, there are no doubts of its reliability. Consequently, our linear results are trustworthy in the interval of

0.01 M–0.1 M for surface charges lower or equal to $0.015\,\mathrm{C/m^2}$ and $0.05\,\mathrm{C/m^2}$, respectively.

### 2.4.2 The concentration profiles for different solid electrode geometries

In order to compare the co-ion and counter-ion distribution functions for the different solid electrode geometries, one needs first to understand how much influence does the radius have on the concentration profiles. This influence can be analyzed for two cases: by fixing the *unscreened electrode's electrical field* or by fixing the electrode's surface charge density.

Quite generally, by Gauss' law, the ***effective or net*** electrical field for a charged electrode of any geometry, E(r), at a distance $r$ from the electrode's surface is given by

$$E(r) = \frac{4\,\pi}{\varepsilon}\,\sigma(r), \tag{2.42}$$

where $\sigma(r)$ is the effective charge density, i.e., the electrode's surface charge density plus the induced charge in the electrolyte, up to the distance $r$, and is given by

$$\sigma(r) = -\int_{V(r)}^{\infty} \rho_{el}(\overrightarrow{\mathbf{y}})\,\mathrm{d}^3 y, \tag{2.43}$$

where $\rho_{el}(r)$, the electric charge profile in the fluid next to the electrode is given by Eq. (2.3), and $V(r)$ is the volume contained between the distance $r$, from the coordinates' origin, to infinity. The expressions for the net surface charge densities, at the distance $r$ from the coordinates origin around the different solid electrodes considered here are given by Eqs. (2.10) and (2.19), for $\sigma_P(x)$, Eq. (2.28), for $\sigma_C(r)$, and Eq. (2.37), for $\sigma_S(r)$.

In particular, in terms of surface charge density of a planar electrode, $\sigma_P \equiv \sigma_M$, the ***unscreened or bare electrical field***, as a function of the distance to the center of the coordinates system is

$$E_P^u(x) = \frac{4\,\pi}{\varepsilon}\,\sigma_P, \tag{2.44}$$

where here $x$ is the distance to the surface of the planar electrode, whereas, for an electrode of cylindrical geometry with surface charge density $\sigma_C$, we have

$$E_C^u(r) = \frac{4\,\pi\,R}{\varepsilon\,r}\,\sigma_C, \tag{2.45}$$

and for an electrode of spherical geometry, of surface charge density $\sigma_S$, this is

$$E_S^u(r) = \frac{4\,\pi\,R^2}{\varepsilon\,r^2}\,\sigma_S. \tag{2.46}$$

In Eq. (2.45) and Eq. (2.46), $r$ is the distance to the center of the cylindrical and spherical electrodes, respectively.

In terms, ***now of the distance to the surface of the electrode***, $x$, these two last expressions become,

$$E_C^u(x) = \frac{4\,\pi}{\varepsilon\,(1 + x/R)}\,\sigma_C, \tag{2.47}$$

and

$$E_S^u(x) = \frac{4\,\pi}{\varepsilon\,(1 + x/R)^2}\,\sigma_S. \tag{2.48}$$

Let us here point out again that Eqs. (2.44) to (2.48), are for the ***unscreened electrical fields***. Hence, if the unscreened electrical fields of the different geometries are chosen to be equal at the distance of maximum approach of the ions, i.e., at $r = R + a/2$ for the cylindrical and spherical electrodes, and at $x = a/2$ for the planar electrode, the surface charge densities on the different electrodes geometries must be chosen accordingly with the following relations

$$\sigma_C = \left(1 + \frac{a}{2\,R}\right) \sigma_P \tag{2.49}$$

and

$$\sigma_S = \left(1 + \frac{a}{2\,R}\right)^2 \sigma_P. \tag{2.50}$$

and thence Eq. (2.47) and Eq. (2.48), can be expressed in terms of the unscreened planar electrode electrical field, $\forall\, x$, as

$$E^u_C(x) = \frac{\left(1 + \frac{a}{2\,R}\right)}{(1 + x/R)}\, E^u_P(x) \tag{2.51}$$

and

$$E^u_S(x) = \frac{\left(1 + \frac{a}{2\,R}\right)^2}{(1 + x/R)^2}\, E^u_P(x) \tag{2.52}$$

In particular,

$$E^u_S(x) = \frac{\left(1 + \frac{a}{2\,R}\right)}{(1 + x/R)}\, E^u_C(x). \tag{2.53}$$

Thus, if we chose to compare results of a planar electrode against a cylindrical electrode, both with the *same surface electrical field*, from Eq. (2.49), the surface charge density on the cylindrical electrode, $\sigma_C$, must be $(1 + \frac{a}{2\,R})$ larger than that for the planar electrode $\sigma_P$, and on a spherical electrode, from Eq. (2.50), $\sigma_S$ must be $(1 + \frac{a}{2\,R})^2$ larger than $\sigma_P$. Of course one can make a comparison with the same charge density on all the electrodes' geometries. For a planar electrode, there is no difference between results obtained at constant electrical field or surface charge density, since the bare electrical field and thus the mean electrostatic potential at the distance of maximum approach for the ions, $x = \frac{a}{2}$, $\psi_H$, do not depend on $x$ (see Eqs. (2.2) and (2.44)).

In Fig. 2.7 the geometry's influence on the co-ion and counter-ion distribution functions, for equal electric fields or equal surface charge densities is shown for different spherical and cylindrical electrodes' radii. It is observed that as the radii of the solid cylindrical and spherical electrodes increases, their concentration profiles' tend to the values of the planar electrodes, as it should be, i.e., expanding Eq. (2.51) and Eq. (2.52), to first order in a Taylor series in terms of $x$, they become

$$E^u_C(x) = \left(1 + \frac{a}{2\,R}\right)\left(1 - \frac{x}{R}\right)\, E^u_P(x), \tag{2.54}$$

and

$$E^u_C(x) = \left(1 + \frac{a}{2\,R}\right)^2\left(1 - 2\frac{x}{R}\right)\, E^u_P(x), \tag{2.55}$$

i.e., for a given value of $R$, the larger $x$, the weaker $E^u_C(x)$ and $E^u_S(x)$ become. However, $\lim\limits_{R\to\infty} E^u_C(x) \to E^u_P(x)$, and $\lim\limits_{R\to\infty} E^u_S(x) \to E^u_P(x)$. Hence, the SEDL of the cylindrical and spherical solid electrodes are more intense and thick as their radii increases. Also, notice the dependence of the cylindrical and

spherical electric fields on the relation of the ionic size, $a$, to the radius of the electrode, $R$, i.e., $a/R$, particularly at the electrode-ion contact, i.e., from Eqs. (2.45) and (2.46)

$$E_C^u\left(r = R + \frac{a}{2}\right) = \frac{4\,\pi\,R}{\varepsilon\,\left(R + \frac{a}{2}\right)}\,\sigma_C = \frac{4\,\pi}{\varepsilon\left(1 + \frac{a}{2\,R}\right)}\,\sigma_C, \tag{2.56}$$

and

$$E_S^u\left(r = R + \frac{a}{2}\right) = \frac{4\,\pi\,R}{\varepsilon\,\left(R + \frac{a}{2}\right)^2}\,\sigma_S = \frac{4\,\pi}{\varepsilon\left(1 + \frac{a}{2\,R}\right)^2}\,\sigma_S. \tag{2.57}$$

Thence, the larger the ionic diameter, the lower the intensity of $E_C^u\left(r = R + \frac{a}{2}\right)$ and $E_S^u(r = R + \frac{a}{2})$, and in the limit of $a \to \infty$, $E_C^u\left(r = R + \frac{a}{2}\right)$ and $E_S^u\left(r = R + \frac{a}{2}\right) \to 0$. Consequently, the larger the spherical or cylindrical electrodes radii, the closer become their corresponding distribution functions to those for a charged plate, and, thus, the smaller the difference between calculations at constant surface charge with those at constant electrical potential. In this thesis, the effect of the ionic size is not discussed.

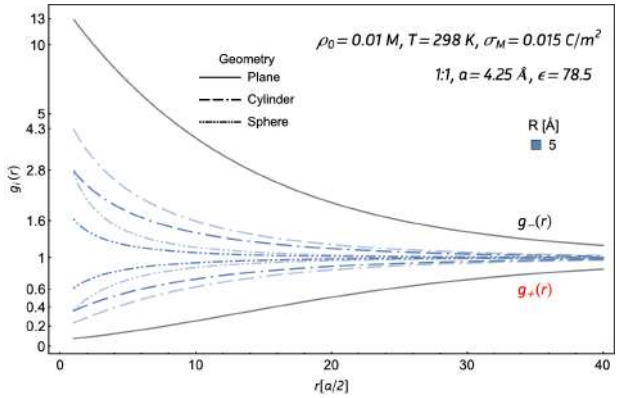


(a) The concentration profiles for $R = 5\,\text{Å} \cong 1.2\,a$.

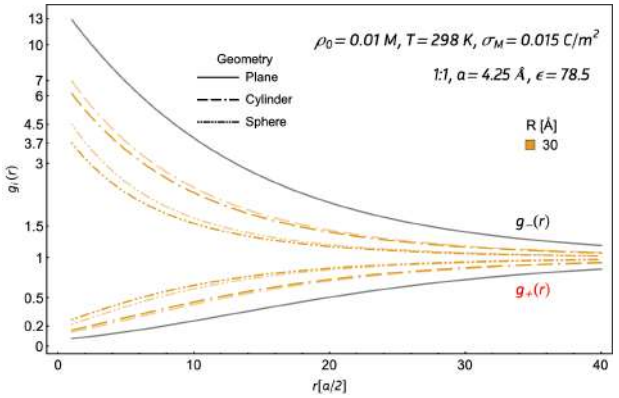


(b) The concentration profiles for $R = 30\,\text{Å} \cong 7.1\,a$.

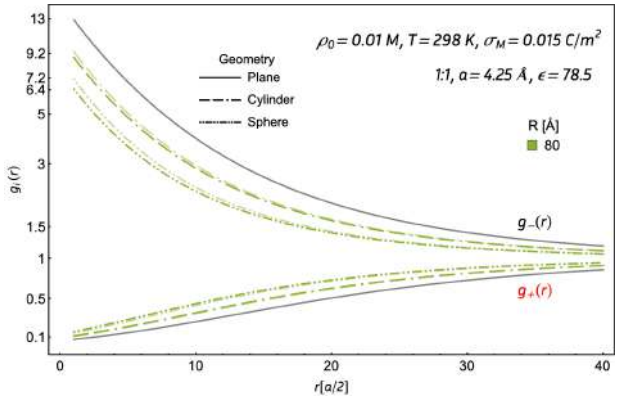


(c) The concentration profiles for $R = 80\,\text{Å} \cong 18.8\,a$.

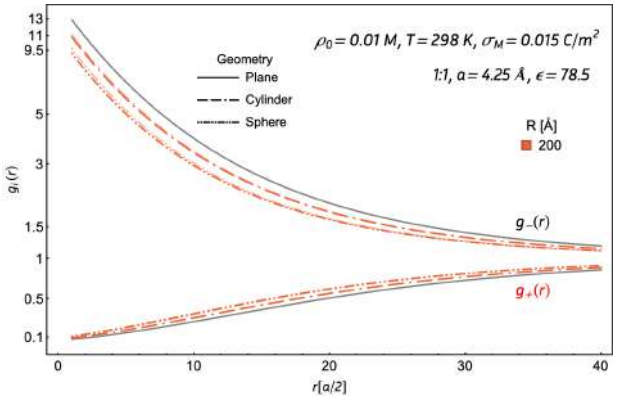


(d) The concentration profiles for $R = 200\,\text{Å} \cong 47.1\,a$.

Figure 2.7: The co-ion, $g_+(r)$, and counter-ion, $g_-(r)$, distribution functions of different solid electrode geometries with distinct radii values. The lighter and darker lines are for equal *unscreened electric fields* $[E_M^u(r = a/2) = \frac{4\,\pi}{\varepsilon}\sigma_M = 2.4 \times 10^{-3}\,\text{C/m}^2]$ or equal surface charges densities $[\sigma_M = 0.015\,\text{C/m}^2]$, respectively. The solid lines are for the planar electrode, since the *unscreened electrical field*, $E_M^u(r) = \frac{4\,\pi}{\varepsilon}\sigma_M$, $\forall\, r$.

In Fig. 2.7 we show a comparison of the ionic distribution functions, at constant surface charge with those for equal electrical potential, at $x = a/2$ for the three electrodes' geometries considered above, and for different radii sizes for the cylindrical and spherical nano-electrodes. Whence, accordingly with the above discussion, it is found that the planar electrode achieves the highest contact values of the concentration profiles, followed by the cylindrical and spherical electrodes, respectively. This is expected, since although all electrodes have the same value of the *unscreened electrical field* at $x = a/2$, for $x > a/2$ the unscreened electrical fields of the cylindrical and spherical electrodes rapidly decrease, as $1/r$ and $1/r^2$, respectively, which, in turn, imply a smaller attraction of subsequent layers of both counter-ions and co-ions, and therefore the *net electrical fields* for the three electrodes geometries satisfy the following relation $E_P(x) > E_C(x) > E_S(x) \,\forall\, x > a/2$, and as a consequence their corresponding electrical double layers are weaker and narrower. On the other hand, the ionic distribution functions of the cylindrical and spherical electrodes are weaker and narrower for the corresponding constant surface charge density calculations, and this so, because by fixing the surface charge on the electrode, by fixing the electrical field at $x = 0$, the unscreened electrical field weakens for $x = a/2$, as $1/(1 + \frac{a}{2R})$ and $1/(1 + \frac{a}{2R})^2$, respectively (see Eqs. (2.47) and (2.48)).

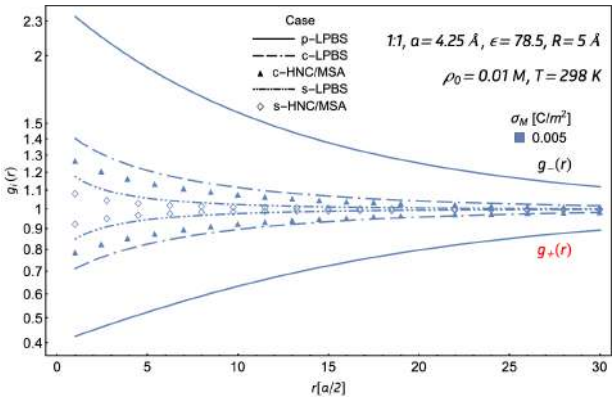


(a) The concentration profiles for $\sigma_M = 0.005\,\mathrm{C/m^2}$.

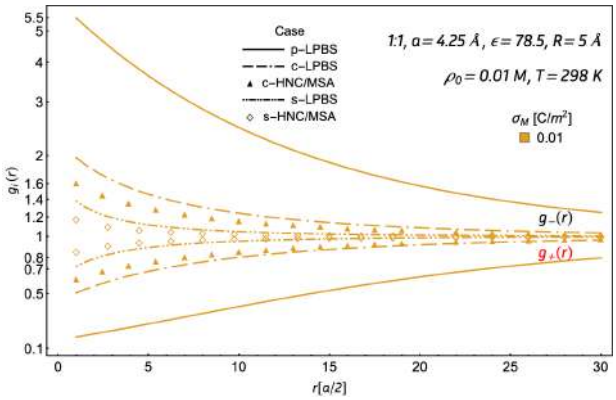


(b) The concentration profiles for $\sigma_M = 0.01\,\mathrm{C/m^2}$.

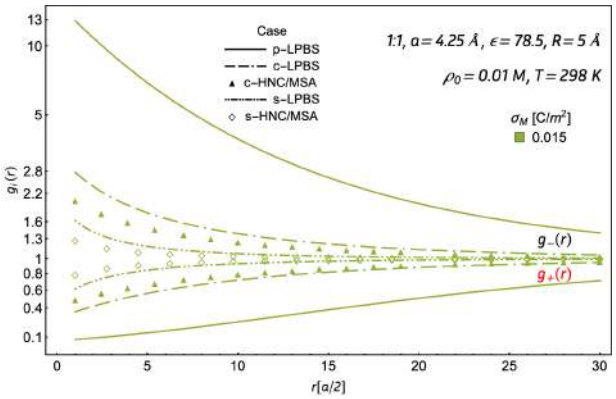


(c) The concentration profiles for $\sigma_M = 0.015\,\mathrm{C/m^2}$.

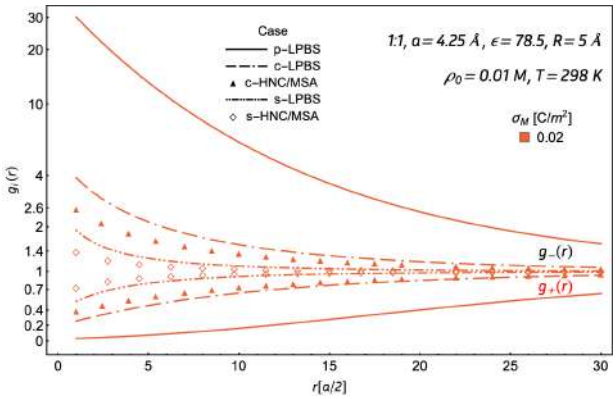


(d) The concentration profiles for $\sigma_M = 0.02\,\mathrm{C/m^2}$.

Figure 2.8: The concentration profile functions, $g_i(r)$, of our LPBS, and the HNC/MSA of Lozada-Cassou for different electrode geometries. A radius of $5\,\text{Å} \cong 1.2\,a$ is used, while the electrode's surface charge, $\sigma_M$, is varied. The prefixes "p", "c", and "s", are used for the planar, cylindrical and spherical electrodes.

To study the impact of the solid-electrode's geometry on the structure of the electrical double layer, the reduced co-ion and counter-ion concentration profiles were calculated for various system's

parameters, i.e., electrode's surface charge density and radii, and salt concentration and temperature. As mentioned before, as the radii of the solid cylindrical and spherical electrode increases, their concentration profiles' tend to the values of the planar electrode. Therefore, as we are interested in the geometrical impact of the electrode alongside other system parameters we will delimit the radii size up to 80 Å, as beyond this radius the geometrical impact disappears. In all the cases presented below, the salt is a 1:1 electrolyte, with dielectric constant, $\varepsilon = 78.5$, and such that $\sigma_P = \sigma_C = \sigma_S = \sigma_M$, i.e., all the electrodes have the same surface charge density, $\sigma_M$.

In Fig. 2.8, we show concentration profiles for electrodes with a radius of $R$ =5 Å, and four values of their surface charge density, $\sigma_M$, 0.005 C/m$^2$, 0.01 C/m$^2$, 0.015 C/m$^2$ and 0.02 C/m$^2$. These concentration profiles were obtained with our LPBS, and the HNC/MSA of Lozada-Cassou *et al* [77, 73, 78], for the solid cylindrical (c-HNC/MSA) and solid spherical (s-HNC/MSA) electrodes. The results of the HNC/MSA of the solid planar electrode were not added to Fig. 2.8, as they have been already discussed in the previous section. It is observed that our linear solutions, compared to the HNC/MSA of the cylindrical and spherical electrodes, overestimate the concentration profiles, due to the entropic effect associated to the ion's size; the additional ion-ion, repulsion due to their size, reduces the proximity among them, thus reducing the local concentration profile. Nonetheless, our LPBS results still provide a fair quantitative approximation for surface charges lower than 0.02 C/m$^2$, and even for up to 0.02 C/m$^2$, the LPBS provides a very good *qualitative approximation*.

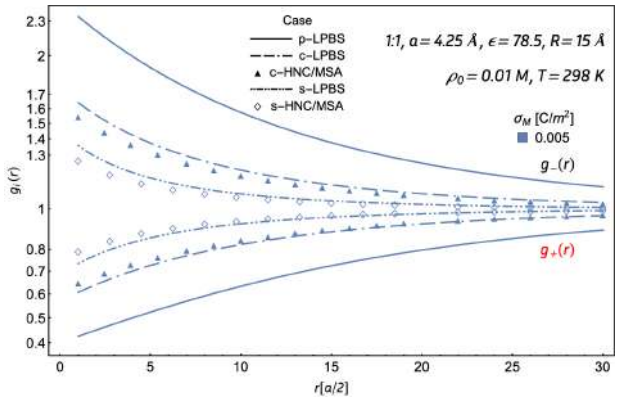


(a) The concentration profiles for $\sigma_M = 0.005\,\mathrm{C/m^2}$.

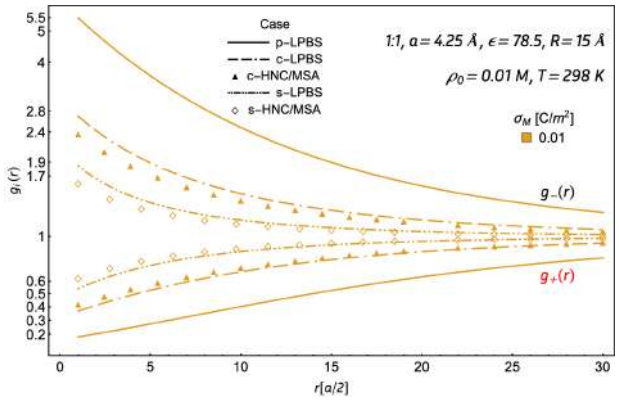


(b) The concentration profiles for $\sigma_M = 0.01\,\mathrm{C/m^2}$.

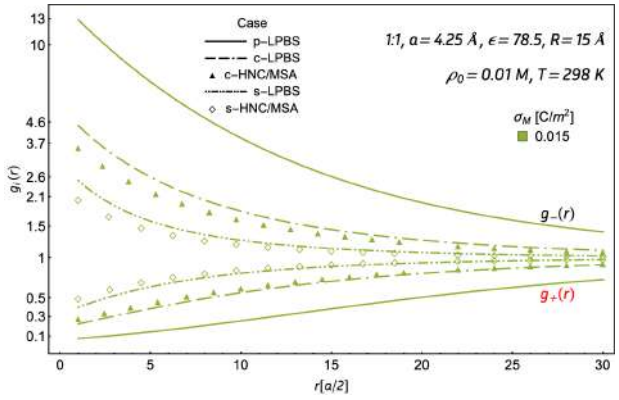


(c) The concentration profiles for $\sigma_M = 0.015\,\mathrm{C/m^2}$.

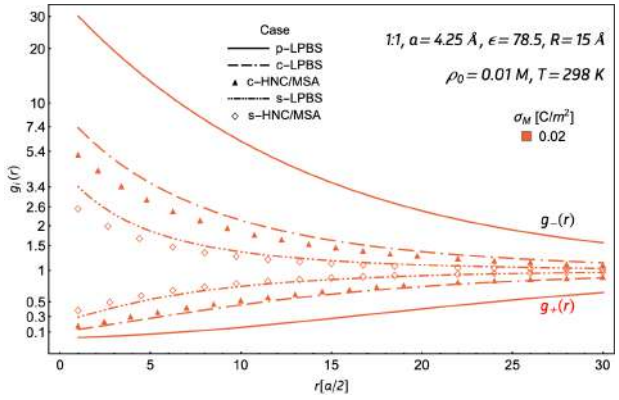


(d) The concentration profiles for $\sigma_M = 0.02\,\mathrm{C/m^2}$.

Figure 2.9: The concentration profile functions, $g_i(r)$, of our LPBS, and the HNC/MSA of Lozada-Cassou for different electrode geometries. A radius of 15 Å $\cong 3.5\,a$ is used, while the surface charge, $\sigma_M$, is varied. The prefixes used have the same meaning as in Fig. 2.8.

In general, our linear solution of the EDL for a solid spherical electrode is a better fit to the corresponding EDL of the HNC/MSA equations, than that for a solid cylindrical electrode, and, in turn, the LPBS EDL for the cylindrical electrode is a better fit to corresponding HNC/MSA, than the analogous comparison for the planar electrode. This is because the unscreened electrical field for the distinct electrode's geometries, at a constant surface charge density, $\sigma_M$, are $\cdot \ni \cdot$

$$E_S^u(x) = \frac{E_P^u(x)}{(1+\frac{x}{R})^2} < E_C^u(x) = \frac{E_P^u(x)}{(1+\frac{x}{R})} < E_P^u(x) = \frac{4\,\pi\,\sigma_M}{\varepsilon}, \quad \forall\, x > 0 \tag{2.58}$$

i.e., the lower the electrical field, the better the linear approximation (see Eqs. (2.47) and (2.48)). *Therefore, for* $\sigma_M \leqslant 0.02\,\mathrm{C/m^2}$ *the LPBS is a good qualitative and/or quantitative approximation for solid planar, cylindrical and spherical solid electrodes, with radius of* 5 Å.

In Fig. 2.9, as in Fig. 2.8, the LPBS co-ion and counter-ion distribution functions are compared with those of the HNC/MSA, but now for a radius of 15 Å, and various surface charge densities, $\sigma_M$. From these figures it is seen that when the radius of the electrode increases from 5 Å to 15 Å, the LPBS continues being a good quantitative approximation to the HNC/MSA results of Lozada-Cassou *et al*, for surface charges smaller or equal than $0.015\,\mathrm{C/m^2}$, and it is a very good qualitative approximation for $0.02\,\mathrm{C/m^2}$. Once again, it is observed that the LPBS equation is a better fit of the HNC/MSA for the solid spherical electrode than for the cylindrical electrode, and their concentration profile distribution

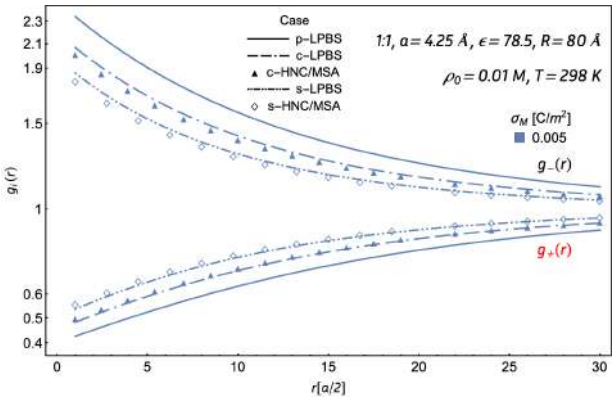


(a) The concentration profiles for $\sigma_M = 0.005\,\mathrm{C/m^2}$.

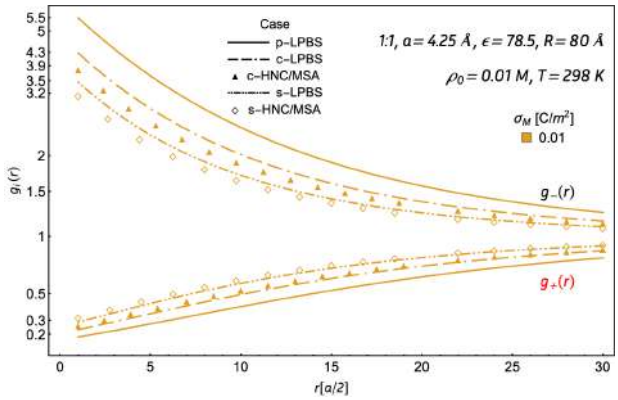


(b) The concentration profiles for $\sigma_M = 0.01\,\mathrm{C/m^2}$.

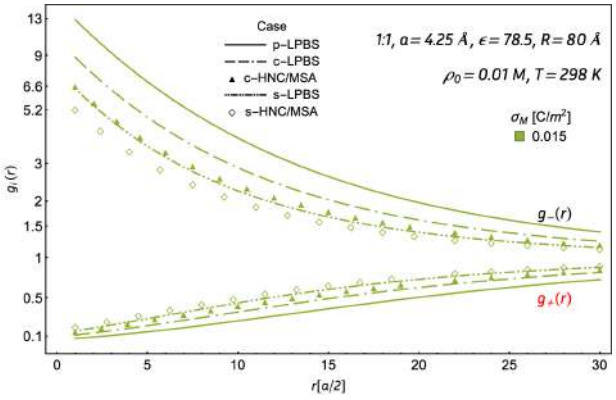


(c) The concentration profiles for $\sigma_M = 0.015\,\mathrm{C/m^2}$.

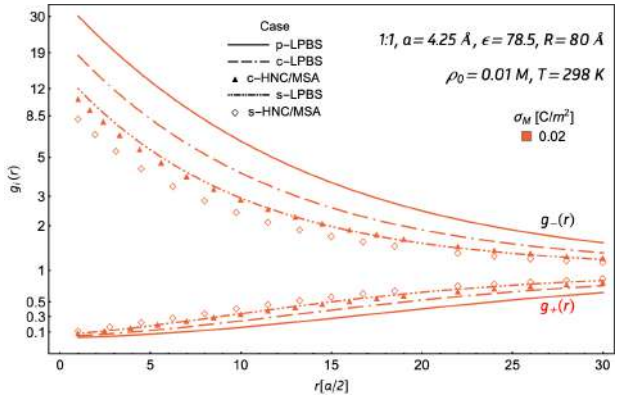


(d) The concentration profiles for $\sigma_M = 0.02\,\mathrm{C/m^2}$.

Figure 2.10: The concentration profile functions, $g_i(r)$, of our LPBS, and the HNC/MSA of Lozada-Cassou for different electrode geometries. A radius of 80 Å $\cong$ 18.8 $a$ is used, while the electrode's surface charge, $\sigma_M$, is varied. The prefixes used have the same meaning as in Fig. 2.8.

functions slightly exceed the HNC/MSA of Lozada-Cassou *et al*, $\forall\, r \geqq a/2$, due to $x$-dependence of their corresponding unscreened electrical fields, and the consideration of the ionic size in HNC/MSA, respectively, as discussed above. Comparatively, these overestimations are slightly smaller than those for an electrode's radius of 5 Å, we will come back to this point bellow. *Therefore, for both radii,* 5 Å *and* 15 Å*, our LPBS is a good quantitative approximation of the HNC/MSA for surface charges lower or equal than* $0.015\,\mathrm{C/m^2}$*, and a very good qualitative approximation for* $\sigma_M \leqslant 0.02\,\mathrm{C/m^2}$.

Lastly, in Fig. 2.10 the concentration profiles of our LPBS are plotted against the HNC/MSA results of Lozada-Cassou *et al*, for a radius of 80 Å. It is observed that our LPBS still holds for this radius, when $\sigma_M \leqslant 0.01\,\mathrm{C/m^2}$. However, it remains a very good qualitative approximation for $\sigma_M \leqslant 0.02\,\mathrm{C/m^2}$. Since now, when our previously used surface charge limit is utilized, the difference between our LPBS and the HNC/MSA of Lozada-Cassou *et al* becomes apparent, as our s-LPBS overlaps to the c-HNC/MSA. Therefore, it is found that the interval of validity of the electrodes' surface charge is consistent up to a radius of 80 Å. However, it is not advisable to stay very close to the upper limit of the surface charge for a radius of 80 Å.

Equations (2.51) and (2.52) can be rewritten as

$$E_C^u(y) = \frac{1}{\left(1 + \frac{y}{1+\frac{a}{2R}}\right)} E_P^u(y), \tag{2.59}$$

and

$$E_S^u(y) = \frac{1}{\left(1 + \frac{y}{1+\frac{a}{2R}}\right)^2} E_P^u(y), \tag{2.60}$$

where $y = x - a/2$, i.e., the distance to the first layer of adsorbed ions to the electrodes. From these equations, is clear that the larger the electrode's radius, the less important is the contribution of the ionic size on the unscreened electrical field, and, hence, the better the approximation to the HNC/MSA results, where the ionic size is considered. However, it must be emphasized that this agreement between the LPBS and the HNC/MSA will certainly deteriorate with increasing salt valence and concentration, since, then, the ionic size will become very relevant.

From here forward, unless stated otherwise, only the concentration profile functions of our LPBS will be shown. In the following figures, the plots of the concentration profile functions for our three radii, 5 Å, 15 Å and 80 Å, are shown, while varying the electrolyte's molar concentration. In Fig. 2.11, the concentration profiles functions of our three solid electrodes are shown for different molar concentrations, with an electrode's surface charge density of $0.015\,\mathrm{C/m^2}$, and a radius of 5 Å. Once again, both cases, for equal electric fields and surface charges are shown. From it, one can observe that for the lowest molar concentrations, the difference between the concentration profiles of the cylindrical and spherical electrodes against the planar electrode is utterly different. Whereas, when the molar concentration is increased the difference between each case is smaller. Furthermore, when equal electric fields are used for the highest molar concentrations the difference between contact concentration profiles is significantly smaller. Moreover, for equal electric fields and a molar concentration of 0.5 M, the solid spherical electrode achieves the highest contact values of the concentration profile, followed by the the solid cylindrical electrode and lastly by planar electrode. Nonetheless, these higher values are overrun by the plane's at a distance $a$ from the surface of the electrode. At higher electrolyte concentration, the electrical double layer becomes narrower, and for this point-ion model of the electrolyte, the decrement of the electrical field become less relevant. Still, the EDL for the planar electrode is, nevertheless, wider than those for the cylindrical electrode, and this last is wider than that for the spherical electrode, when varying the other parameters, as before. The crossover of the planar EDL over the cylindrical and spherical EDL's results from the electroneutrality condition, i.e., the lower adsorption of counter-ions

near the planar electrode, must be compensated by a wider EDL, to cancel the electrode's electrical field.

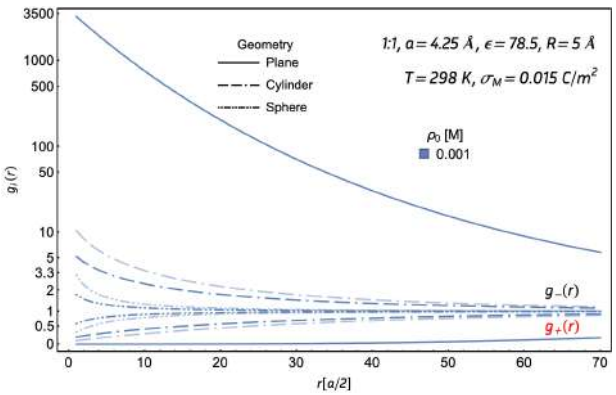


(a) The concentration profiles for $\rho_0 = 0.001\,\mathrm{M}$.

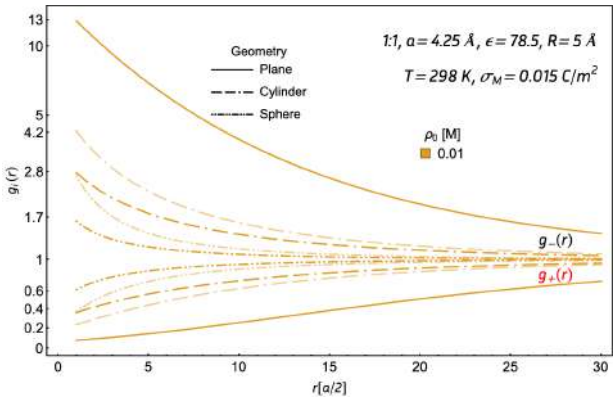


(b) The concentration profiles for $\rho_0 = 0.01\,\mathrm{M}$.

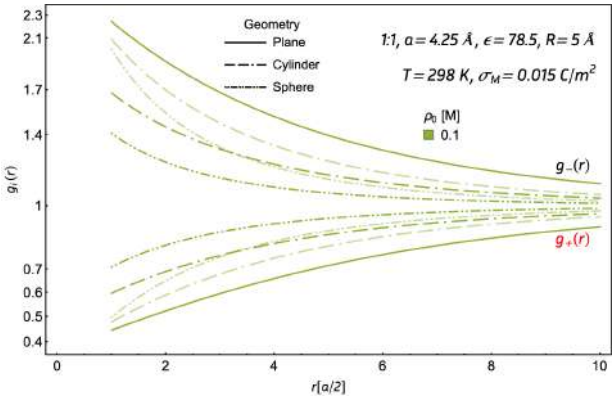


(c) The concentration profiles for $\rho_0 = 0.1\,\mathrm{M}$.

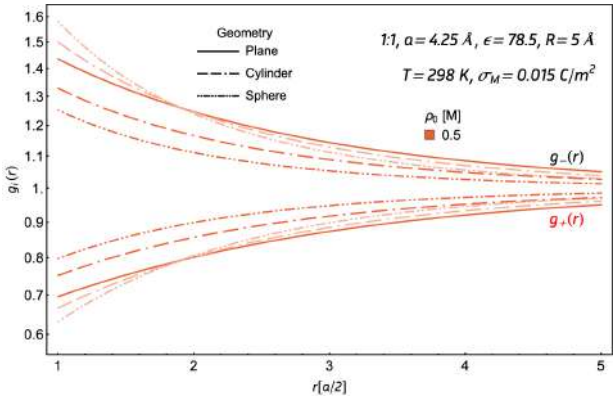


(d) The concentration profiles for $\rho_0 = 0.5\,\mathrm{M}$.

Figure 2.11: The concentration profile functions, $g_i(r)$, of our LPBS for the different electrode's geometries, for a radius of $5\,\text{Å} \cong 1.2\,a$, while the molar concentration, $\rho_0$, is increased. The lighter and darker lines represent two distinct cases, when equal electric fields and surface charges are used.

Now, in Fig. 2.12 the concentration profile functions for the different solid electrodes are plotted for a radius of 15 Å and a surface charge of $0.015\,\mathrm{C/m^2}$. According with our previous discussion on the role of the electrical field, when the radius is increased from 5 Å to 15 Å, it is observed that the intensity of the EDL increases for all molar concentrations, and that the difference between equal electric fields and surface charges diminishes as well. For the highest molar concentration, when equal electric fields are used, once again the spherical electrode achieves the highest contact values followed by the cylindrical electrode and lastly the planar electrode. Also as discussed above, this higher values of the concentration profiles at contact, only last there, as when the distance from the surface slightly increases, the planar electrode overtakes the spherical and cylindrical electrodes. Furthermore, for the highest molar concentrations it is found that the concentration profiles of the cylindrical and spherical electrodes are almost completely identical to the planar electrode, even though the radius increment was small. This, again, is an effect of the compactness of the EDL at high salt concentration.

Continuously, in Fig. 2.13 the concentration profiles of the different electrode's geometries, for a radius of 80 Å, are plotted while the molar concentration is increased. Again, when the radius grows from 15 Å to 80 Å the concentration profiles of the cylindrical and spherical electrodes largely increase for all the molar concentrations. As the case of equal electric fields is given by the relation

of Eqs. (2.49) and (2.50), when the radius is big enough, the relation by which the surface charge of

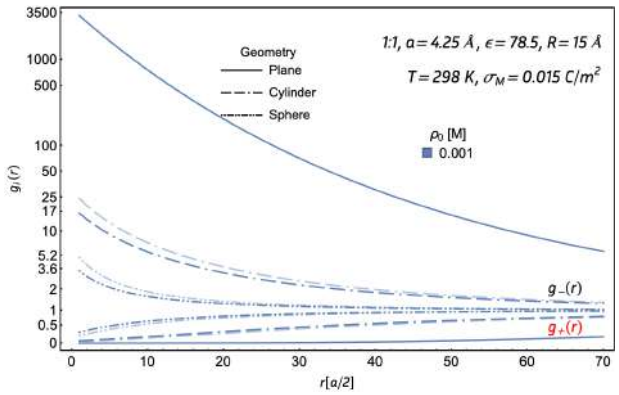


(a) The concentration profiles for $\rho_0 = 0.001\,\mathrm{M}$.

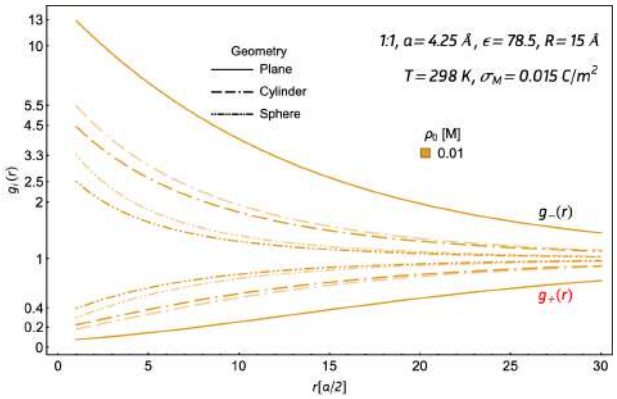


(b) The concentration profiles for $\rho_0 = 0.01\,\mathrm{M}$.

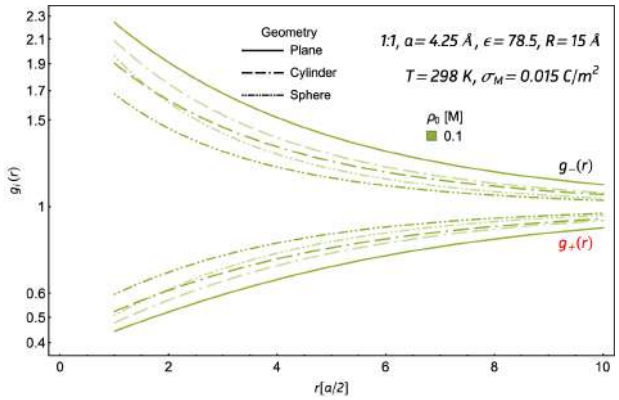


(c) The concentration profiles for $\rho_0 = 0.1\,\mathrm{M}$.

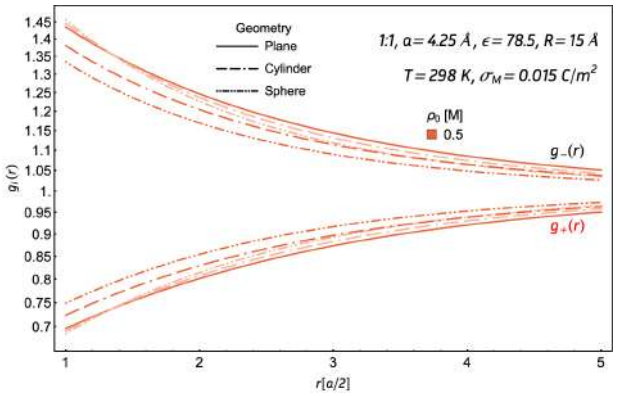


(d) The concentration profiles for $\rho_0 = 0.5\,\mathrm{M}$.

Figure 2.12: The concentration profile functions, $g_i(r)$, of the LPBS for the different electrode's geometries, for a radius of $15\,\text{Å} \cong 3.5\,a$, while the molar concentration, $\rho_0$, is increased. The lighter and darker lines have the same meaning as in Fig. 2.11.

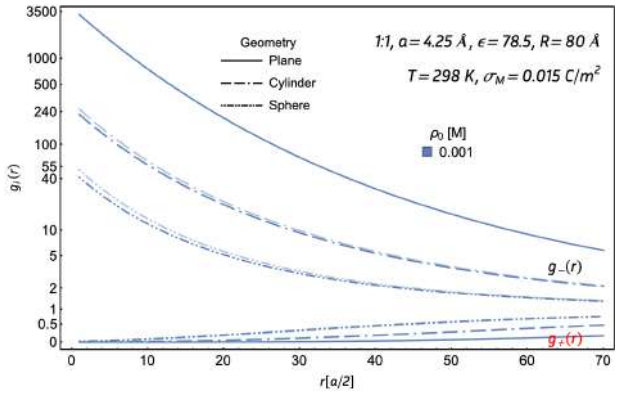


(a) The concentration profiles for $\rho_0 = 0.001\,\mathrm{M}$.

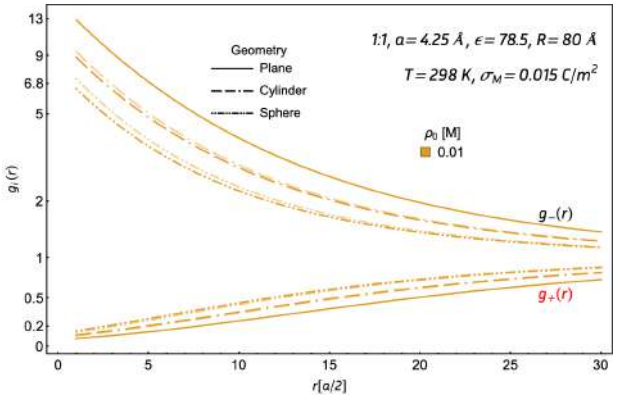


(b) The concentration profiles for $\rho_0 = 0.01\,\mathrm{M}$.

Figure 2.13: The concentration profile functions, $g_i(r)$, of LPBS for the different electrode's geometries, for a radius of $80\,\text{Å} \cong 18.8\,a$, while the molar concentration, $\rho_0$, is increased. The lighter and darker lines have the same meaning as in Fig. 2.11.

the planar electrode is multiplied is almost equal to unity. Therefore both cases (equal electric fields and surface charges) are identical to each other. Furthermore, as it was seen in Fig. 2.12, when higher molar concentrations are used, a small increment on the radius generates an exponential raise on the concentration profiles of higher molar concentration. For this reason, the higher concentrations for $R = 80\,\text{Å}$ were not plotted, as the concentration profiles of the three electrode geometries overlap into the concentration profiles of the planar electrode.

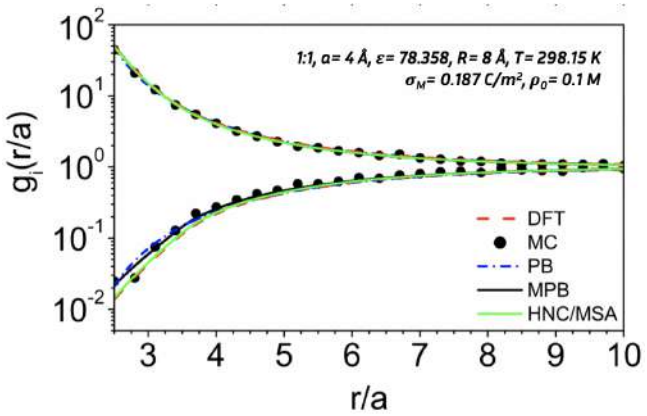


Figure 2.14: Ion's distribution for the restricted primitive model of the cylindrical double layer. "Reprinted" adapted with permission from González-Tovar *et al.* [73].

González-Tovar *et al.* [73] did a comparison of their HNC/MSA equations of the cylindrical electrode against MC simulations. They found that the validity of their cylinder's HNC/MSA equations certainly holds for molar concentrations of 0.1 M for symmetric electrolytes (1:1), and, in fact for up to 2 M concentration for a 1:1 electrolyte, or up to a 1 M concentration for a 2:2 salt, and unsymmetrical electrolytes. Figure 2.14 illustrates this, by showing the concentration profile for the density functional theory (DFT), MC, non linear PB (PB), modified PB (MPB), and the HNC/MSA equations. There-

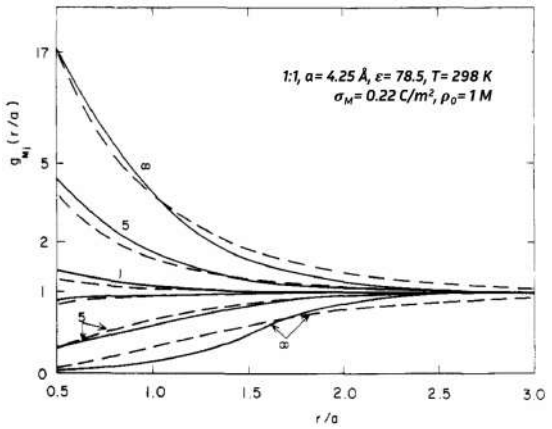


(a) Results of González-Tovar and Lozada-Cassou [78]. "Reprinted" adapted with permission from González-Tovar and Lozada-Cassou [78].

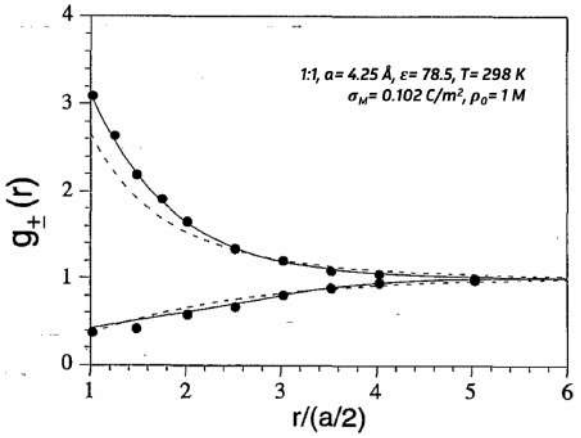


(b) Results of Degrève *et al.* [68]. "Reprinted" adapted with permission from Degrève *et al.* [68].

Figure 2.15: Reduced concentration profiles of a monovalent electrolyte for both various sphere radii, and a radius of 15 Å in Figs. 2.15a and 2.15b, respectively. The solid and broken curves give the HNC/MSA, PBS, and MC results.

fore, from their work it is found that their HNC/MSA equation for of the cylindrical electrode is a good theory. By consequence our linear Poisson-Boltzmann model with the Stern restriction is a good approximation as well, as proved in Figs. 2.8 to 2.10.

In addition, the work of González-Tovar and Lozada-Cassou [78] found that the validity of the nLPBS model of the spherical electrode against the HNC/MSA equations is good for molar concentrations from 0.01 M to 1 M, and for small mean electrostatic potentials. However, their work does not compare against MC results, as the data were not available. On the other hand, Degrève *et al.* [68] also performed a comparison against MC results. As seen in Fig. 2.15, the concentration profiles for a molar concentration of 1 M are shown for both the non-linear PBS, the HNC/MSA, and MC results of the spherical electrode. From it, it is observed that the HNC/MSA theory is a good approximation of the MC results for $\rho_0 = 1\,\mathrm{M}$. Furthermore, another interesting result found by González-Tovar and Lozada-Cassou [78, 73], that we observe as well, is that the results obtained for an infinite radii' cylindrical or spherical electrodes are almost identical to those with a radius equal to 80 Å. From both the results of Gonzaléz-Tovar and Lozada-Cassou, and Degrève *et al.* it is found that the HNC/MSA is a good approximation of the EDL of the spherical electrode, and that by extension, our linear solution of the EDL of the spherical electrode is also a good approximation.

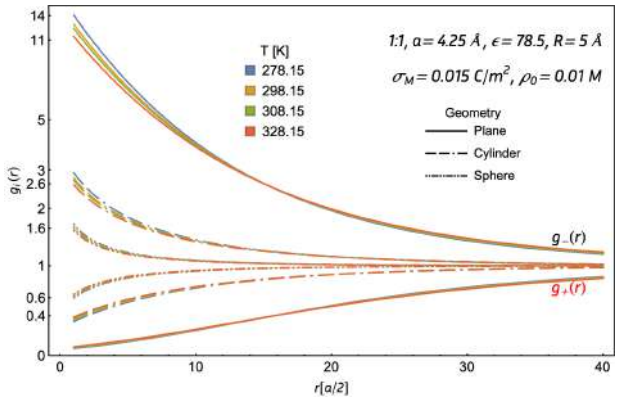


(a) The concentration profiles for $R = 5\,\text{Å} \cong 1.2\,a$.

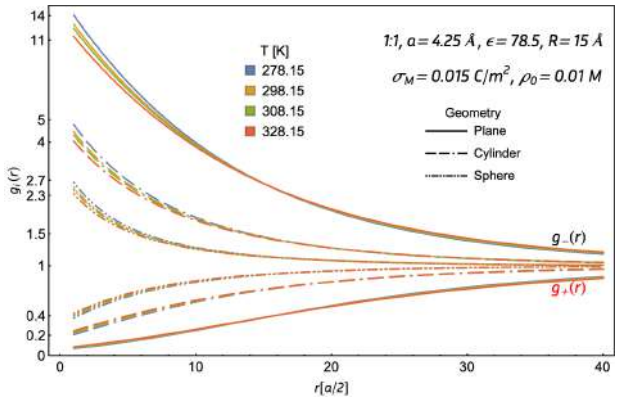


(b) The concentration profiles for $R = 15\,\text{Å} \cong 3.5\,a$.

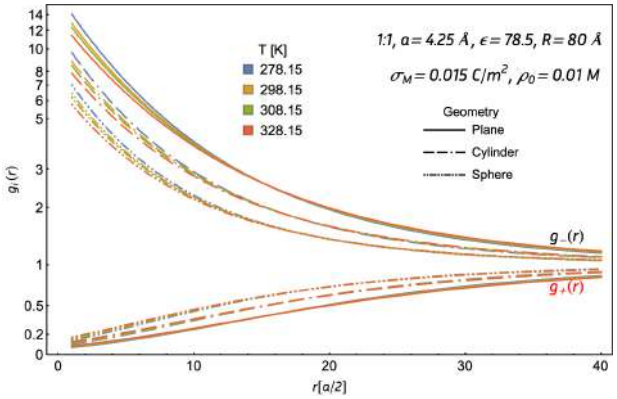


(c) The concentration profiles for $R = 80\,\text{Å} \cong 18.8\,a$.

Figure 2.16: The concentration profile functions, $g_i(r)$, of LPBS for the different electrode's geometries, for three radii, while the temperature, $T$, is varied.

Finally, in Fig. 2.16 the concentration profiles for three geometries of the solid electrodes, with three radii values are plotted, while the temperature is varied. A molar concentration of 0.01 M and a surface

charge of $0.015\,\mathrm{C/m^2}$ is used. For all the electrodes' geometries it is seen that when the temperature increases the intensity of the co-ion and counter-ion distribution functions slightly decreases, regardless of the radius used. However, the most visible difference between temperatures is found at the contact values for the highest radius. Moreover, it is observed that the contact value of the concentration profiles is higher for the lower temperatures, for any geometry and radius. Quite generally, the Poisson-Boltzmann equation (PB), for any geometry, is given by Eqs. (2.1) to (2.4), or its linear expression, by Eqs. (2.6) and (2.7). Thus, it is clear that Poisson-Boltzmann counter-ion and co-ion distribution functions, for any electrode's geometry, exponentially decrease/increase, with increasing temperature, respectively. In its linearized form these distribution functions increase/decrease inversely linear with increasing temperature. Hence, increasing the temperature has a similar tendency but not in magnitude to decreasing the ionic valence or the salt concentration, or the surface charge density.

On the other hand, if one looks closely to Fig. 2.16, at a distance close to $7\,a$, the previous tendency is tenuously reversed. Such that, when the temperature increases beyond this point, the intensity of the EDL subtly boosts. This increase in the counter-ion concentration profile, at $7\,a$, for say $T = 328.15\,\mathrm{K}^\circ$ is due to the necessity of the system of maintaining electroneutrality, i.e., the lower contact value is compensated by a thicker electrical double layer.

*In general, it is found that the parameter that exerts the least influence on the EDL is, without a doubt, the temperature, irrespective of the electrode's geometry or radius size.*

# Chapter 3

# The electrical double layer for nano-pore electrodes

In this chapter we study three distinct nano-pores electrodes: slit, cylindrical, and spherical pores, through the analytical solution of the LPBS of the EDL. For this purpose, we first exactly solve the Laplace and Poisson equations of the electrostatics, for these three topological different geometries, i.e., no approximations are involved in these derivations. In particular, the mean electrostatic potential, the surface charge density, the co-ion and counter-ion distribution functions, and the capacitance are obtained for the different nano-pores.

## 3.1 The electrical double layer of two parallel plates electrodes (slit-pore)

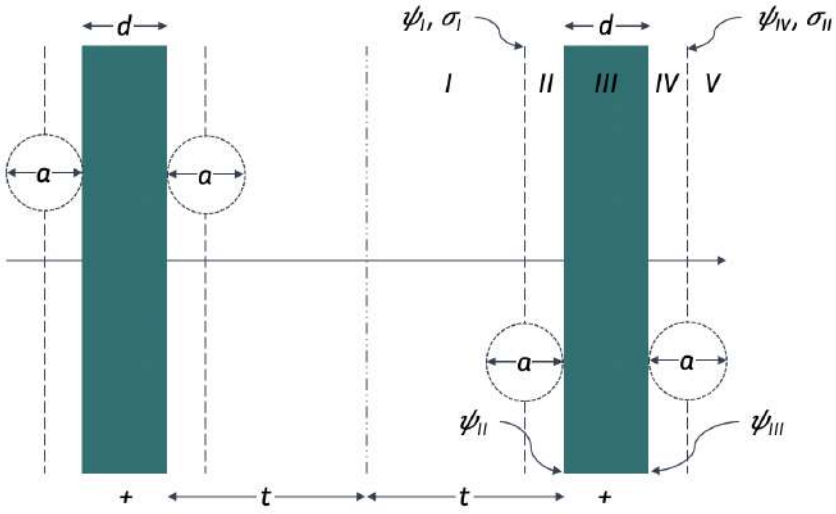


Figure 3.1: The geometry of two interacting charged symmetric plates'.

The model for two interacting charged parallel plates (slit-pore) is depicted in Fig. 3.1. Both plates are positively charged, they are separated by a distance of $2\,t$, and have a thickness of $d$. The electrolyte is modeled as a fluid of hard spheres of diameter $a$, with charge in their centers. Both, the plates and the electrolyte are assumed to have the same dielectric constant, $\varepsilon$, to avoid image potentials. The plates

are permeable, so the electrolyte outside and inside the plates are at the same chemical potential. As pointed out above, we will first solve the Laplace equation, i.e.,

$$\nabla^2\psi(x) = 0, \tag{3.1}$$

and the Poisson equation,

$$\nabla^2\psi(x) = -\frac{4\,\pi}{\varepsilon}\,\rho_{el}(x), \tag{3.2}$$

for this model, where $\rho_{el}(x)$ is the charge concentration distribution function, and $\psi(x)$ is the mean electrostatic potential. The solution of these equations for this model is presented below, and is quite general, since no assumption is made at this point for, $\rho_{el}(x)$, which for $n$ species of charges, can be expressed as

$$\rho_{el}(x) = \sum_{i=1}^{n} e\,z_i\,\rho_i(x), \tag{3.3}$$

where $\rho_i(x)$ is the species' spacial distribution of the charges, and $z_i$ the species' ion valence. However, to obtain the electrical double layer structure, the Eq. (3.2) will be solved assuming that $\rho_{el}(x)$ is given by the canonical Boltzmann distribution function of the ions in the electrolyte, i.e.,

$$\rho_{el}(x) = \rho_{i0}\exp(e\,z_i\,\beta\,\psi(x)), \tag{3.4}$$

where $\rho_{i0}$ is the bulk concentration of ions of species $i$, and $\beta = \frac{1}{kT}$, being $k$, the Boltzmann constant. Thus, Eq. (3.2) becomes the Poisson-Boltzmann equation,

$$\nabla^2\psi(x) = -\frac{4\,\pi}{\varepsilon}\sum_{i=1}^{n}\rho_{i0}\exp(e\,z_i\,\beta\,\psi(x)). \tag{3.5}$$

It will be further assumed that the ions are point ions, and their size is taken into account only in their interaction with the plates, i.e., the Stern correction. In addition, to finally obtain the EDL for the different nano-pores, Eq. (3.5) will be linearized, and analytically solved for a two-species electrolyte.

### 3.1.1 The electrostatics of a slit-pore in an electrolyte

Due to the symmetry of the slit-pore, the left side and the right side of the center of the pore are symmetrical. Hence, to solve the electrostatics, the system is divided only into five regions (see Fig. 3.1). In regions II, III, and IV, the mean electrostatic potential is governed by Laplace equation (Eq. (3.1)), and in regions I and V, by the Poisson equation (Eq. (3.2)).

1. **Region V:** $x \geq t + d + \frac{a}{2}$

The boundary conditions are

$$\lim_{x\to\infty}\psi_5(x) = 0$$

and

$$\lim_{x\to\infty}\frac{\mathrm{d}\psi_5(x)}{\mathrm{d}x} = 0$$

Therefore, from Eq. (3.2), we find

$$\frac{\mathrm{d}\psi_5(x)}{\mathrm{d}x} = \frac{4\,\pi}{\varepsilon}\int_x^{\infty}\rho_{el}(y)\,\mathrm{d}y \tag{3.6}$$

Thus,

$$\psi_5(x) = -\frac{4\,\pi}{\varepsilon}\int_x^\infty \mathrm{d}x' \int_{x'}^\infty \rho_{el}(y)\,\mathrm{d}y$$

Namely,

$$\psi_5(x) = \frac{4\,\pi}{\varepsilon}\int_x^\infty (x-y)\,\rho_{el}(y)\,\mathrm{d}y$$

For $x = t + d + \frac{a}{2}$

$$\psi_{IV} \equiv \psi_5\left(t+d+\frac{a}{2}\right) = \frac{4\,\pi}{\varepsilon}\int_{t+d+\frac{a}{2}}^\infty \left(t+d+\frac{a}{2}-y\right)\rho_{el}(y)\,\mathrm{d}y \tag{3.7}$$

**2. Region IV:** $t + d \le x \le t + d + \frac{a}{2}$

If the dielectric constant, $\varepsilon$, of the plates and the solution are considered equal, to avoid image forces, the boundary conditions are

$$\psi_4\left(t+d+\frac{a}{2}\right) = \psi_{IV} \tag{3.8}$$

$$\varepsilon\left(\frac{\mathrm{d}\psi_5(x)}{\mathrm{d}x}\right)_{t+d+\frac{a}{2}} - \varepsilon\left(\frac{\mathrm{d}\psi_4(x)}{\mathrm{d}x}\right)_{t+d+\frac{a}{2}} = 0 \tag{3.9}$$

From Eq. (3.1),

$$\mathrm{d}\psi_4(x)\,/\,\mathrm{d}x = \text{constant} \tag{3.10}$$

Integrating Eq. (3.10) and using Eqs. (3.6) to (3.9), we find

$$\psi_4(x) = \frac{4\,\pi}{\varepsilon}\int_{t+d+\frac{a}{2}}^\infty (x-y)\,\rho_{el}(y)\,\mathrm{d}y \tag{3.11}$$

In particular,

$$\psi_{III} \equiv \psi_4(t+d) = \frac{4\,\pi}{\varepsilon}\int_{t+d+\frac{a}{2}}^\infty (t+d-y)\,\rho_{el}(y)\,\mathrm{d}y \tag{3.12}$$

**3. Region III:** $t \le x \le t + d$

The boundary conditions are

$$\psi_3(t+d) = \psi_{III} \tag{3.13}$$

$$\varepsilon\left(\frac{\mathrm{d}\psi_4(x)}{\mathrm{d}x}\right)_{t+d} - \varepsilon\left(\frac{\mathrm{d}\psi_3(x)}{\mathrm{d}x}\right)_{t+d} = -4\,\pi\,\sigma_{II} \tag{3.14}$$

From Eqs. (3.1) and (3.11) to (3.14)

$$\psi_3(x) = -\frac{4\,\pi\,\sigma_{II}}{\varepsilon}\,(t+d-x) + \frac{4\,\pi}{\varepsilon}\int_{t+d+\frac{a}{2}}^\infty (x-y)\,\rho_{el}(y)\,\mathrm{d}y \tag{3.15}$$

In particular,

$$\psi_{II} \equiv \psi_3(t) = -\frac{4\,\pi\,\sigma_{II}}{\varepsilon}\,d + \frac{4\,\pi}{\varepsilon}\int_{t+d+\frac{a}{2}}^\infty (t-y)\,\rho_{el}(y)\,\mathrm{d}y \tag{3.16}$$

For two plates (slit-pore) electrodes, the electro-neutrality condition is

$$\sigma_I + \sigma_{II} = -\int_0^{t-\frac{a}{2}} \rho_{el}(y)\,\mathrm{d}y - \int_{t+d+\frac{a}{2}}^\infty \rho_{el}(y)\,\mathrm{d}y\,, \tag{3.17}$$

i.e, the total effective charge in the system must be zero. Manipulating Eqs. (3.12), (3.16) and (3.17), we find

$$\psi_{II} = \psi_{III} - \frac{4\,\pi\,\sigma_{II}}{\varepsilon}\,d - \frac{4\,\pi\,d}{\varepsilon}\int_{t+d+\frac{a}{2}}^{\infty}\rho_{el}(y)\,\mathrm{d}y$$

or

$$\psi_{II} = \psi_{III} + \frac{4\,\pi\,\sigma_{I}}{\varepsilon}\,d + \frac{4\,\pi\,d}{\varepsilon}\int_{0}^{t-\frac{a}{2}}\rho_{el}(y)\,\mathrm{d}y$$

If we make $\psi_{II} = \psi_{III}$ then the inside part of the electrolyte cancels $\sigma_I$ and the outside part cancels $\sigma_{II}$, hence

$$\sigma_I = -\int_{0}^{t-\frac{a}{2}}\rho_{el}(y)\,\mathrm{d}y$$

and

$$\sigma_{II} = -\int_{t+d+\frac{a}{2}}^{\infty}\rho_{el}(y)\,\mathrm{d}y$$

**4. Region II:** $t - \frac{a}{2} \leq x \leq t$

In this region, the boundary conditions are

$$\psi_2(t) = \psi_{II} \tag{3.18}$$

$$\varepsilon\left(\frac{\mathrm{d}\psi_3(x)}{\mathrm{d}x}\right)_t - \varepsilon\left(\frac{\mathrm{d}\psi_2(x)}{\mathrm{d}x}\right)_t = -4\,\pi\,\sigma_I \tag{3.19}$$

From Eqs. (3.1), (3.15), (3.17) and (3.19)

$$\left(\frac{\mathrm{d}\psi_2(x)}{\mathrm{d}x}\right)_t = -\frac{4\,\pi}{\varepsilon}\int_{0}^{t-\frac{a}{2}}\rho_{el}(y)\,\mathrm{d}y \tag{3.20}$$

Integrating and using Eq. (3.18),

$$\psi_2(x) = \psi_{II} + \frac{4\,\pi}{\varepsilon}(t-x)\int_{0}^{t-\frac{a}{2}}\rho_{el}(y)\,\mathrm{d}y$$

In particular

$$\psi_I \equiv \psi_2\left(t - \frac{a}{2}\right) = \psi_{II} + \frac{2\,\pi\,a}{\varepsilon}\int_{0}^{t-\frac{a}{2}}\rho_{el}(y)\,\mathrm{d}y \tag{3.21}$$

If $\psi_{II} = \psi_{III}$, Eq. (3.21) reduces to the familiar term

$$\psi_I = \psi_{II} - \frac{2\,\pi\,a}{\varepsilon}\sigma_I$$

**5. Region I:** $0 \leq x \leq t - \frac{a}{2}$

Here the boundary conditions are

$$\psi_1\left(t - \frac{a}{2}\right) = \psi_I \tag{3.22}$$

and

$$\varepsilon\left(\frac{\mathrm{d}\psi_1(x)}{\mathrm{d}x}\right)_{t-\frac{a}{2}} - \varepsilon\left(\frac{\mathrm{d}\psi_2(x)}{\mathrm{d}x}\right)_{t-\frac{a}{2}} = 0 \tag{3.23}$$

Integrating Eq. (3.2) and using Eqs. (3.20) and (3.23),

$$\frac{\mathrm{d}\psi_1(x)}{\mathrm{d}x} = -\frac{4\,\pi}{\varepsilon}\int_0^{t-\frac{a}{2}} \rho_{el}(y)\,\mathrm{d}y + \frac{4\,\pi}{\varepsilon}\int_x^{t-\frac{a}{2}} \rho_{el}(y)\,\mathrm{d}y \tag{3.24}$$

Integrating by parts Eq. (3.24) and using Eqs. (3.21) and (3.22)

$$\psi_1(x) = \psi_{II} + \frac{4\,\pi}{\varepsilon}(t-x)\int_0^{t-\frac{a}{2}} \rho_{el}(y)\,\mathrm{d}y + \frac{4\,\pi}{\varepsilon}\int_x^{t-\frac{a}{2}} (x-y)\rho_{el}(y)\,\mathrm{d}y$$

In particular,

$$\psi_0 \equiv \psi_1(0) = \psi_{II} + \frac{4\,\pi}{\varepsilon}\int_x^{t-\frac{a}{2}} (x-y)\rho_{el}(y)\,\mathrm{d}y$$

### 3.1.2 The analytical solution of the LPBS for the electrical double layer of two parallel plates electrodes (slit-pore)

In order to obtain the analytical solution of the LPBS for the electrical double layer of two symmetrical plates electrodes, one needs to solve a system of five differential equations. Regions II, III, and IV are governed by Laplace equation in Eq. (3.1), and regions I and IV are ruled by Poisson-Boltzmann equation in Eq. (3.2).

In Section 2.1.1 it was seen from Eq. (2.6) that the linearization of the PB-eq (Eq. (3.5)) leads to

$$\nabla^2\psi(x) = \kappa^2\,\psi(x) \tag{3.25}$$

Hence, the general solutions of the Laplace and Poisson-Boltzmann equations are, with their respective derivatives

$$\psi(x) = A + B\,x \qquad \frac{\mathrm{d}\psi}{\mathrm{d}x} = B \tag{3.26}$$

$$\psi(x) = A\,e^{\kappa\,x} + B\,e^{-\kappa\,x} \qquad \frac{\mathrm{d}\psi}{\mathrm{d}x} = A\,\kappa\,e^{\kappa\,x} - B\,\kappa\,e^{-\kappa\,x} \tag{3.27}$$

Now, the five regions will be treated individually with their respective boundary conditions (BC). Each region will be introduced by their interval, and with their respective solution of the mean electrostatic potential. Furthermore, in each region two BC will be introduced in order to find the values of their constants. This is true for all the regions, with the exception of regions V and I, where one and three BC are used, respectively.

**1. Region V:** $x \geq t + d + \frac{a}{2}$

Here, the solution of the PB equation is $\psi_5(x) = c_1\,e^{\kappa\,x} + c_2\,e^{-\kappa\,x}$, and the BC is that, at $x \to \infty$, the electric field is equal to zero. From the Gauss' law, we know that the electric field is equal to minus the divergence of the electric potential. Hence,

$$\lim_{x\to\infty} E(x) = 0 \qquad\qquad E(x) = -\boldsymbol{\nabla}\cdot\psi(x) = -c_1\,\kappa\,e^{\kappa\,x} + c_2\,\kappa\,e^{-\kappa\,x}$$

$$\lim_{x\to\infty} E(x) = -c_1\,\kappa\,e^{\kappa\,x} + c_2\,\kappa\,\cancelto{0}{e^{-\kappa\,x}} = 0 \qquad\qquad \therefore \quad c_1 = 0 \tag{3.28}$$

Thus, the mean electrostatic potential in this interval and its derivative are

$$\psi_5(x) = c_2\,e^{-\kappa\,x} \qquad\qquad \frac{\mathrm{d}\psi_5}{\mathrm{d}x} = -c_2\,\kappa\,e^{-\kappa\,x}$$

**2. Region IV:** $t + d \leq x \leq t + d + \frac{a}{2}$

Here, $\psi_4(x) = c_3 + c_4\, x$, and the BC is the continuity of the mean electrostatic potential between intervals. Thus, $\psi_5(x)$ and $\psi_4(x)$ are equal at their border, $t + d + \frac{a}{2}$. Furthermore, if the dielectric constant of the electrodes and electrolyte are equal, the subtraction of the derivatives of the mean electrostatic potential ($\psi_5(x)$ and $\psi_4(x)$) is equal to zero at their border, $t + d + \frac{a}{2}$. Therefore,

$$\psi_5\left(t + d + \frac{a}{2}\right) = \psi_4\left(t + d + \frac{a}{2}\right) \quad \longrightarrow \quad c_2\, e^{-\kappa\left(t+d+\frac{a}{2}\right)} = c_3 + c_4\left(t + d + \frac{a}{2}\right)$$

$$c_3 = c_2\, e^{-\kappa\left(t+d+\frac{a}{2}\right)} - c_4\left(t + d + \frac{a}{2}\right) \tag{3.29}$$

$$\varepsilon\left(\frac{\mathrm{d}\psi_5(x)}{\mathrm{d}x}\right)_{t+d+\frac{a}{2}} - \varepsilon\left(\frac{\mathrm{d}\psi_4(x)}{\mathrm{d}x}\right)_{t+d+\frac{a}{2}} = 0 \quad \longrightarrow \quad c_4 = -c_2\,\kappa\, e^{-\kappa\left(t+d+\frac{a}{2}\right)} \tag{3.30}$$

**3. Region III:** $t \leq x \leq t + d$

Here, $\psi_3(x) = c_5 + c_6\, x$, and once again we have the BC of continuity, between $\psi_4(x)$ and $\psi_3(x)$ at $t+d$. But, the difference between the derivative of $\psi_4(x)$ and $\psi_3(x)$ is now equal to $-4\,\pi\,\sigma_{II}$. Therefore,

$$\psi_4(t + d) = \psi_3(t + d) \quad \longrightarrow \quad c_3 + c_4(t + d) = c_5 + c_6(t + d)$$

$$c_5 = c_3 + (c_4 - c_6)(t + d) \tag{3.31}$$

$$\varepsilon\left(\frac{\mathrm{d}\psi_4(x)}{\mathrm{d}x}\right)_{t+d} - \varepsilon\left(\frac{\mathrm{d}\psi_3(x)}{\mathrm{d}x}\right)_{t+d} = -4\,\pi\,\sigma_{II} \quad \longrightarrow \quad c_4 - c_6 = -\frac{4\,\pi\,\sigma_{II}}{\varepsilon}$$

$$c_6 = c_4 + \frac{4\,\pi\,\sigma_{II}}{\varepsilon} \tag{3.32}$$

**4. Region II:** $t - \frac{a}{2} \leq x \leq t$

Here, $\psi_2(x) = c_7 + c_8\, x$, and one of our BC is the continuity, between $\psi_3(x)$ and $\psi_2(x)$ at $t$. Whereas, the difference between the derivative of $\psi_3(x)$ and $\psi_2(x)$ is now equal to $-4\,\pi\,\sigma_I$. Consequently,

$$\psi_3(t) = \psi_2(t) \quad \longrightarrow \quad c_5 + c_6\, t = c_7 + c_8\, t$$

$$c_7 = c_5 + (c_6 - c_8)\, t \tag{3.33}$$

$$\varepsilon\left(\frac{\mathrm{d}\psi_3(x)}{\mathrm{d}x}\right)_{t} - \varepsilon\left(\frac{\mathrm{d}\psi_2(x)}{\mathrm{d}x}\right)_{t} = -4\,\pi\sigma_I \quad \longrightarrow \quad c_6 - c_8 = -\frac{4\,\pi\,\sigma_I}{\varepsilon}$$

$$c_8 = c_6 + \frac{4\,\pi\,\sigma_I}{\varepsilon} \tag{3.34}$$

**5. Region I:** $0 \leq x \leq t - \frac{a}{2}$

Lastly, here, $\psi_1(x) = c_9\, e^{\kappa\, x} + c_{10}\, e^{-\kappa\, x}$, and one of the final BCs is that the electric field at the center of the plates, $x = 0$, is equal to zero. From the Gauss' law, the electric field is equal to minus the divergence of the electric potential. Therefore,

$$\lim_{x\to 0} E(x) = 0 \qquad E(x) = -\boldsymbol{\nabla}\cdot\psi(x) = -c_9\,\kappa\, e^{\kappa\, x} + c_{10}\,\kappa\, e^{-\kappa\, x}$$

$$\lim_{x\to 0} E(x) = -c_9\,\kappa\,\cancelto{1}{e^{\kappa\, x}} + c_{10}\,\kappa\,\cancelto{1}{e^{-\kappa\, x}} = 0 \qquad \therefore \quad c_9 = c_{10} \tag{3.35}$$

Hence, the mean electrostatic potential in this interval and its derivative are

$$\psi_1(x) = 2\,c_9\,\cosh(\kappa\,x) \qquad\qquad \frac{\mathrm{d}\psi_1}{\mathrm{d}x} = 2\,\kappa\,c_9\,\sinh(\kappa\,x)$$

Furthermore, the last two BCs are of continuity between $\psi_2(x)$ and $\psi_1(x)$ at $t - a/2$, and that the difference between the derivative of $\psi_2(x)$ and $\psi_1(x)$ is equal to zero. Hence,

$$\psi_2\left(t-\frac{a}{2}\right) = \psi_1\left(t-\frac{a}{2}\right) \quad\longrightarrow\quad c_7 + c_8\left(t-\frac{a}{2}\right) = 2\,c_9\,\cosh\!\left(\kappa\left(t-\frac{a}{2}\right)\right)$$

$$c_7 = 2\,c_9\,\cosh\!\left(\kappa\left(t-\frac{a}{2}\right)\right) - c_8\left(t-\frac{a}{2}\right) \tag{3.36}$$

$$\varepsilon\left(\frac{\mathrm{d}\psi_2(x)}{\mathrm{d}x}\right)_{t-\frac{a}{2}} - \varepsilon\left(\frac{\mathrm{d}\psi_1(x)}{\mathrm{d}x}\right)_{t-\frac{a}{2}} = 0 \quad\longrightarrow\quad c_8 = 2\,\kappa\,c_9\,\sinh\!\left(\kappa\left(t-\frac{a}{2}\right)\right) \tag{3.37}$$

Now, from Eqs. (3.28) to (3.37) we have ten linear equations with ten unknown variables.

$$\begin{cases} c_1 = 0 \\ c_3 = c_2\,e^{-\kappa\left(t+d+\frac{a}{2}\right)} - c_4\left(t+d+\frac{a}{2}\right) \\ c_4 = -c_2\,\kappa\,e^{-\kappa\left(t+d+\frac{a}{2}\right)} \\ c_5 = c_3 + (c_4 - c_6)(t+d) \\ c_6 = c_4 + \frac{4\,\pi\,\sigma_{II}}{\varepsilon} \\ c_7 = c_5 + (c_6 - c_8)\,t \\ c_8 = c_6 + \frac{4\,\pi\,\sigma_I}{\varepsilon} \\ c_9 = c_{10} \\ c_7 = 2\,c_9\,\cosh\!\left(\kappa\left(t-\frac{a}{2}\right)\right) - c_8\left(t-\frac{a}{2}\right) \\ c_8 = 2\,\kappa\,c_9\,\sinh\!\left(\kappa\left(t-\frac{a}{2}\right)\right) \end{cases} \tag{3.38}$$

Solving Eq. (3.38), one finds the value of $c_2$, and consequently all the other constants

$$c_2 = \frac{\frac{4\,\pi}{\varepsilon}\left\{\sigma_{II}\left[d+\frac{a}{2}+\frac{\coth\left(\kappa\left(t-\frac{a}{2}\right)\right)}{\kappa}\right] + \sigma_I\left[\frac{a}{2}+\frac{\coth\left(\kappa\left(t-\frac{a}{2}\right)\right)}{\kappa}\right]\right\}}{1+\kappa\,(d+a)+\coth\!\left(\kappa\left(t-\frac{a}{2}\right)\right)}\,e^{\kappa\left(t+d+\frac{a}{2}\right)} \tag{3.39}$$

Therefore the mean electrostatic potential is

$$\psi(x) = \begin{cases} 2\,c_9\,\cosh(\kappa\,x) & 0 \le x \le t-\frac{a}{2} \\ c_7 + c_8\,x & t-\frac{a}{2} \le x \le t \\ c_5 + c_6\,x & t \le x \le t+d \\ c_3 + c_4\,x & t+d \le x \le t+d+\frac{a}{2} \\ c_2\,e^{-\kappa\,x} & x \ge t+d+\frac{a}{2} \end{cases} \tag{3.40}$$

Meanwhile, the induced surface charge density is given by

$$\begin{aligned} \sigma(x) = -\int_x^\infty \rho_{el}(x)\,\mathrm{d}x = \frac{\varepsilon}{4\,\pi}\int_x^\infty \frac{\mathrm{d}^2\psi}{\mathrm{d}x^2}\,\mathrm{d}x = \frac{\varepsilon}{4\,\pi}\int_0^x \frac{\mathrm{d}^2\psi_1}{\mathrm{d}x^2}\,\mathrm{d}x + \frac{\varepsilon}{4\,\pi}\int_x^\infty \frac{\mathrm{d}^2\psi_5}{\mathrm{d}x^2}\,\mathrm{d}x \\ = \frac{\varepsilon}{4\,\pi}\left(\frac{\mathrm{d}\psi_1}{\mathrm{d}x}\right)_x - \frac{\varepsilon}{4\,\pi}\left(\frac{\mathrm{d}\psi_5}{\mathrm{d}x}\right)_x \end{aligned} \tag{3.41}$$

Thence, it is divided into three intervals. After obtaining the derivatives and evaluating, we have that the induced surface charge density is

$$\sigma(x) = \begin{cases} \frac{\varepsilon\,\kappa}{2\,\pi}\, c_9\, \sinh(\kappa\, x) & 0 \le x \le t - \frac{a}{2} \\ 0 & t - \frac{a}{2} < x < t + d + \frac{a}{2} \\ \frac{\varepsilon\,\kappa}{4\,\pi}\, c_2\, e^{-\kappa\, x} & x \ge t + d + \frac{a}{2} \end{cases} \tag{3.42}$$

Meanwhile, the co-ion and counter-ion distribution functions are given once again by Eqs. (2.12) and (2.13)

$$g_+(x) = \begin{cases} \exp\!\left(-\frac{2\,z\,e}{k\,T}\, c_9\, \cosh(\kappa\, x)\right) & 0 \le x \le t - \frac{a}{2} \\ 0 & t - \frac{a}{2} < x < t + d + \frac{a}{2} \\ \exp\!\left(-\frac{z\,e}{k\,T}\, c_2\, e^{-\kappa\, x}\right) & x \ge t + d + \frac{a}{2} \end{cases} \tag{3.43}$$

$$g_-(x) = \begin{cases} \exp\!\left(\frac{2\,z\,e}{k\,T}\, c_9\, \cosh(\kappa\, x)\right) & 0 \le x \le t - \frac{a}{2} \\ 0 & t - \frac{a}{2} < x < t + d + \frac{a}{2} \\ \exp\!\left(\frac{z\,e}{k\,T}\, c_2\, e^{-\kappa\, x}\right) & x \ge t + d + \frac{a}{2} \end{cases} \tag{3.44}$$

Finally, in order to obtain the total differential capacitance we must derive $\psi_d$ with respect to $\sigma$. Where $\sigma = \sigma_I = \sigma_{II}$ and $\psi_d$ is the value of $\psi(x)$ at its' center. Such as,

$$\psi_d \equiv \lim_{x \to 0} \psi(x) = 2\, c_9 \cancelto{1}{\cosh(\kappa\, x)} = 2\, c_9 \tag{3.45}$$

The total differential capacitance is obtained deriving Eq. (3.45) with respect to $\sigma$ and using Eqs. (3.38) and (3.39). Therefore,

$$C_T \equiv \frac{\mathrm{d}\psi_d}{\mathrm{d}\sigma} = \frac{\frac{8\,\pi}{\varepsilon\,\kappa} - \frac{4\,\pi}{\varepsilon}\left[d + a + \frac{2\,\coth\left(\kappa\left(t - \frac{a}{2}\right)\right)}{\kappa}\right]}{\sinh\left(\kappa\,\left(t - \frac{a}{2}\right)\right)} \tag{3.46}$$

## 3.2 The electrical double layer of a cylindrical nano-pore electrode

A model for a cylindrical, charged nano-pore, open at both extremes, is depicted in Fig. 3.2, where the inner radius of the pore is $R$ and its wall thickness is $d$. The cylinder is permeable, so that the electrolyte inside and outside the pore is at the same chemical potential. The electrolyte ions have a diameter $a$. Other model parameters are as in Section 3.1. Due to the symmetry of the cylinder, the electrostatics of the nano-pore is divided into the five regions shown in Fig. 3.2.
Since there is no charge in regions II, III, and IV, the mean electrostatic potential is governed by Laplace equation, in cylindrical coordinates,

$$\frac{1}{r}\frac{\partial}{\partial r}\left(r\frac{\partial \psi}{\partial r}\right) = 0, \tag{3.47}$$

whereas in regions I and V the PB-eq, in cylindrical coordinates, is valid

$$\frac{1}{r}\frac{\partial}{\partial r}\left(r\frac{\partial \psi}{\partial r}\right) = -\frac{4\,\pi}{\varepsilon}\rho_{el}(r) \tag{3.48}$$

where $\psi(r)$ is the mean electrostatic potential.

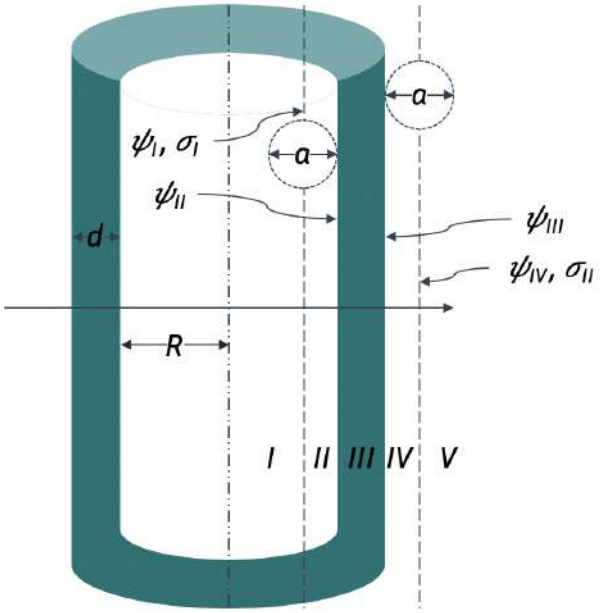


Figure 3.2: The geometry of the electrical double layer in a cylindrical nano-pore.

### 3.2.1 The electrostatics of the cylindrical nano-pore

**1. Region V:** $r \leq R + d + \frac{a}{2}$

The boundary conditions are

$$\lim_{r\to\infty} \psi_5(r) = 0$$

and

$$\lim_{r\to\infty} \frac{\mathrm{d}\psi_5(r)}{\mathrm{d}r} = 0$$

Integrating Eq. (3.48), we get

$$\psi_5(r) = -\frac{4\,\pi}{\varepsilon} \int_r^\infty \frac{\mathrm{d}r'}{r'} \int_{r'}^\infty x\,\rho_{el}(x)\,\mathrm{d}x$$

Integrating the right hand side by parts

$$\psi_5(r) = -\frac{4\,\pi}{\varepsilon} \left( -\ln(r) \int_r^\infty r'\,\rho_{el}(r')\,\mathrm{d}r' + \int_r^\infty \ln\left(r'\right) r'\,\rho_{el}(r')\,\mathrm{d}r' \right)$$

$$\psi_5(r) = -\frac{4\,\pi}{\varepsilon} \int_r^\infty \ln\left(\frac{r}{r'}\right) r'\,\rho_{el}(r')\,\mathrm{d}r'$$

At $r = R + d + \frac{a}{2}$

$$\psi_{IV} \equiv \psi_5\left(R + d + \frac{a}{2}\right) = -\frac{4\,\pi}{\varepsilon} \int_{R+d+\frac{a}{2}}^\infty \ln\left(\frac{R + d + \frac{a}{2}}{r'}\right) r'\,\rho_{el}(r')\,\mathrm{d}r'$$

**2. Region IV:** $R + d \leq x \leq R + d + \frac{a}{2}$

If the dielectric constant, $\varepsilon$, of the electrode and electrolyte are considered equal, to avoid image forces, the boundary conditions are

$$\psi_4\left(R + d + \frac{a}{2}\right) = \psi_{IV}$$

$$\left(\frac{\mathrm{d}\psi_5(r)}{\mathrm{d}r}\right)_{R+d+\frac{a}{2}} - \left(\frac{\mathrm{d}\psi_4(r)}{\mathrm{d}r}\right)_{R+d+\frac{a}{2}} = 0$$

From Eq. (3.47), and integrating once gives,

$$\psi_4(r) = c_1 + c_2\,\ln(r)$$

and using the boundary conditions, yields

$$\psi_4(r) = \frac{4\,\pi}{\varepsilon}\int_{R+d+\frac{a}{2}}^{\infty} \ln\!\left(\frac{r}{r'}\right) r'\,\rho_{el}(r')\,\mathrm{d}r' \tag{3.49}$$

In particular,

$$\psi_{III} \equiv \psi_4(R+d) = \frac{4\,\pi}{\varepsilon}\int_{R+d+\frac{a}{2}}^{\infty} \ln\!\left(\frac{R+d}{r'}\right) r'\,\rho_{el}(r')\,\mathrm{d}r' \tag{3.50}$$

**3. Region III:** $R \le r \le R+d$

The boundary conditions are

$$\psi_3(R+d) = \psi_{III} \tag{3.51}$$

$$\varepsilon\left(\frac{\mathrm{d}\psi_4(r)}{\mathrm{d}r}\right)_{R+d} - \varepsilon\left(\frac{\mathrm{d}\psi_3(r)}{\mathrm{d}r}\right)_{R+d} = -4\,\pi\,\sigma_{II} \tag{3.52}$$

From Eqs. (3.49) to (3.52)

$$\psi_3(r) = \psi_{III} + \frac{4\,\pi\,\sigma_{II}}{\varepsilon}(R+d)\ln\!\left(\frac{r}{R+d}\right) + \frac{4\,\pi}{\varepsilon}\ln\!\left(\frac{r}{R+d}\right)\int_{R+d+\frac{a}{2}}^{\infty} r'\,\rho_{el}(r')\,\mathrm{d}r'$$

or

$$\psi_3(r) = \frac{4\,\pi\,\sigma_{II}}{\varepsilon}(R+d)\ln\!\left(\frac{r}{R+d}\right) + \frac{4\,\pi}{\varepsilon}\int_{R+d+\frac{a}{2}}^{\infty} \ln\!\left(\frac{r}{r'}\right) r'\,\rho_{el}(r')\,\mathrm{d}r' \tag{3.53}$$

In particular,

$$\psi_{II} \equiv \psi_3(R) = \psi_{III} + \frac{4\,\pi\,\sigma_{II}}{\varepsilon}(R+d)\ln\!\left(\frac{R}{R+d}\right) + \frac{4\,\pi}{\varepsilon}\ln\!\left(\frac{R}{R+d}\right)\int_{R+d+\frac{a}{2}}^{\infty} r'\,\rho_{el}(r')\,\mathrm{d}r'$$

or

$$\psi_{II} = \frac{4\,\pi\,\sigma_{II}}{\varepsilon}(R+d)\ln\!\left(\frac{R}{R+d}\right) + \frac{4\,\pi}{\varepsilon}\int_{R+d+\frac{a}{2}}^{\infty} \ln\!\left(\frac{R}{r'}\right) r'\,\rho_{el}(r')\,\mathrm{d}r'$$

Using the electro-neutrality condition,

$$(R+d)\,\sigma_{II} + R\,\sigma_I = -\int_0^{\infty} r'\,\rho_{el}(r')\,\mathrm{d}r' \tag{3.54}$$

it can be rewritten as

$$\psi_{II} = \psi_{III} - \frac{4\,\pi\,R\,\sigma_I}{\varepsilon}\ln\!\left(\frac{R}{R+d}\right) - \frac{4\,\pi}{\varepsilon}\ln\!\left(\frac{R}{R+d}\right)\int_0^{R-\frac{a}{2}} r'\,\rho_{el}(r')\,\mathrm{d}r'$$

**4. Region II:** $R - \frac{a}{2} \le r \le R$

In this region the boundary conditions are

$$\psi_2(R) = \psi_{II} \tag{3.55}$$

$$\varepsilon \left(\frac{\mathrm{d}\psi_3(r)}{\mathrm{d}r}\right)_R - \varepsilon \left(\frac{\mathrm{d}\psi_2(r)}{\mathrm{d}r}\right)_R = -4\,\pi\,\sigma_I \tag{3.56}$$

From Eqs. (3.53), (3.54) and (3.56) we have

$$R\left(\frac{\mathrm{d}\psi_2(r)}{\mathrm{d}r}\right)_R = -\frac{4\,\pi}{\varepsilon}\int_0^{R-\frac{a}{2}} r'\,\rho_{el}(r')\,\mathrm{d}r'$$

Integrating Eq. (3.47) and using Eq. (3.55),

$$\psi_2(r) = \psi_{II} + \frac{4\,\pi}{\varepsilon}\ln\!\left(\frac{R}{r}\right)\int_0^{R-\frac{a}{2}} r'\,\rho_{el}(r')\,\mathrm{d}r'$$

In particular,

$$\psi_I \equiv \psi_2\left(R-\frac{a}{2}\right) = \psi_{II} + \frac{4\,\pi}{\varepsilon}\ln\!\left(\frac{R}{R-\frac{a}{2}}\right)\int_0^{R-\frac{a}{2}} r'\,\rho_{el}(r')\,\mathrm{d}r' \tag{3.57}$$

**Region I:** $0 \le r \le R-\frac{a}{2}$

Here, the boundary conditions are

$$\psi_1\left(R-\frac{a}{2}\right) = \psi_I \tag{3.58}$$

$$\left(\frac{\mathrm{d}\psi_2(r)}{\mathrm{d}r}\right)_{R-\frac{a}{2}} - \left(\frac{\mathrm{d}\psi_1(r)}{\mathrm{d}r}\right)_{R-\frac{a}{2}} = 0 \tag{3.59}$$

Integrating Eq. (3.48) and using Eq. (3.59)

$$r\left(\frac{\mathrm{d}\psi_1(r)}{\mathrm{d}r}\right) = -\frac{4\,\pi}{\varepsilon}\int_0^{R-\frac{a}{2}} r'\,\rho(r')\,\mathrm{d}r' + \frac{4\,\pi}{\varepsilon}\int_r^{R-\frac{a}{2}} r'\,\rho(r')\,\mathrm{d}r' \tag{3.60}$$

Integrating Eq. (3.60) by parts and using Eqs. (3.57) and (3.58)

$$\psi_1(r) = \psi_{II} + \frac{4\,\pi}{\varepsilon}\ln\!\left(\frac{R}{r}\right)\int_0^{R-\frac{a}{2}} r'\,\rho_{el}(r')\,\mathrm{d}r' + \frac{4\,\pi}{\varepsilon}\int_r^{R-\frac{a}{2}} \ln\!\left(\frac{r}{r'}\right) r'\,\rho_{el}(r')\,\mathrm{d}r'$$

In particular,

$$\psi_0 \equiv \psi_1(0) = \psi_{II} + \frac{4\,\pi}{\varepsilon}\int_0^{R-\frac{a}{2}} \ln\!\left(\frac{r}{r'}\right) r'\,\rho_{el}(r')\,\mathrm{d}r'$$

### 3.2.2 The analytical solution of the LPBS for the electrical double layer of a cylindrical nano-pore electrode

In Section 2.2 it was seen from Eq. (2.24) that the linearization of the Laplace and Poisson-Boltzmann equations in cylindrical coordinates are

$$\frac{\mathrm{d}^2\psi}{\mathrm{d}r^2} + \frac{1}{r}\frac{\mathrm{d}\psi}{\mathrm{d}r} = 0 \tag{3.61}$$

$$\frac{\mathrm{d}^2\psi}{\mathrm{d}r^2} + \frac{1}{r}\frac{\mathrm{d}\psi}{\mathrm{d}r} = \kappa^2\,\psi(r) \tag{3.62}$$

Hence, their general solutions, and derivatives are

$$\psi(r) = A + B\,\ln(r) \qquad \frac{\mathrm{d}\psi}{\mathrm{d}r} = \frac{B}{r} \tag{3.63}$$

$$\psi(r) = A\, I_0(\kappa\, r) + B\, K_0(\kappa\, r) \qquad \frac{\mathrm{d}\psi}{\mathrm{d}r} = A\,\kappa\, I_1(\kappa\, r) - B\,\kappa\, K_1(\kappa\, r) \tag{3.64}$$

where $I_0$ and $I_1$ are the modified Bessel functions of first kind of zero order and first order, respectively. Now, the five regions will be treated individually with their respective BC. Each region will be introduced by their interval and with their respective solutions of the mean electrostatic potential. As for the slit-pore, in each region two BC will be introduced in order to find the values of the constants. This is true for all the regions, with the exception of regions V and I, where one and three BC are used, respectively.

**1. Region V:** $r \geq R + d + \frac{a}{2}$

Here, $\psi_5(r) = c_1\, I_0(\kappa\, r) + c_2\, K_0(\kappa\, r)$. The BC is that the electric field is equal to zero at infinity. From the Gauss' law, we know that the electric field is equal to minus the divergence of the electric potential. Hence, $\lim_{r\to\infty} E(r) = 0$, and since $E(r) = -\boldsymbol{\nabla}\cdot\psi(r) = -c_1\,\kappa\, I_1(\kappa\, r) + c_2\,\kappa\, K_1(\kappa\, r)$,

$$\lim_{r\to\infty} E(r) = -c_1\,\kappa\,\cancelto{\infty}{I_1(\kappa\, r)} + c_2\,\kappa\,\cancelto{0}{K_1(\kappa\, r)} = 0 \qquad \therefore \quad c_1 = 0 \tag{3.65}$$

Thus, the mean electrostatic potential in this interval and its derivative are

$$\psi_5(r) = c_2\, K_0(\kappa\, r) \qquad \frac{\mathrm{d}\psi_5}{\mathrm{d}r} = -c_2\,\kappa\, K_1(\kappa\, r)$$

**2. Region IV:** $R + d \leq r \leq R + d + \frac{a}{2}$

Here, $\psi_4(r) = c_3 + c_4\, \ln(r)$. The next BC is the continuity of the mean electrostatic potential. Therefore, $\psi_5(r)$ and $\psi_4(r)$ are equal at $R + d + \frac{a}{2}$. Furthermore, if the dielectric constant of the electrode and electrolyte are equal, the difference between the derivatives of the mean electrostatic potential, $\psi_5(r)$ and $\psi_4(r)$, are equal to zero at $R + d + \frac{a}{2}$. Consequently,

$$\psi_5\left(R + d + \frac{a}{2}\right) = \psi_4\left(R + d + \frac{a}{2}\right) \quad \longrightarrow \quad c_2\, K_0\left(\kappa\, \left(R + d + \frac{a}{2}\right)\right) = c_3 + c_4\, \ln\left(R + d + \frac{a}{2}\right)$$

$$c_3 = c_2\, K_0\left(\kappa\, \left(R + d + \frac{a}{2}\right)\right) - c_4\, \ln\left(R + d + \frac{a}{2}\right) \tag{3.66}$$

$$\varepsilon \left(\frac{\mathrm{d}\psi_5(r)}{\mathrm{d}r}\right)_{R+d+\frac{a}{2}} - \varepsilon \left(\frac{\mathrm{d}\psi_4(r)}{\mathrm{d}r}\right)_{R+d+\frac{a}{2}} = 0$$

$$c_4 = -c_2\,\kappa\, \left(R + d + \frac{a}{2}\right)\, K_1\left(\kappa\, \left(R + d + \frac{a}{2}\right)\right) \tag{3.67}$$

**3. Region III:** $R \leq r \leq R + d$

Here, $\psi_3(r) = c_5 + c_6\, \ln(r)$. Once again, we have the BC of continuity, between $\psi_4(r)$ and $\psi_3(r)$ at $R + d$. However, the difference between the derivative of $\psi_4(r)$ and $\psi_3(r)$ is now equal to $-4\,\pi\,\sigma_{II}$. Therefore,

$$\psi_4(R + d) = \psi_3(R + d) \quad \longrightarrow \quad c_3 + c_4\, \ln(R + d) = c_5 + c_6\, \ln(R + d)$$

$$c_5 = c_3 + (c_4 - c_6)\, \ln(R + d) \tag{3.68}$$

$$\varepsilon \left(\frac{\mathrm{d}\psi_4(r)}{\mathrm{d}r}\right)_{R+d} - \varepsilon \left(\frac{\mathrm{d}\psi_3(r)}{\mathrm{d}r}\right)_{R+d} = -4\,\pi\sigma_{II} \quad \longrightarrow \quad \frac{c_4}{R+d} - \frac{c_6}{R+d} = -\frac{4\,\pi\,\sigma_{II}}{\varepsilon}$$

$$c_6 = c_4 + \frac{4\,\pi\,\sigma_{II}}{\varepsilon}(R + d) \tag{3.69}$$

**4. Region II:** $R - \frac{a}{2} \leq r \leq R$

Here, $\psi_2(r) = c_7 + c_8\,\ln(r)$. Again, one BC is of continuity, between $\psi_3(r)$ and $\psi_2(r)$, at $R$. Whereas, the difference between the derivatives of $\psi_3(r)$ and $\psi_2(r)$ is now equal to $-4\,\pi\,\sigma_I$. Hence,

$$\psi_3(R) = \psi_2(R) \quad \longrightarrow \quad c_5 + c_6\,\ln(R) = c_7 + c_8\,\ln(R)$$

$$c_7 = c_5 + (c_6 - c_8)\,\ln(R) \tag{3.70}$$

$$\varepsilon\left(\frac{\mathrm{d}\psi_3(r)}{\mathrm{d}r}\right)_R - \varepsilon\left(\frac{\mathrm{d}\psi_2(r)}{\mathrm{d}r}\right)_R = -4\,\pi\sigma_I \quad \longrightarrow \quad \frac{c_6}{R} - \frac{c_8}{R} = -\frac{4\,\pi\,\sigma_I}{\varepsilon}$$

$$c_8 = c_6 + \frac{4\,\pi\,\sigma_I}{\varepsilon}\,R \tag{3.71}$$

**5. Region I:** $0 \le r \le R - \frac{a}{2}$

Lastly, here $\psi_1(r) = c_9\,I_0(\kappa\,r) + c_{10}\,K_0(\kappa\,r)$, and one of the final BCs is that the electric field at the pore's center, $r = 0$, is equal to zero. From the Gauss' law, the electric field is equal to minus the divergence of the electric potential. Therefore,

$$\lim_{r\to 0} E(r) = 0 \qquad\qquad E(r) = -\boldsymbol{\nabla}\cdot\psi(r) = -c_9\,\kappa\,I_1(\kappa\,r) + c_{10}\,\kappa\,K_1(\kappa\,r)$$

$$\lim_{r\to 0} E(r) = -c_9\,\kappa\,\cancelto{0}{I_1(\kappa\,r)} + c_{10}\,\kappa\,\cancelto{\infty}{K_1(\kappa\,r)} = 0 \qquad\qquad \therefore \quad c_{10} = 0 \tag{3.72}$$

Thus, the mean electrostatic potential in this interval and its derivative are

$$\psi_1(r) = c_9\,I_0(\kappa\,r) \qquad\qquad \frac{\mathrm{d}\psi_1}{\mathrm{d}r} = c_9\,\kappa\,I_1(\kappa\,r)$$

Furthermore, the last two BCs are that of continuity between $\psi_2(r)$ and $\psi_1(r)$ at $R - a/2$, and the difference between the derivatives of $\psi_2(r)$ and $\psi_1(r)$ is equal to zero. Therefore,

$$\psi_2\left(R - \frac{a}{2}\right) = \psi_1\left(R - \frac{a}{2}\right) \quad \longrightarrow \quad c_7 + c_8\,\ln\!\left(R - \frac{a}{2}\right) = c_9\,\kappa\,I_1\left(\kappa\,\left(R - \frac{a}{2}\right)\right)$$

$$c_7 = c_9\,\kappa\,I_1\left(\kappa\,\left(R - \frac{a}{2}\right)\right) - c_8\,\ln\!\left(R - \frac{a}{2}\right) \tag{3.73}$$

$$\varepsilon\left(\frac{\mathrm{d}\psi_2(r)}{\mathrm{d}r}\right)_{R-\frac{a}{2}} - \varepsilon\left(\frac{\mathrm{d}\psi_1(r)}{\mathrm{d}r}\right)_{R-\frac{a}{2}} = 0 \quad \longrightarrow \quad \frac{c_8}{R - \frac{a}{2}} = c_9\,\kappa\,I_1\left(\kappa\,\left(R - \frac{a}{2}\right)\right)$$

$$c_8 = c_9\,\kappa\,\left(R - \frac{a}{2}\right)\,I_1\left(\kappa\,\left(R - \frac{a}{2}\right)\right) \tag{3.74}$$

Now, from Eqs. (3.65) to (3.74) we have ten linear equations with ten unknown variables.

$$\begin{cases} c_1 = 0 \\ c_3 = c_2\,K_0\left(\kappa\,\left(R + d + \frac{a}{2}\right)\right) - c_4\,\ln\!\left(R + d + \frac{a}{2}\right) \\ c_4 = -c_2\,\kappa\,\left(R + d + \frac{a}{2}\right)\,K_1\left(\kappa\,\left(R + d + \frac{a}{2}\right)\right) \\ c_5 = c_3 + (c_4 - c_6)\,\ln(R + d) \\ c_6 = c_4 + \frac{4\,\pi\,\sigma_{II}}{\varepsilon}(R + d) \\ c_7 = c_5 + (c_6 - c_8)\,\ln(R) \\ c_8 = c_6 + \frac{4\,\pi\,\sigma_I}{\varepsilon}\,R \\ c_{10} = 0 \\ c_7 = c_9\,\kappa\,I_1\left(\kappa\,\left(R - \frac{a}{2}\right)\right) - c_8\,\ln\!\left(R - \frac{a}{2}\right) \\ c_8 = c_9\,\kappa\,\left(R - \frac{a}{2}\right)\,I_1\left(\kappa\,\left(R - \frac{a}{2}\right)\right) \end{cases} \tag{3.75}$$

Solving Eq. (3.75), one finds the value of $c_2$, and consequently of all constants

$$c_2 = \frac{\frac{4\,\pi}{\varepsilon}\left\{\sigma_I\, R\left[\frac{I_0\left(\kappa\left(R-\frac{a}{2}\right)\right)}{\kappa\left(R-\frac{a}{2}\right) I_1\left(\kappa\left(R-\frac{a}{2}\right)\right)} - \ln\left(\frac{R-\frac{a}{2}}{R}\right)\right] + \sigma_{II}\,(R+d)\left[\frac{I_0\left(\kappa\left(R-\frac{a}{2}\right)\right)}{\kappa\left(R-\frac{a}{2}\right) I_1\left(\kappa\left(R-\frac{a}{2}\right)\right)} - \ln\left(\frac{R-\frac{a}{2}}{R+d}\right)\right]\right\}}{K_0\left(\kappa\left(R+d+\frac{a}{2}\right)\right) + \kappa\left(R+d+\frac{a}{2}\right) K_1\left(\kappa\left(R+d+\frac{a}{2}\right)\right)\left[\frac{I_0\left(\kappa\left(R-\frac{a}{2}\right)\right)}{\kappa\left(R-\frac{a}{2}\right) I_1\left(\kappa\left(R-\frac{a}{2}\right)\right)} - \ln\left(\frac{R-\frac{a}{2}}{R+d+\frac{a}{2}}\right)\right]} \tag{3.76}$$

Thence, the mean electrostatic potential is

$$\psi(r) = \begin{cases} c_9\, I_0(\kappa\, r) & 0 \le r \le R - \frac{a}{2} \\ c_7 + c_8\, \ln(r) & R - \frac{a}{2} \le r \le R \\ c_5 + c_6\, \ln(r) & R \le r \le R + d \\ c_3 + c_5\, \ln(r) & R + d \le r \le R + d + \frac{a}{2} \\ c_2\, K_0(\kappa\, r) & r \ge R + d + \frac{a}{2} \end{cases} \tag{3.77}$$

Meanwhile, the induced surface charge density is given by

$$\begin{aligned} \sigma(r) = -\frac{1}{r}\int_r^\infty \rho_{el}(t)\, t\, \mathrm{d}t = \sigma(r) = \frac{1}{r}\frac{\varepsilon}{4\,\pi}\int_r^\infty \frac{1}{t}\frac{\mathrm{d}}{\mathrm{d}t}\left(t\frac{\mathrm{d}\psi}{\mathrm{d}t}\right) t\, \mathrm{d}t = \frac{1}{r}\frac{\varepsilon}{4\,\pi}\int_r^\infty t\frac{\mathrm{d}\psi_1}{\mathrm{d}t} \\ + \frac{1}{r}\frac{\varepsilon}{4\,\pi}\int_r^\infty t\frac{\mathrm{d}\psi_5}{\mathrm{d}t} = \frac{\varepsilon}{4\,\pi}\left(\frac{\mathrm{d}\psi_1}{\mathrm{d}r}\right)_r - \frac{\varepsilon}{4\,\pi}\left(\frac{\mathrm{d}\psi_5}{\mathrm{d}r}\right)_r \end{aligned} \tag{3.78}$$

whence, it is divided into three intervals. After obtaining the derivatives and evaluating, we have that the induced surface charge density is

$$\sigma(r) = \begin{cases} \frac{\varepsilon\,\kappa}{4\,\pi}\, c_9\, I_1(\kappa\, r) & 0 \le r \le R - \frac{a}{2} \\ 0 & R - \frac{a}{2} < r < R + d + \frac{a}{2} \\ \frac{\varepsilon\,\kappa}{4\,\pi}\, c_2\, K_1(\kappa\, r) & r \ge R + d + \frac{a}{2} \end{cases} \tag{3.79}$$

Meanwhile, the co-ion and counter-ion distribution functions are given by Eqs. (2.12) and (2.13)

$$g_+(r) = \begin{cases} \exp\left(-\frac{z\,e}{k\,T}\, c_9\, I_0(\kappa\, r)\right) & 0 \le r \le R - \frac{a}{2} \\ 0 & R - \frac{a}{2} < r < R + d + \frac{a}{2} \\ \exp\left(-\frac{z\,e}{k\,T}\, c_2\, K_0(\kappa\, r)\right) & r \ge R + d + \frac{a}{2} \end{cases} \tag{3.80}$$

$$g_-(r) = \begin{cases} \exp\left(\frac{z\,e}{k\,T}\, c_9\, I_0(\kappa\, r)\right) & 0 \le r \le R - \frac{a}{2} \\ 0 & R - \frac{a}{2} < r < R + d + \frac{a}{2} \\ \exp\left(\frac{z\,e}{k\,T}\, c_2\, K_0(\kappa\, r)\right) & r \ge R + d + \frac{a}{2} \end{cases} \tag{3.81}$$

Lastly, in order to obtain the total differential capacitance we must derive $\psi_d$ with respect of $\sigma$. Where $\sigma = \sigma_I = \sigma_{II}$ and $\psi_d$ is the value of $\psi(r)$ at the cylinder's center. Such as,

$$\psi_d \equiv \lim_{r\to 0}\psi(r) = c_9\, \cancelto{1}{I_0(\kappa\, r)} = c_9 \tag{3.82}$$

The total differential capacitance is obtained deriving Eq. (3.82) with respect of $\sigma$. Therefore, using Eqs. (3.75) and (3.76) we find,

$$C_T \equiv \frac{\mathrm{d}\psi_d}{\mathrm{d}\sigma} = \frac{\frac{4\,\pi}{\varepsilon}\left\{2\,R + d - \frac{(2\,R+d)\frac{I_0\left(\kappa\left(R-\frac{a}{2}\right)\right)}{\kappa\left(R-\frac{a}{2}\right) I_1\left(\kappa\left(R-\frac{a}{2}\right)\right)} - R\,\ln\left(\frac{R-\frac{a}{2}}{R}\right) - (R+d)\,\ln\left(\frac{R-\frac{a}{2}}{R+d}\right)}{\frac{K_0\left(\kappa\left(R+d+\frac{a}{2}\right)\right)}{\kappa\left(R+d+\frac{a}{2}\right) K_1\left(\kappa\left(R+d+\frac{a}{2}\right)\right)} + \frac{I_0\left(\kappa\left(R-\frac{a}{2}\right)\right)}{\kappa\left(R-\frac{a}{2}\right) I_1\left(\kappa\left(R-\frac{a}{2}\right)\right)} - \ln\left(\frac{R-\frac{a}{2}}{R+d+\frac{a}{2}}\right)}\right\}}{\kappa\,\left(R-\frac{a}{2}\right)\, I_1\left(\kappa\left(R-\frac{a}{2}\right)\right)} \tag{3.83}$$

## 3.3 The electrical double layer of a spherical nano-pore electrode

The electrical double layer of a spherical nano-pore electrode is shown in Fig. 3.3. The radius of the sphere is $R$ and the sphere's wall thickness is $d$. The sphere is permeable, so that the chemical potentials outside and inside the pore are equal. The ion's size diameter is equal to $a$. Other model parameters are the same as those described in Section 3.1. Due to the symmetry of this nano-pore, the electrostatics in Fig. 3.3 is divided into five regions.

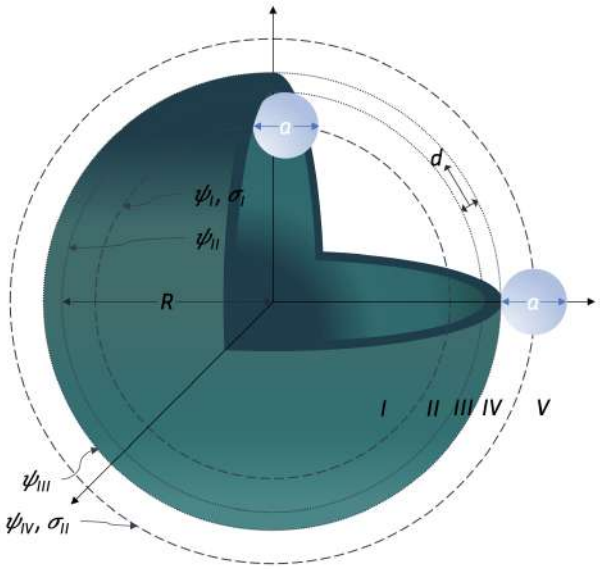


Figure 3.3: The geometry of the electrical double layer in a spherical nano-pore.

Since there is no charge in regions II, III, and IV, the mean electrostatic potential is governed by the Laplace equation, which in spherical coordinates is,

$$\frac{1}{r^2}\frac{\partial}{\partial r}\left(r^2\frac{\partial\psi(r)}{\partial r}\right)=0 \tag{3.84}$$

whereas, in regions I and V the PB-eq, in spherical coordinates, is valid

$$\frac{1}{r^2}\frac{\partial}{\partial r}\left(r^2\frac{\partial\psi(r)}{\partial r}\right)=-\frac{4\,\pi}{\varepsilon}\rho_{el}(r) \tag{3.85}$$

where $\psi(r)$ is the mean electrostatic potential

### 3.3.1 The electrostatics of a spherical pore

**1. Region V:** $r \geq R + d + \frac{a}{2}$

The boundary conditions are given by

$$\lim_{r\to\infty}\psi_5(r)=0$$

$$\lim_{r\to\infty}\frac{\mathrm{d}\psi_5(r)}{\mathrm{d}r}=0$$

Integrating Eq. (3.85) yields

$$\psi_5(r)=-\frac{4\,\pi}{\varepsilon}\int_r^\infty\frac{\mathrm{d}r'}{r'^2}\int_{r'}^\infty x^2\rho_{el}(x)\,\mathrm{d}x$$

Thus,

$$\psi_5(r) = \frac{4\,\pi}{\varepsilon\, r}\int_r^\infty r'\left(r - r'\right)\rho_{el}(r')\,\mathrm{d}r' \tag{3.86}$$

For $r = R + d + \frac{a}{2}$

$$\psi_{IV} \equiv \psi_5\left(R + d + \frac{a}{2}\right) = \frac{4\,\pi}{\varepsilon\,\left(R + d + \frac{a}{2}\right)}\int_{R+d+\frac{a}{2}}^\infty r'\left(R + d + \frac{a}{2} - r'\right)\rho_{el}(r')\,\mathrm{d}r'$$

**2. Region IV:** $R + d \le r \le R + d + \frac{a}{2}$

To avoid image forces we assume that the dielectric constant of the spherical pore is equal to that of the solution. Then the boundary conditions are given by

$$\psi_4\left(R + d + \frac{a}{2}\right) = \psi_{IV}$$

$$\left(\frac{\mathrm{d}\psi_5(r)}{\mathrm{d}r}\right)_{R+d+\frac{a}{2}} - \left(\frac{\mathrm{d}\psi_4(r)}{\mathrm{d}r}\right)_{R+d+\frac{a}{2}} = 0$$

Integrating Eq. (3.84) and applying the boundary conditions yields

$$r^2\frac{\mathrm{d}\psi_4(r)}{\mathrm{d}r} = \frac{4\,\pi}{\varepsilon}\int_{R+d+\frac{a}{2}}^\infty r^2\rho_{el}(r)\,\mathrm{d}r$$

Integrating the above and using the continuous potential boundary conditions, we find

$$\psi_4(r) = \frac{4\,\pi}{\varepsilon\, r}\int_{R+d+\frac{a}{2}}^\infty r'\left(r - r'\right)\rho_{el}(r')\,\mathrm{d}r' \tag{3.87}$$

In particular,

$$\psi_{III} \equiv \psi_4\left(R + d\right) = \frac{4\,\pi}{\varepsilon\,(R + d)}\int_{R+d+\frac{a}{2}}^\infty r'\left(R + d - r'\right)\rho_{el}(r')\,\mathrm{d}r' \tag{3.88}$$

**3. Region III:** $R \le r \le R + d$

The boundary conditions are

$$\psi_3(R + d) = \psi_{III}$$

$$\varepsilon\left(\frac{\mathrm{d}\psi_4(r)}{\mathrm{d}r}\right)_{R+d} - \varepsilon\left(\frac{\mathrm{d}\psi_3(r)}{\mathrm{d}r}\right)_{R+d} = -4\,\pi\,\sigma_{II}$$

From Eq. (3.84) and applying the boundary conditions, we obtain

$$\psi_3(r) = -\frac{4\,\pi\,(R + d)^2\,\sigma_{II}}{\varepsilon}\left(\frac{1}{r} - \frac{1}{R + d}\right) + \frac{4\,\pi}{\varepsilon\, r}\int_{R+d+\frac{a}{2}}^\infty r'\left(r - r'\right)\rho_{el}(r')\,\mathrm{d}r'$$

In particular,

$$\psi_{II} \equiv \psi_3(R) = -\frac{4\,\pi\,(R + d)^2\,\sigma_{II}}{\varepsilon}\left(\frac{1}{R} - \frac{1}{R + d}\right) + \frac{4\,\pi}{\varepsilon\, R}\int_{R+d+\frac{a}{2}}^\infty r'\left(R - r'\right)\rho_{el}(r')\,\mathrm{d}r'$$

From Eqs. (3.87) and (3.88) it follows that

$$\psi_{II} = \psi_{III} - \left(\frac{1}{R} - \frac{1}{R + d}\right)\left[\frac{4\,\pi\,(R + d)^2\,\sigma_{II}}{\varepsilon} + \frac{4\,\pi}{\varepsilon}\int_{R+d+\frac{a}{2}}^\infty r'\left(R - r'\right)\rho_{el}(r')\,\mathrm{d}r'\right]$$

**4. Region II:** $R - \frac{a}{2} \leq r \leq R$

Here the boundary conditions are

$$\psi_2(R) = \psi_{II} \tag{3.89}$$
$$\varepsilon \left(\frac{\mathrm{d}\psi_3(r)}{\mathrm{d}r}\right)_R - \varepsilon \left(\frac{\mathrm{d}\psi_2(r)}{\mathrm{d}r}\right)_R = -4\,\pi\,\sigma_I$$

From Eq. (3.84) and the boundary conditions, we find

$$r^2 \frac{\mathrm{d}\psi_2(r)}{\mathrm{d}r} = \frac{4\,\pi\,R^2\,\sigma_I}{\varepsilon} + \frac{4\,\pi\,(R+d)^2\,\sigma_{II}}{\varepsilon} + \frac{4\,\pi}{\varepsilon}\int_{R+d+\frac{a}{2}}^{\infty} r'^2 \rho_{el}(r')\,\mathrm{d}r'$$

Integrating the above and using Eq. (3.89), we obtain

$$\psi_2(r) = \frac{4\,\pi\,R^2\,\sigma_I}{\varepsilon}\left(\frac{1}{R} - \frac{1}{r}\right) + \frac{4\,\pi\,(R+d)^2\,\sigma_{II}}{\varepsilon}\left(\frac{1}{R+d} - \frac{1}{r}\right) - \frac{4\,\pi}{\varepsilon\,r}\int_0^{R-\frac{a}{2}} r'\left(r'-r\right)\rho_{el}(r')\,\mathrm{d}r'$$

In particular,

$$\psi_I \equiv \psi_2\left(R - \frac{a}{2}\right) = \frac{4\,\pi}{\varepsilon\left(R-\frac{a}{2}\right)}\left[R\,\sigma_I\,\frac{a}{2} - (R+d)\,\sigma_{II}\left(d+\frac{a}{2}\right) - \int_0^{R-\frac{a}{2}} r'\left(r'-R+\frac{a}{2}\right)\rho_{el}(r')\,\mathrm{d}r'\right]$$

**5. Region I:** $0 \leq r \leq R - \frac{a}{2}$

The boundary conditions are the following

$$\psi_1\left(R - \frac{a}{2}\right) = \psi_I$$
$$\left(\frac{\mathrm{d}\psi_2(r)}{\mathrm{d}r}\right)_{R-\frac{a}{2}} - \left(\frac{\mathrm{d}\psi_1(r)}{\mathrm{d}r}\right)_{R-\frac{a}{2}} = 0$$

Integrating Eq. (3.85) and applying the boundary conditions yields

$$\begin{aligned}\psi_1(r) = &-\frac{4\,\pi}{\varepsilon\,r}\int_0^{R-\frac{a}{2}} r'\left(r'-r\right)\rho(r')\,\mathrm{d}r' - \frac{4\,\pi}{\varepsilon\,r}\int_{R+d+\frac{a}{2}}^{\infty} r'\left(r'-r\right)\rho(r')\,\mathrm{d}r' \\ &+\frac{4\,\pi\,R^2\,\sigma_I}{\varepsilon}\left(\frac{1}{R}-\frac{1}{r}\right) + \frac{4\,\pi\,(R+d)^2\,\sigma_{II}}{\varepsilon}\left(\frac{1}{R+d}-\frac{1}{r}\right)\end{aligned} \tag{3.90}$$

### 3.3.2 The analytical solution of the LPBS for the electrical double layer of a spherical nano-pore electrode

In Section 2.3 it was seen from Eq. (2.33) that the linearization of the Laplace and Poisson-Boltzmann equations in spherical coordinates are given by

$$\frac{\mathrm{d}^2\psi}{\mathrm{d}r^2} + \frac{2}{r}\frac{\mathrm{d}\psi}{\mathrm{d}r} = 0 \tag{3.91}$$

$$\frac{\mathrm{d}^2\psi}{\mathrm{d}r^2} + \frac{2}{r}\frac{\mathrm{d}\psi}{\mathrm{d}r} = \kappa^2\,\psi(r) \tag{3.92}$$

Hence, their general solutions, and derivatives are

$$\psi(r) = A + \frac{B}{r} \qquad \frac{\mathrm{d}\psi}{\mathrm{d}r} = -\frac{B}{r^2} \tag{3.93}$$

$$\psi(r) = A\,\frac{e^{\kappa\,r}}{r} + B\,\frac{e^{-\kappa\,r}}{r} \qquad \frac{\mathrm{d}\psi}{\mathrm{d}r} = \frac{A\,e^{\kappa\,r}(\kappa\,r+1) - B\,e^{-\kappa\,r}(\kappa\,r+1)}{r^2} \tag{3.94}$$

Continuously, the five regions are treated individually with their respective BCs. Each region will be introduced through its interval and solution of the mean electrostatic potential. As for the slit-pore or the cylindrical pore, in each region two BCs will be introduced in order to find the values of the constants. This is true for all the regions, with the exception of regions V and I, where one and three BC are used, respectively.

**1. Region V:** $r \geq R + d + \frac{a}{2}$

Here, $\psi_5(r) = c_1\,\frac{e^{\kappa\,r}}{r} + c_2\,\frac{e^{-\kappa\,r}}{r}$, and the first BC is that the electric field is equal to zero at infinity. From the Gauss' law, we know that the electric field is equal to minus the divergence of the electric potential. Hence,

$$\lim_{r\to\infty} E(r) = 0 \qquad E(r) = -\boldsymbol{\nabla}\cdot\psi(r) = -\frac{c_1\,e^{\kappa\,r}(\kappa\,r+1) - c_2\,e^{-\kappa\,r}(\kappa\,r+1)}{r^2}$$

$$\lim_{r\to\infty} E(r) = -\frac{c_1\,\cancelto{\infty}{e^{\kappa\,r}(\kappa\,r+1)} - c_2\,\cancelto{0}{e^{-\kappa\,r}(\kappa\,r+1)}}{r^2} = 0 \qquad \therefore \quad c_1 = 0 \tag{3.95}$$

Hence, the mean electrostatic potential in this interval and its derivative are

$$\psi_5(r) = c_2\,\frac{e^{-\kappa\,r}}{r} \qquad \frac{\mathrm{d}\psi_5}{\mathrm{d}r} = -c_2\,\frac{e^{-\kappa\,r}(\kappa\,r+1)}{r^2}$$

**2. Region IV:** $R + d \leq r \leq R + d + \frac{a}{2}$

Here, $\psi_4(r) = c_3 + \frac{c_4}{r}$. The next BC is the continuity of the mean electrostatic potential. Hence, $\psi_5(r)$ and $\psi_4(r)$ are equal at $R + d + \frac{a}{2}$. Furthermore, if the dielectric constant of the electrodes and electrolytes are equal, the difference between their derivatives, $\psi_5(r)$ and $\psi_4(r)$, is equal to zero at $R + d + \frac{a}{2}$. Hence,

$$\psi_5\left(R + d + \frac{a}{2}\right) = \psi_4\left(R + d + \frac{a}{2}\right) \quad \longrightarrow \quad c_2\,\frac{e^{-\kappa\left(R+d+\frac{a}{2}\right)}}{R + d + \frac{a}{2}} = c_3 + \frac{c_4}{R + d + \frac{a}{2}}$$

$$c_3 = \frac{1}{R + d + \frac{a}{2}}\left(c_2\,e^{-\kappa\left(R+d+\frac{a}{2}\right)} - c_4\right) \tag{3.96}$$

$$\varepsilon\left(\frac{\mathrm{d}\psi_5(r)}{\mathrm{d}r}\right)_{R+d+\frac{a}{2}} - \varepsilon\left(\frac{\mathrm{d}\psi_4(r)}{\mathrm{d}r}\right)_{R+d+\frac{a}{2}} = 0$$

$$c_4 = c_2\,e^{-\kappa\left(R+d+\frac{a}{2}\right)}\left[\kappa\left(R + d + \frac{a}{2}\right) + 1\right] \tag{3.97}$$

**3. Region III:** $R \leq r \leq R + d$

Here, $\psi_3(r) = c_5 + \frac{c_6}{r}$. Once again, we have the BC of continuity, between $\psi_4(r)$ and $\psi_3(r)$ at $R + d$. However, the difference between the derivative of $\psi_4(r)$ and $\psi_3(r)$ is now equal to $-4\,\pi\,\sigma_{II}$. Therefore,

$$\psi_4(R + d) = \psi_3(R + d) \quad \longrightarrow \quad c_3 + \frac{c_4}{R + d} = c_5 + \frac{c_6}{R + d}$$

$$c_5 = c_3 + \frac{c_4 - c_6}{R + d} \tag{3.98}$$

$$\varepsilon\left(\frac{\mathrm{d}\psi_4(r)}{\mathrm{d}r}\right)_{R+d}-\varepsilon\left(\frac{\mathrm{d}\psi_3(r)}{\mathrm{d}r}\right)_{R+d}=-4\,\pi\,\sigma_{II}\quad\longrightarrow\quad-\frac{c_4}{(R+d)^2}+\frac{c_6}{(R+d)^2}=-\frac{4\,\pi\,\sigma_{II}}{\varepsilon}$$

$$c_6=c_4-\frac{4\,\pi\,\sigma_{II}}{\varepsilon}(R+d)^2 \tag{3.99}$$

**4. Region II:** $R-\frac{a}{2}\leq r\leq R$

Here, $\psi_2(r)=c_7+\frac{c_8}{r}$. Again, one of the BCs is of continuity, between $\psi_3(r)$ and $\psi_2(r)$, at $R$. On the other hand, the difference between the derivative of $\psi_3(r)$ and $\psi_2(r)$ is now equal to $-4\,\pi\,\sigma_I$. Therefore,

$$\psi_3(R)=\psi_2(R)\quad\longrightarrow\quad c_5+\frac{c_6}{R}=c_7+\frac{c_8}{R}$$

$$c_7=c_5+\frac{c_6-c_8}{R} \tag{3.100}$$

$$\varepsilon\left(\frac{\mathrm{d}\psi_3(r)}{\mathrm{d}r}\right)_{R}-\varepsilon\left(\frac{\mathrm{d}\psi_2(r)}{\mathrm{d}r}\right)_{R}=-4\,\pi\sigma_I\quad\longrightarrow\quad-\frac{c_6}{R^2}+\frac{c_8}{R^2}=-\frac{4\,\pi\,\sigma_I}{\varepsilon}$$

$$c_8=c_6-\frac{4\,\pi\,\sigma_I}{\varepsilon}\,R^2 \tag{3.101}$$

**5. Region I:** $0\leq r\leq R-\frac{a}{2}$

Lastly, here $\psi_1(r)=c_9\,\frac{e^{\kappa\,r}}{r}+c_{10}\,\frac{e^{-\kappa\,r}}{r}$, and one of the final BCs is that the electric field at the pore's center, $r=0$, is equal to zero. From the Gauss' law, the electric field is equal to minus the divergence of the electric potential. Therefore,

$$\lim_{r\to0}E(r)=0\qquad\qquad E(r)=-\boldsymbol{\nabla}\cdot\psi(r)=-\frac{c_9\,e^{\kappa\,r}(\kappa\,r+1)-c_{10}\,e^{-\kappa\,r}(\kappa\,r+1)}{r^2}$$

$$\lim_{r\to0}E(r)=-\frac{c_9\,\cancel{e^{\kappa\,r}(\kappa\,r+1)}^{\,1}-c_{10}\,\cancel{e^{-\kappa\,r}(\kappa\,r+1)}^{\,1}}{r^2}=0\qquad\therefore\quad c_9=-c_{10} \tag{3.102}$$

Hence, the mean electrostatic potential in this interval and its derivative are

$$\psi_1(r)=2\,c_9\,\frac{\sinh(\kappa\,r)}{r}\qquad\qquad\frac{\mathrm{d}\psi_1}{\mathrm{d}r}=2\,c_9\,\frac{\kappa\,r\,\cosh(\kappa\,r)-\sinh(\kappa\,r)}{r^2}$$

Furthermore, the last two BCs are of continuity between $\psi_2(r)$ and $\psi_1(r)$ at $R-a/2$, and that the difference between the derivative of $\psi_2(r)$ and $\psi_1(r)$ is equal to zero. Hence,

$$\psi_2\left(R-\frac{a}{2}\right)=\psi_1\left(R-\frac{a}{2}\right)\quad\longrightarrow\quad c_7+\frac{c_8}{R-\frac{a}{2}}=2\,c_9\,\frac{\sinh\left(\kappa\,\left(R-\frac{a}{2}\right)\right)}{R-\frac{a}{2}}$$

$$c_7=\frac{1}{R-\frac{a}{2}}\left[2\,c_9\,\sinh\left(\kappa\,\left(R-\frac{a}{2}\right)\right)-c_8\right] \tag{3.103}$$

$$\varepsilon\left(\frac{\mathrm{d}\psi_2(r)}{\mathrm{d}r}\right)_{R-\frac{a}{2}}-\varepsilon\left(\frac{\mathrm{d}\psi_1(r)}{\mathrm{d}r}\right)_{R-\frac{a}{2}}=0$$

$$-\frac{c_8}{(R-\frac{a}{2})^2}=2\,c_9\,\frac{\kappa\,\left(R-\frac{a}{2}\right)\,\cosh\left(\kappa\,\left(R-\frac{a}{2}\right)\right)-\sinh\left(\kappa\,\left(R-\frac{a}{2}\right)\right)}{\left(R-\frac{a}{2}\right)^2}$$

$$c_8=-2\,c_9\left[\kappa\,\left(R-\frac{a}{2}\right)\,\cosh\left(\kappa\,\left(R-\frac{a}{2}\right)\right)-\sinh\left(\kappa\,\left(R-\frac{a}{2}\right)\right)\right] \tag{3.104}$$

Now, from Eqs. (3.95) to (3.104) we have ten linear equations with ten unknown variables.

$$\begin{cases} c_1 = 0 \\ c_3 = \frac{1}{R+d+\frac{a}{2}} \left( c_2\, e^{-\kappa\left(R+d+\frac{a}{2}\right)} - c_4 \right) \\ c_4 = c_2\, e^{-\kappa\left(R+d+\frac{a}{2}\right)} \left[ \kappa \left( R+d+\frac{a}{2} \right) + 1 \right] \\ c_5 = c_3 + \frac{c_4 - c_6}{R+d} \\ c_6 = c_4 - \frac{4\,\pi\,\sigma_{II}}{\varepsilon} (R+d)^2 \\ c_7 = c_5 + \frac{c_6 - c_8}{R} \\ c_8 = c_6 - \frac{4\,\pi\,\sigma_I}{\varepsilon}\, R^2 \\ c_9 = -c_{10} \\ c_7 = \frac{1}{R-\frac{a}{2}} \left[ 2\, c_9\, \sinh\left( \kappa \left( R - \frac{a}{2} \right) \right) - c_8 \right] \\ c_8 = -2\, c_9 \left[ \kappa \left( R - \frac{a}{2} \right) \cosh\left( \kappa \left( R - \frac{a}{2} \right) \right) - \sinh\left( \kappa \left( R - \frac{a}{2} \right) \right) \right] \end{cases} \tag{3.105}$$

Solving Eq. (3.105), one finds the value of $c_2$ and consequently all the other constants

$$c_2 = \frac{\frac{4\,\pi}{\varepsilon\,\kappa} \left\{ \sigma_I\, R \left[ \tanh\left( \kappa \left( R - \frac{a}{2} \right) \right) + \frac{\kappa\, a}{2} \right] + \sigma_{II}\, (R+d) \left[ \tanh\left( \kappa \left( R - \frac{a}{2} \right) \right) + \kappa \left( d + \frac{a}{2} \right) \right] \right\}}{\tanh\left( \kappa \left( R - \frac{a}{2} \right) \right) + \kappa\, (d+a) + 1}\, e^{\kappa\left(R+d+\frac{a}{2}\right)} \tag{3.106}$$

Hence the mean electrostatic potential is

$$\psi(r) = \begin{cases} 2\, c_9\, \frac{\sinh(\kappa\, r)}{r} & 0 \le r \le R - \frac{a}{2} \\ c_7 + \frac{c_8}{r} & R - \frac{a}{2} \le r \le R \\ c_5 + \frac{c_6}{r} & R \le r \le R + d \\ c_3 + \frac{c_4}{r} & R + d \le r \le R + d + \frac{a}{2} \\ c_2\, \frac{e^{-\kappa\, r}}{r} & r \ge R + d + \frac{a}{2} \end{cases} \tag{3.107}$$

Meanwhile, the induced surface charge density is given by

$$\begin{aligned} \sigma(r) = -\frac{1}{r^2} \int_r^\infty \rho_{el}(t)\, t^2\, \mathrm{d}t = \frac{1}{r^2}\, \frac{\varepsilon}{4\,\pi} \int_r^\infty \frac{1}{t^2}\, \frac{\mathrm{d}}{\mathrm{d}t} \left( t^2\, \frac{\mathrm{d}\psi}{\mathrm{d}t} \right) t^2\, \mathrm{d}t = \frac{1}{r^2}\, \frac{\varepsilon}{4\,\pi} \int_r^\infty t^2\, \frac{\mathrm{d}\psi_1}{\mathrm{d}t} \\ + \frac{1}{r^2}\, \frac{\varepsilon}{4\,\pi} \int_r^\infty t^2\, \frac{\mathrm{d}\psi_5}{\mathrm{d}t} = \frac{\varepsilon}{4\,\pi} \left( \frac{\mathrm{d}\psi_1}{\mathrm{d}r} \right)_r - \frac{\varepsilon}{4\,\pi} \left( \frac{\mathrm{d}\psi_5}{\mathrm{d}r} \right)_r \end{aligned} \tag{3.108}$$

Hence, it is divided into three intervals. After obtaining the derivatives and evaluating, we have that the induced surface charge density is

$$\sigma(r) = \begin{cases} \frac{\varepsilon}{2\,\pi}\, c_9\, \frac{\kappa\, r\, \cosh(\kappa\, r) - \sinh(\kappa\, r)}{r^2} & 0 \le r \le R - \frac{a}{2} \\ 0 & R - \frac{a}{2} < r < R + d + \frac{a}{2} \\ \frac{\varepsilon}{4\,\pi}\, c_2\, \frac{e^{-\kappa\, r} (\kappa\, r + 1)}{r^2} & r \ge R + d + \frac{a}{2} \end{cases} \tag{3.109}$$

Further, the co-ion and counter-ion distribution functions are given by Eqs. (2.12) and (2.13)

$$g_+(r) = \begin{cases} \exp\left( -\frac{2\, z\, e}{k\, T}\, c_9\, \frac{\sinh(\kappa\, r)}{r} \right) & 0 \le r \le R - \frac{a}{2} \\ 0 & R - \frac{a}{2} < r < R + d + \frac{a}{2} \\ \exp\left( -\frac{z\, e}{k\, T}\, c_2\, \frac{e^{-\kappa\, r}}{r} \right) & r \ge R + d + \frac{a}{2} \end{cases} \tag{3.110}$$

$$g_{-}(r) = \begin{cases} \exp\left(\frac{2\,z\,e}{k\,T}\,c_9\,\frac{\sinh(\kappa\,r)}{r}\right) & 0 \le r \le R - \frac{a}{2} \\ 0 & R - \frac{a}{2} < r < R + d + \frac{a}{2} \\ \exp\left(\frac{z\,e}{k\,T}\,c_2\,\frac{e^{-\kappa\,r}}{r}\right) & r \ge R + d + \frac{a}{2} \end{cases} \tag{3.111}$$

Finally, in order to obtain the total differential capacitance we must derive $\psi_d$ with respect of $\sigma$. In this case $\sigma = \sigma_{I} = \sigma_{II}$ and $\psi_d$ is the value of $\psi(r)$ at the pore's center. Such as,

$$\psi_d \equiv \lim_{r\to 0}\psi(r) = 2\,c_9\,\frac{\sinh(\kappa r)}{r}^{\to 1} = 2\,c_9 \tag{3.112}$$

The total differential capacitance, $C_{T}$, is obtained deriving Eq. (3.112) with respect of $\sigma$ and using Eqs. (3.105) and (3.106). Hence,

$$C_{T} \equiv \frac{\mathrm{d}\psi_d}{\mathrm{d}\sigma} = \frac{\frac{4\,\pi}{\varepsilon\,\kappa}\left\{\kappa\left[R^2 + (R+d)^2\right] - \frac{(2\,R+d)\tanh\left(\kappa\left(R-\frac{a}{2}\right)\right)+R[\kappa(d+a)]+d\left[\kappa\left(d+\frac{a}{2}\right)\right]}{\frac{\tanh\left(\kappa\left(R-\frac{a}{2}\right)\right)+\kappa(d+a)+1}{\kappa\left(R+d+\frac{a}{2}\right)+1}}\right\}}{\kappa\,\left(R-\frac{a}{2}\right)\,\cosh\left(\kappa\left(R-\frac{a}{2}\right)\right) - \sinh\left(\kappa\left(R-\frac{a}{2}\right)\right)} \tag{3.113}$$

## 3.4 Topological dependence of the co-ion and counter-ion distribution functions on nano-pores' electrodes

In this section a comparison between the co-ion and counter-ion distribution functions of the different nano-pore electrodes topology is made. However, due to the complexity of our systems, in this thesis we will limit ourselves to the case in which the inner and outer surface charges are equal [$\sigma = \sigma_{I} = \sigma_{II}$] or the unscreened electrical fields, are equal [$E^{u}_{\omega}(r = R - a/2) = E^{u}_{\omega}(r = R + d + a/2) \quad \cdot \ni \cdot \quad \omega = P, C, S$], and the wall's thickness, $d$, is always fixed to $d = 5\,\text{Å}$. Therefore, here we explore only the dependence of these density profiles on the nano-pore's charge and size, and the electrolyte's molar concentration, $\rho_0$, and temperature, $T$. Thus, in order to compare the co-ion and counter-ion distribution functions among the different nano-pores, we first explore the influence that the pores' size has on the electric double layer. As in Section 2.4, for the solid nano-pores, the influence that the pore's radius has on the different pore's topology also depends on whether the *unscreened electric fields* or surface charges are fixed (see Fig. 3.4, and Eqs. (2.44) to (2.46)), i.e., in addition to studying the constant surface charge density boundary conditions, the following boundary conditions are also considered;

$$\begin{aligned} E^{u}_{P}(r = t - a/2) &= E^{u}_{P}(r = t + d + a/2) \\ E^{u}_{C}(r = R - a/2) &= E^{u}_{C}(r = R + d + a/2) \\ E^{u}_{S}(r = R - a/2) &= E^{u}_{S}(r = R + d + a/2) \end{aligned} \tag{3.114}$$

From Fig. 3.4, it can be seen that, as in Section 2.4, the higher contact values of the density profiles are obtained when equal unscreened electric fields are used. Concretely, the difference between the constant surface charge and the constant unscreened electrical fields reduced concentration profiles is remarkably higher for the smaller radius, as it would be expected from the relations of Eqs. (2.49) and (2.50). As the radius increases, the difference between both cases becomes significantly smaller, such that at a pore's radius of 200 Å, they basically overlap. It is worth noting that outside the pore, regardless of the pore's size, the adsorption of co-ions and counter-ions follows the same tendency, the higher values are obtained for the slit-pore, followed by the cylindrical and spherical pores. As the radius increases the density profiles outside the pore tend rapidly to those of the plates. However, it is only in the limit of $R \to \infty$ that the inside and outside concentration distribution functions become

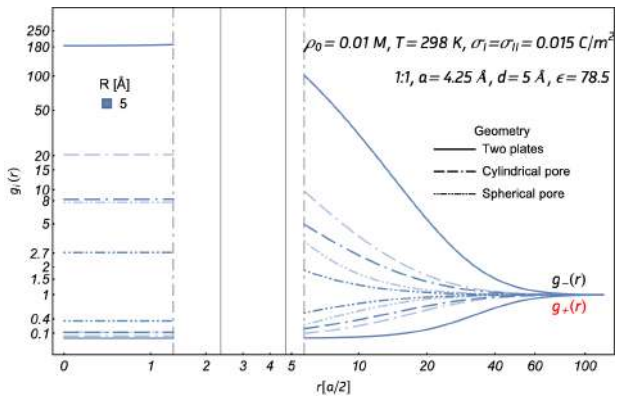


(a) The density profiles for $R = 5\,\text{Å} \cong 1.2\,\text{a}$.

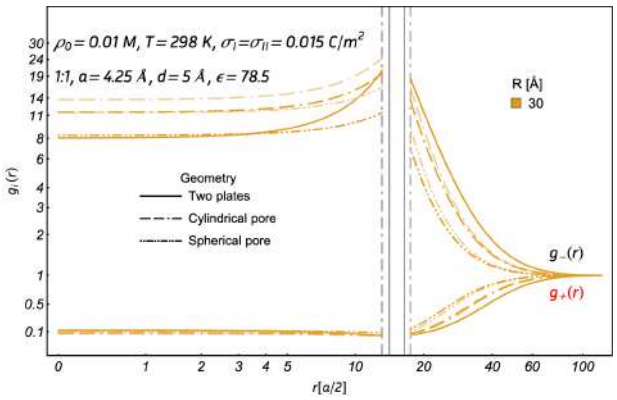


(b) The density profiles for $R = 30\,\text{Å} \cong 7.1\,\text{a}$.

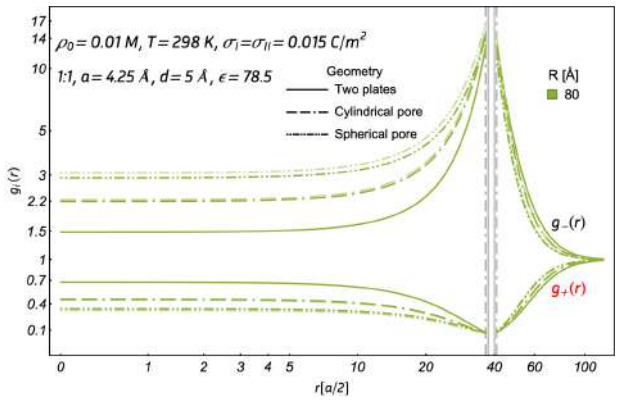


(c) The density profiles for $R = 80\,\text{Å} \cong 18.8\,\text{a}$.

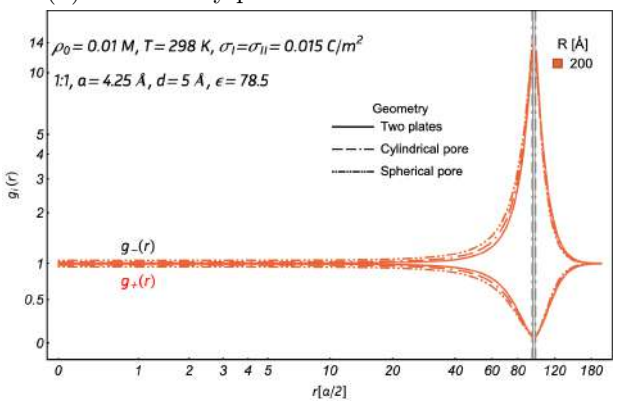


(d) The density profiles for $R = 200\,\text{Å} \cong 47.1\,\text{a}$.

Figure 3.4: The co-ion, $g_+(r)$, and counter-ion, $g_-(r)$, distribution functions of the LPBS of three nano-pore geometries, for different pores' sizes. The lighter and darker lines represent when equal electric fields and surface charges are used. The vertical dashed and straight lines represent the outer Helmholtz plane (OHP), and inner Helmholtz plane (IHP).

symmetrically equal [79], and equivalent to the solid slit nano-pore discussed in Section 2.4. In general, the EDLs inside and outside the pores are correlated; this correlation depends on the radius, $R$, and the thickness, $d$ of the pore's wall [80]. Notwithstanding, here we will only consider the $d = 5\,\text{Å}$ case, and leave the study of this correlation with other values of $d$ for a future work.

For a radius of 5 Å, it is observed that inside the pores, i.e., for $0 \leqslant r \leqslant (R - a/2) = (5 - 2.125)\,\text{Å} \cong 2.35\,a/2$, the adsorption of co-ions and counter-ions is constant, and it is highest for the slit-pore, followed by the cylindrical and spherical pores. At this small radius, only a little more than two ions in straight line, can be fitted. These adsorptions are higher for the constant electrical field boundary conditions, where $E(r = R - a/2)$, implies a higher surface charge density, as discussed in Section 2.4.2.

When the pore's radius is increased, the inner reduced counter-ion concentration profiles, $g_-(r)$, of all the nano-pores, decay in the entire inner interval. The opposite is true for the co-ions concentration profiles, $g_+(r)$, i.e., the absorption of counter-ions, inside the pores, surmount that of the co-ions, as one could expect. For a radius of 30 Å, the counter-ion concentration profile of the cylindrical pore, $g_-^c(r)$, at constant unscreened electrical field, becomes higher than those for the other two pore's geometries. However, for both boundary conditions, i.e., constant charge and constant unscreened electrical field, the cylindrical, $g_-^c(r)$, and spherical, $g_-^s(r)$, surpass that of the slit-pore, $g_-^p(r)$, at least in part of the interval inside the pores. For a larger radius, $R = 80\,\text{Å}$, $g_-^s(r) > g_-^c(r) > g_-^p(r), \quad \forall\, r \quad \cdot \ni \cdot \quad 0 \leqslant$

$r \leqslant R - a/2$. If the radius is increased enough, i.e., $R = 200\,\text{Å}$, the concentration profiles of all the pores become nearly equal to that of the solid electrode discussed in Section 2.4.2, $\forall r \;\; \cdot \ni \cdot \;\; 0 \leqslant r \leqslant R - a/2 \;\; \bigcup \;\; R + d + a/2 \leqslant r \leqslant \infty$, as could be expected. Nevertheless, even at this large pore radius, for $0 \leqslant r \leqslant R - a/2$, the counter-ion profile of the spherical pore slightly overcomes that of the cylindrical pore, and this last surpass that of the slit-pore. Increasing $R$, implies augmenting the charge on the spherical and cylindrical pores, while that of the slit is independent of inter-plate distance $t$; with more charge on the spherical pore than in the cylindrical pore, for a given value of $R$, of course. This explains the observed higher counter-ion contact values of the spherical and cylindrical nano-pores, over that of the slit-pore. However, this effect can not explain, not only the lower counter-ion contact values of all the pores, with increasing $R$, but also the lower counter-ion profiles of all the nano-pores, for all $r$, inside and outside of the pores. *This is a confinement effect, due to the need of the systems to maintain the inner chemical potential equal to that outside the pore.* External to the pores the chemical potential is that of the bulk electrolyte, which is the same, of course, for all the pore geometries here considered, since the bulk concentration profile is taken to be same for all the pore geometries, i.e., $\rho_0 = 0.01\,\text{M}$. *The Poisson-Boltzmann equation is basically a statistical mechanics version of the Gauss' law, where the charge density is taken from the canonical partition function of the system. Hence this equation forces the conservation of charge, energy and probability in the system where it is applied, and, therefore, guaranties a constant chemical potential throughout the system [43].*

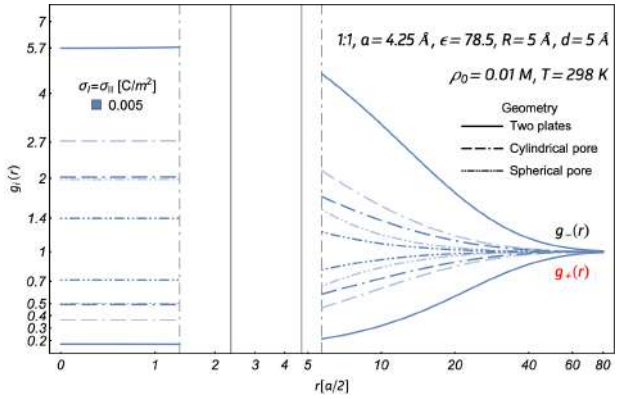


(a) The density profiles for $\sigma = 0.005\,\text{C/m}^2$.

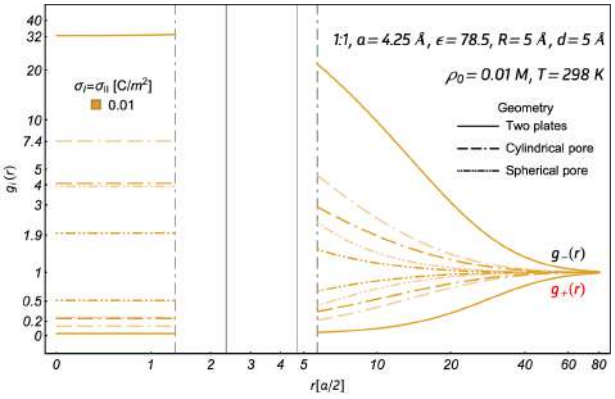


(b) The density profiles for $\sigma = 0.01\,\text{C/m}^2$.

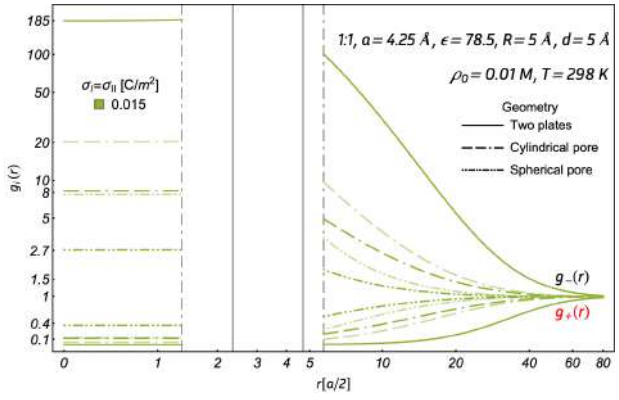


(c) The density profiles for $\sigma = 0.015\,\text{C/m}^2$.

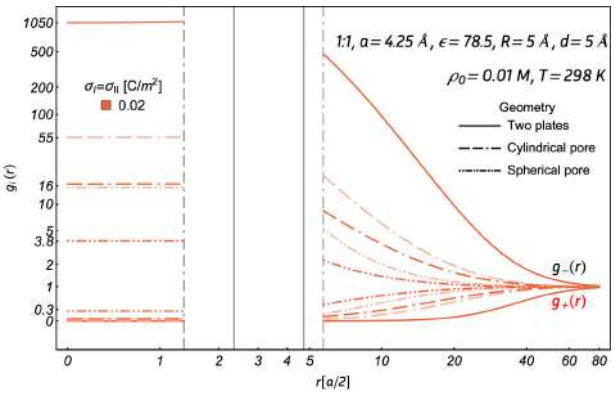


(d) The density profiles for $\sigma = 0.02\,\text{C/m}^2$.

Figure 3.5: The density profiles, $g_i(r)$, of the LPBS for three pore geometries, while the electrodes' surface charges, $\sigma = \sigma_I = \sigma_{II}$, are varied for a monovalent electrolyte, and a pore's radius of 5 Å $\cong$ 1.2 a. The lighter and darker lines, and the vertical lines have the same meaning as in Fig. 3.4.

As seen, in Fig. 3.4 if one wishes to observe the impact that the electrodes' charge density, and electrolytes' molar concentration, and temperature have on the co-ion and counter-ion distribution functions of the different pores, one needs to choose the pore's radius. Since we are interested in small nano-pores, we choose three pores' radii, 5 Å, 15 Å and 80 Å. With these radii, we will obtain the density profiles for different parameters; the electrodes' charge density, the electrolytes' concentration and temperature.

In Fig. 3.5 the density profiles are plotted for the different pore geometries, for a pores' radius of 5 Å, while the electrode's surface charge is varied, for both the equal electric field case and surface charge case. As expected, it is observed that for all the electrodes' surface charges, the adsorption of ions is higher when equal electric fields are used. Furthermore, it should also not come as a surprise, that when the electrode's surface charge increases, the case of equal electric fields rises more than that of equal surface charges. Nonetheless, the equal electric fields concentration profiles of the cylindrical and spherical pores, never reach close to that of the slit-pore, as the plates' density profiles increase exponentially. As in Fig. 3.4, the co-ion and counter-ion distributions remained constant through the inside of the pore, regardless of the electrode's surface charge. This behavior translates in that due to the small pore's radii, the pores are filled with counter-ions, with a very strong attraction to counter-ions and a very strong repulsion to co-ions. If the ionic size had been considered in the ion-ion interaction potential, the ionic size would be an additional obstacle for the co-ions to squeeze into the pores.

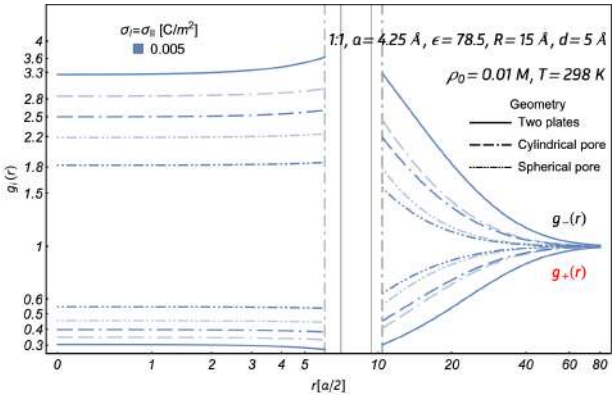


(a) The density profiles for $\sigma = 0.005\,\mathrm{C/m^2}$.

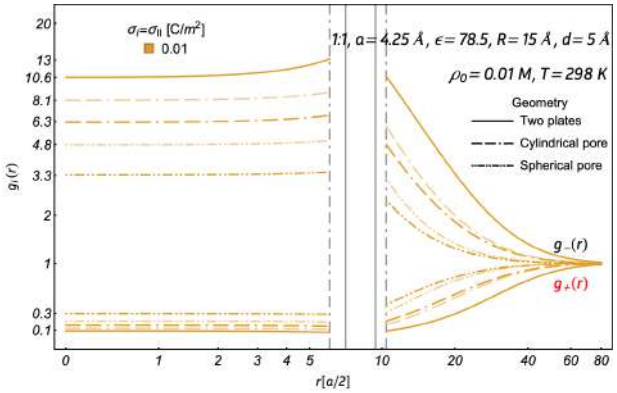


(b) The density profiles for $\sigma = 0.01\,\mathrm{C/m^2}$.

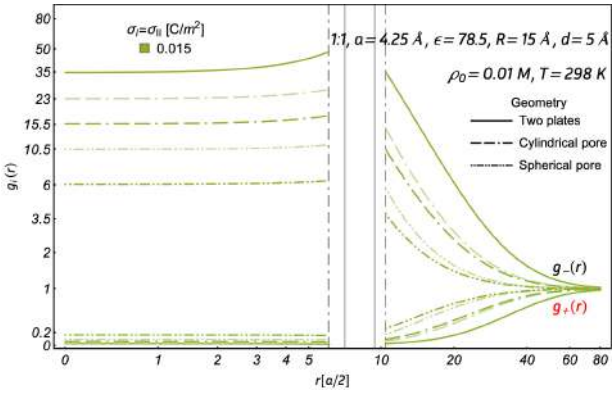


(c) The density profiles for $\sigma = 0.015\,\mathrm{C/m^2}$.

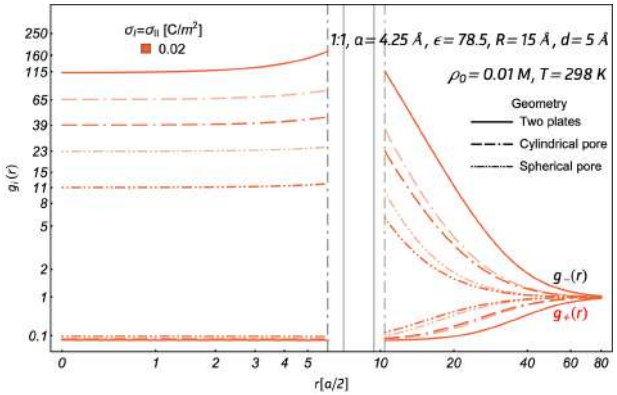


(d) The density profiles for $\sigma = 0.02\,\mathrm{C/m^2}$.

Figure 3.6: The density profiles, $g_i(r)$, of the LPBS for three pore geometries, while the electrodes' surface charges, $\sigma = \sigma_I = \sigma_{II}$, are varied for a monovalent electrolyte, and a pore's radius of 15 Å $\cong$ 3.5 a. The lighter and darker lines, and the vertical lines have the same meaning as in Fig. 3.4.

In Fig. 3.6 the density profiles are plotted for the different pore geometries, for a pore's radius of 15 Å, while varying the electrodes' surface charges, for equal electric fields and surface charges. It is observed that when the pores' radius increases from 5 Å to 15 Å, the slit-pore concentration profiles, decrease considerably, and those for the cylindrical and spherical nano-pores density profiles become closer to those of the plates. Furthermore, it is also observed that now, for higher radii, the inner contact values of the density profiles, do not stay constant through all the pore. It is observed that this value softly decays as it approaches the pore's center. Therefore, the counter-ions are not as highly compacted as before, since their concentration slightly decreases at the pore's center. Moreover, when Figs. 3.4b and 3.6 are compared, it is found out that at a radius of 15 Å the pores are not large enough for breaking down the slit-pore' domination over the other pores' density profiles.

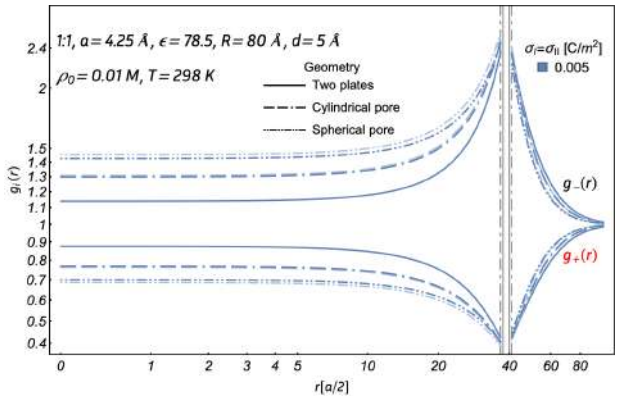


(a) The density profiles for $\sigma = 0.005\,\mathrm{C/m^2}$.

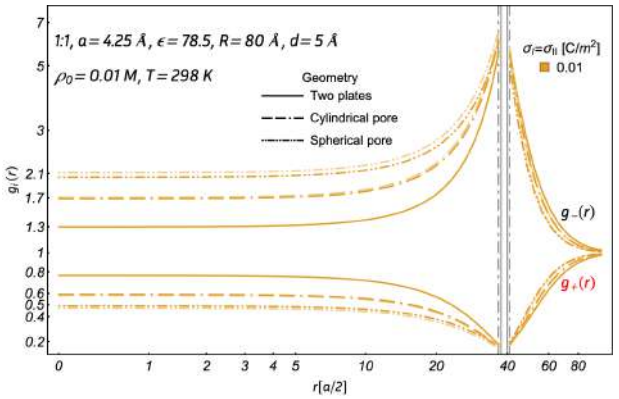


(b) The density profiles for $\sigma = 0.01\,\mathrm{C/m^2}$.

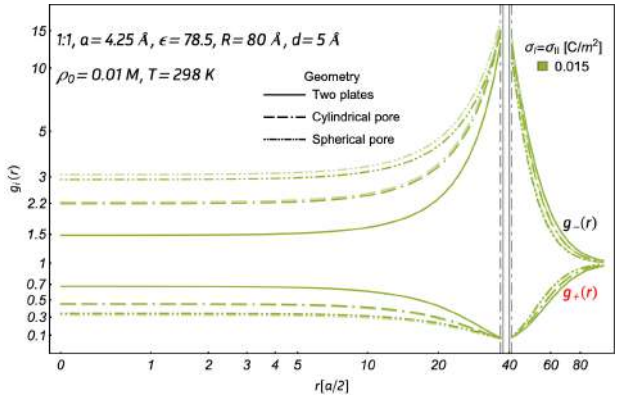


(c) The density profiles for $\sigma = 0.015\,\mathrm{C/m^2}$.

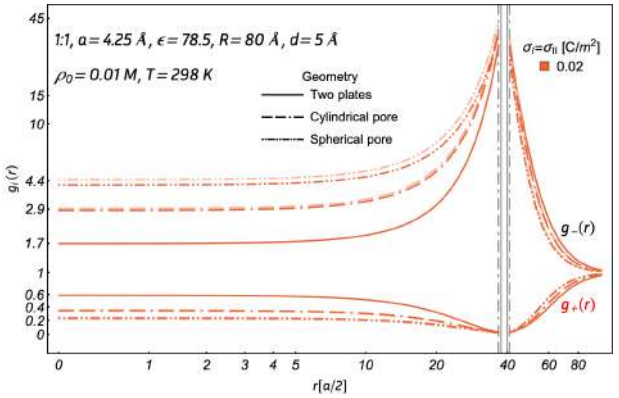


(d) The density profiles for $\sigma = 0.02\,\mathrm{C/m^2}$.

Figure 3.7: The density profiles, $g_i(r)$, of the LPBS for three pore geometries, while the electrodes' surface charges, $\sigma = \sigma_I = \sigma_{II}$, are varied for a monovalent electrolyte, and a pore's radius of 80 Å $\cong$ 18.8 a. The lighter and darker lines, and the vertical lines have the same meaning as in Fig. 3.4.

In Fig. 3.7 the density profiles for different pore geometries, at a pore's radius of 80 Å, are shown for equal electric fields and surface charges. Once again, as for all the other previously shown plots, it is observed that as the electrode's surface charge density increases the density profiles follow. However, now the pore's radius is large enough such that the cases of equal electric fields and surface charges are nearly equal. Furthermore, as the radius was increased from 15 Å to 80 Å it was found that the density profiles, inside the pores, of the cylindrical and spherical pores overpass the slit-pore'. However, they do not surmount that of the slit, outside the pores. This is a confinement effect, and as we will see in Chapter 4, the induced charge inside the slit-pore is higher than those of the spherical and cylindrical

pores. Moreover, it is observed that for this pore's radius there is a significant drop of the density profile inside the pore. Therefore, there is a higher amount of counter-ions close to the pores' wall, and lower on its center. If the radius is increased further, the counter-ion and co-ion distributions drop will be nearly the same as that of a solid electrode.

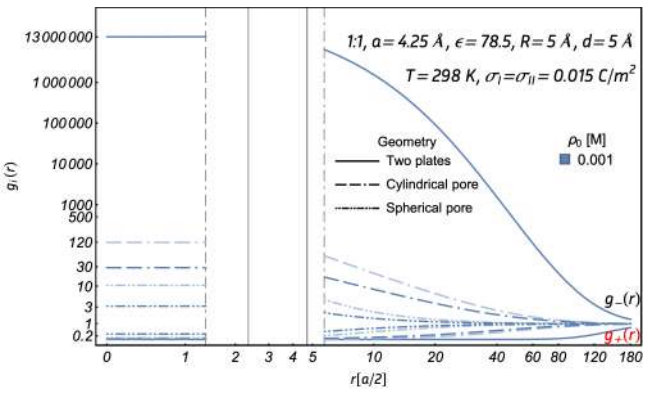


(a) The density profiles for $\rho_0 = 0.001\,\mathrm{M}$.

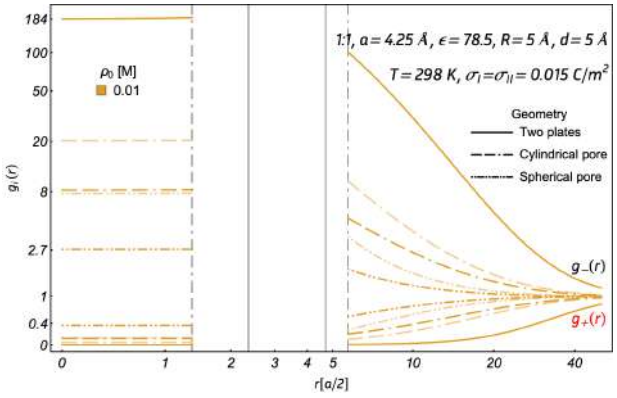


(b) The density profiles for $\rho_0 = 0.01\,\mathrm{M}$.

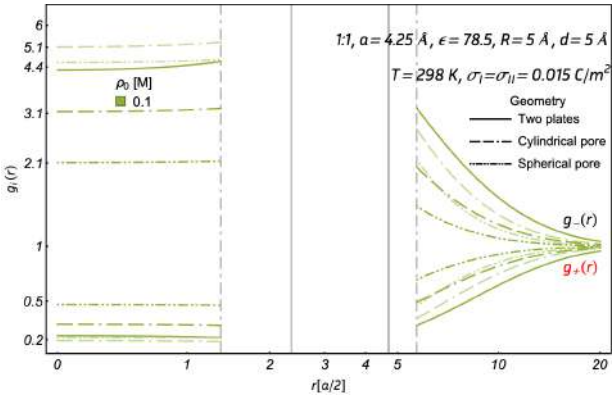


(c) The density profiles for $\rho_0 = 0.1\,\mathrm{M}$.

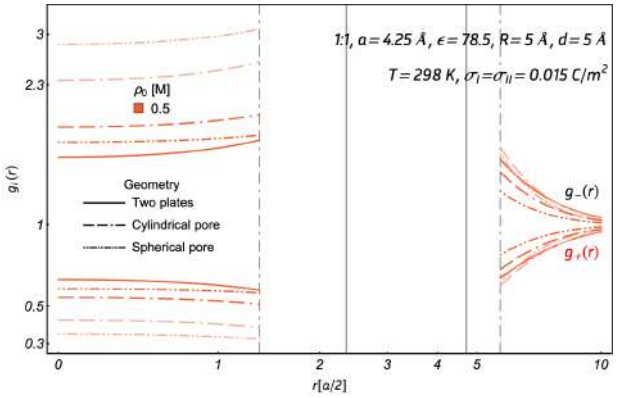


(d) The density profiles for $\rho_0 = 0.5\,\mathrm{M}$.

Figure 3.8: The density profiles of the three pore geometries obtained for varied molar concentrations, $\rho_0$, of a monovalent electrolyte. A pore's radius of $5\,\text{Å} \cong 1.2\,\mathrm{a}$ is used. The lighter and darker lines, and the vertical lines have the same meaning as in Fig. 3.4.

In Fig. 3.8 the impact that the electrolyte's molar concentration, $\rho_0$, has on the co-ion and counter-ion distribution functions for a pore's size of $5\,\text{Å}$ is shown, for an electrodes' surface charge density of $0.015\,\mathrm{C/m^2}$. The cases of equal electric fields and of equal surface charge density are presented. It is found that the *reduced* concentration profiles diminish as the electrolyte's molar concentration increases. Furthermore, it is observed that for the lower molar concentrations, $0.001\,\mathrm{M}$ and $0.01\,\mathrm{M}$, the density profiles inside the pore remain constant. On the other hand, when the molar concentration reaches values equal or higher than $0.1\,\mathrm{M}$, the density profiles inside the pore start decreasing from their inner contact value. Furthermore, it is observed that the inner density profile of the plates is overcome by the spherical and cylindrical pores for equal electric fields and for a molar concentration of $0.1\,\mathrm{M}$. Moreover, it is also overcome for equal surface charges for a concentration of $0.5\,\mathrm{M}$. Meanwhile, for the outer pore, the concentration profiles also diminish when the concentration increases, and for the highest bulk concentration ($0.5\,\mathrm{M}$), for the equal electric field cases', the spherical and cylindrical pores' concentration profiles overcome the contact values of the plates. Notice the ample, higher, difference between the inner and outer contact values, implying a lower effective electric field at $r = R + d + a/2$,

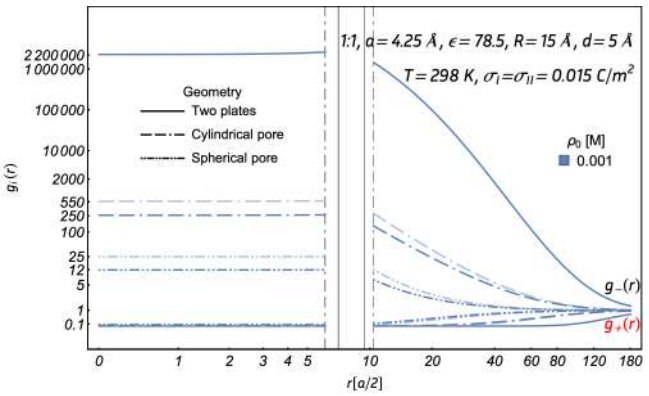


(a) The density profiles for $\rho_0 = 0.001\,\mathrm{M}$.

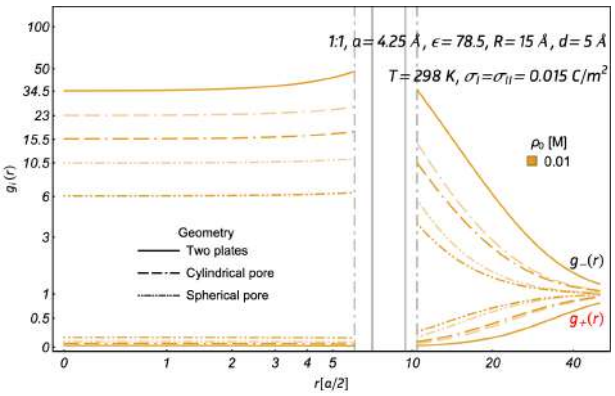


(b) The density profiles for $\rho_0 = 0.01\,\mathrm{M}$.

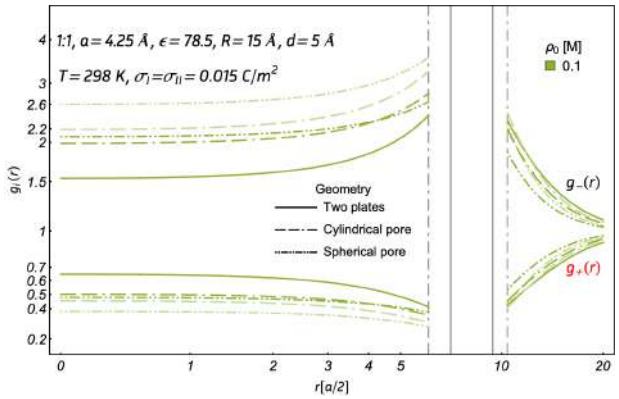


(c) The density profiles for $\rho_0 = 0.1\,\mathrm{M}$.

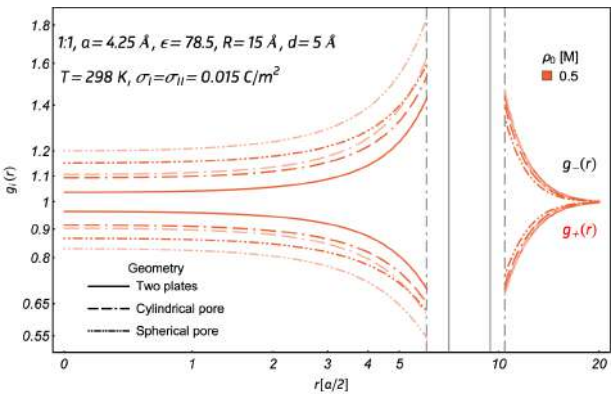


(d) The density profiles for $\rho_0 = 0.5\,\mathrm{M}$.

Figure 3.9: The density profiles of the three pore geometries obtained for varied molar concentrations, $\rho_0$, of a monovalent electrolyte. A pore's radius of $15\,\text{Å} \cong 3.5\,\mathrm{a}$ is used. The lighter and darker lines, and the vertical lines have the same meaning as in Fig. 3.4.

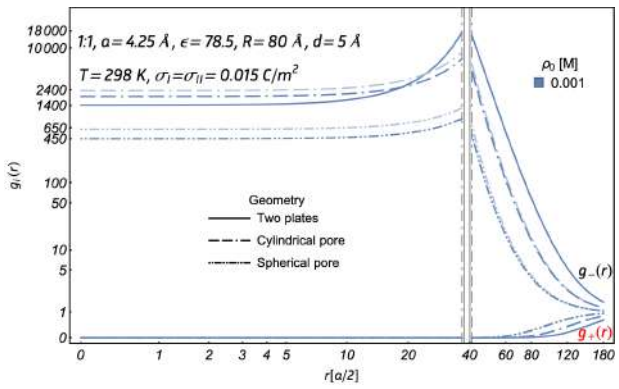


(a) The density profiles for $\rho_0 = 0.001\,\mathrm{M}$.

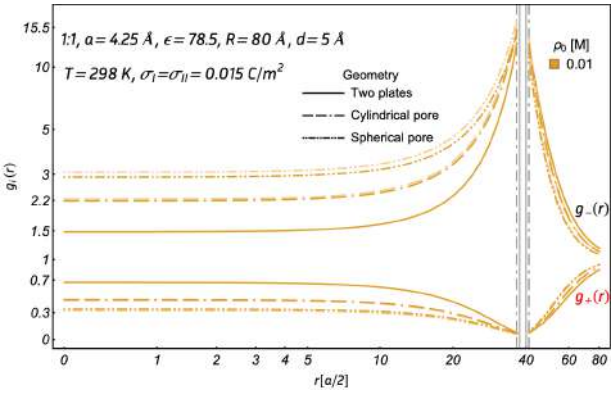


(b) The density profiles for $\rho_0 = 0.01\,\mathrm{M}$.

Figure 3.10: The density profiles of the three pore geometries obtained for varied molar concentrations, $\rho_0$, of a monovalent electrolyte. A pore's radius of $80\,\text{Å} \cong 18.8\,\mathrm{a}$ is used. The lighter and darker lines, and the vertical lines have the same meaning as in Fig. 3.4.

as a result of the need of the systems of satisfying their general electroneutrality. This also implies that the induced electric field produced by the confined electrolyte goes across the pore walls, hence,

explaining in part the correlation between the inside and outside electrical double layers.

In Fig. 3.9 the impact that the molar concentration, $\rho_0$, has on the co-ion and counter-ion distribution functions for the different nano-pore electrodes is shown, when a pore's size of 15 Å is used. The same electrode's surface charge density used in Fig. 3.8 is used for Fig. 3.9, and also the equal electric fields and surface charges are shown. Therefore, when the pores' radii is increases from 5 Å to 15 Å it is found that the concentration profiles intensity decreases. Also the difference between the inner and outer contact values decrease. These phenomena are the result of a complex combination of the need of the systems of satisfying the chemical potential and electroneutrality. Furthermore, it is found that for the highest molar concentrations, 0.1 M and 0.5 M, both the equal electric fields and surface charges of the cylindrical and spherical pores overcome the density profile of the slit-pore. Moreover, it is observed that at such concentrations the inner pore resembles more a solid electrode when compared against their respective concentrations of Fig. 3.8. The very high values of counter-ion concentration profiles, inside and outside the pores, seen in Figs. 3.8a and 3.9a show that at this very low concentration the counter-ions are very highly adsorbed to the pores walls. It is tempting to adjudicate this behavior to the fact that in this point-ion model, the ion-ion hard-core interactions are neglected. However, if the ionic size is considered, as for example in the Restricted Primitive Model, the qualitative and quantitative agreement with the present results is surprisingly good (not shown). However, this study

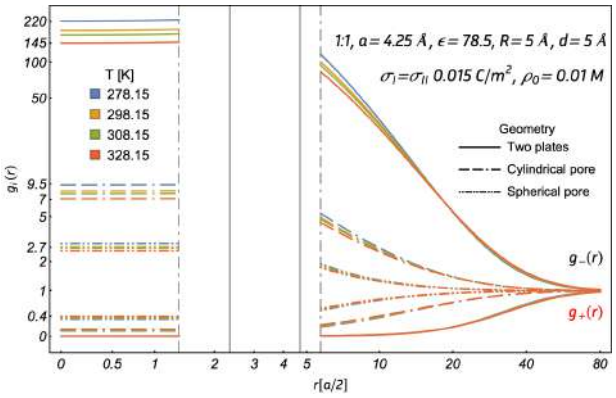


(a) The density profiles for $R = 5$ Å $\cong 1.2$ a.

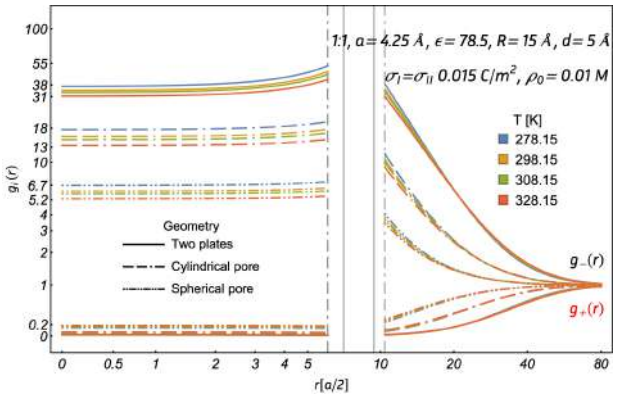


(b) The density profiles for $R = 15$ Å $\cong 3.5$ a.

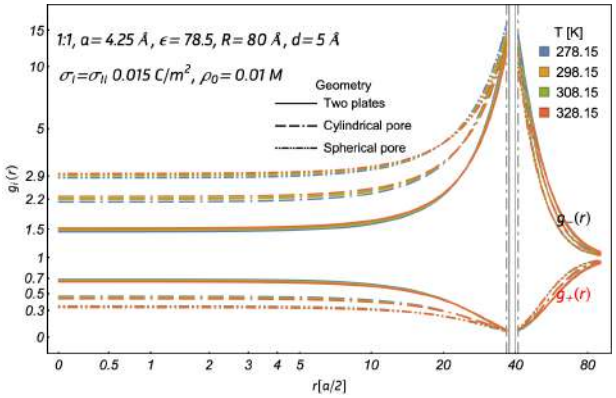


(c) The density profiles for $R = 80$ Å $\cong 18.8$ a.

Figure 3.11: The density profile functions, $g_i(r)$, of three pore electrodes, for three radii, while the temperature, $T$, is varied. The lighter and darker lines, and the vertical lines have the same meaning as in Fig. 3.4.

will be left to a forthcoming investigation. On the other hand, it has been shown that at very narrow pore's size, the non-linear Poisson-Boltzmann equation deviates from the HNC/MSA result [81], but it has also been shown that the non-linear Poisson-Boltzmann theory has a remarkable good quantitative and qualitative agreement with HNC/MSA, in the calculation of transport properties of confined electrolytes, at very narrow pores and very low electrolyte concentration [82]. Thus, the strong increase in the inner *reduced* concentration profile is basically a confinement effect. We will come back to this point in Section 4.2.2.

In Fig. 3.10 the impact the molar concentration, $\rho_0$, has on the co-ion and counter-ion distribution functions for the different pores is shown, for a pore's radius of 80 Å. From Figs. 3.8 and 3.9, it was found that when the molar concentration and the pores' radius are increased simultaneously, the density profiles inside and outside the pore quickly tend to that of a solid electrode. Consequently, for a pore's radius of 80 Å we decided not to include the cases of higher molar concentration as they are almost identical to that of a solid electrode. Nevertheless, for a low molar concentration of 0.001 M it is found that the density profile of a cylindrical pore overruns that of the slit-pore. And for a higher concentration, 0.01 M, the slit-pore density profiles come last, as they are overtaken by the spherical and cylindrical pores' density profiles.

Lastly, in Fig. 3.11 the co-ion and counter-ion distribution functions of the different nano-pores are shown for different radii, while the temperature is increased. It is found that for the smaller radii, 5 Å and 15 Å, the density profiles inside the pore decrease as the temperature increases. On the other hand, for a radius of 80 Å, this behavior is only seen close to the pores' walls (both inside and outside), while away from the the wall, the tendency is inverted. Close to the pores' wall when the temperature increases, the density profiles decrease, but when the distance from the pores' wall is long enough, around 6 a, this tendency is inverted. Then, after a distance of 6 a from the inside wall, toward the center of the pore, when the temperature is increased the density profiles increase as well, for any pore. The distribution functions are given by Eq. (3.4), thus an increase in temperature, can also be seen as a decrease of ionic valence or surface charge. The crossover of the distribution functions, for 6 a, is a consequence of the electroneutrality condition.

# Chapter 4

# Mean electrostatic potential, induced charge density and differential capacitance

In this chapter, the results of the mean electrostatic potential, the induced surface charge density profiles and the differential capacitance are obtained for the solid and nano-pores electrode's geometries. These are presented in the first and second section, respectively. The mean electrostatic potentials and the induced surface charge density profiles are obtained for different electrodes' radii, and surface charge densities, and for different electrolytes molar concentration, and temperature for both solid and nano-pore geometries. Further, the differential capacitance is calculated for different electrodes' radii, and for various electrolytes' temperatures, and molar concentrations.

## 4.1 The single electric double layer for solid electrodes

The electrical parameters used in Chapter 2 for the different solid electrodes are merged together in the following subsections. An analysis is performed between each geometry to find out which one performs best.

Firstly, the mean electrostatic potential is plotted for the p-LPBS and p-nLPBS to observe how does our linearization behave against our non-linearized solution. The same interval of validity found for the density profiles is used. Afterwards, a comparison is made between the linear results of the mean electrostatic potential for all the electrode geometries. Subsequently, the same comparison against the p-LPBS and p-nLPBS is performed for the surface charge density, as well as against other solid electrode geometries.

Secondly, the differential capacitance is calculated and compared for the different electrodes. A comparison between the linear (independent of $\sigma_M$) and the non-linear (dependent on $\sigma_M$) capacitance is done for the solid planar electrode, while different electrolytes' molar concentrations and temperatures are used. Subsequently, a comparison between the linear differential capacitances of the solid cylindrical and spherical electrodes is performed for different electrodes' radii, while the electrolytes' temperature and molar concentration are changed.

It is worth noting that we consider an aqueous symmetric electrolyte (1:1) with an electric permittivity of 78.5, and an ion's size of 4.25 Å, at a room temperature of 298 K, unless stated otherwise.

### 4.1.1 The mean electrostatic potentials of solid electrodes

In this subsection, our results of the mean electrostatic potentials are shown for different electrode's geometries. Firstly, a comparison between the linear and non-linear mean electrostatic potential is made

for a plane electrode. Secondly, we perform a comparison of the linear mean electrostatic potentials of the different electrodes. We start by varying the electrode's size, and afterwards its surface charge density, whereas for the electrolyte we vary its molar concentration and temperature.

#### 4.1.1.1 The linear and non-linear mean electrostatic potentials of a solid planar electrode

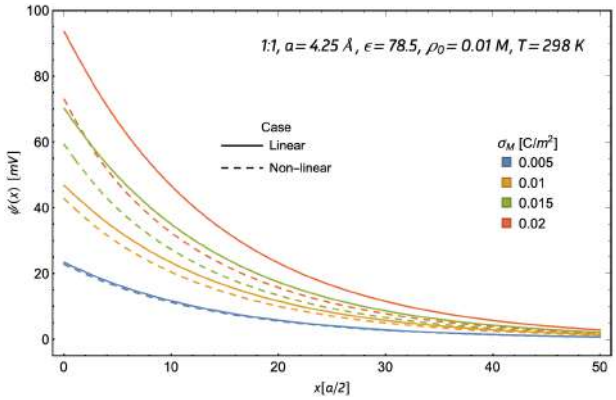


(a) $\psi(x)$ for $\rho_0 = 0.01\,\mathrm{M}$.

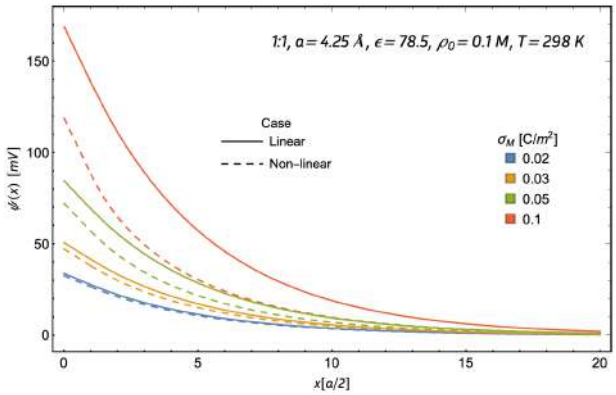


(b) $\psi(x)$ for $\rho_0 = 0.1\,\mathrm{M}$.

Figure 4.1: The linear and non-linear mean electrostatic potential, $\psi(x)$, of a solid planar electrode for different electrode's surface charge densities, $\sigma_M$. The linear and non-linear mean electrostatic potentials are represented by a solid and dashed line, respectively.

In Fig. 4.1 the linear and non-linear mean electrostatic potentials of a solid planar electrode are plotted for different electrode's surface charge densities. It is observed that the linear approximation is a good fit of the non-linear mean electrostatic potential for low surface charges. As it was expected, from Section 2.4.1, our linear solutions of the mean electrostatic potentials are a good fit of the non-linear ones for surface charge up to $0.015\,\mathrm{C/m^2}$ and $0.05\,\mathrm{C/m^2}$ for molar concentrations of $0.01\,\mathrm{M}$ and $0.1\,\mathrm{M}$, respectively. This is due to the fact that at such limit points our non-linear mean electrostatic potential approaches an asymptotic limit. On the other hand, the linear mean electrostatic potentials

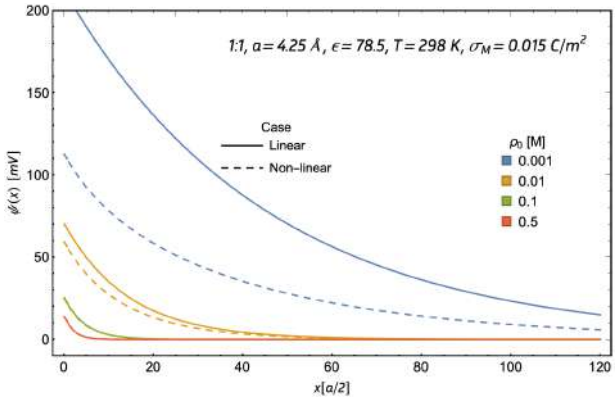


(a) $\psi(x)$ for $\sigma_M = 0.015\,\mathrm{C/m^2}$.

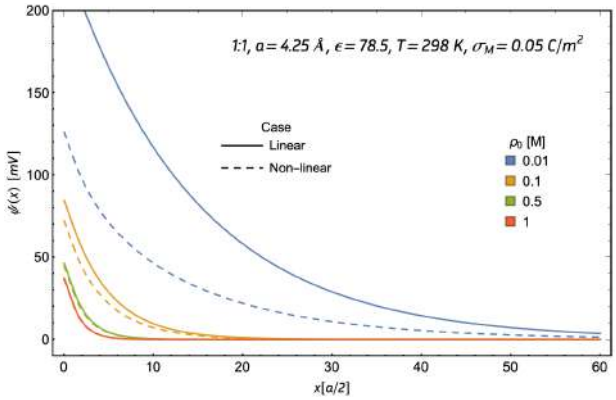


(b) $\psi(x)$ for $\sigma_M = 0.05\,\mathrm{C/m^2}$.

Figure 4.2: The linear and non-linear mean electrostatic potential, $\psi(x)$, of a solid planar electrode while the molar concentration, $\rho_0$, is varied. The solid and a dashed lines have the same meaning as in Fig. 4.1.

do not, they steadily grow, surpassing this limit. Hence, it is not advisable to work for surface charge densities higher than $0.015\,\mathrm{C/m^2}$ and $0.05\,\mathrm{C/m^2}$ for molar concentrations of 0.01 M and 0.1 M, when considering the linear case, as it stops being an accurate representation of the non-linear case.

It was found for the plane's linear mean electrostatic potentials in Fig. 4.1 that the upper limits of the electrodes' surface charge are $0.015\,\mathrm{C/m^2}$ and $0.05\,\mathrm{C/m^2}$ at molar concentrations of 0.01 M and 0.1 M. Now, in order to find the interval of validity of the molar concentrations, these surface charges are used while the electrolyte's molar concentration is varied, in Fig. 4.2. From this figure it is observed that our linear mean electrostatic potential is a good approximation of the non-linear when the molar concentrations are higher than or equal to, 0.01 M and 0.1 M, for their respective surface charge, $0.015\,\mathrm{C/m^2}$ and $0.05\,\mathrm{C/m^2}$. Therefore it is observed that our linear solution of the mean electrostatic potential can withstand higher surface charges for higher molar concentrations, without jeopardizing the validity of the linear mean electrostatic potential against the non-linear one. Furthermore, it is observed that the voltage is inversely proportional to the molar concentration.

#### 4.1.1.2 The mean electrostatic potentials of different geometries

From here forward, unless stated otherwise, only the mean electrostatic potentials of our LPBS while be shown. Firstly, a comparison between the mean electrostatic potentials of different solid electrodes

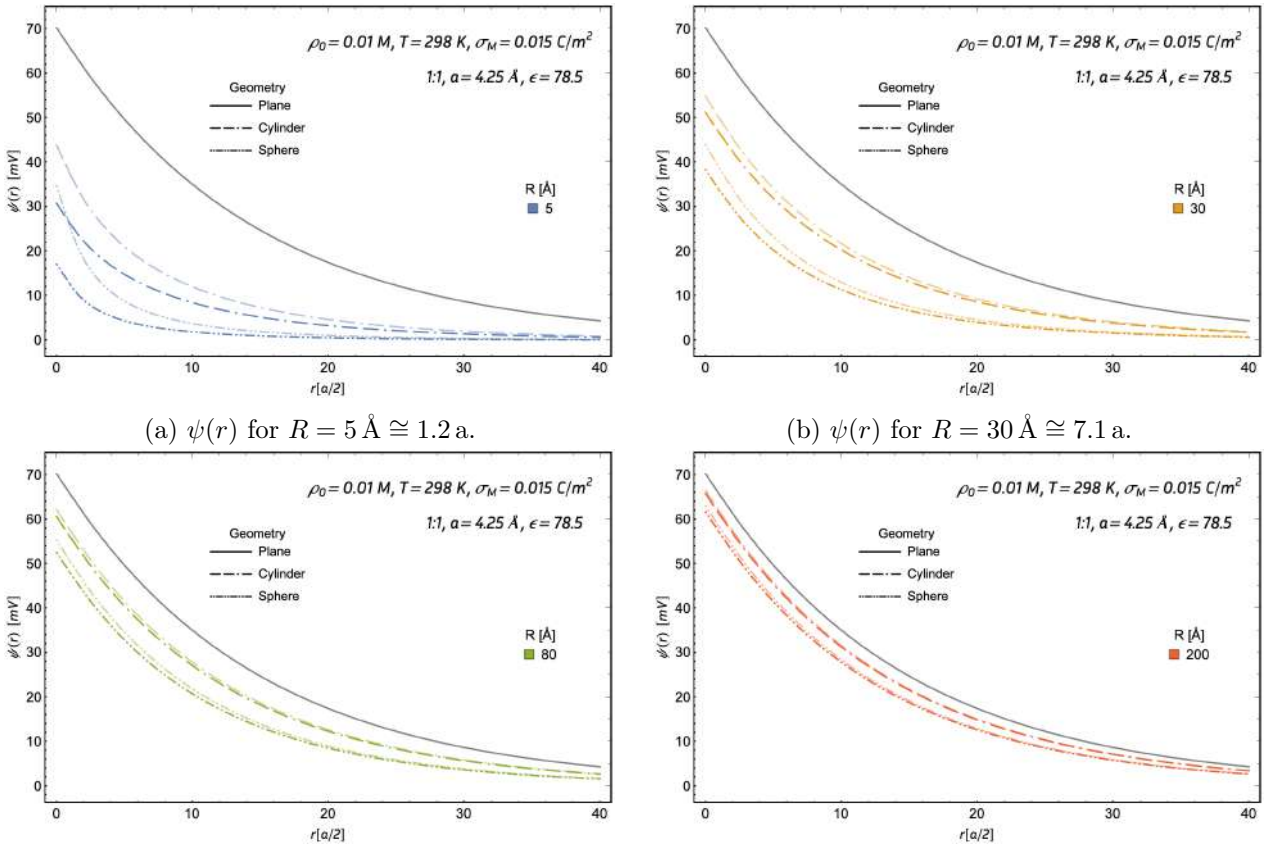


(a) $\psi(r)$ for $R = 5\,\text{Å} \cong 1.2\,\text{a}$.

(b) $\psi(r)$ for $R = 30\,\text{Å} \cong 7.1\,\text{a}$.

(c) $\psi(r)$ for $R = 80\,\text{Å} \cong 18.8\,\text{a}$.

(d) $\psi(r)$ for $R = 200\,\text{Å} \cong 47.1\,\text{a}$.

Figure 4.3: The mean electrostatic potentials, $\psi(r)$, of the different solid electrode geometries for various radii values. The lighter and darker lines represent two distinct cases, when equal electric fields and surface charges are used.

is made. Because the solid cylindrical and spherical electrodes depend on their radius, their mean electrostatic potentials are plotted for different radii in Fig. 4.3. They are plotted for the two cases used in Chapters 2 and 3, when equal electric fields and surface charges are used. Meanwhile, the linear mean electrostatic potential of the solid planar electrode is plotted as well for comparison purposes.

From Fig. 4.3 it is seen that the highest mean electrostatic potentials are always achieved for the solid planar electrode. Furthermore, it is also found that when equal electric fields are used, specially for low radii, higher values of the mean electrostatic potentials are achieved when compared against the equal surface charge cases. Furthermore, it is seen that the mean electrostatic potentials of the cylindrical and spherical electrodes are directly proportional to the radii size. Their mean electrostatic potentials intensity and extension, increase when a bigger radius is used. Additionally, it is observed that the mean electrostatic potential of the solid cylindrical electrode is always higher and more intensive than the spherical one, for the same radii. Lastly, but not least, when the radius is large enough, both the solid cylindrical and spherical electrodes' mean electrostatic potentials tend to the mean electrostatic potential of the solid planar electrode. As seen in Fig. 4.3, if one wishes to compare the influence of the electrode's surface charge density, and the electrolyte's molar concentration and temperature have on the mean electrostatic potential of different electrodes, a fixed radius must be chosen. For this purpose, we will use three radii, 5 Å, 15 Å and 80 Å, to see the collective impact that the radius and other electric parameters have on the mean electrostatic potential.

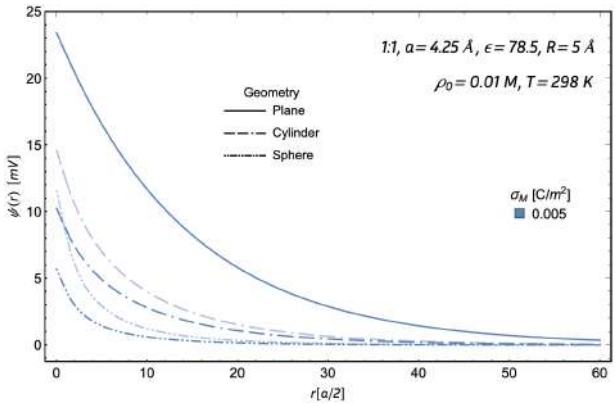


(a) $\psi(r)$ for $\sigma_M = 0.005\,\mathrm{C/m^2}$.

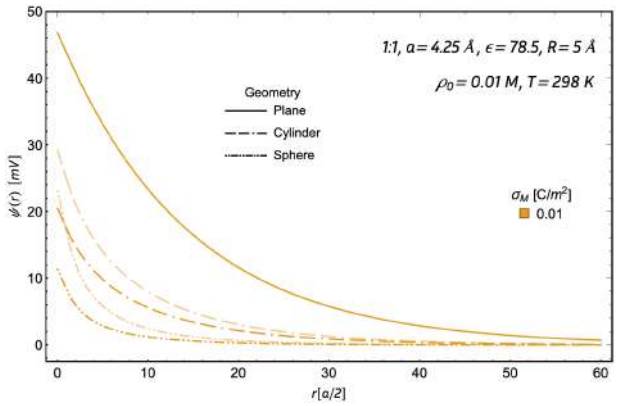


(b) $\psi(r)$ for $\sigma_M = 0.01\,\mathrm{C/m^2}$.

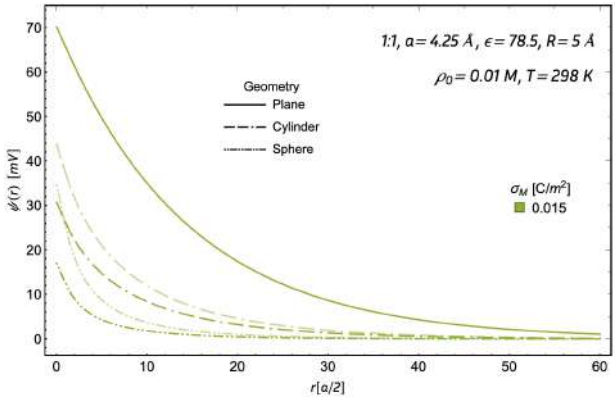


(c) $\psi(r)$ for $\sigma_M = 0.015\,\mathrm{C/m^2}$.

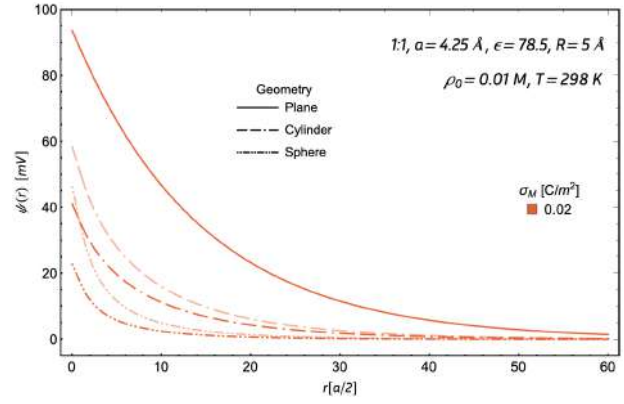


(d) $\psi(r)$ for $\sigma_M = 0.02\,\mathrm{C/m^2}$.

Figure 4.4: The linear mean electrostatic potentials, $\psi(r)$, of a solid planar, a cylindrical, and a spherical electrodes. A radius of 5 Å $\cong$ 1.2 a is used, while the electrodes' surface charge, $\sigma_M$, is varied. The lighter and darker lines have the same meaning as in Fig. 4.3.

Therefore, in Fig. 4.4 the mean electrostatic potentials of the three solid electrodes are plotted for different surface charges, with a radius of 5 Å. The equal electric field case and surface charge are shown. It is observed that as the surface charge increases, the mean electrostatic potential intensity and extension increase steadily, regardless of whether the electric fields are equivalent or not. The mean electrostatic potential at $r = R + a/2$, $\psi(r = R + a/2)$ is referred to as the Helmholtz potential or $\zeta$-potential, and often assumed as the ion's stagnation layer under dynamical conditions. Hence, this potential is of a major relevance in, for example, electrophoresis studies. As expected from Eqs. (2.49) and (2.50), the $\zeta$-potential for the constant electric potential case overcomes that for the constant surface charge case, for both the cylindrical and spherical electrodes. These differences increase with increasing surface charge on the electrodes. The cylinder $\zeta$-potentials are always higher than the corresponding ones for the spherical electrode, expressing the fact that the amount of energy required to bring an ion from infinity to the surface of an electrode, through a $\ln(r)$ electric potential is higher than that through a $1/r$ electric potential.

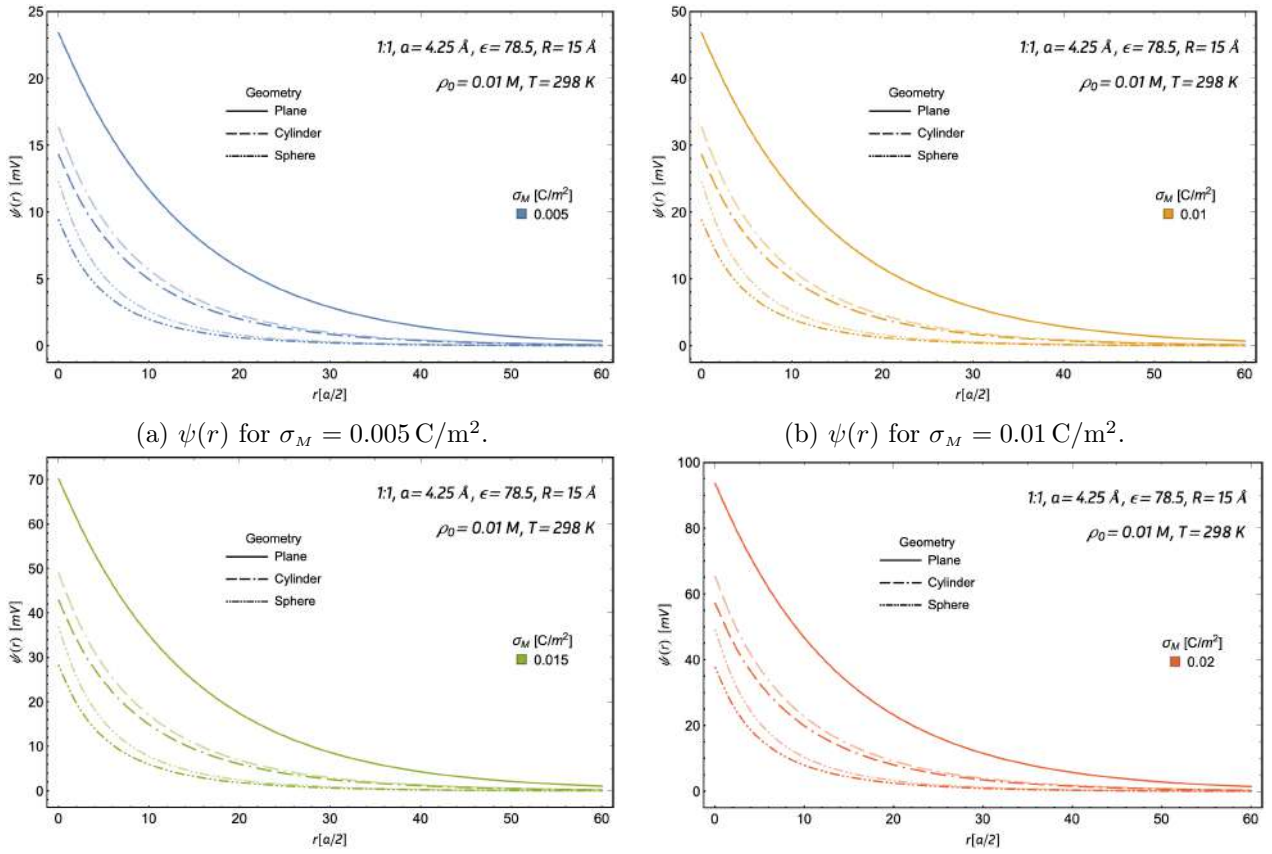


(a) $\psi(r)$ for $\sigma_M = 0.005\,\mathrm{C/m^2}$.

(b) $\psi(r)$ for $\sigma_M = 0.01\,\mathrm{C/m^2}$.

(c) $\psi(r)$ for $\sigma_M = 0.015\,\mathrm{C/m^2}$.

(d) $\psi(r)$ for $\sigma_M = 0.02\,\mathrm{C/m^2}$.

Figure 4.5: The linear mean electrostatic potentials, $\psi(r)$, of a solid planar, a cylindrical, and a spherical electrodes. A radius of 15 Å $\cong$ 3.5 a is used, while the electrodes' surface charge, $\sigma_M$, is varied. The lighter and darker lines have the same meaning as in Fig. 4.3.

Now, in Fig. 4.5 the mean electrostatic potentials of the three solid electrodes are plotted for different surface charges, when a radius of 15 Å is used. Once again, both cases of equal electric fields and surface charges are shown. For this radius, it is clearly observed that the $\zeta$-potentials are larger for $R = 15$ Å than for $R = 5$ Å, since a larger radius implies a stronger mean electrostatic potential, as a function of the distance to the electrode, i.e., from Eqs. (2.54) and (2.55), $\lim_{R\to\infty} E_C^u(x) \to E_P^u(x)$,

and the $\lim_{R\to\infty} E_S^u(x) \to E_P^u(x)$. Hence, the mean electrostatic potentials of the cylindrical and spherical solid electrodes are more intense and thick as their radii increase. Thus, when the radius increases from 5 Å to 15 Å it is found that the mean electrostatic potential increases. However, the differences between the cases of equal electric fields and surface charges decrease.

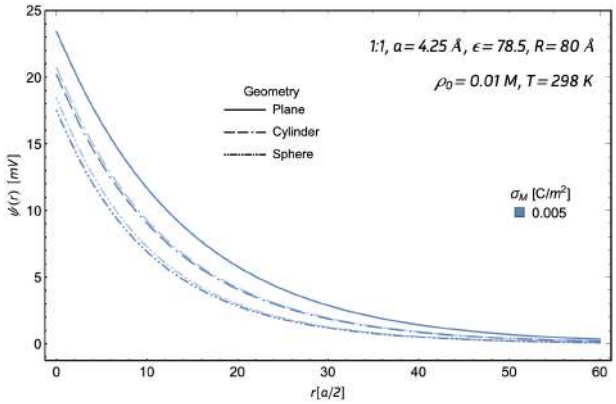


(a) $\psi(r)$ for $\sigma_M = 0.005\,\mathrm{C/m^2}$.

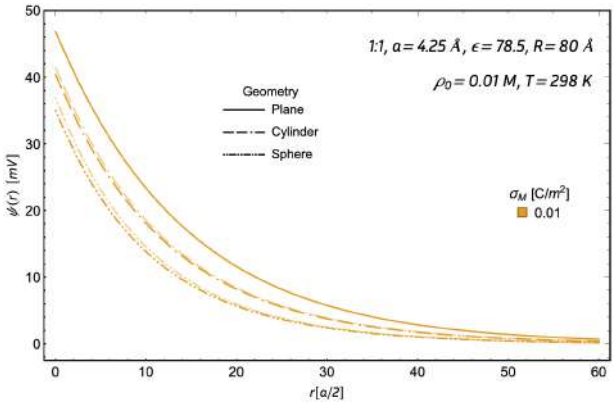


(b) $\psi(r)$ for $\sigma_M = 0.01\,\mathrm{C/m^2}$.

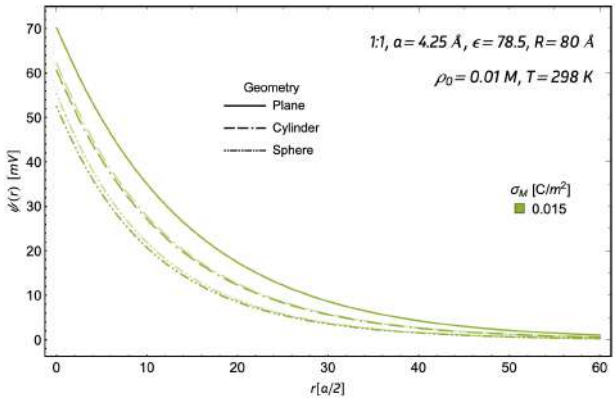


(c) $\psi(r)$ for $\sigma_M = 0.015\,\mathrm{C/m^2}$.

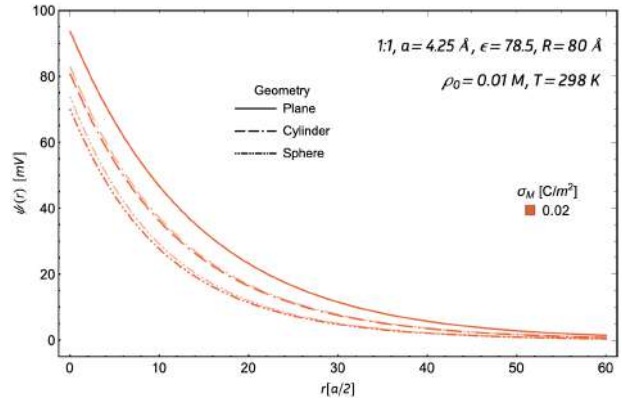


(d) $\psi(r)$ for $\sigma_M = 0.02\,\mathrm{C/m^2}$.

Figure 4.6: The linear mean electrostatic potentials, $\psi(r)$, of a solid planar, a cylindrical, and a spherical electrodes. A radius of 80 Å $\cong$ 18.8 a is used, while the electrodes' surface charge, $\sigma_M$, is varied. The lighter and darker lines have the same meaning as in Fig. 4.3.

In Fig. 4.6 the mean electrostatic potentials of the three solid electrodes are plotted for different surface charges, when a radius of 80 Å is used. Again, the cases of equal electric fields and surface charges are shown. It is observed, that now, the radius is large enough such that the equal electric field and surface charges cases overlap. Furthermore, when the radius increase from 15 Å to 80 Å it is found that the mean electrostatic potential of the cylindrical and spherical electrodes are almost identical to that of the planar electrode.

To continue our analysis, the mean electrostatic potentials for our three radii, 5 Å, 15 Å and 80 Å, are calculated, while varying the electrolyte's molar concentration. In Fig. 4.7 the mean electrostatic potentials are computed for the solid planar, cylindrical, and spherical electrodes for different molar concentrations. It is observed that for the lowest electrolyte's molar concentration the highest mean electrostatic potentials are achieved, while for the highest molar concentrations, the lowest mean electrostatic potentials are obtained. Furthermore, for the highest molar concentrations the mean electrostatic potential quickly disappears when the distance form the surface is increased. All this is a consequence of the screening of the electrodes' electrical field, by the induced charge on the ions, i.e.,

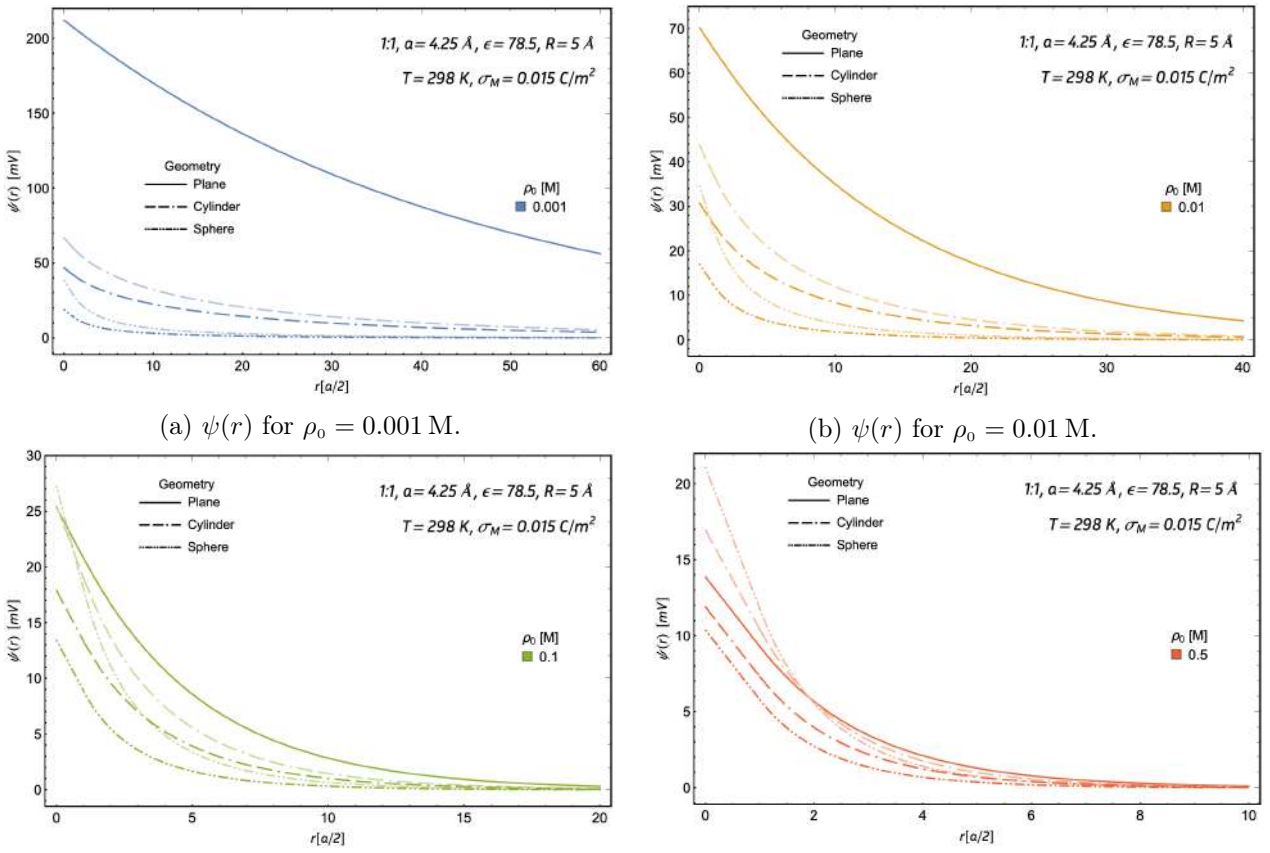


(a) $\psi(r)$ for $\rho_0 = 0.001\,\mathrm{M}$.

(b) $\psi(r)$ for $\rho_0 = 0.01\,\mathrm{M}$.

(c) $\psi(r)$ for $\rho_0 = 0.1\,\mathrm{M}$.

(d) $\psi(r)$ for $\rho_0 = 0.5\,\mathrm{M}$.

Figure 4.7: The linear mean electrostatic potential, $\psi(r)$, of different solid electrodes, with a radius of $5\,\text{Å} \cong 1.2\,\text{Å}$, while the electrolytes' molar concentration, $\rho_0$, is varied. The lighter and darker lines have the same meaning as in Fig. 4.3.

the higher the bulk concentration, the higher the ionic screening. Meanwhile, for the equal electric field cases, when the molar concentration reaches 0.1 M, the $\zeta$-potential of both, the solid cylindrical and spherical electrodes, surpass that of the plate. This is due to a combination of induced charge and the higher surface charge on the cylindrical and spherical electrodes, to keep the corresponding electrical fields equal to that of the plate.

Comparatively, in Fig. 4.8 the mean electrostatic potentials of the different solid electrodes are shown for a radius of 15 Å, for the equal electric fields and surface charges cases. It can be observed that when the radius is increased from 5 Å to 15 Å, the mean electrostatic potential of the equal electric field case does not increase as much as before. Furthermore, it is observed that for the highest molar concentration, 0.5 M, the three geometries tend to virtually the same values of the mean electrostatic potential. Hence, it is recognized from Figs. 4.7 and 4.8, that when the molar concentration and the radius increase simultaneously the mean electrostatic potentials from the different solid electrode geometries tend to the values of the mean electrostatic potential of the planar electrode. For this reason, in Fig. 4.9 we omit to show the plots of the mean electrostatic potential for higher molar concentrations as their values completely overlap.

So, in Fig. 4.9 the mean electrostatic potentials of the different solid electrodes geometries are shown for a radius of 80 Å and a molar concentration of 0.001 M and 0.01 M. It is found that when the radius is increased from 15 Å to 80 Å, the mean electrostatic potentials of the different electrode

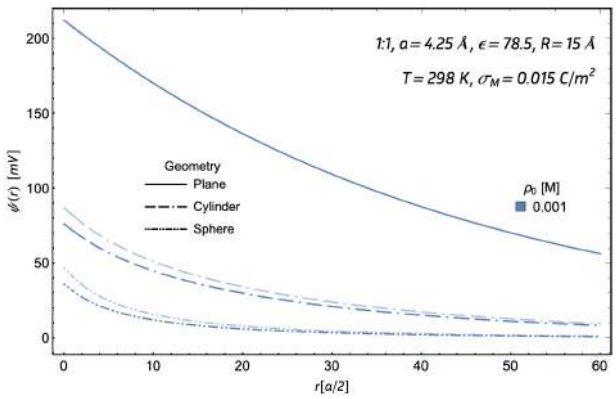


(a) $\psi(r)$ for $\rho_0 = 0.001\,\mathrm{M}$.

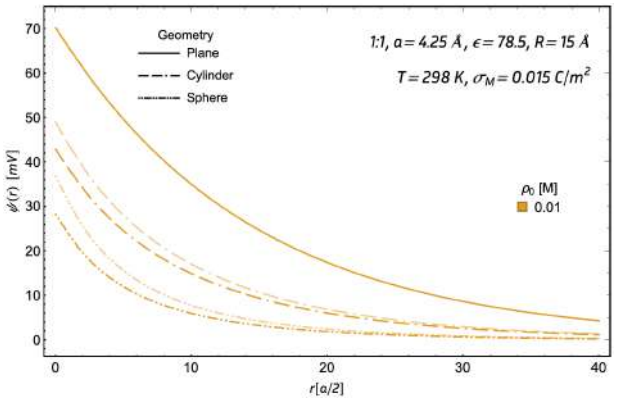


(b) $\psi(r)$ for $\rho_0 = 0.01\,\mathrm{M}$.

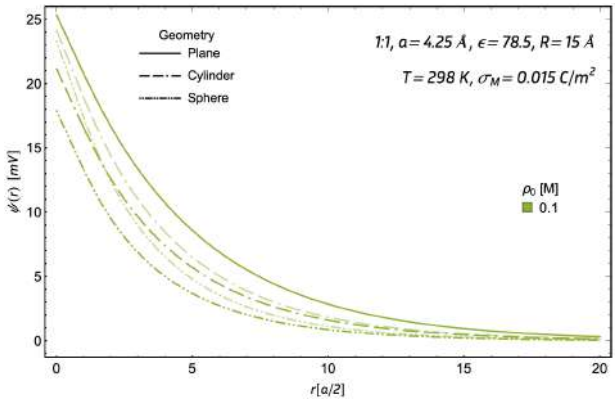


(c) $\psi(r)$ for $\rho_0 = 0.1\,\mathrm{M}$.

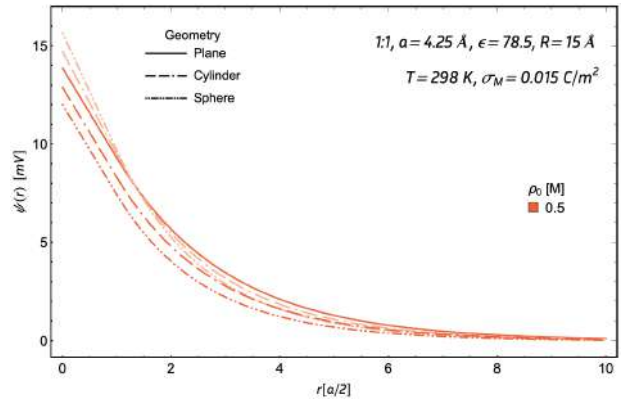


(d) $\psi(r)$ for $\rho_0 = 0.5\,\mathrm{M}$.

Figure 4.8: The linear mean electrostatic potential, $\psi(r)$, of different solid electrodes, with a radius of $15\,\text{Å} \cong 3.5\,\text{Å}$, while the electrolytes' molar concentration, $\rho_0$, is varied. The lighter and darker lines have the same meaning as in Fig. 4.3.

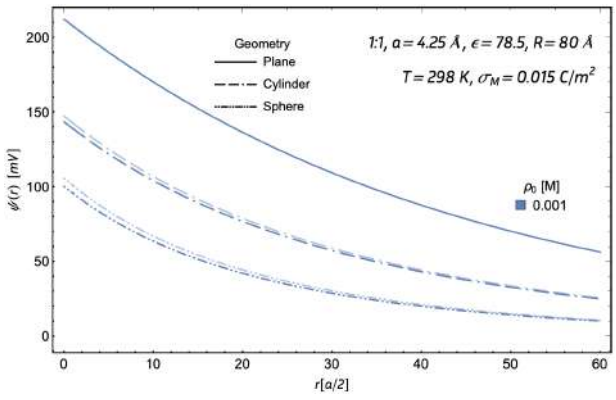


(a) $\psi(r)$ for $\rho_0 = 0.001\,\mathrm{M}$.

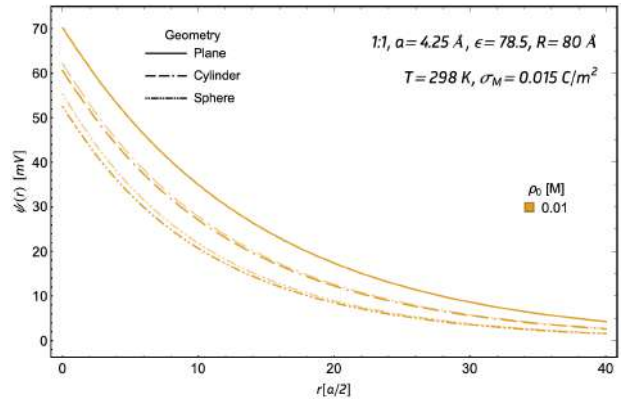


(b) $\psi(r)$ for $\rho_0 = 0.01\,\mathrm{M}$.

Figure 4.9: The linear mean electrostatic potential, $\psi(r)$, of different solid electrodes, with a radius of $5\,\text{Å} \cong 18.8\,\text{Å}$, while the electrolytes' molar concentration, $\rho_0$, is varied. The lighter and darker lines have the same meaning as in Fig. 4.3.

geometries increase rapidly. Therefore, from Figs. 4.7 to 4.9 we can observe two main things. The radius' size of the electrode is an important parameter to increase the mean electrostatic potential of the electrodes. On the other hand, a high electrolytes' molar concentration substantially decreases the mean electrostatic potential. Hence if one wishes to obtain high mean electrostatic potentials it is advisable to have a large radius and a low molar concentration.

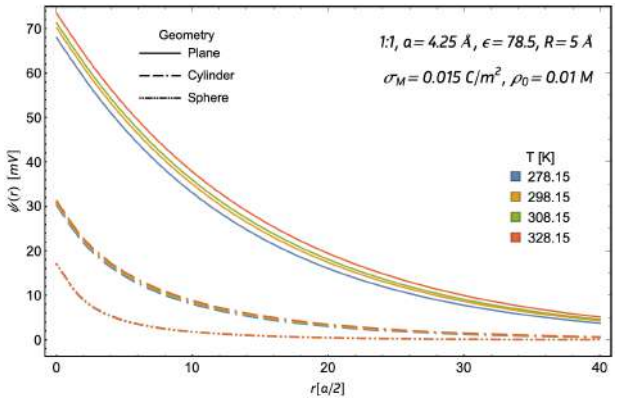


(a) $\psi(r)$ for $R = 5\,\text{Å}$.

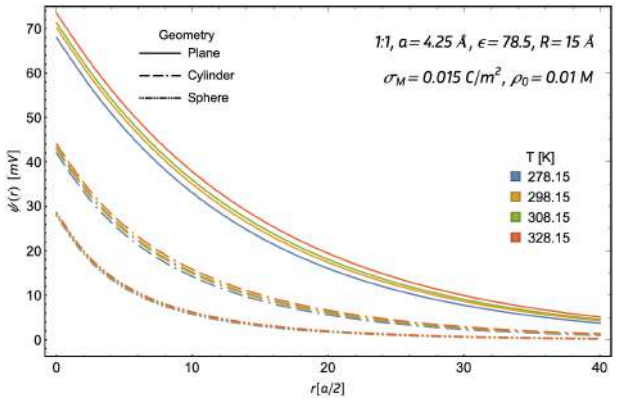


(b) $\psi(r)$ for $R = 15\,\text{Å}$.

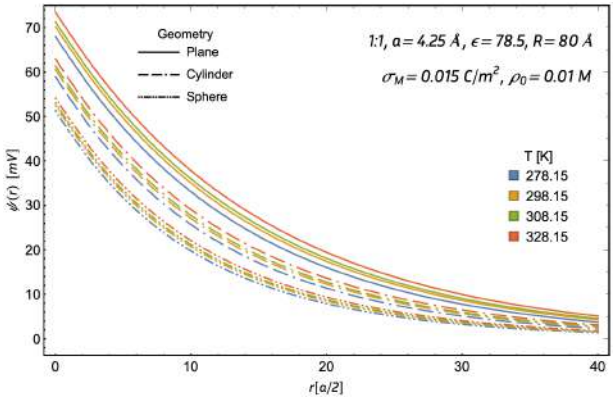


(c) $\psi(r)$ for $R = 80\,\text{Å}$.

Figure 4.10: The mean electrostatic potentials, $\psi(r)$, for the different geometries, for three radii, while the temperature, $T$, is varied.

Finally, in Fig. 4.10 the mean electrostatic potentials of the three solid electrodes are plotted while the temperature is varied, for our three radii. It is observed, that the mean electrostatic potential intensity and extension are directly proportional to the electrolyte's temperature. Nonetheless, it is found that the effect that the temperature has on the mean electrostatic potential is highly influenced by the value of the radius. For higher radius, the increase of the temperature has a higher impact on the mean electrostatic potentials, whereas for lower radius the increment of the temperature has a minimal effect on them. Therefore, it is observed that the planar electrode is the most influenced by the temperature, followed by the cylindrical electrode and lastly the spherical electrode. Furthermore, due to the small effect that the temperature has on the mean electrostatic potential, as seen from Eq. (2.7), there are almost no differences between the linear and non-linear planar electrode. In addition, the circumstances under which one would have extremely high or low temperatures are not a concern, since the electrolyte, being of aqueous base, would break or freeze on either case. Hence, it is reasonable

to assume that the temperature can safely be varied between over the freezing and under the boiling temperature of water.

### 4.1.2 The induced surface charge density of solid electrodes

Now, the results of the induced surface charge densities are shown for the different electrode's geometries. Firstly, we compare our linear and non-linear induced surface charge densities of a planar electrode. Secondly, a comparison between the induced surface charge densities of all the electrodes' geometries is performed when the radii size is varied. Finally, the influence that the electrode's surface charge density, and the electrolyte's molar concentration, and temperature play on the induced surface charge density for all the electrode's geometries, are studied.

Let us first give a little discussion on the induced surface charge density profile, $\sigma(r)$. From Eqs. (2.42) and (2.43), it is easy to see that

$$\sigma_M = -\int_{V(r=R+a/2)}^{\infty} \rho_{el}(\overrightarrow{\mathbf{y}})\,\mathrm{d}^3y = -\int_{V(r=R+a/2)}^{V(r)} \rho_{el}(\overrightarrow{\mathbf{y}})\,\mathrm{d}^3y - \int_{V(r)}^{\infty} \rho_{el}(\overrightarrow{\mathbf{y}})\,\mathrm{d}^3y, \tag{4.1}$$

where $\sigma_M$ is the electrode's given surface charge. Thus,

$$\frac{\varepsilon}{4\,\pi}\,E(r) = \sigma(r) = \sigma_M + \int_{V(r=R+a/2)}^{V(r)} \rho_{el}(\overrightarrow{\mathbf{y}})\,\mathrm{d}^3y = -\int_{V(r)}^{\infty} \rho_{el}(\overrightarrow{\mathbf{y}})\,\mathrm{d}^3y \tag{4.2}$$

Hence, for $r = R + a/2$, $\sigma(r)$, indeed reduces to $\sigma_M$. For the planar electrode Eqs. (4.1) and (4.2) reduce to Eqs. (A.9) and (A.12), respectively.

#### 4.1.2.1 The linear and non-linear induced surface charge density of a solid planar electrode

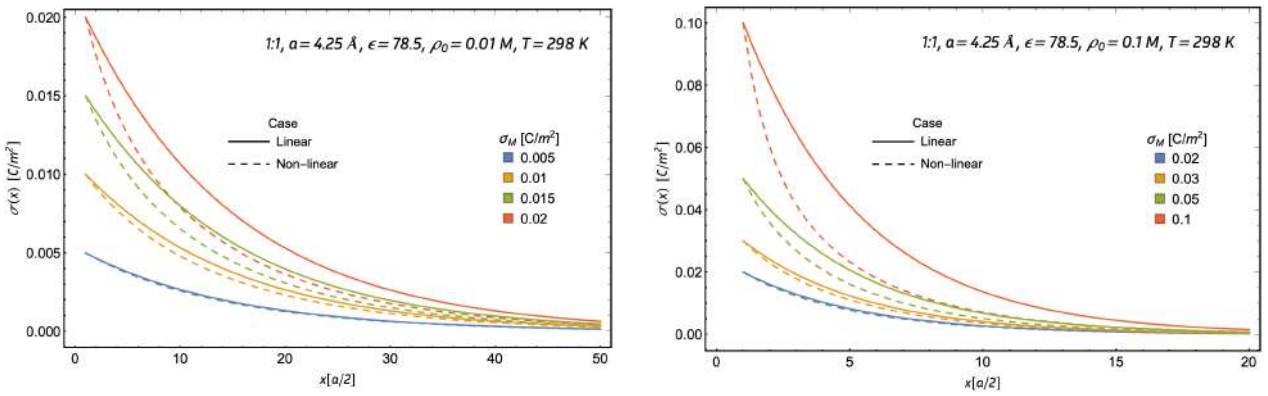


(a) $\sigma(x)$ for $\rho_0 = 0.01\,\mathrm{M}$. (b) $\sigma(x)$ for $\rho_0 = 0.1\,\mathrm{M}$.

Figure 4.11: The linear and non-linear induced surface charge density, $\sigma(x)$, of a solid electrode for different electrode's surface charge density, $\sigma_M$. The linear and non-linear induced surface charge densities are represented by a solid and a dashed line, respectively.

The linear and non-linear induced surface charge densities of the planar electrode are plotted for different electrode's surface charges in Fig. 4.11. It is observed that, for both the linear and non-linear cases, the contact value of the induced surface charge density is equal to the electrode's surface charge density, as it should be, according with the above discussion. Furthermore, when the linear and

non-linear induced surface charge densities are compared it is found that our linear induced surface charge density is a good approximation of the non-linear one up to electrodes' surface charge densities

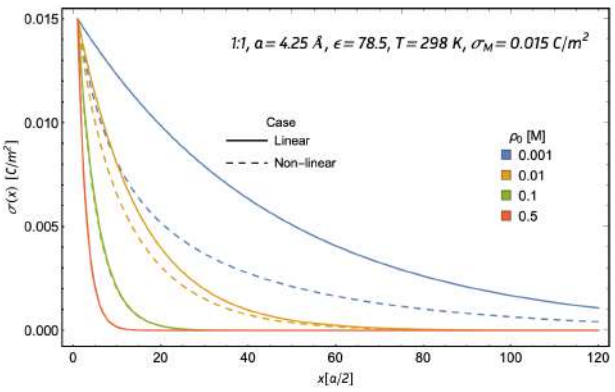


(a) $\sigma(x)$ for $\sigma_{_M} = 0.015\,\mathrm{C/m^2}$.

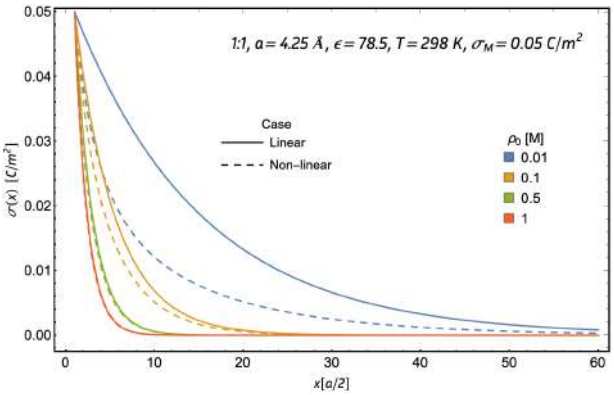


(b) $\sigma(x)$ for $\sigma_{_M} = 0.05\,\mathrm{C/m^2}$.

Figure 4.12: The linear and non-linear induced surface charge density, $\sigma(x)$, of a solid planar electrode while the electrolyte's molar concentration, $\rho_0$, is varied. The solid and dashed lines have the same meaning as in Fig. 4.11.

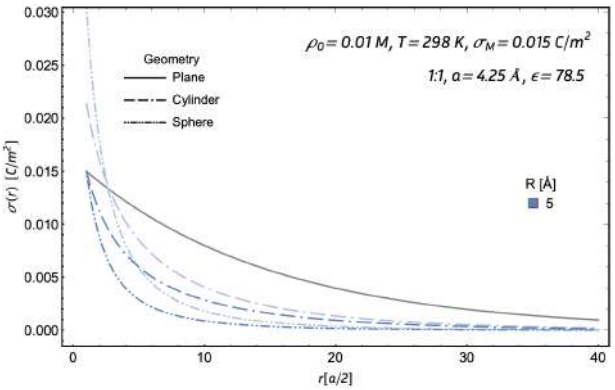


(a) $\sigma(r)$ for $R = 5\,\text{Å} \cong 1.2\,\text{Å}$.

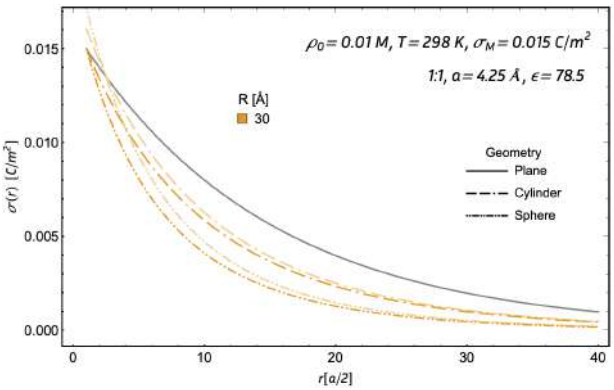


(b) $\sigma(r)$ for $R = 30\,\text{Å} \cong 7.1\,\text{Å}$.

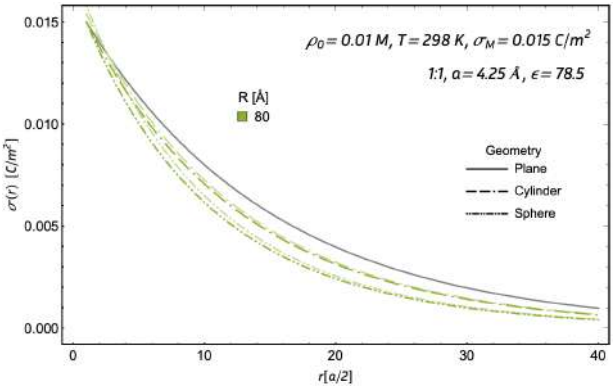


(c) $\sigma(r)$ for $R = 80\,\text{Å} \cong 18.8\,\text{Å}$.

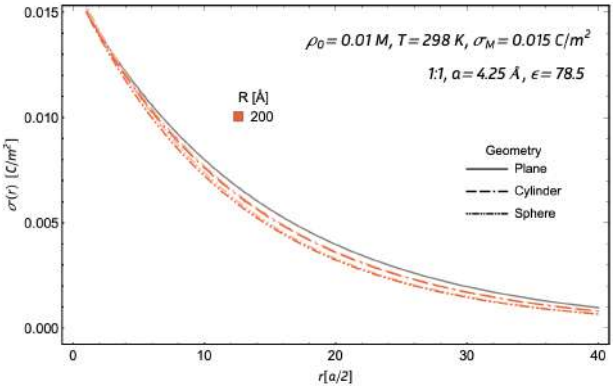


(d) $\sigma(r)$ for $R = 200\,\text{Å} \cong 47.1\,\text{Å}$.

Figure 4.13: The linear induced surface charge densities, $\sigma(r)$, of the solid electrodes, for different radii values. The lighter and darker lines represent two distinct cases, when equal electric fields and surface charges are used.

of $0.015\,\mathrm{C/m^2}$ and $0.05\,\mathrm{C/m^2}$ at molar concentrations of 0.01 M and 0.1 M, respectively. When the electrodes' surface charge densities exceed these values, our linear solutions of the induced surface charge densities overestimate $\sigma(x)$.

Of course, in Fig. 4.11 the upper limits of the electrodes' surface charge densities are $0.015\,\mathrm{C/m^2}$ and $0.05\,\mathrm{C/m^2}$ at molar concentrations of 0.01 M and 0.1 M. We now proceed to find the interval of validity of the electrolytes' molar concentration. Consequently, in Fig. 4.12 these electrodes' surface charges are used while the electrolyte's concentration is varied. It is found that our linear induced surface charge density is a good approximation of its non-linear counterpart for electrolytes' molar concentrations higher than or equal to 0.01 M and 0.1 M, for their respective electrodes' surface charges $0.015\,\mathrm{C/m^2}$ and $0.05\,\mathrm{C/m^2}$. Therefore, it is visualized that the linear induced surface charge density can tolerate a high electrode's surface charge and electrolyte's molar concentration without loosing validity against its non-linear analogue.

#### 4.1.2.2 The induced surface charge density of different solid electrodes

From here forward, unless stated otherwise, only the induced surface charge density of our LPBS is shown. We start with a comparison of the induced surface charge density of the different solid electrodes, for various radii. Therefore in Fig. 4.13 these induced surface charge densities are shown for two different cases, when equal electric fields and surface charges are used.

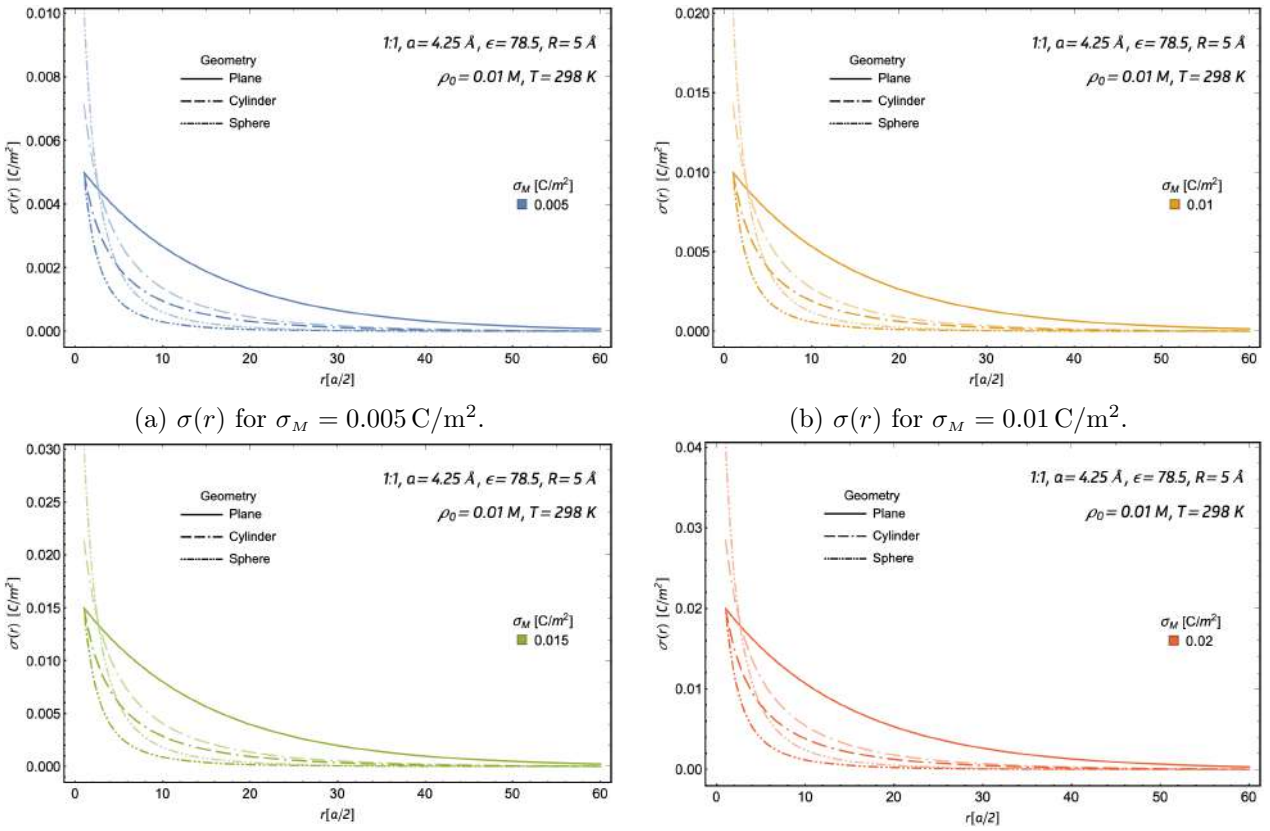


(a) $\sigma(r)$ for $\sigma_M = 0.005\,\mathrm{C/m^2}$.

(b) $\sigma(r)$ for $\sigma_M = 0.01\,\mathrm{C/m^2}$.

(c) $\sigma(r)$ for $\sigma_M = 0.015\,\mathrm{C/m^2}$.

(d) $\sigma(r)$ for $\sigma_M = 0.02\,\mathrm{C/m^2}$.

Figure 4.14: The linear induced surface charge densities, $\sigma(r)$, of solid electrodes. A radius of 5 Å $\cong$ 1.2 a is used, while the electrode's surface charge density, $\sigma_M$, is varied. The lighter and darker lines have the same meaning as Fig. 4.13.

In Fig. 4.13 it is observed that for all the electrodes geometries, the contact induced surface charge density is the same value. This is true when the surface charge densities are equal between the electrodes' geometry, regardless of the radii used. Whereas, for the case of equal electric fields, the spherical electrode achieves the highest contact values of the induced surface charge density, followed by the cylindrical electrode and lastly by the planar electrode, no matter the radii used. Furthermore, it is observed that the highest deviations of the induced surface charge density between the equal electric field and surface charge density cases are obtained for the lowest radius, as a result of the higher charge given to the spherical and cylindrical electrodes, in order to match the same electric fields. For the highest radius it is found that both cases of the cylindrical and spherical electrodes tend to the values of the induced surface charge density of the planar electrode as expected, since the higher the radius the closer the electric field becomes to that of a plate. Even though the contact values of the induced surface charge density of the spherical and cylindrical electrodes are higher than those of the planar electrode, when low radii and equal electric fields are used, it is observed that the later still has a thicker electrical double layer than their counterparts. This is due to the geometry of the spherical and cylindrical electrodes and their size, as they are capable of gathering most of the available charge at their small surface, so when the distance from the surface is increased there is only a small amount of free charge. Therefore, when the radius is increased they loose the capability of gathering as much charge, as before, close to the electrodes' surface, and consequently they have more charge available away from the electrode's surface.

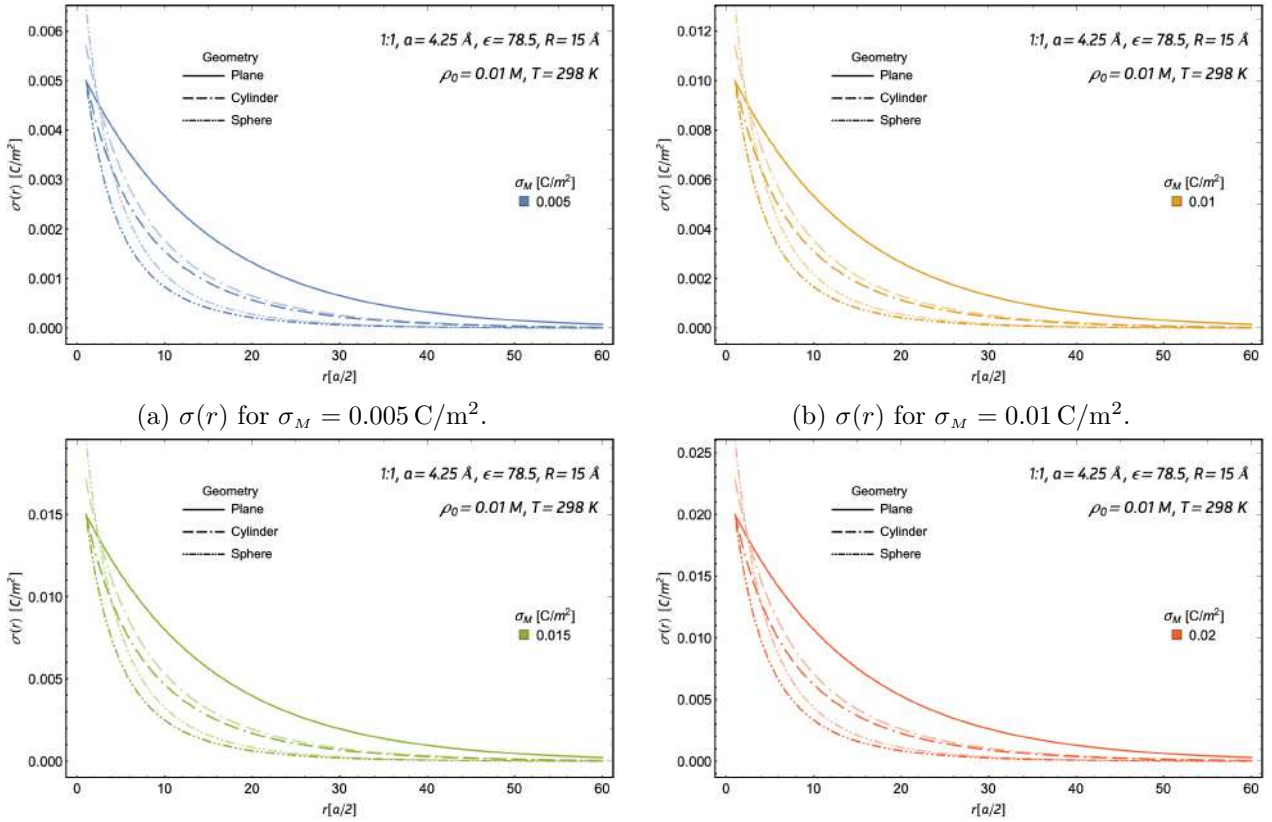


(a) $\sigma(r)$ for $\sigma_M = 0.005\,\mathrm{C/m^2}$.

(b) $\sigma(r)$ for $\sigma_M = 0.01\,\mathrm{C/m^2}$.

(c) $\sigma(r)$ for $\sigma_M = 0.015\,\mathrm{C/m^2}$.

(d) $\sigma(r)$ for $\sigma_M = 0.02\,\mathrm{C/m^2}$.

Figure 4.15: The linear induced surface charge densities, $\sigma(r)$, of solid electrodes. A radius of $15\,\text{Å} \cong 3.5\,\mathrm{a}$ is used, while the electrode's surface charge density, $\sigma_M$, is varied. The lighter and darker lines have the same meaning as Fig. 4.13.

Whence, as seen in Fig. 4.13 if we wish to observe the influence that the electrode's surface charge density, and the electrolyte's molar concentration and temperature have on the induced surface charge density, we must choose a fixed radius. Therefore, as we are interested in small electrodes, we will choose three different radii, 5 Å, 15 Å and 80 Å, to observe the collective impact that the cylindrical and spherical electrodes radius with the other parameters have on the induced surface charge density.

In Fig. 4.14 the induced surface charge density of the solid electrodes with a radius of 5 Å is shown, while the electrodes' surface charge density is increased. These induced surface charge densities are plotted for two cases, when equal electric fields and surface charges are used. It is found that the equal electric field case achieves higher contact values than the equal surface charge case. And that both induced surface charge densities are directly proportional to $\sigma_M$. Furthermore, it is clearly observed that when the electrodes' surface charge density increases so does the global extension of the induced surface charge density regardless of the case.

Continuously, in Fig. 4.15 the induced surface charge density of the solid electrodes with a radius of 15 Å is shown, while the electrodes' surface charge density is increased. These induced surface charge densities are plotted for two cases, when equal electric fields and surface charges are used. It is found that when the radius is increased from 5 Å to 15 Å the induced surface charge density for equal surface charges and electric fields, increases and decreases respectively. Therefore, the biggest differences between both cases are shown for low radii, as could be expected.

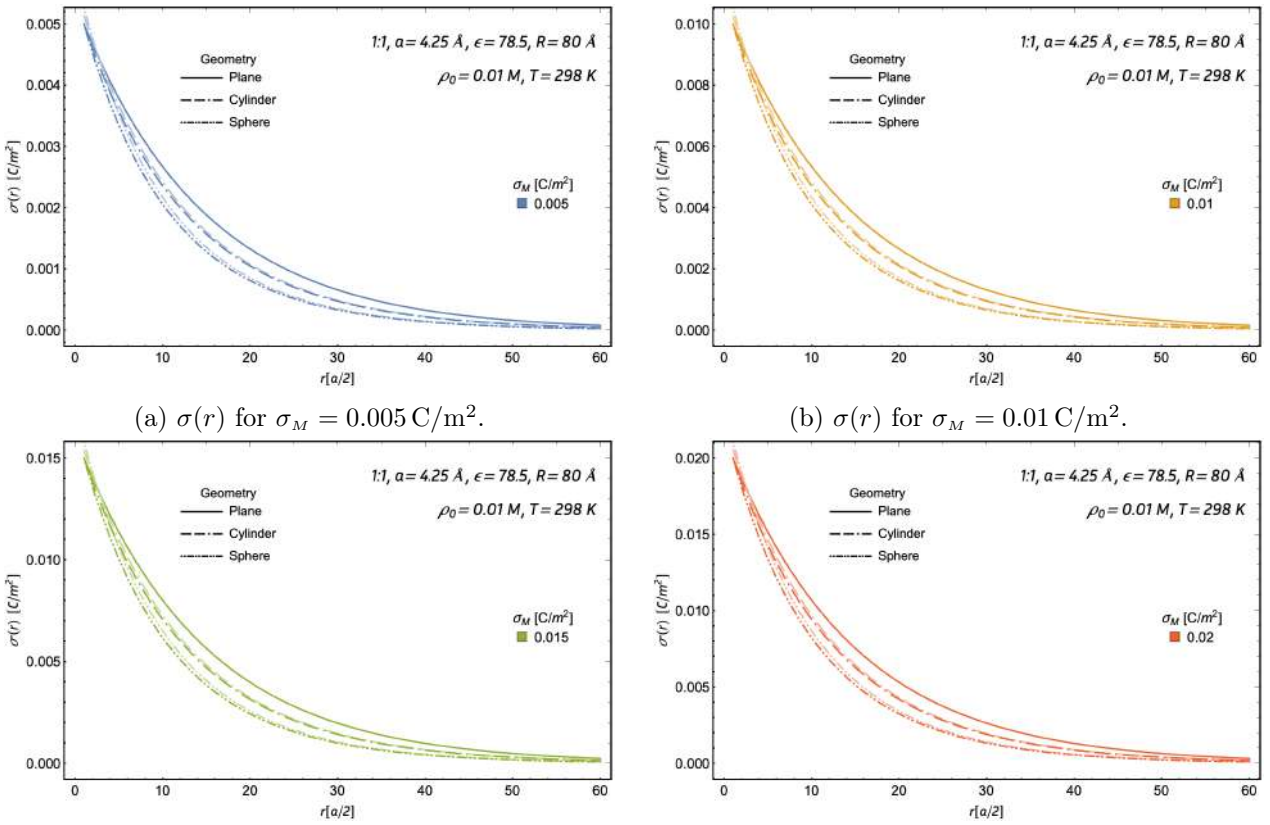


(a) $\sigma(r)$ for $\sigma_M = 0.005\,\mathrm{C/m^2}$.

(b) $\sigma(r)$ for $\sigma_M = 0.01\,\mathrm{C/m^2}$.

(c) $\sigma(r)$ for $\sigma_M = 0.015\,\mathrm{C/m^2}$.

(d) $\sigma(r)$ for $\sigma_M = 0.02\,\mathrm{C/m^2}$.

Figure 4.16: The linear induced surface charge densities, $\sigma(r)$, of solid electrodes. A radius of 80 Å $\cong$ 18.8 a is used, while the electrode's surface charge density, $\sigma_M$, is varied. The lighter and darker lines have the same meaning as Fig. 4.13.

In Fig. 4.16 the induced surface charge density of the solid electrodes is shown now for a radius

of 80 Å, for different electrodes' surface charge densities. These induced surface charge densities are plotted for two cases, when equal electric fields and surface charges are used. Again, it is found that when the radius is increased from 15 Å to 80 Å the contact value of the induced surface charge density for equal surface charges and electric fields, increases and decreases respectively. Moreover, as the radius of 80 Å is large enough, the induced surface charge of both cases tends to the same value since the electric field influence blurs.

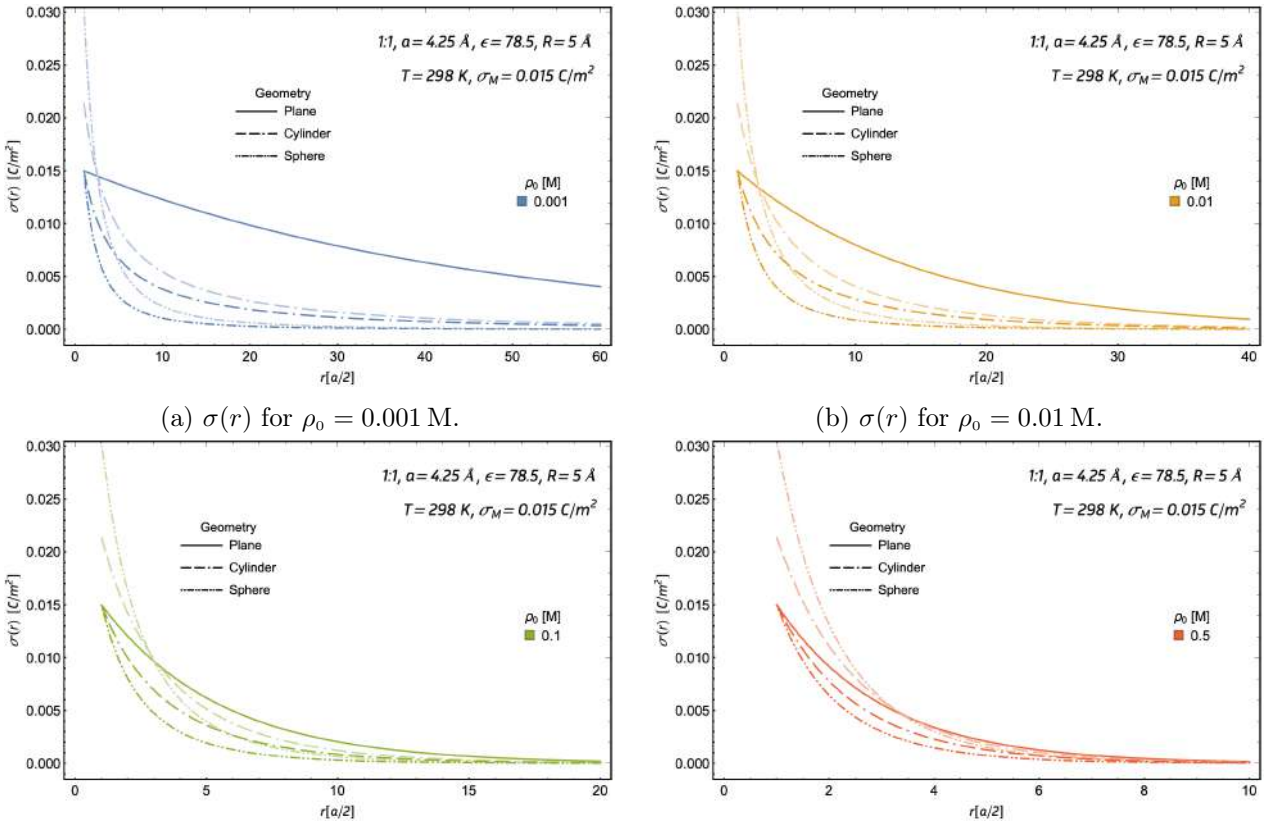


(a) $\sigma(r)$ for $\rho_0 = 0.001\,\mathrm{M}$.

(b) $\sigma(r)$ for $\rho_0 = 0.01\,\mathrm{M}$.

(c) $\sigma(r)$ for $\rho_0 = 0.1\,\mathrm{M}$.

(d) $\sigma(r)$ for $\rho_0 = 0.5\,\mathrm{M}$.

Figure 4.17: The linear induced surface charge densities, $\sigma(r)$, of solid electrodes. A radius of 5 Å $\cong$ 1.2 Å is used, while the electrolyte's molar concentration, $\rho_0$, increases. The lighter and darker lines have the same meaning as Fig. 4.13.

Now, in the following figures we will show the induced surface charge density of our three radii, 5 Å, 15 Å and 80 Å, while the electrolyte's molar concentration is increased, for our two cases, when equal electric fields and surface charges are used. In Fig. 4.17, the induced surface charge density of our three solid electrodes are shown for different molar concentrations, with an electrode's surface charge density of $0.015\,\mathrm{C/m^2}$, and a radius of 5 Å. It is found that as the molarity is increased, the intensity and extension of the induced surface charge density decreases, for both cases. It is also found that for the highest electrolytes' molar concentration, 0.5 M, the induced surface charge density of the case of equal electric fields is not only higher at its contact value, but has even higher values of the overall induced surface charge than the case of equal surface charges. Furthermore, it is also observed that the induced surface charge of the planar electrode decreases more rapidly than its other counterparts when the molar concentration is increased. For this reason, when the molar concentration is increased, the cylindrical and spherical electrodes tend to quickly reassemble the induced surface charge density of the planar electrode. The higher the bulk concentration, the thinner the electrical

double layer becomes, and, in a way it is somewhat equivalent to have a larger radius for the spherical and cylindrical electrodes.

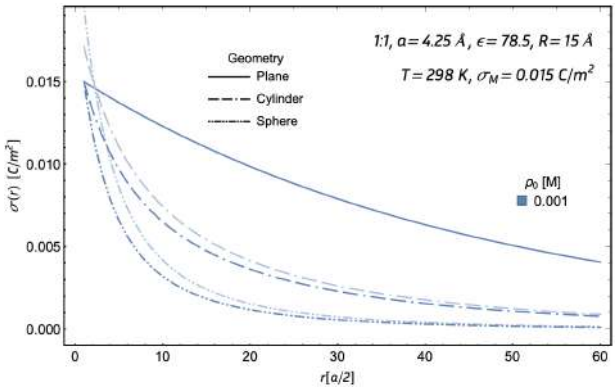


(a) $\sigma(r)$ for $\rho_0 = 0.001\,\mathrm{M}$.

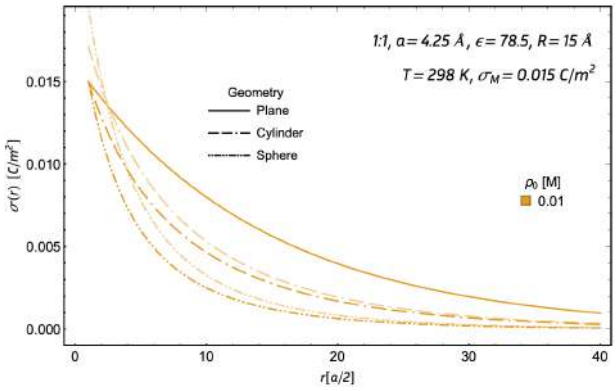


(b) $\sigma(r)$ for $\rho_0 = 0.01\,\mathrm{M}$.

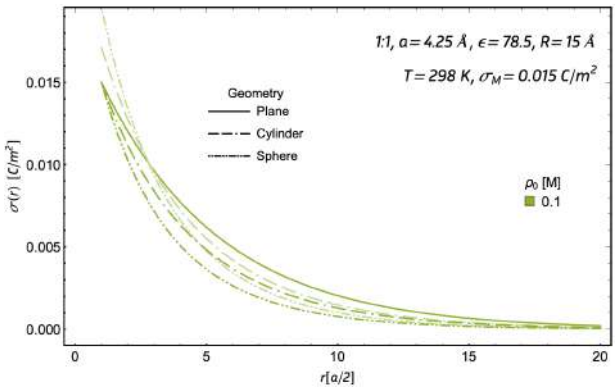


(c) $\sigma(r)$ for $\rho_0 = 0.1\,\mathrm{M}$.

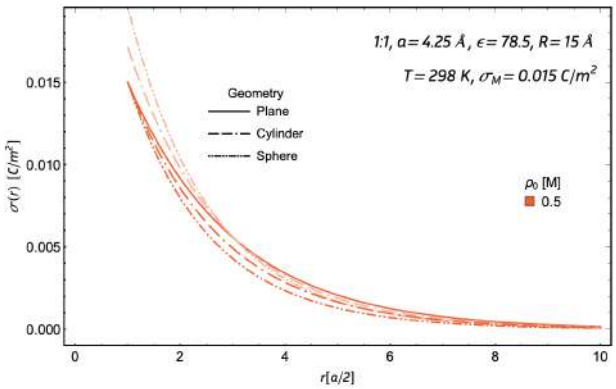


(d) $\sigma(r)$ for $\rho_0 = 0.5\,\mathrm{M}$.

Figure 4.18: The linear induced surface charge densities, $\sigma(r)$, of solid electrodes. A radius of $15\,\text{Å} \cong 3.5\,\text{Å}$ is used, while the electrolyte's molar concentration, $\rho_0$, increases. The lighter and darker lines have the same meaning as Fig. 4.13.

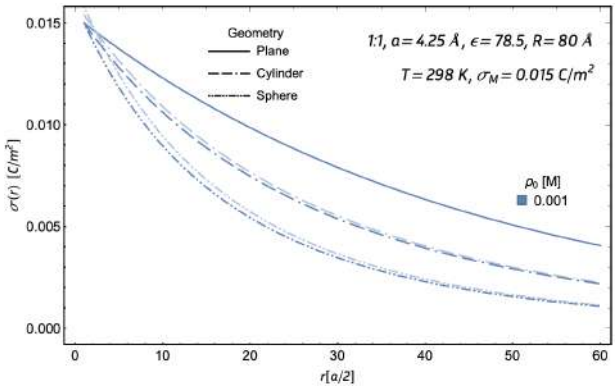


(a) $\sigma(r)$ for $\rho_0 = 0.001\,\mathrm{M}$.

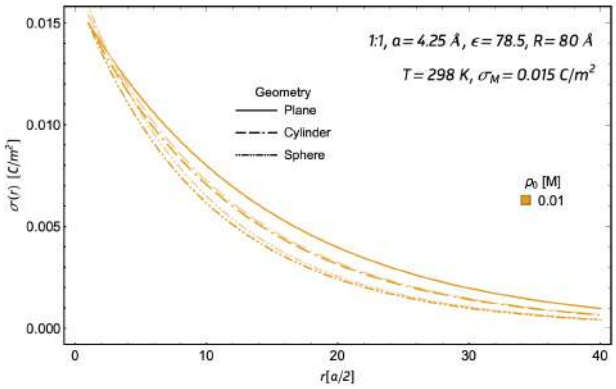


(b) $\sigma(r)$ for $\rho_0 = 0.01\,\mathrm{M}$.

Figure 4.19: The linear induced surface charge densities, $\sigma(r)$, of solid electrodes. A radius of $80\,\text{Å} \cong 18.8\,\text{Å}$ is used, while the electrolyte's molar concentration, $\rho_0$, increases. The lighter and darker lines have the same meaning as Fig. 4.13.

In Fig. 4.18 the induced surface charge densities are shown for the three solid electrodes with a radius of 15 Å and an electrode's surface charge density $0.015\,\mathrm{C/m^2}$. It is observed that when the radius increases from 5 Å to 15 Å, as expected, the contact values of the induced surface charge density of the cylindrical and spherical electrodes, for equal electric fields and surface charges, decrease and increase, respectively. Furthermore, as noted before in Fig. 4.17, the values of the induced surface charge density of the planar electrode decrease more rapidly than those of the cylindrical and spherical electrodes, when the molar concentration increases. Therefore, for the highest molar concentrations with equal surface charges, the induced surface charge densities tend to the planar electrodes' results. On the other hand, when equal electric fields are used this tendency is not as marked, as both cases are still recognizable.

Figure 4.19 shows the induced surface charge densities for the three solid electrodes while the molar concentration is increased, when a radius of 80 Å and an electrodes' surface charge density of $0.015\,\mathrm{C/m^2}$ are used. These induced surface charge densities are plotted when equal electric fields and surface charges are used. Again, it is found that when the radius increases, now from 15 Å to 80 Å, the induced surface charge density of the cylindrical and spherical electrodes increases as well. Furthermore, as it was observed from Fig. 4.18 if the molar concentration is large enough, and so is the radius, the induced surface charge density of the cylindrical and spherical electrodes tend to the plane electrode values, for both the equal electric fields and surface charges cases. Therefore, in Fig. 4.19

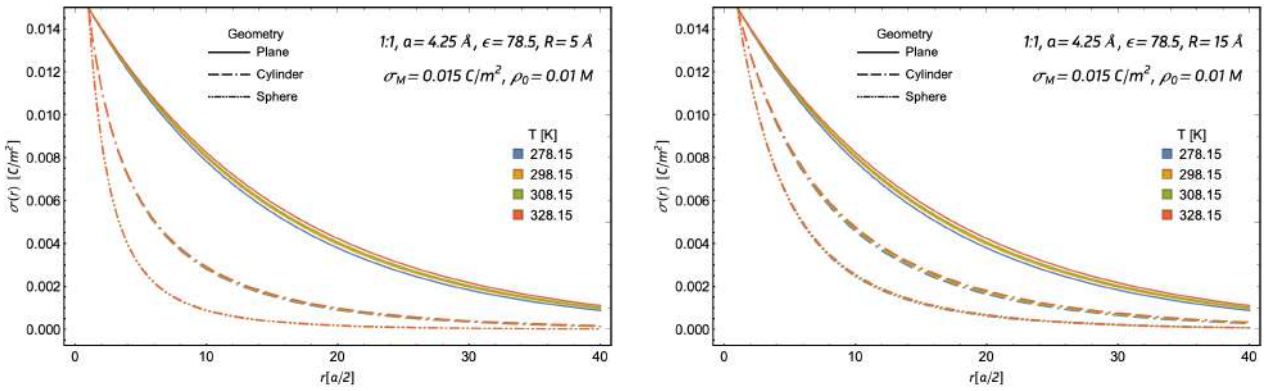


(a) $\sigma(r)$ for $R = 5\,\text{Å} \cong 1.2\,\text{a}$.




(b) $\sigma(r)$ for $R = 15\,\text{Å} \cong 3.5\,\text{a}$.

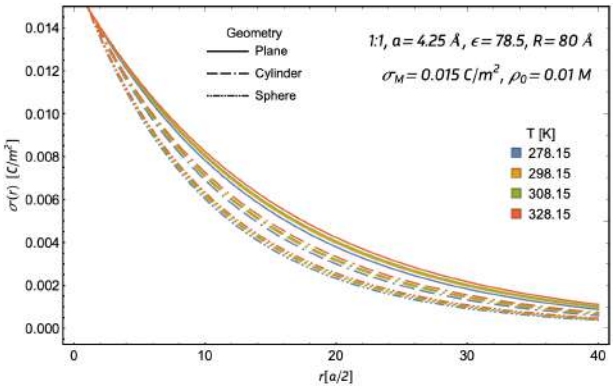


(c) $\sigma(r)$ for $R = 80\,\text{Å} \cong 18.8\,\text{a}$.

Figure 4.20: The linear induced surface charge densities, $\sigma(r)$, of solid electrodes, while the electrolyte's temperature, $T$, is varied. The lighter and darker lines have the same meaning as Fig. 4.13.

we do not include the higher molar concentrations as they overlap with the induced surface charge densities of the planar electrode.

Finally, in Fig. 4.20 the induced surface charge densities of the three solid electrodes are plotted while the temperature is varied, for our three radii. It is found that the extension of the induced surface charge density is directly proportional to the electrolyte's temperature, as the contact value of the induced surface charge density is the same for all the geometries. However, the effect that the temperature has on the induced surface charge density is highly influenced by the radius size. As for low radii, the raise of the induced surface charge density when the temperature increases is not as marked as for high radii. Moreover, it is seen that the electrolyte's temperature is the studied parameter with less impact on the induced surface charge density of the electrodes' geometry.

### 4.1.3 The differential capacitance of solid electrodes

Lastly, the results of the differential capacitances are obtained for the different electrode's geometries, unless stated otherwise, they are obtained for a monovalent electrolyte (1:1) with a dielectric constant of 78.5, a molar concentration of 0.01 M, and a temperature of 298.15 K. The linear and non-linear differential capacitances of the solid planar electrode are calculated from Eqs. (2.16) and (2.23). The main difference between the linear and non-linear differential capacitances is that the latter depends on the electrode's surface charge density, $\sigma_M$, whereas the other one does not. Therefore, in Table 4.1 and Fig. 4.21 the linear and non-linear differential capacitances are calculated, while the electrolyte's molar concentration increases. Consequently, for the linear case only the dependence on the electrolyte's molar concentration is shown, while for the non-linear one the dependence on the electrolyte's molar concentration and on the electrode's surface charge are shown. From, Table 4.1 and Fig. 4.21 it is found that the our linear differential capacitance is, in general, a very good approximation of the non-linear one when low electrode's surface charges are used, except for $\rho_0 = 0.001\,\mathrm{M}$, and $\sigma_M \geq 0.005 \frac{\mathrm{C}}{\mathrm{m}^2}$.

| $\rho_0$ [M] | Linear | Non-linear | | | |
|---|---|---|---|---|---|
| | | $\sigma_M \left[\frac{\mathrm{C}}{\mathrm{m}^2}\right]$ 0.005 | 0.01 | 0.015 | 0.02 |
| 0.001 | 0.036 | 0.060 | 0.103 | 0.149 | 0.196 |
| 0.01 | 0.110 | 0.120 | 0.145 | 0.179 | 0.218 |
| 0.1 | 0.325 | 0.328 | 0.337 | 0.351 | 0.369 |
| 0.5 | 0.648 | 0.649 | 0.652 | 0.658 | 0.666 |

Table 4.1: The linear and non-linear differential capacitances, $C_T\,[\mathrm{F/m^2}]$, of a planar electrode for different electrolyte's molar concentrations, $\rho_0$.

In Table 4.2 and Fig. 4.22 the linear and non-linear differential capacitances of a planar electrode are calculated while the electrolyte's temperature is varied, for a molar concentration of 0.01 M. Once again, the non-linear dependence on the electrode's surface charge density is shown. Therefore, from Table 4.2 and Fig. 4.22 it is found that conversely to the mean electrostatic potentials and the induced surface charge density, the differential capacitance is inversely proportional to the temperature. When the temperature increases, the differential capacitance drops. However, it is observed that for the linear differential capacitance as well as for the non-linear one with low electrode's surface charge, the temperature's effect on the differential capacitance is minimal.

Therefore, from Tables 4.1 and 4.2 and Figs. 4.21 and 4.22 it is found that the only restriction that our linear solution of the differential capacitance has against the non-linear one, is that at very low electrolyte concentration, the electrode's surface charge density should be lower or equal than $0.005\,\mathrm{C/m^2}$.

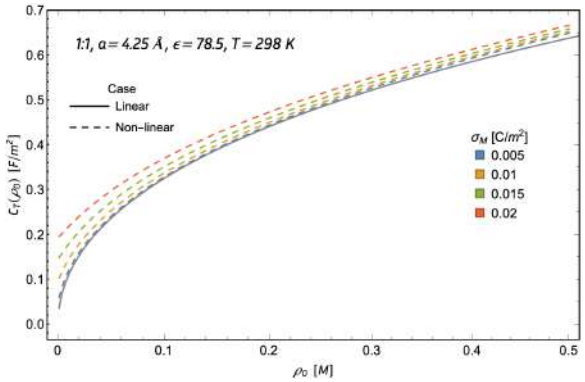


Figure 4.21: The linear and non-linear differential capacitances, $C_T$, of a planar electrode against the electrolyte's molar concentration, $\rho_0$.

| $T$ [K] | Linear | Non-linear | | | |
|---|---|---|---|---|---|
| | | $\sigma_M \left[\frac{\text{C}}{\text{m}^2}\right]$ 0.005 | 0.01 | 0.015 | 0.02 |
| 278.15 | 0.114 | 0.125 | 0.152 | 0.189 | 0.231 |
| 298.15 | 0.110 | 0.120 | 0.145 | 0.179 | 0.218 |
| 308.15 | 0.109 | 0.118 | 0.142 | 0.174 | 0.212 |
| 328.15 | 0.105 | 0.114 | 0.136 | 0.166 | 0.201 |

Table 4.2: The linear and non-linear differential capacitances, $C_T$ [F/m$^2$], of a planar electrode, while varying the electrolyte's temperature. In all cases, $\rho_0 = 0.01M$.

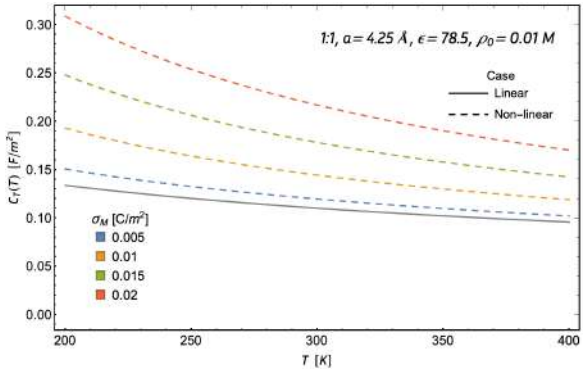


Figure 4.22: The linear and non-linear differential capacitance, $C_T$, of a planar electrode against the electrolyte's temperature, $T$.

When this restriction is followed, our linear differential capacitance is a good approximation of the non-linear one, regardless of the electrolyte's molar concentration or temperature.

In Fig. 4.23 and Table 4.3 the differential capacitanes of solid cylindrical and spherical electrodes are obtained for four radii, 5 Å, 15 Å, 30 Å and 80 Å, while varying the electrolyte's molar concentration. It is found that the highest differential capacitance for solid electrodes, is achieved for a small spherical electrode, followed by a small cylindrical electrode. Furthermore, as the radius increases for both the cylindrical and spherical electrodes, their differential capacitances become more alike. And for high a enough radius, 80 Å, both electrodes tend to the differential capacitance of the planar electrode.

| | $R = 5\,\text{Å} \cong 1.2\,\text{a}$ | | $R = 15\,\text{Å} \cong 3.5\,\text{a}$ | | $R = 30\,\text{Å} \cong 7.1\,\text{a}$ | | $R = 80\,\text{Å} \cong 18.8\,\text{a}$ | |
|---|---|---|---|---|---|---|---|---|
| $\rho_0$ [M] | Cylinder | Sphere | Cylinder | Sphere | Cylinder | Sphere | Cylinder | Sphere |
| 0.001 | 0.168 | 0.452 | 0.101 | 0.223 | 0.075 | 0.138 | 0.053 | 0.077 |
| 0.01 | 0.264 | 0.508 | 0.185 | 0.289 | 0.153 | 0.208 | 0.129 | 0.149 |
| 0.1 | 0.481 | 0.674 | 0.398 | 0.481 | 0.366 | 0.410 | 0.342 | 0.359 |
| 0.5 | 0.782 | 0.928 | 0.708 | 0.772 | 0.681 | 0.716 | 0.661 | 0.675 |

Table 4.3: The linear differential capacitances, $C_T$ [F/m$^2$], of the cylindrical and spherical electrodes, for different radii, while the electrolyte's molar concentration, $\rho_0$, is varied.

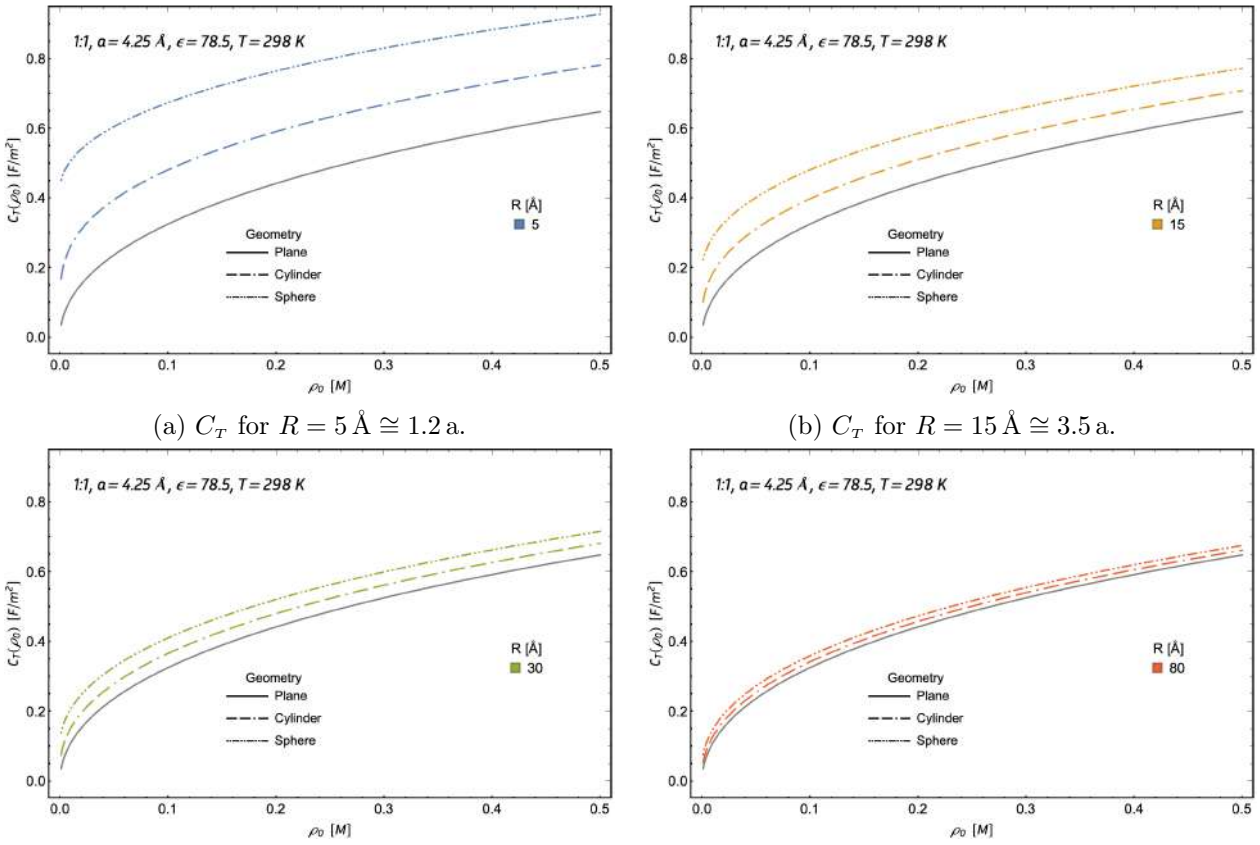


(a) $C_T$ for $R = 5\,\text{Å} \cong 1.2\,\text{a}$.

(b) $C_T$ for $R = 15\,\text{Å} \cong 3.5\,\text{a}$.

(c) $C_T$ for $R = 30\,\text{Å} \cong 7.1\,\text{a}$.

(d) $C_T$ for $R = 80\,\text{Å} \cong 18.8\,\text{a}$.

Figure 4.23: The linear differential capacitances, $C_T$, of solid electrodes against the molar concentration, $\rho_0$, for four radii.

In contrast, in Fig. 4.24 and Table 4.4 the linear differential capacitance of solid cylindrical and spherical electrodes are obtained for four radii, 5 Å, 15 Å, 30 Å and 80 Å, while the electrolyte's temperature is varied. Once again, it is found that the differential capacitance is inversely proportional to the electrolyte's temperature, and electrode's size. Therefore, to enhance the differential capacitance, the optimal geometry is a small spherical electrode at a high electrolyte's molar concentration, and with a low temperature.

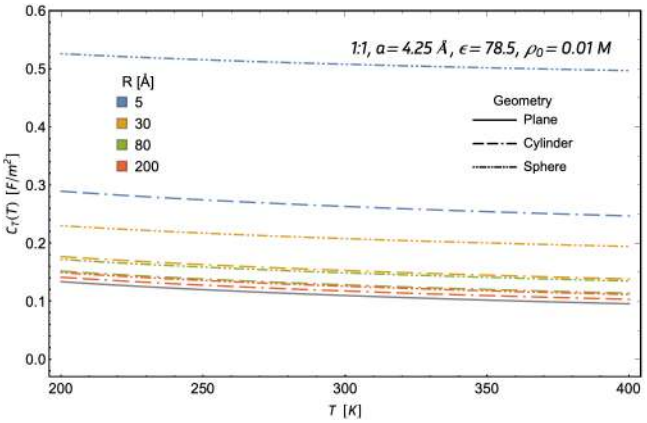


Figure 4.24: The linear differential capacitance, $C_T$, of solid electrodes against the temperature, $T$, for different radii.

| | $R = 5\,\text{Å} \cong 1.2\,\text{a}$ | | $R = 15\,\text{Å} \cong 3.5\,\text{a}$ | | $R = 30\,\text{Å} \cong 7.1\,\text{a}$ | | $R = 80\,\text{Å} \cong 18.8\,\text{a}$ | |
|---|---|---|---|---|---|---|---|---|
| $T$ [K] | Cylinder | Sphere | Cylinder | Sphere | Cylinder | Sphere | Cylinder | Sphere |
| 278.15 | 0.268 | 0.511 | 0.189 | 0.292 | 0.157 | 0.212 | 0.132 | 0.153 |
| 298.15 | 0.264 | 0.508 | 0.185 | 0.289 | 0.153 | 0.208 | 0.129 | 0.149 |
| 308.15 | 0.262 | 0.507 | 0.183 | 0.288 | 0.152 | 0.207 | 0.127 | 0.148 |
| 328.15 | 0.258 | 0.505 | 0.180 | 0.285 | 0.148 | 0.204 | 0.124 | 0.144 |

Table 4.4: The linear differential capacitances, $C_T$ [F/m$^2$], of a cylindrical and spherical electrodes for different radii, while the electrolyte's temperature, $T$, is varied.

## 4.2 The electrical double layer for different nano-pore electrodes geometries

In here, the electrical parameters obtained in Chapter 3 for different nano-pore electrode geometries are merged together in the following subsections. An analysis is performed between each topology to find out which one performs the best. This analysis is made considering that the inner and outer electrode's surface charge densities are the same, $\sigma = \sigma_I = \sigma_{II}$, and an electrode's constant pores' width of 5 Å is kept for all cases.

Firstly, the mean electrostatic potentials are plotted for our three nano-pores. A comparison of the mean electrostatic potential of the slit-pore, the cylindrical and spherical pores is made while the electrode's radii, and surface charge density, and the electrolyte's molar concentration, and temperature are varied. These variances are kept inside our interval of validity, found on Chapter 2.

Secondly, the induced surface charge densities are obtained for the three nano-pores. Identically, as for the mean electrostatic potentials, the electrode's radius, surface charge density, and the electrolyte's molar concentration, and temperature are given different values to observe their impact over the induced surface charge densities.

Lastly, the differential capacitances of the three nano-pores are calculated for different electrode's radii. These differential capacitances, are obtained while varying the electrolyte's molar concentration, and temperature. An analysis is performed to find out which topology maximizes the differential capacitance for each variable and electrode's radius.

As for the last section, unless stated otherwise, all our charts are obtained assuming that we are

dealing with an aqueous symmetric electrolyte (1:1) with an electric permittivity of 78.5, an ions' size of 4.25 Å and at a room temperature of 298 K.

### 4.2.1 The mean electrostatic potentials of nano-pore electrodes

In this subsection, the results of our mean electrostatic potentials are shown for different nano-pore electrode's geometries. Firstly, a comparison on the pore's radii influence over the mean electrostatic potentials is made in Fig. 4.25, for equal electric fields and surface charges. From it, two different tendencies between the cylindrical, and spherical nano-pores and the slit-pore are observed.

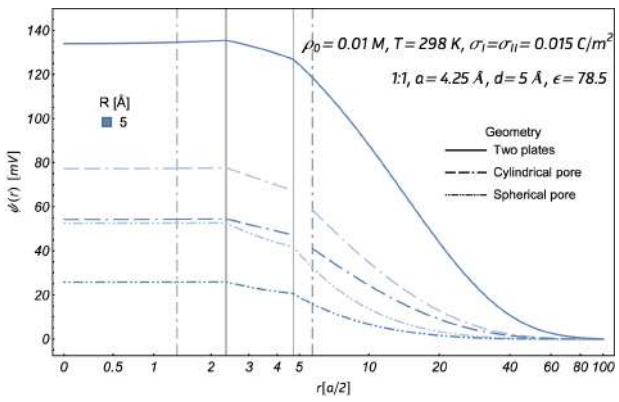


(a) $\psi(r)$ for $R = 5\,\text{Å} \cong 1.2\,\text{a}$.

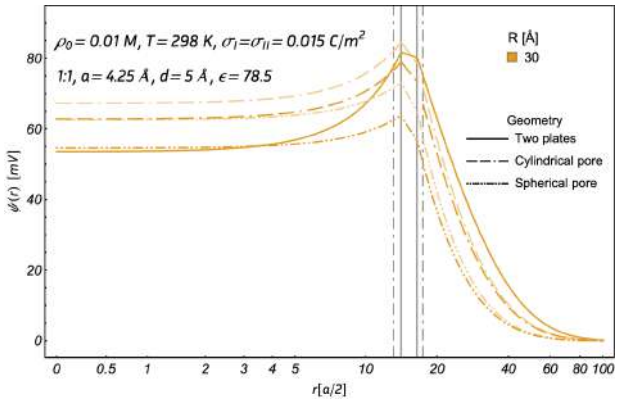


(b) $\psi(r)$ for $R = 30\,\text{Å} \cong 7.1\,\text{a}$.

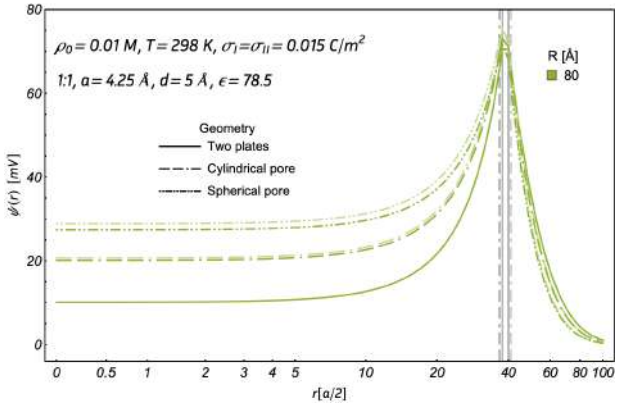


(c) $\psi(r)$ for $R = 80\,\text{Å} \cong 18.8\,\text{a}$.

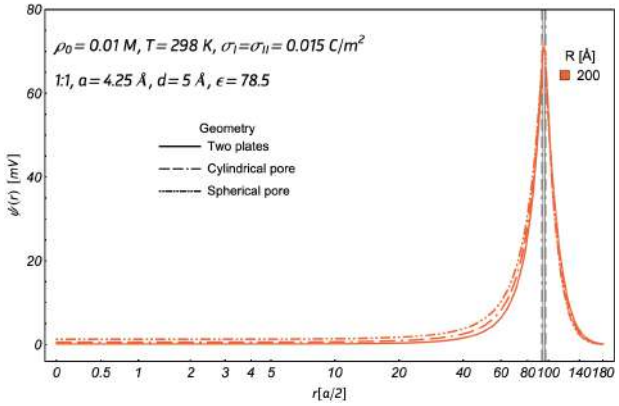


(d) $\psi(r)$ for $R = 200\,\text{Å} \cong 47.1\,\text{a}$.

Figure 4.25: The mean electrostatic potentials, $\psi(r)$, of the different nano-pores geometries, while the radius, $R$, is varied. The lighter and darker lines represent two distinct cases, when equal electric fields and surface charges are used. The vertical dashed and solid lines represent the OHP, and IHP.

On the one hand, for the slit-pore, the highest mean electrostatic potentials at the pore's center, $\psi_d$, is achieved for the lowest radius, as when the radii increases, $\psi_d$ decreases. On the other hand, for the cylindrical and spherical pores, an interesting tendency is found: $\psi_d$ shows a non-linear behavior with a increasing radius, at least in the case of constant surface charge. Therefore, both the cylindrical and spherical pores achieve a peak value for $\psi_d$ between a radius of 5 Å–30 Å, since at such radii the value of $\psi_d$ increases, and afterwards it decreases. Remarkably, when the radius reaches 200 Å, these different tendencies between pores overlap. At such radius, it is found that the inside and outside pores are almost identical. Furthermore, it is observed once again that the highest values of the mean electrostatic potentials for low radius are obtained for the case of equal electric fields. However, as the

radius increases the differences between equal electric fields and surface charge tends to zero. Moreover, it is observed that a radius of 200 Å is big enough that the mean electrostatic potential inside the nano-pore reassembles that of the solid electrode. Therefore, as we are interested solely on the pore we will limit to a radii equal to or smaller than 80 Å, where a couple of interesting results are found. Therefore, from this point forward the mean electrostatic potentials of the different nano-pores will be obtained for three radii, 5 Å, 15 Å and 80 Å, while different electrode's and electrolyte's parameters are varied. This is done in order to find the influence these parameters have and how the mean electrostatic potentials can be maximized.

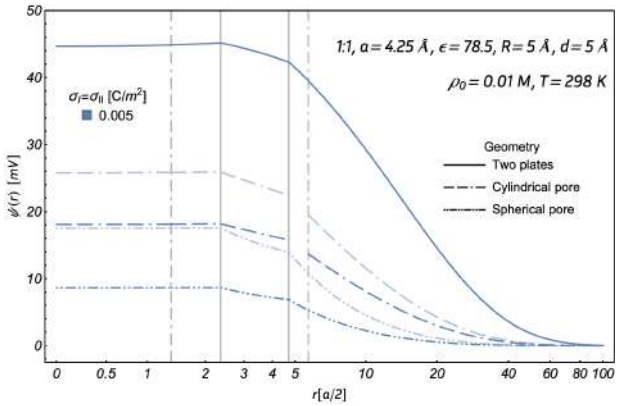


(a) $\psi(r)$ for $\sigma_M = 0.005\,\mathrm{C/m^2}$.

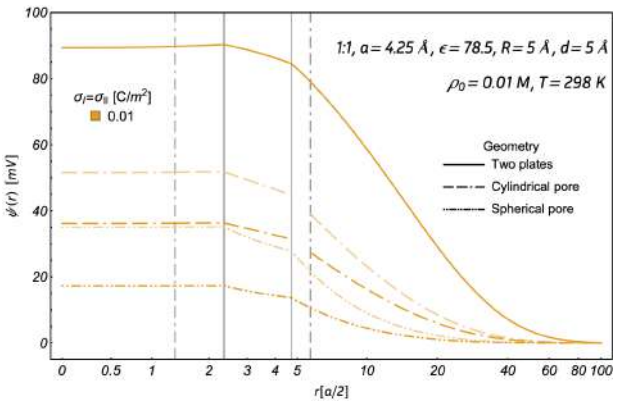


(b) $\psi(r)$ for $\sigma_M = 0.01\,\mathrm{C/m^2}$.

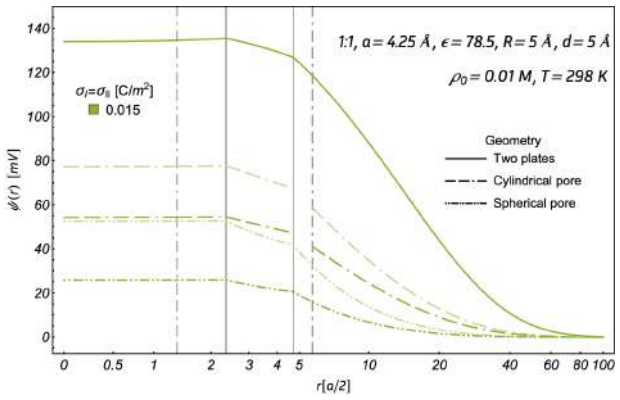


(c) $\psi(r)$ for $\sigma_M = 0.015\,\mathrm{C/m^2}$.

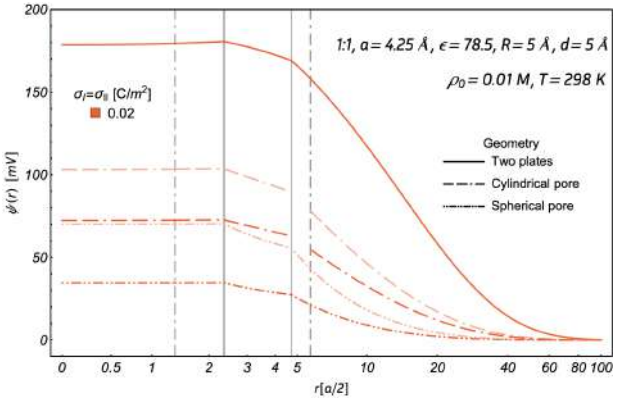


(d) $\psi(r)$ for $\sigma_M = 0.02\,\mathrm{C/m^2}$.

Figure 4.26: The mean electrostatic potentials, $\psi(r)$, of three nano-pore electrodes. A radius of 5 Å $\cong$ 1.2 a is used, while the electrode's surface charges are varied. The lighter and darker lines, and the vertical lines have the same meaning as in Fig. 4.25.

Therefore, in Fig. 4.26 the mean electrostatic potentials of the different nano-pore electrodes are obtained for a radius of 5 Å, while the electrode's surface charge is varied. The cases for equal electric fields and surface charge are shown. From Fig. 4.26 it is found that for all the electrode's surface charges, the slit-pore always has a higher overall mean electrostatic potential than their counterparts, regardless if they have equal electric fields or surface charges. Moreover, as for solid electrodes, the pores' mean electrostatic potential is directly proportional to their surface charge. The equal electric fields cases always achieve higher mean electrostatic potentials than the equal surface charge cases. At this small pore's size the mean electrostatic potential is maintained constant all through the pore's inside, and from the pore's walls to the pore's outside the mean electrostatic potential drops.

In Fig. 4.27 the mean electrostatic potentials of the different nano-pore electrodes are obtained for

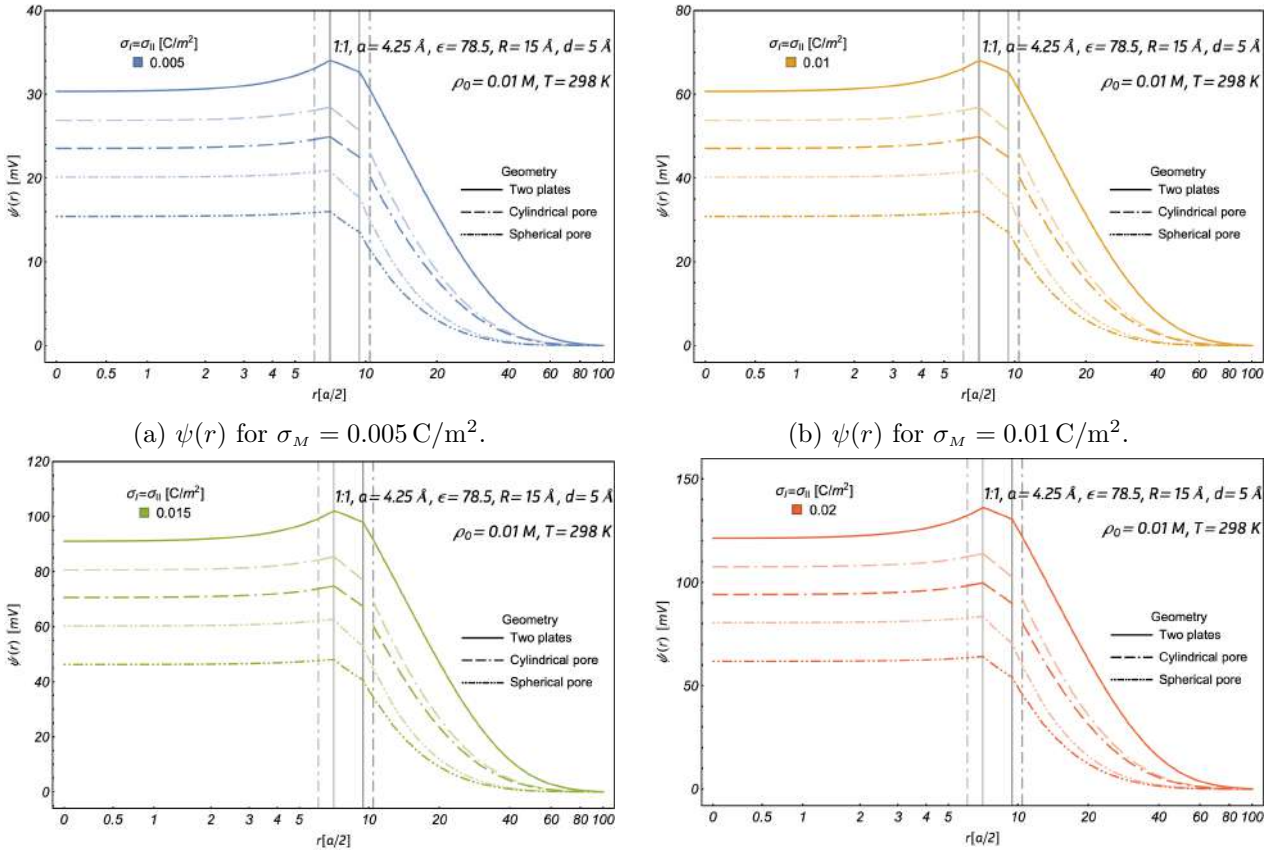


(a) $\psi(r)$ for $\sigma_M = 0.005\,\mathrm{C/m^2}$.

(b) $\psi(r)$ for $\sigma_M = 0.01\,\mathrm{C/m^2}$.

(c) $\psi(r)$ for $\sigma_M = 0.015\,\mathrm{C/m^2}$.

(d) $\psi(r)$ for $\sigma_M = 0.02\,\mathrm{C/m^2}$.

Figure 4.27: The mean electrostatic potentials, $\psi(r)$, of three nano-pore electrodes. A radius of $15\,\text{Å} \cong 3.5\,\mathrm{a}$ is used, while the electrode's surface charges are varied. The lighter and darker lines, and the vertical lines have the same meaning as in Fig. 4.25.

a radius of 15 Å, while the electrode's surface charge is varied. The cases for equal electric fields and surface charge are shown. When the radius is increased from 5 Å to 15 Å it is observed that the slit-pore mean electrostatic potentials decrease, whereas the cylindrical and spherical pores mean electrostatic potential increases. However, this decrease or increase of the mean electrostatic potentials for the slit-pore, and cylindrical and spherical pores do not affect the overall tendencies; as the slit-pore still has the highest mean electrostatic potentials, followed by the cylindrical and spherical pores. Nonetheless it is observed, that the mean electrostatic potentials of the spherical pore increase more, with increasing radius, than the cylindrical pore, for the same electrode's surface charge densities. Once again, it is observed that the difference between the two cases, equal electric fields and surface charges, decreases when the radius increases. Comparatively, now in Fig. 4.27 the pore's size is big enough, so that there is a potential drop inside the pore, which was not observed for a smaller radii.

Next, in Fig. 4.28 the mean electrostatic potentials of the different nano-pore electrodes are obtained for a radius of 80 Å, while the electrode's surface charge is varied. The cases for equal electric fields and surface charges are shown. When the radius is increased from 15 Å to 80 Å it is observed that the overall mean electrostatic potentials decrease for all the pores. However, now the values of $\psi_d$ are higher for the spherical pore, followed by the cylindrical pore and lastly by the slit-pore. This is due to the geometry, as for a sphere the confinement of the ions is greater than in the cylinder and consequently than in the two plates, which translates on a higher ionic concentration inside the pore,

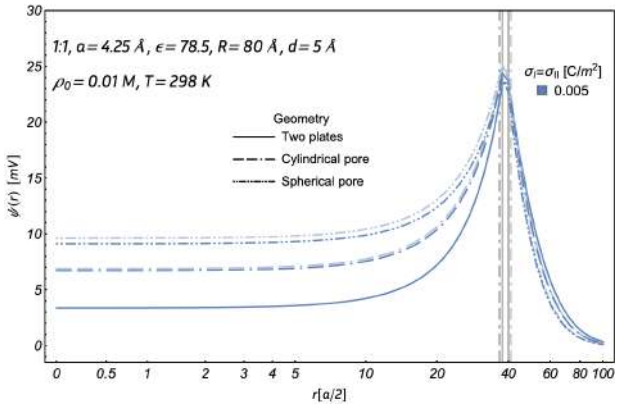


(a) $\psi(r)$ for $\sigma_M = 0.005\,\mathrm{C/m^2}$.

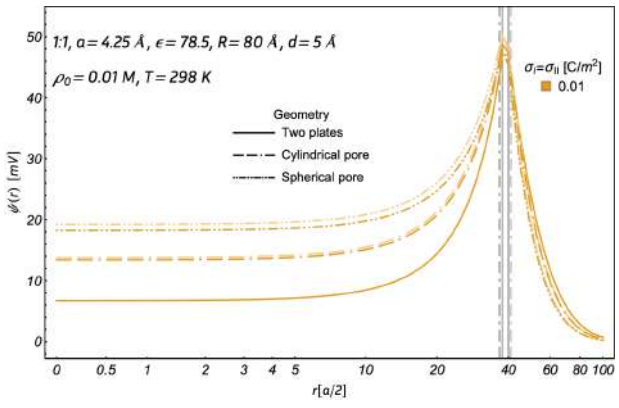


(b) $\psi(r)$ for $\sigma_M = 0.01\,\mathrm{C/m^2}$.

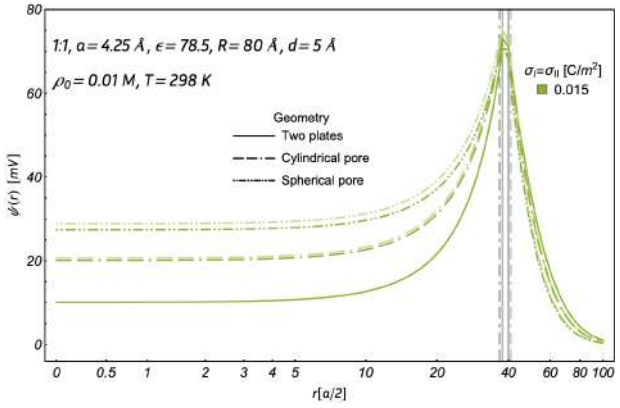


(c) $\psi(r)$ for $\sigma_M = 0.015\,\mathrm{C/m^2}$.

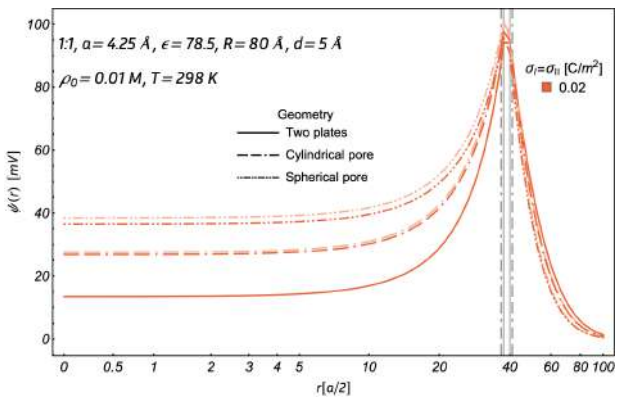


(d) $\psi(r)$ for $\sigma_M = 0.02\,\mathrm{C/m^2}$.

Figure 4.28: The mean electrostatic potentials, $\psi(r)$, of three nano-pore electrodes. A radius of $80\,\text{Å} \cong 18.8\,\mathrm{a}$ is used, while the electrode's surface charges are varied. The lighter and darker lines, and the vertical lines have the same meaning as in Fig. 4.25.

to maintain the constant chemical potential. Moreover, as the radii increase enough, the equal electric fields and surface charge cases of the mean electrostatic potential, become closely indistinguishable. Meanwhile, outside the pore the mean electrostatic potentials tend to the values of the solid electrodes.

Comparatively, in the following figures the mean electrostatic potentials of our pore electrodes are shown while the electrolyte's molar concentration is varied for three radii, 5 Å, 15 Å and 80 Å. Therefore in Fig. 4.29 the mean electrostatic potentials for a pore's size of 5 Å is obtained, when the electrolyte's molar concentration is varied, for two different cases, when equal electric fields and surface charge are used. It is found that the mean electrostatic potential is inversely proportional to the electrolyte's molar concentration. Furthermore, for $\rho_0 = 0.001\,\mathrm{M}$ it is observed that the mean electrostatic potential inside the pore is completely constant, whereas when $\rho_0 = 0.01\,\mathrm{M}$ the mean electrostatic potential, despite being almost constant inside the pore, has a clear maximum at the IHP inside the pore. At higher bulk electrolyte concentrations this maximum becomes more evident, and the mean electrostatic potential inside the pore starts dropping from its value at the pore's wall. Furthermore, when the molar concentration increases, the deviations between both cases increase. In addition, when $\rho_0 = 0.1\,\mathrm{M}$ the equal electric fields cases of the cylindrical and spherical pores start overcoming the mean electrostatic potential inside the slit-pore, and when the molar concentration increases further, 0.5 M, both the equal electric fields and surface charge cases of the cylindrical and spherical pores overcome the mean electrostatic potential inside the slit-pore.

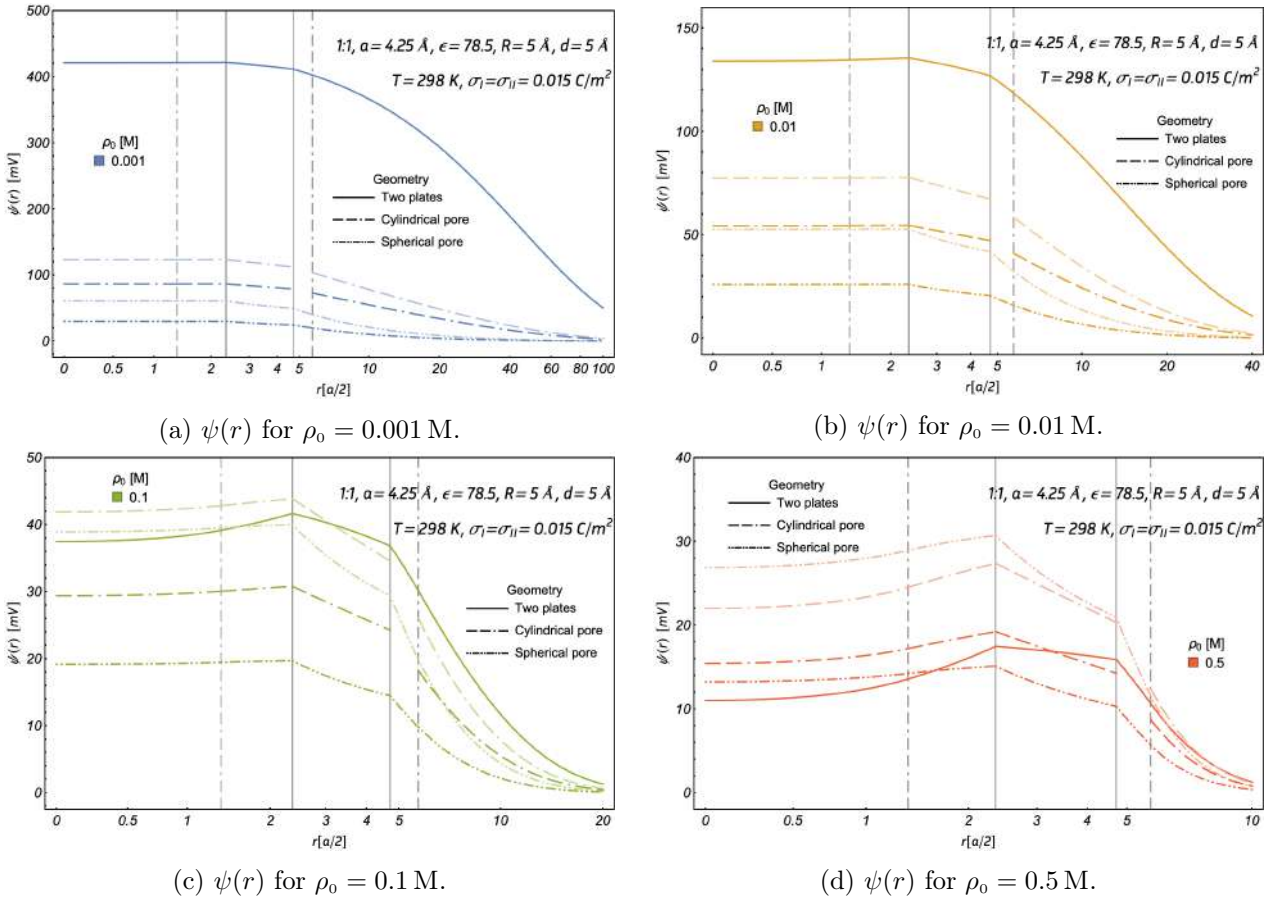


(a) $\psi(r)$ for $\rho_0 = 0.001\,\mathrm{M}$.

(b) $\psi(r)$ for $\rho_0 = 0.01\,\mathrm{M}$.

(c) $\psi(r)$ for $\rho_0 = 0.1\,\mathrm{M}$.

(d) $\psi(r)$ for $\rho_0 = 0.5\,\mathrm{M}$.

Figure 4.29: The mean electrostatic potentials, $\psi(r)$, of nano-pore electrodes, with a radius of $5\,\text{Å} \cong 1.2\,\mathrm{a}$, while the electrolyte's molar concentration, $\rho_0$, is varied. The lighter and darker lines, and the vertical lines have the same meaning as in Fig. 4.25.

In Fig. 4.30 the mean electrostatic potentials of pore electrodes are shown, for a pore's size of 15 Å, while the electrolyte's molar concentration is varied. The equal electric fields and surface charge cases are shown. It is found that when the pore's size increases from 5 Å to 15 Å the mean electrostatic potential decreases. For the lowest molar concentration, 0.001 M, it is found that the mean electrostatic potential stops being constant inside the pore, but is starts to very softly dwindle from its value on the inner pore wall. On the other hand, for the other electrolyte's molar concentrations the mean electrostatic potentials of the slit-pore decreases, and the cylindrical and spherical pores start increasing. Such that now, for a radius of 15 Å the mean electrostatic potential of the slit-pore is overcome by that of the cylindrical and spherical pore, for both equal electric fields and surface charge, at a molar concentration of 0.1 M. Furthermore, the increase of both the radius and molar concentration, for 0.5 M makes the mean electrostatic potential of all the pore electrodes to compact into one single mean electrostatic potential.

In Fig. 4.31 the mean electrostatic potentials of pore electrodes are plotted, for a pore's size of 80 Å, while the electrolyte's molar concentration is varied. The equal electric fields and surface charge cases are shown. From Fig. 4.30 it is observed that as the radius increases, the mean electrostatic potentials, for high molar concentrations, 0.1 M and 0.5 M, tend to the same values as those of the slit, for both the inside and outside of the pore. Therefore, the higher molar concentrations were not shown for $R = 80\,\text{Å}$, as they simply are that of a slit, for the all the pores geometries. Nonetheless, when

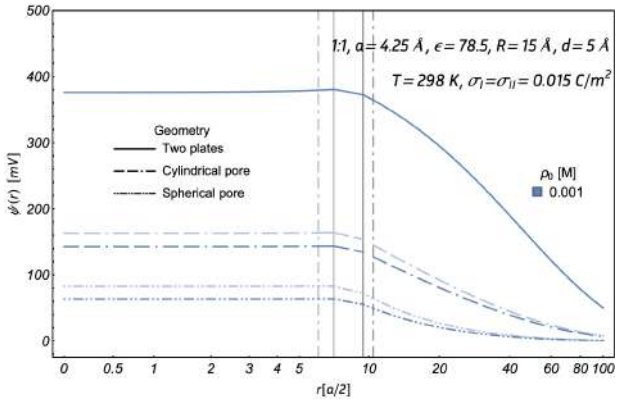


(a) $\psi(r)$ for $\rho_0 = 0.001\,\mathrm{M}$.

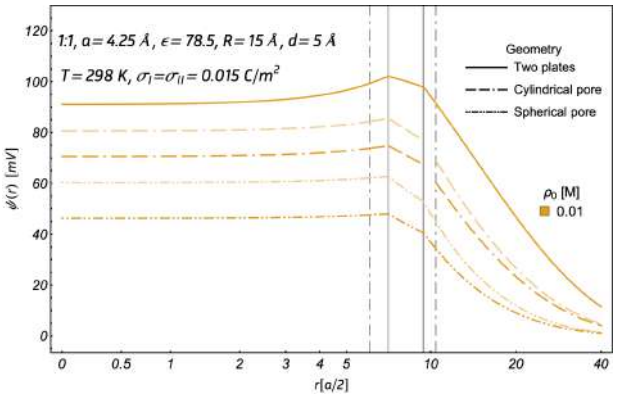


(b) $\psi(r)$ for $\rho_0 = 0.01\,\mathrm{M}$.

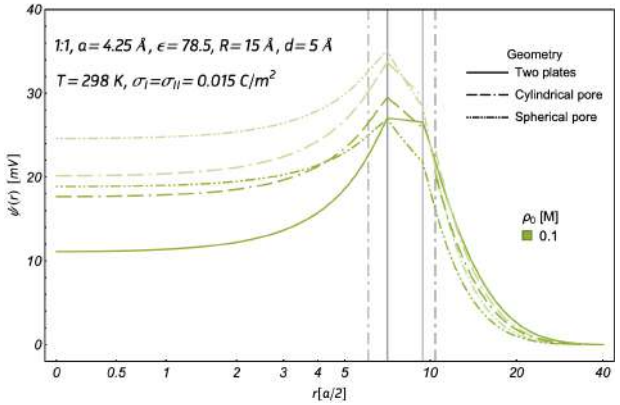


(c) $\psi(r)$ for $\rho_0 = 0.1\,\mathrm{M}$.

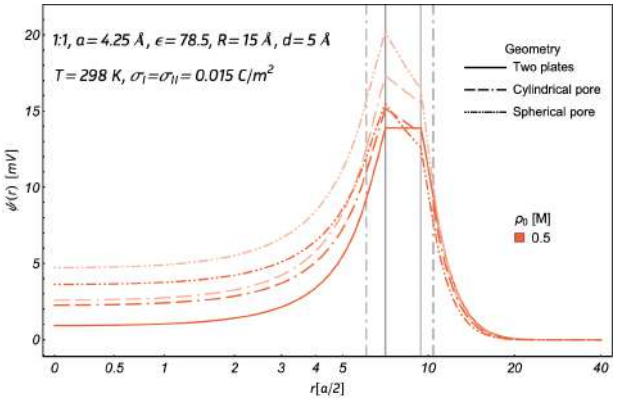


(d) $\psi(r)$ for $\rho_0 = 0.5\,\mathrm{M}$.

Figure 4.30: The mean electrostatic potentials, $\psi(r)$, of nano-pore electrodes, with a radius of $15\,\text{Å} \cong 3.5\,\mathrm{a}$, while the electrolyte's molar concentration, $\rho_0$, is varied. The lighter and darker lines, and the vertical lines have the same meaning as in Fig. 4.25.

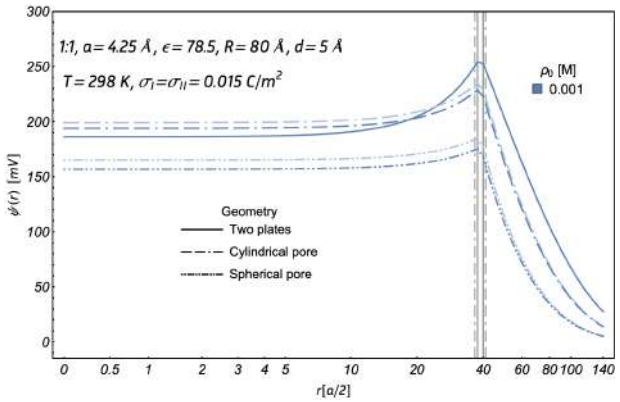


(a) $\psi(r)$ for $\rho_0 = 0.001\,\mathrm{M}$.

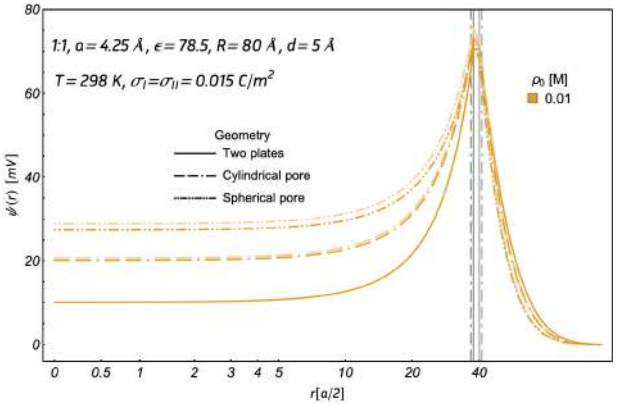


(b) $\psi(r)$ for $\rho_0 = 0.01\,\mathrm{M}$.

Figure 4.31: The mean electrostatic potentials, $\psi(r)$, of nano-pore electrodes, with a radius of $80\,\text{Å} \cong 18.8\,\mathrm{a}$, while the electrolyte's molar concentration, $\rho_0$, is varied. The lighter and darker lines, and the vertical lines have the same meaning as in Fig. 4.25.

the radius is increased from 15 Å to 80 Å one can observe that for the lowest molar concentration the slit-pore has the highest values at the inner wall of the pore, but the cylindrical pore overpasses the values of the slit-pore' mean electrostatic potential at the pores' center. Moreover, the equal electric fields and surface charge cases almost completely overlap, as we are dealing with a large enough radius for which their differences almost disappear. In addition, for a molar concentration of 0.01 M the slit-pore' mean electrostatic potential is almost equal to that of a solid electrode, followed by the cylindrical pore. On the other hand, the spherical pore's mean electrostatic potential is the furthest to resemble to that of a solid electrode. As discussed earlier, due to the geometry of the sphere, the electrons are more compacted than in either the cylinder or plates. Hence, it achieves a higher mean electrostatic potentials than either pore.

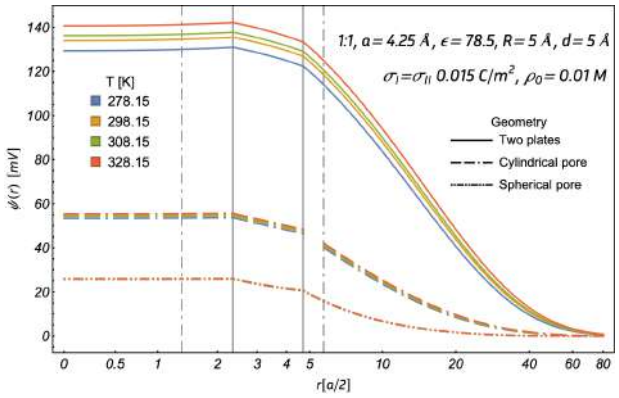


(a) $\psi(r)$ for $R = 5\,\text{Å} \cong 1.2\,\text{a}$.

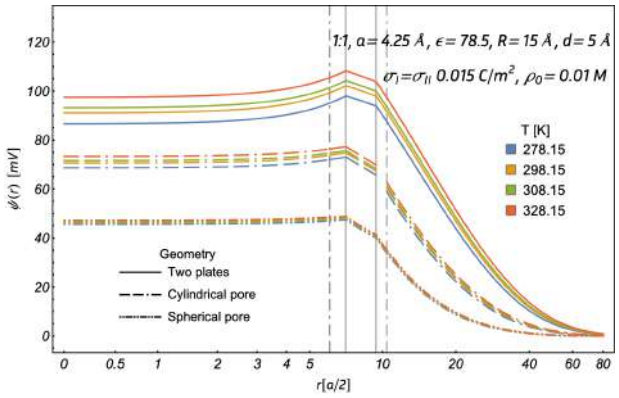


(b) $\psi(r)$ for $R = 15\,\text{Å} \cong 3.5\,\text{a}$.

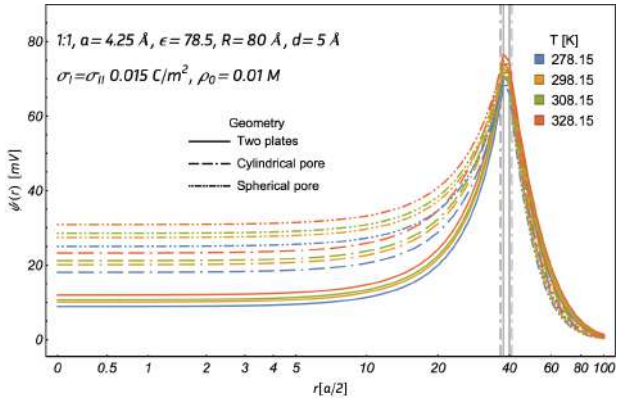


(c) $\psi(r)$ for $R = 80\,\text{Å} \cong 18.8\,\text{a}$.

Figure 4.32: The mean electrostatic potential, $\psi(r)$, of three pore electrode, for three radii, while the temperature, $T$, is varied. The lighter and darker lines, and the vertical lines have the same meaning as in Fig. 4.25.

Lastly but not least, in Fig. 4.32 the mean electrostatic potentials of our pore electrodes are shown for three radii, 5 Å, 15 Å and 80 Å, while the electrolyte's temperature is varied for two different cases, for equal electric fields and surface charge. It is found that as the electrical potential of the solid electrode, the pores' mean electrostatic potential is directly proportional to the temperature. As for higher temperatures, the mean electrostatic potential steadily grows through all the interval.

Therefore, it is found that the mean electrostatic potential can be easily boosted by regulating its electrode size and surface charge density. Whereas, if one wishes to decrease its intensity and

extension one should increase its electrolyte's molar concentration. Meanwhile, if the intention is to increase the mean electrostatic potential throughout the entire interval one needs to increase the electrolyte's temperature.

### 4.2.2 The induced surface charge densities of nano-pore electrodes

Here, the induced surface charge densities are shown for different pores' electrodes. Firstly, the pore's radius influence on the induced surface charge densities for the different pores' electrodes, when two distinct cases are calculated for equal electric fields and surface charge, is studied in Fig. 4.33.

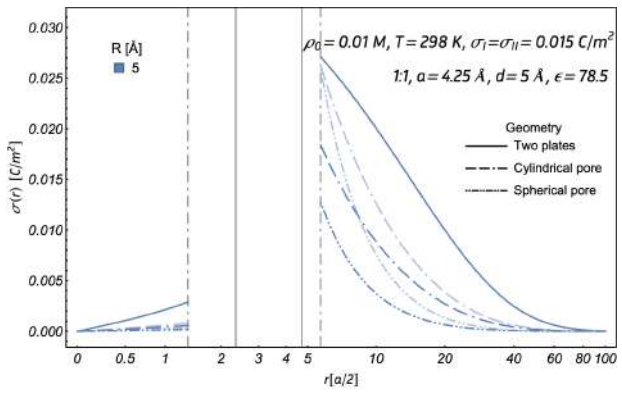


(a) $\sigma(r)$ for $R = 5\,\text{Å} \cong 1.2\,\text{a}$.

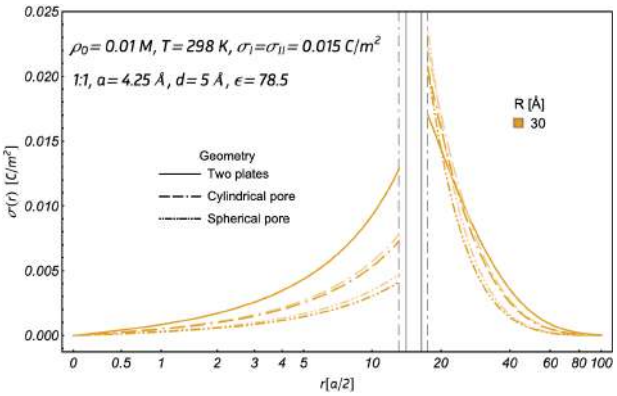


(b) $\sigma(r)$ for $R = 30\,\text{Å} \cong 7.1\,\text{a}$.

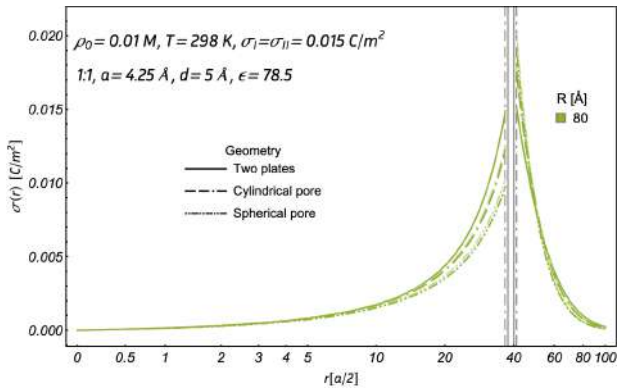


(c) $\sigma(r)$ for $R = 80\,\text{Å} \cong 18.8\,\text{a}$.

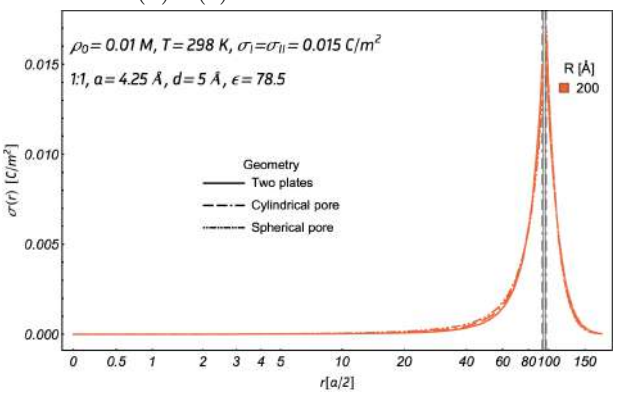


(d) $\sigma(r)$ for $R = 200\,\text{Å} \cong 47.1\,\text{a}$.

Figure 4.33: The induced surface charge densities, $\sigma(r)$, of pore electrodes, while the electrode's radius is varied. The lighter and darker lines represent when equal electric fields and surface charge are used. The vertical dashed and solid lines represent the OHP, and IHP.

In Fig. 4.33 it is observed that now the induced surface charge density is different from the electrode's surface charge density. In fact, the electrode's surface charge density is uniformly distributed inside and outside the pore. It is observed that the induced surface charge density inside the pore increases when the radius increases, while the outside induced surface charge density decreases. This is true up to the point when the radius is large enough so that the inner and outer induced surface charge densities are equal. Furthermore, it is observed that the pore's inner induced surface charge density for the slit-pore is always higher than in the other counterparts, regardless of the radii size, followed by the cylindrical pore and lastly the spherical pore. This is clearly a confinement effect, and implies a violation of the local electroneutrality condition. Of course, the sum of the inner and outer induced charge densities is equal and of opposite sign to that of $\sigma_I + \sigma_{II}$.

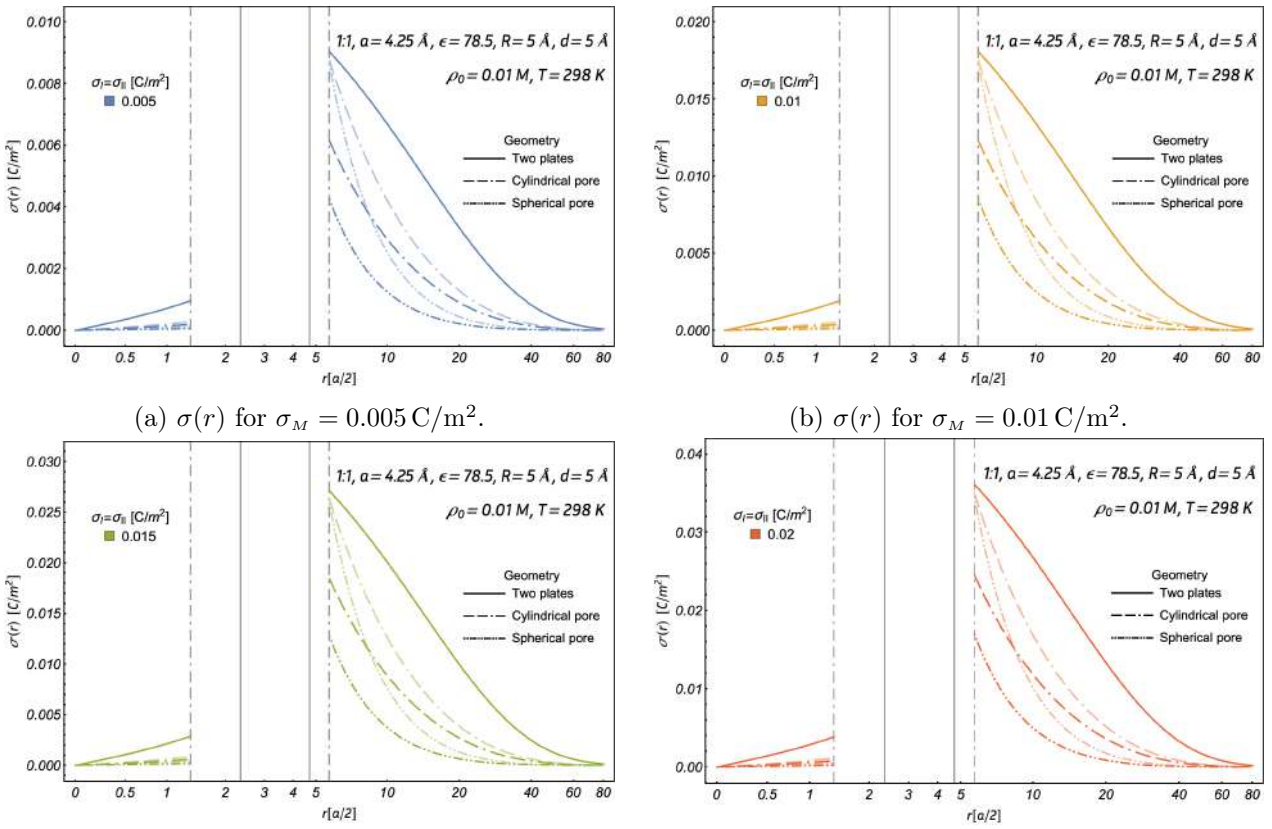


(a) $\sigma(r)$ for $\sigma_M = 0.005\,\mathrm{C/m^2}$.

(b) $\sigma(r)$ for $\sigma_M = 0.01\,\mathrm{C/m^2}$.

(c) $\sigma(r)$ for $\sigma_M = 0.015\,\mathrm{C/m^2}$.

(d) $\sigma(r)$ for $\sigma_M = 0.02\,\mathrm{C/m^2}$.

Figure 4.34: The induced surface charge densities, $\sigma(r)$, of three nano-pore electrodes. A radius of $5\,\text{Å} \cong 1.2\,\mathrm{a}$ is used while the electrode's surface charge density is varied. The lighter and darker lines, and the vertical lines have the same meaning as in Fig. 4.33.

As we are studying the behavior of the induced surface charge densities for nano-pores, we will choose three radii, 5 Å, 15 Å and 80 Å, while varying some other electrode's and electrolyte's parameters. Therefore, in Fig. 4.34 the induced surface charge density of three nano-pores, with a radius of 5 Å, is shown while the electrode's surface charge density is varied. As expected, it is observed that when the electrode's surface charge density increases, the induced surface charge density follows proportionally, to guarantee total electroneutrality. It is interesting noticing that on the pore's inside, the induced surface charge density is close to zero for all the pores, but in particular for the spherical and cylindrical pores. This is due to the fact that since the space inside the pore is very small, only a few number of counter-ions can be settled inside, making the available charge minimal. Hence, although is not clearly seen in Fig. 4.34, inside the pores the slit-pore can store more charge than the cylindrical pore, and this last one can store more charge than the spherical pores. Furthermore, as the induced surface charge density inside the pore is very small the differences between the two cases of equal electric fields and surface charge are almost identical, whereas outside the pore the induced surface charge density for equal electric fields and equal surface charge have important differences. Also notice that for the equal electric field case, the induced surface charge at $r = R + d + a/2$ has almost the same value for three pore geometries, and is almost identical to the induced surface charge densities of the corresponding solid electrodes.

In Fig. 4.35 the induced surface charge density of the three nano-pore electrode's, for a radius

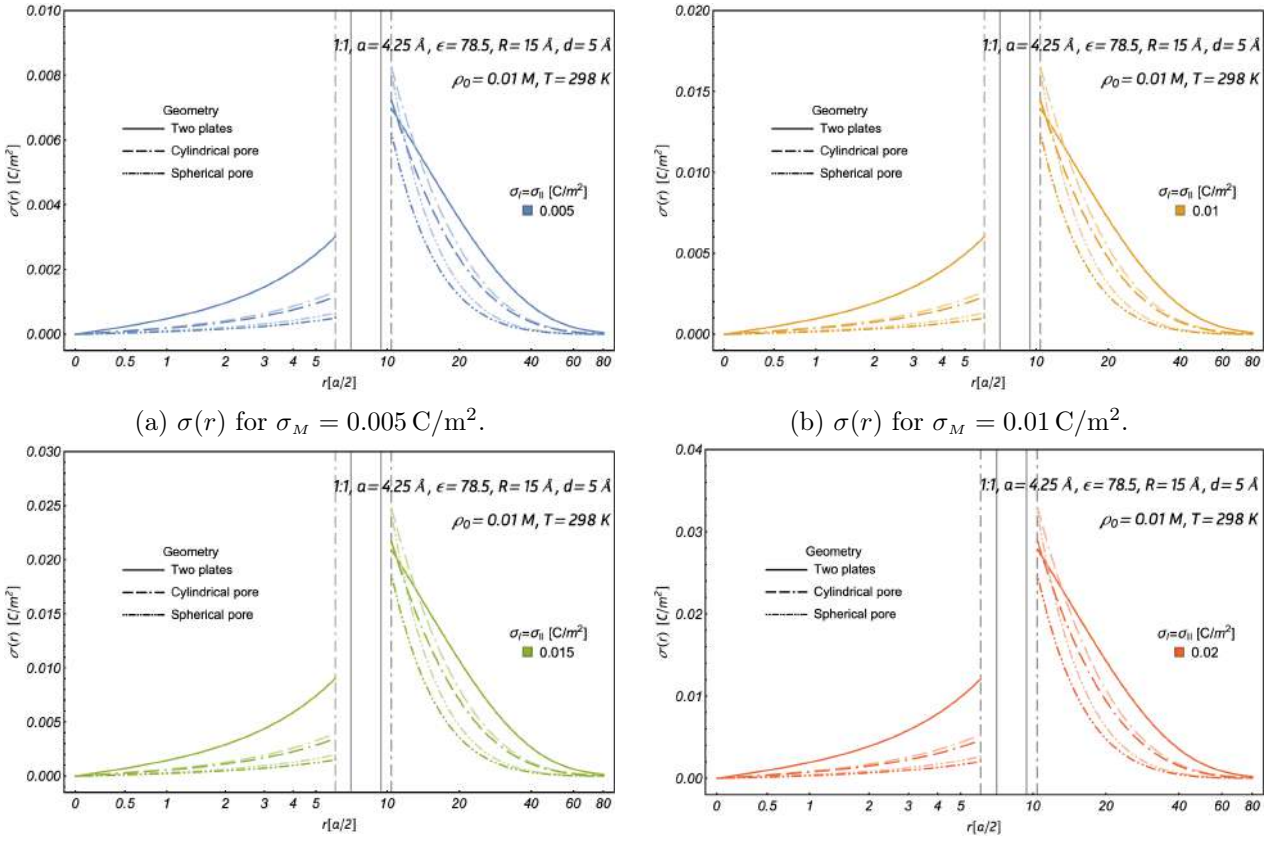


(a) $\sigma(r)$ for $\sigma_M = 0.005\,\mathrm{C/m^2}$.

(b) $\sigma(r)$ for $\sigma_M = 0.01\,\mathrm{C/m^2}$.

(c) $\sigma(r)$ for $\sigma_M = 0.015\,\mathrm{C/m^2}$.

(d) $\sigma(r)$ for $\sigma_M = 0.02\,\mathrm{C/m^2}$.

Figure 4.35: The induced surface charge densities, $\sigma(r)$, of three nano-pore electrodes. A radius of 15 Å $\cong$ 3.5 a is used while the electrode's surface charge density is varied. The lighter and darker lines, and the vertical lines have the same meaning as in Fig. 4.33.

of 15 Å, is plotted for different electrode's surface charge densities. The equal electric fields and surface charges are shown. It is observed that when the radius increases from 5 Å to 15 Å the induced surface charge inside the pore increases considerably for all the geometries. Furthermore, in the outer pore the induce surface charge density decreases for all the pores, as could be expected if the total electroneutrality condition of the system is satisfied. This decrement on the induced surface charge is not equal for all the pores, as the slit-pore drops quicker. Also, the induced surface charge in the outer wall of the pore is higher for the cylindrical pore than for the slit-pore. Moreover, it is also observed that outside the pore the equal electric fields cases achieve a higher contact value on the outer wall of the pore than the slit-pore. Therefore, around a radius of 15 Å the induced surface charge density of the slit-pore outside starts being overtaken by that of the cylindrical and spherical pores.

In Fig. 4.36 the induced surface charge densities of the three nano-pore electrodes, with a radius of 80 Å, is shown while the electrode's surface charge is varied, for cases when equal electric fields and surface charges are used. Hence, it is observed that when the radius of the pore is increased from 15 Å to 80 Å the induced surface charge density inside the pore increases almost to the values of the outside pore. Therefore, the behavior of the induced surface charge density in the inner and outer pore is that of a solid electrode.

In the following figures the influence that the electrodes' radius and the electrolyte's concentration have on the induced surface charge is compared. For this purpose we will plot the induced surface

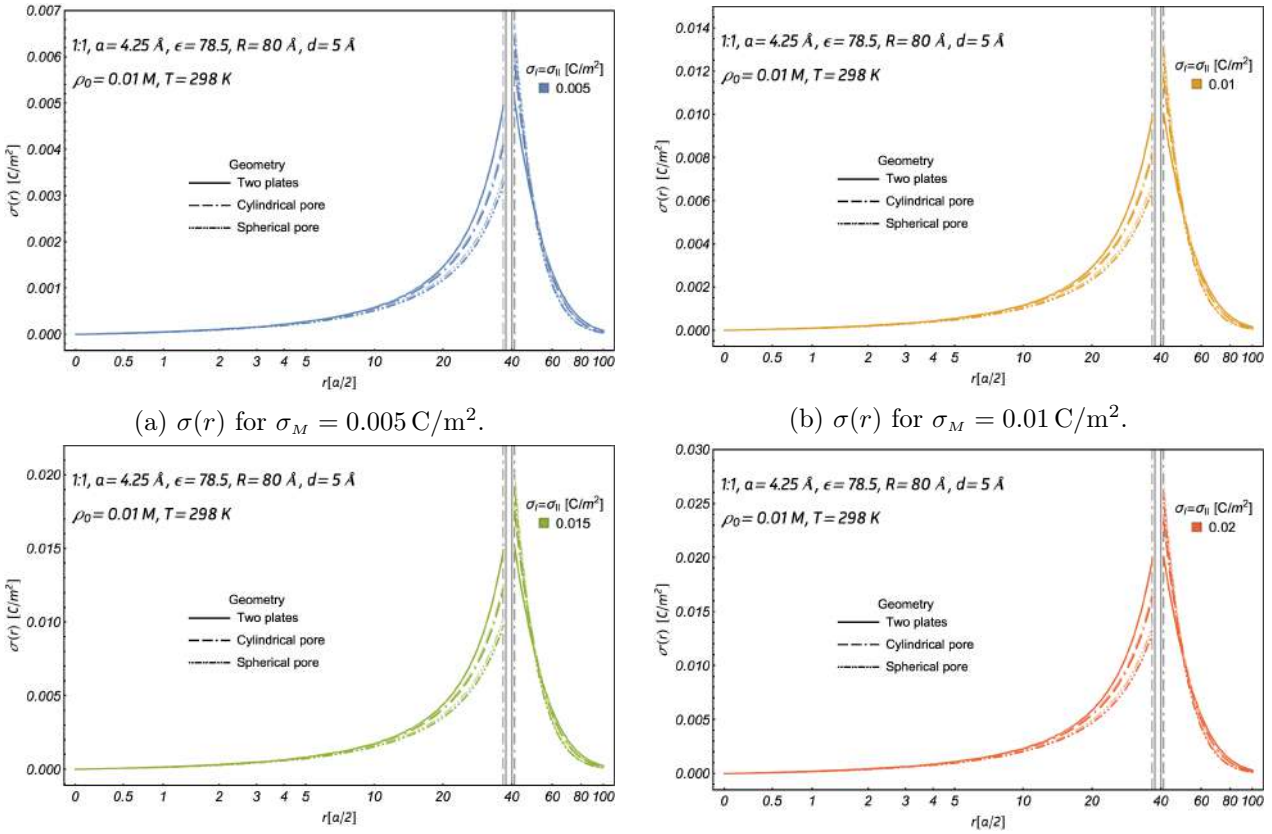


(a) $\sigma(r)$ for $\sigma_M = 0.005\,\mathrm{C/m^2}$.

(b) $\sigma(r)$ for $\sigma_M = 0.01\,\mathrm{C/m^2}$.

(c) $\sigma(r)$ for $\sigma_M = 0.015\,\mathrm{C/m^2}$.

(d) $\sigma(r)$ for $\sigma_M = 0.02\,\mathrm{C/m^2}$.

Figure 4.36: The induced surface charge densities, $\sigma(r)$, of three nano-pore electrodes. A radius of $80\,\text{Å} \cong 18.8\,\text{a}$ is used while the electrode's surface charge density is varied. The lighter and darker lines, and the vertical lines have the same meaning as in Fig. 4.33.

charge densities for the same radii and, for the two cases as before, namely for equal electric fields and surface charges. Therefore, in Fig. 4.37 the induced surface charge densities of the different pores are obtained when the molar concentration is varied at a radius of 5 Å. It is found that when the molar concentration increases, the induced surface charge densities inside the pores increase, whereas the induced surface charge densities outside the pore diminish. Therefore, when we increase the electrolyte's molar concentration, we obtain a similar result that when we increase the electrodes' size, since a higher bulk concentration reduces the thickness of the electrical double layer, and, hence, the confinement is reduced, as when the radius of the pore is increased. Thus, both changes have similar physical implications in the interaction between the electrodes and electrolytes. As previously, it is observed that the difference between induced surface charge densities of the equal electric fields and surface charge cases, for the lowest molar concentration, are almost zero. However, as the molarity increases these differences become more apparent. For instance, for a molar concentration of 0.5 M the cylindrical pores' induced surface charge density of equal electric fields overlaps to the values of the one of the slit-pore.

In Fig. 4.38 the induced surface charge densities of the different pores are computed when the molar concentration is varied and a radius of 15 Å is employed. Hence, it is observed that when the radius size is changed from 5 Å to 15 Å, the induced surface charge inside and outside the pore increase and decrease, respectively, faster when the electrolyte's molar concentration increases. Therefore,

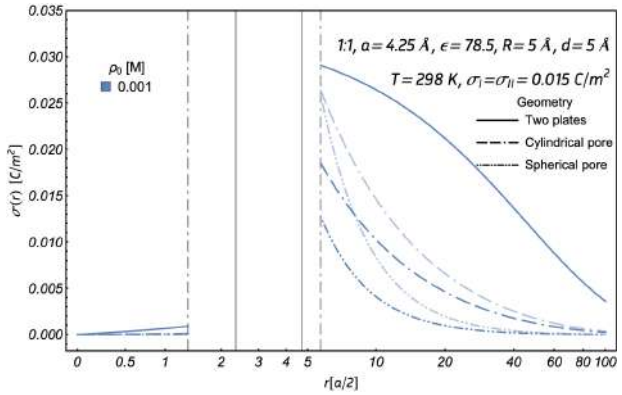


(a) $\sigma(r)$ for $\rho_0 = 0.001\,\mathrm{M}$.

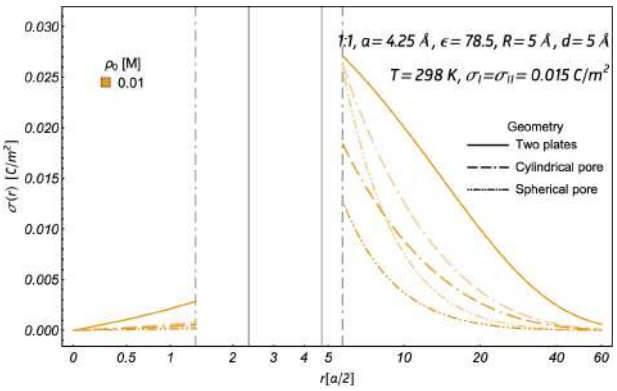


(b) $\sigma(r)$ for $\rho_0 = 0.01\,\mathrm{M}$.

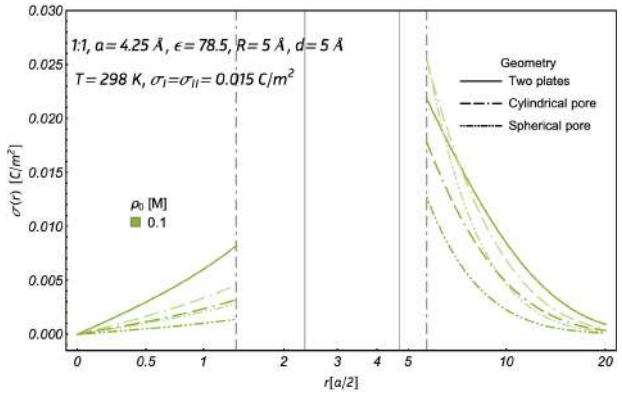


(c) $\sigma(r)$ for $\rho_0 = 0.1\,\mathrm{M}$.

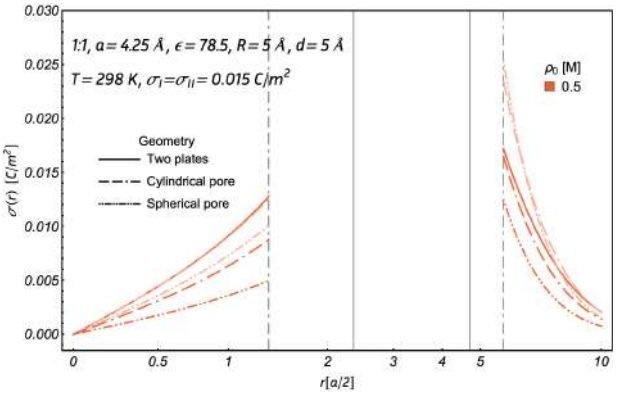


(d) $\sigma(r)$ for $\rho_0 = 0.5\,\mathrm{M}$.

Figure 4.37: The induced surface charge density, $\sigma(r)$, of our nano-pore electrodes. A radius of $5\,\text{Å} \cong 1.2\,\mathrm{a}$ is used while the electrolyte's molar concentration, $\rho_0$, is varied. The lighter and darker lines, and the vertical lines have the same meaning as in Fig. 4.33.

the induced surface charge density is doubly influenced by the electrolyte's molar concentration and electrode's surface charge densities. For a rather small pore size, 15 Å, the pore's inner induced surface charge density for electrolytes' molar concentration of 0.1 M and 0.5 M resemble a lot the behavior of the induced surface charge densities of a radius of 80 Å. That is, the induced surface charge density inside and outside the pore start reassembling that of a solid electrode.

In Fig. 4.39 the induced surface charge density of the different pores, is shown with a radius of 80 Å, while the molar concentration is varied for the equal electric fields and surface charge cases. Due to the tendency discussed earlier, found from Figs. 4.37 and 4.38, the induced surface charge densities for this radius are not calculated for the higher molar concentrations as they quickly tend to the values of a solid electrolyte both inside and outside. Hence, in Fig. 4.39 it is observed that the induced surface charge densities inside the pore achieve higher contact values at the inner wall for the slit-pore, followed by the cylindrical pore and then by the spherical pore, for both molar concentrations. On the other hand, for the induced surface charge densities outside the pore, the opposite is true, the highest contact values at the outer wall are for the spherical pore, followed by the cylindrical pore and the slit-pore, for both molar concentrations. Meanwhile, as the radius is large enough both cases, equal electric fields and surface charges, overlap for all the induced surface charges.

Lastly, in Fig. 4.40 the induced surface charge densities of our different pores are shown for three radii, 5 Å, 15 Å and 80 Å, while the temperature is varied. Two distinct tendencies for the inner

and outer induced surface charge densities are found. For the latter, it is observed that the induced surface charge is directly proportional to the temperature. Whereas, the opposite is true for the inner

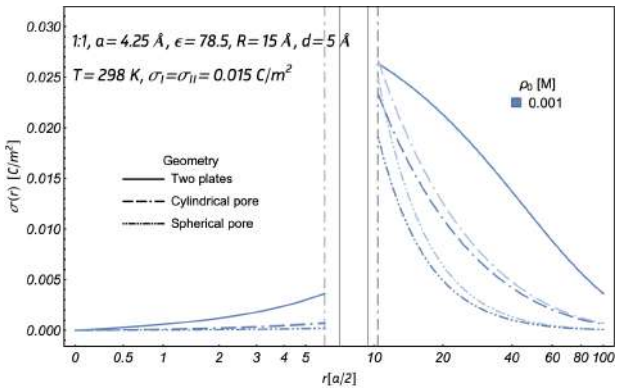


(a) $\sigma(r)$ for $\rho_0 = 0.001\,\mathrm{M}$.

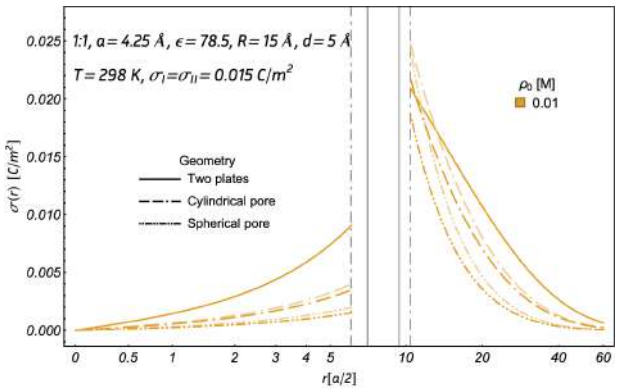


(b) $\sigma(r)$ for $\rho_0 = 0.01\,\mathrm{M}$.

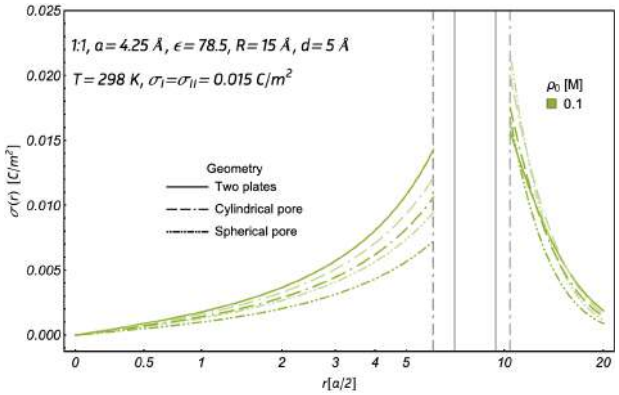


(c) $\sigma(r)$ for $\rho_0 = 0.1\,\mathrm{M}$.

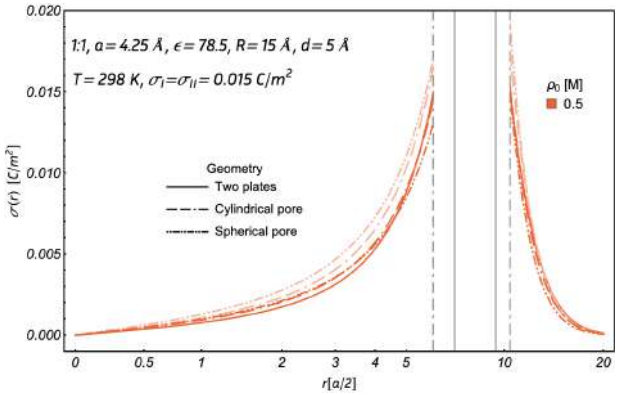


(d) $\sigma(r)$ for $\rho_0 = 0.5\,\mathrm{M}$.

Figure 4.38: The induced surface charge density, $\sigma(r)$, of our nano-pore electrodes. A radius of $15\,\text{Å} \cong 3.5\,\mathrm{a}$ is used while the electrolyte's molar concentration, $\rho_0$, is varied. The lighter and darker lines, and the vertical lines have the same meaning as in Fig. 4.33.

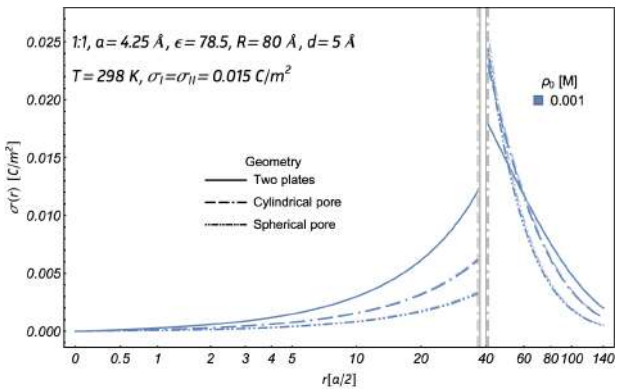


(a) $\sigma(r)$ for $\rho_0 = 0.001\,\mathrm{M}$.

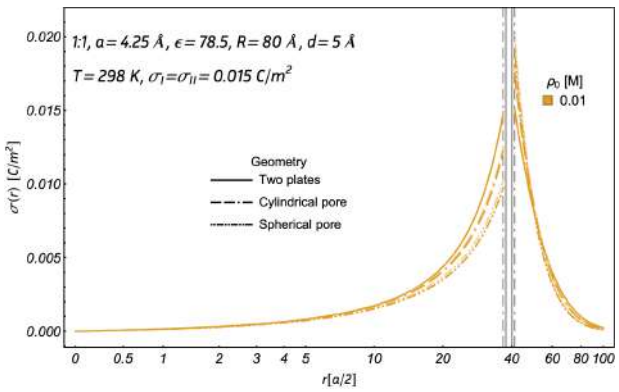


(b) $\sigma(r)$ for $\rho_0 = 0.01\,\mathrm{M}$.

Figure 4.39: The induced surface charge density, $\sigma(r)$, of our nano-pore electrodes. A radius of $80\,\text{Å} \cong 18.8\,\mathrm{a}$ is used while the electrolyte's molar concentration, $\rho_0$, is varied. The lighter and darker lines, and the vertical lines have the same meaning as in Fig. 4.33.

induce surface charge densities, there is an indirect proportionality between the induced surface charge density and the temperature. Both of these opposite tendencies are true for all the radii. As pointed out before, increasing the temperature is somewhat equivalent to decreasing the charge of the pore or the ionic valence; hence, the induced charge inside the pores reduces accordingly with a higher temperature. Then, because of the electroneutrality condition, the reverse tendency is observed in the outside induced charges. Why is not this effect in the opposite behavior? That is, why increasing temperature reduces the outside induced charge and inside the pores increases? The reason seems to be because the restriction imposed to the absorption of ions inside the pores, due to the confinement. In any case, it is clearly shown that the temperature effect on the induced surface charge density is minimal, as the induced surface charge density barely changes.

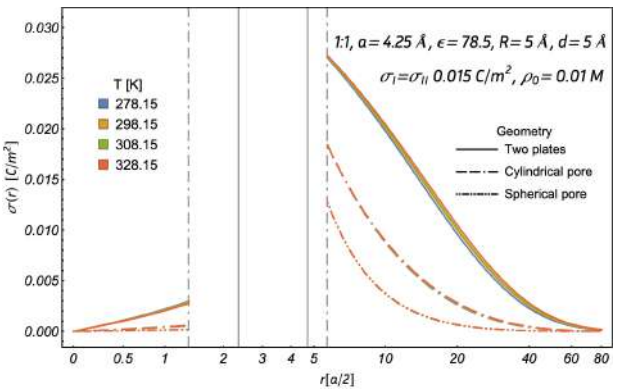


(a) $\sigma(r)$ for $R = 5\,\text{Å} \cong 1.2\,\text{a}$.

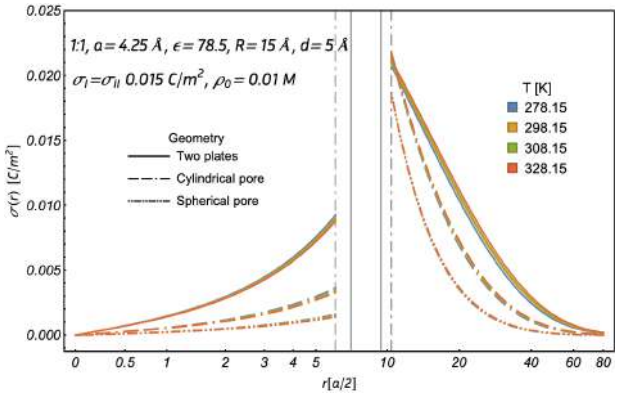


(b) $\sigma(r)$ for $R = 15\,\text{Å} \cong 3.5\,\text{a}$.

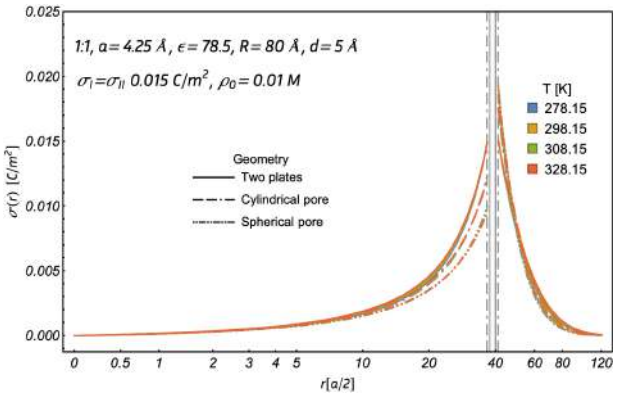


(c) $\sigma(r)$ for $R = 80\,\text{Å} \cong 18.8\,\text{a}$.

Figure 4.40: The induced surface charge densities, $\sigma(r)$, of three pore electrode, for three radii, while the temperature, $T$, is varied. The lighter and darker lines, and the vertical lines have the same meaning as in Fig. 4.33.

As a result, it is found that the induced surface charge density inside and outside the pore is directly proportional to the electrode's surface charge. However, the inner and outer induced surface charge density are observed to be directly and inversely proportional to the pores' radii and electrolyte's molar concentration, respectively. Therefore, if one changes these three parameters one can completely vary the intensity and extension of the induced surface charge density. On the other hand, when the temperature increases the inner and outer induced surface charge densities suffer a uniform decrement or increment, respectively. Hence, varying the electrodes' size, and surface charge density, and the

electrolyte's molar concentration and temperature one can force the induced surface charges to take the values that one wishes, as long as the electroneutrality condition is not violated. Consequently, if you want an inner induced surface charge density with a high contact value, you should either increase the electrode's size or the electrolyte's molar concentration.

### 4.2.3 The differential capacitance of nano-pore electrodes

Lastly, the results of the differential capacitances are obtained for the different nano-pore electrodes for a monovalent electrolyte (1:1) with a dielectric constant of 78.5, an electrolyte's molar concentration of 0.01 M, a temperature of 298.15 K, and a pore's width of 5 Å, unless stated otherwise. The slit-pore, and cylindrical and spherical pores' differential capacitances are obtained from Eqs. (3.46), (3.83) and (3.113), respectively.

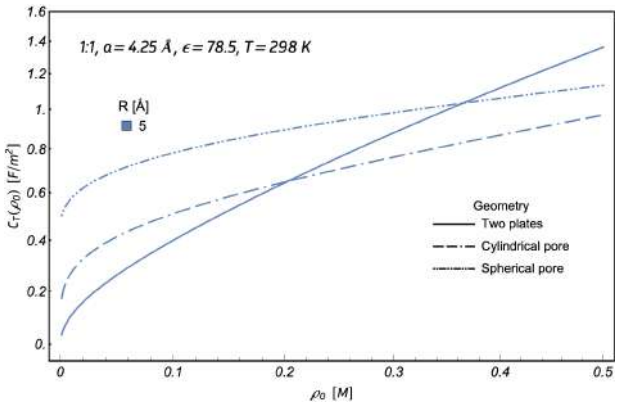


(a) $C_T$ for $R = 5\,\text{Å} \cong 1.2\,\text{a}$.

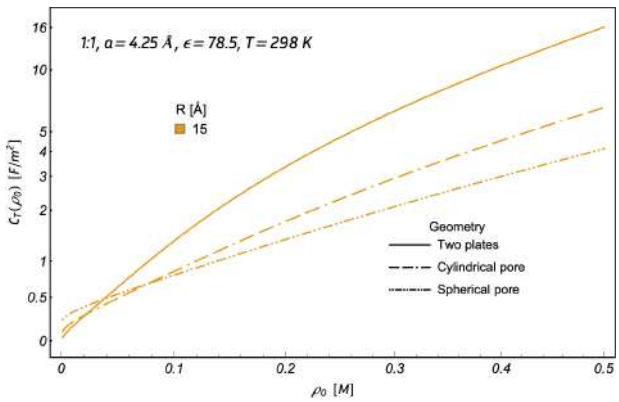


(b) $C_T$ for $R = 15\,\text{Å} \cong 3.5\,\text{a}$.

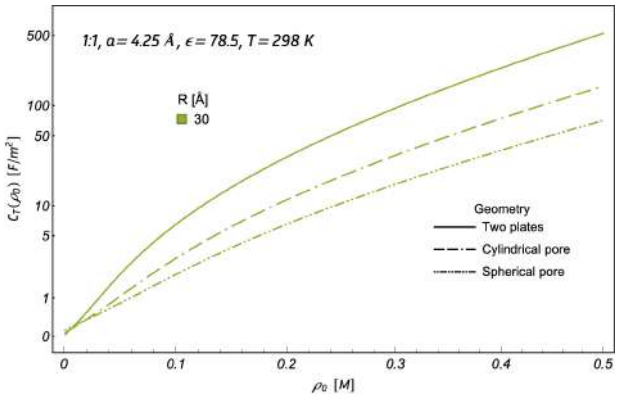


(c) $C_T$ for $R = 30\,\text{Å} \cong 7.1\,\text{a}$.

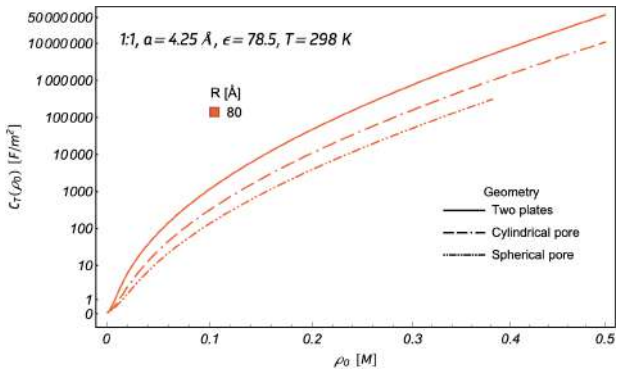


(d) $C_T$ for $R = 80\,\text{Å} \cong 18.8\,\text{a}$.

Figure 4.41: The differential capacitances, $C_T$, of different nano-pore electrodes against the molar concentration, $\rho_0$, for four radii.

Consequently, in Fig. 4.41 and Table 4.5 the differential capacitances of the three pore electrodes are obtained for four radii, while the electrolyte's molar concentration is increased. Some interesting results are found, as each pore has slightly different tendencies for different radii. Therefore, we will first point out the common tendency that the three nano-pore electrodes have. That is, the differential capacitance is directly proportional to the electrolyte's molar concentration. Furthermore, if the molar concentration is sufficiently increased, the differential capacitance of the slit-pore is always higher than that of the other nano-pores; since, the differential capacitance values of the slit raises more rapidly

than the one of the other nano-pores', when the molar concentration increases. However, it is observed that when the radii is small, 5 Å, and the electrolyte's molar concentration is lower than 0.2 M, the highest differential capacitance is achieved for the spherical pore, followed by the cylindrical pore and lastly by the slit-pore. Whereas, for a radius of 15 Å only for molar concentrations lower than 0.03 M do the differential capacitance of the spherical and cylindrical pores have higher values than in the case of the slit-pore.

| | $R = 5$ Å $\cong 1.2$ a | | | $R = 15$ Å $\cong 3.5$ a | | | $R = 30$ Å $\cong 7.1$ a | | | $R = 80$ Å $\cong 18.8$ a | | |
|---|---|---|---|---|---|---|---|---|---|---|---|---|
| $\rho_0$ [M] | P | C | S | P | C | S | P | C | S | P | C | S |
| 0.001 | 0.036 | 0.174 | 0.502 | 0.040 | 0.105 | 0.236 | 0.047 | 0.081 | 0.147 | 0.080 | 0.077 | 0.096 |
| 0.01 | 0.112 | 0.276 | 0.579 | 0.165 | 0.212 | 0.324 | 0.280 | 0.238 | 0.274 | 1.477 | 0.743 | 0.546 |
| 0.1 | 0.400 | 0.510 | 0.782 | 1.347 | 0.848 | 0.794 | 6.544 | 2.933 | 1.967 | 1184 | 327.8 | 138.9 |
| 0.5 | 1.361 | 0.971 | 1.133 | 16.09 | 6.571 | 4.130 | 526.3 | 156.3 | 71.21 | $6 \cdot 10^7$ | $1 \cdot 10^7$ | NA |

Table 4.5: The differential capacitances, $C_T$ [F/m$^2$], of the slit-pore (P), and cylindrical (C) and spherical (S) pores, for different radii, while the molar concentration, $\rho_0$, is varied.

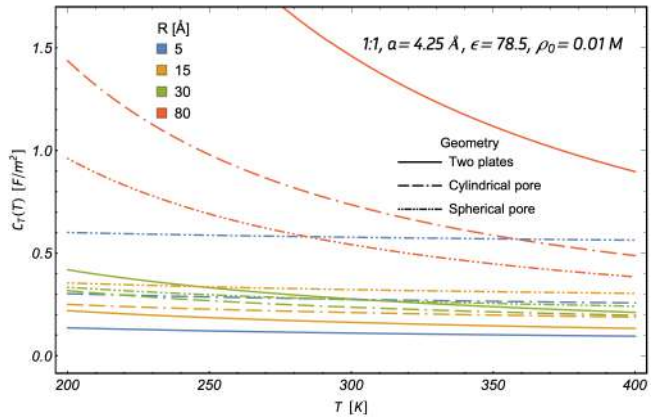


Figure 4.42: The differential capacitances, $C_T$, of nano-pores electrodes against the temperature, $T$, for different radii.

| | $R = 5$ Å $\cong 1.2$ a | | | $R = 15$ Å $\cong 3.5$ a | | | $R = 30$ Å $\cong 7.1$ a | | | $R = 80$ Å $\cong 18.8$ a | | |
|---|---|---|---|---|---|---|---|---|---|---|---|---|
| $T$ [K] | P | C | S | P | C | S | P | C | S | P | C | S |
| 278.15 | 0.116 | 0.281 | 0.582 | 0.173 | 0.218 | 0.329 | 0.299 | 0.250 | 0.283 | 1.674 | 0.827 | 0.598 |
| 298.15 | 0.112 | 0.276 | 0.579 | 0.165 | 0.212 | 0.324 | 0.280 | 0.238 | 0.274 | 1.477 | 0.743 | 0.546 |
| 308.15 | 0.110 | 0.274 | 0.577 | 0.161 | 0.209 | 0.321 | 0.271 | 0.233 | 0.270 | 1.393 | 0.707 | 0.524 |
| 328.15 | 0.107 | 0.270 | 0.574 | 0.154 | 0.204 | 0.317 | 0.255 | 0.224 | 0.263 | 1.248 | 0.644 | 0.485 |

Table 4.6: The differential capacitances, $C_T$ [F/m$^2$], of different nano-pores for four radii, while the temperature, $T$, is varied. The initials (P, C, S) used have the same meaning as in Table 4.5.

In contrast, in Fig. 4.42 and Table 4.6 the differential capacitances of our three pore electrodes are obtained for four radii, while the temperature is varied. It is found that the differential capacitance is inversely proportional to the temperature, for any radius. However, it is observed that this

proportionality depends on the radius size. As for low radii, the differential capacitance drops as the temperature increases is minimal, whereas for large radii there is a more drastic drop. Furthermore, for a radius of 30 Å it is observed that the slit-pore differential capacitance is higher than the one of the other pores for low temperatures. However, as the temperature increases to 310 K the differential capacitance of the spherical pore overpasses the one of the slit-pore. Hence, it is observed that the electrolyte's temperature has a bigger impact on the slit-pore differential capacitance than for the spherical pore. This is further observed when a radius of 80 Å is used, as the drop from the slit-pore and the cylindrical pore are higher than the one of the spherical pore.

It was found that the spherical nano-pore of 5 Å achieve the highest differential capacitances for molar concentrations lower or equal than 0.35 M. However, if either the electrodes' radii or the electrolyte's molar concentration is higher, the slit-pore differential capacitances are larger than the other nano-pores' differential capacitances. Furthermore, it was found that the differential capacitance is inversely proportional to the temperature. However, as the radius increases this inverse proportionality increases, specifically for the slit-pore, followed by the cylindrical pore and lastly by the spherical pore.

An ending remark of this chapter must be made. Even though we did not make a hand to hand comparison with other theoretical results, as in Chapter 2. As in Chapter 3, we assume that the validity of the concentration profiles of solid electrodes in Chapter 2 equally applies for the different electric parameters of solid, and nano-electrodes.

# Chapter 5

# Conclusions

The linearized single electrical double layer of a solid planar, cylindrical and spherical electrodes was derived from the Poisson-Boltzmann model with the Stern restriction. Moreover, for the planar electrode the non-linearized SEDL was also derived for the same model. The electric parameters of the density profiles, mean electrostatic potentials, induced surface charge densities and the differential capacitances were obtained for each geometry and case.

Furthermore, the first results of the linearized electrical double layer of a slit-pore, cylindrical, and spherical pore electrodes were derived as well from the Poisson-Boltzmann model with the Stern restriction. The density profiles, mean electrostatic potentials, induced surface charge densities and the differential capacitances were obtained and plotted for each pore.

From the results, the interval of validity of the Poisson-Boltzmann model with the Stern restriction is found against the HNC/MSA model and from MC results. Furthermore, a thorough study of the impact that the electrode's size, surface charge, and the electrolyte's molar concentration, and temperature have on the density profiles, mean electrostatic potential, induced surface charge and differential capacitance was performed for nano-electrodes of different and equivalent topologies.

Lastly, we also include a brief list on possible future works that could be done as a continuation of this thesis. These works are suggested from inconclusive works performed during the elaboration of this thesis that were not carry out due to time concerns, and from new works concerning the topic.

## 5.1 Interval of validity

In Chapter 2, a comparison between our linear solutions and that of the HNC/MSA model of Lozada-Cassou for solid electrodes was performed. It was found that our solutions work for symmetrical electrolyte (1:1) with electrolyte's molar concentrations in the range between 0.01 M to 0.5 M. And for an electrode's surface charge of $0.015\,\mathrm{C/m^2}$ and $0.05\,\mathrm{C/m^2}$ for molar concentrations of 0.01 M and 0.1 M, respectively. Furthermore, for higher molar concentration it was observed that a higher value of the electrode's surface charge can be used without jeopardizing the validity of our solutions. Moreover, it was also found that our results are a good fit of the HNC/MSA model of Lozada-Cassou when the electrodes' radius is lower than or equal to 80 Å. However, they are a better fit when the radius is smaller. As for a radius of 80 Å the allowed electrode's surface charge density needs to be smaller, $0.01\,\mathrm{C/m^2}$, for an electrolyte's molar concentration of 0.01 M, so our linear solutions are still a viable solution of the HNC/MSA model. Meanwhile, even though the electrolyte's temperature effect on the electric double layer was not compared directly against the HNC/MSA model, it was found from our solutions that the temperature effect is minimal. As we are dealing with an aqueous symmetric electrolyte at a normal atmospheric pressure, in between freezing and boiling temperatures of water, our

electric double layer model holds for such temperatures due to the small impact that the temperature has.

Meanwhile, the same interval of validity found for the solid electrodes in Chapter 2 is assumed to be the same for the nano-pore electrodes. Owing to the fact that both models are obtained equivalently, we expect that their intervals of validity must be comparable between one and the other.

## 5.2 Optimal topology and geometry

It is found that the optimal topologies for the differential capacitance is that of the nano-pore electrodes, as they continuously achieve higher values than those of the solid electrodes. Specifically, it is observed that the higher values are achieved for the smaller radii independently of the topology. Moreover, now each electric parameter will be analyzed on how to modify their values. In Table 5.1 the overall behavior of the different electric parameters is shown when the electrode's surface charge and radius increase and when the electrolyte's molar concentration and temperature increase for the solid electrodes (SE) and the nano-pore electrodes (NPE). The up and down arrows represent an overall increase or decrease of the electric parameter behavior. For the NPE, when two opposite tendencies are found inside and outside the pore, such different tendencies are represented with two opposite arrows, were the first and second arrow represent the electric parameter behavior in the inner and outer pore, respectively. Furthermore, in some cases it is observed an uneven decrement inside and outside the NPE, that is why in some cases two down arrows are presented ($\downarrow\neq\downarrow$). Since, the differential capacitance shown in Table 5.1 is linear, it does not depend on the electrode's surface charge, so this variable is not applicable (N/A) for $C_T$.

| | $g_i$ | | $\psi$ | | $\sigma$ | | $C_T$ | |
|---|---|---|---|---|---|---|---|---|
| | SE | NPE | SE | NPE | SE | NPE | SE | NPE |
| $\uparrow R$ | $\uparrow$ | $\downarrow\neq\downarrow$ | $\uparrow$ | $\downarrow\neq\downarrow$ | $\uparrow$ | $\uparrow\downarrow$ | $\downarrow$ | $\uparrow$ |
| $\uparrow \sigma_M$ | $\uparrow$ | $\uparrow$ | $\uparrow$ | $\uparrow$ | $\uparrow$ | $\uparrow$ | N/A | N/A |
| $\uparrow \rho_0$ | $\downarrow$ | $\downarrow$ | $\downarrow$ | $\downarrow$ | $\downarrow$ | $\uparrow\downarrow$ | $\uparrow$ | $\uparrow$ |
| $\uparrow T$ | $\downarrow$ | $\downarrow$ | $\uparrow$ | $\uparrow$ | $\uparrow$ | $\downarrow\uparrow$ | $\downarrow$ | $\downarrow$ |

Table 5.1: The overall behavior of the density profiles, $g_i$, mean electrostatic potential, $\psi$, induced surface charge density, $\sigma$, and differential capacitance, $C_T$, for solid electrodes (SE) and nano-pore electrodes (NPE), when the electrode's radius, $R$, and surface charge density, $\sigma_M$, and the electrolyte's molar concentration, $\rho_0$, and temperature, $T$, are increased.

The overall behavior of the different electric parameters of the SE shown in Table 5.1 are representative of all the solid electrodes. However, it is good to remember that the planar solid electrode does not depend on the radius, hence the observations mark when the radius increases does not apply to the solid planar electrode. Furthermore, the influence that the different parameters have on the density profiles, mean electrostatic potential and induced surface charge were analyzed by fixing the unscreened electrode's electric field and by fixing the electrode's surface charge density. It was found that the unscreened electric field case achieve higher values than the equal electrode's surface charge case for these electric parameters, where the differences between one case and the other are higher when small radii are used, as when the radius increases these differences disappear. Moreover, it is found that the highest values for the density profile, mean electrostatic potential and induced surface charge are higher for the solid planar electrode, followed by the solid cylindrical and spherical electrodes. Whereas, for the differential capacitance the highest values are achieved for the solid spherical

electrode followed by the solid cylindrical and planar electrodes.

Meanwhile, for the NPE more interesting results were found due to their two component parts, the inner and outer pore, and because of their different topologies. It is found that the density profiles of the NPE are directly and inversely proportional to the electrode's surface charge density and size, respectively. Whereas, they are inversely proportional to the electrolyte's molar concentration. On the other hand, they have a curious behavior when the temperature increases for large radius: as we have an inner and outer pore, the density profiles inside the pore are directly proportional to the electrolyte's temperature, whereas outside they are inversely proportional. All of this is true for three nano-pore electrodes, but the one that achieve the higher values for the same parameter is the slit-pore, followed by the cylindrical and spherical pores.

Correspondingly, it is found that the mean electrostatic potential of NPE are inversely and directly proportional to the electrolyte's molar concentration and temperature, respectively. At the same time, the mean electrostatic potentials are directly and inversely proportional to the electrodes' surface charge density and size. This behavior is found for all nano-pore electrodes. Nonetheless, the slit-pore achieve the highest values of the mean electrostatic potentials, followed by the cylindrical and spherical pores. As for the density profiles, the mean electrostatic potentials of the NPE do not decrease at the same pace inside and outside the pore for the different NPE when the radius increases. As the slit-pore's density profile and mean electrostatic potential drop quicker than the cylindrical and spherical nano-pores inside the pore.

In addition, it is recognized that the overall induced surface charge density of the NPE is directly proportional to the electrodes' surface charge. Meanwhile, the inside and outside parts of this overall induced surface charge density are directly and inversely proportional, respectively, to the electrode's radius and the electrolyte's molar concentration. Moreover, the induced surface charge density inside and outside the pores are inversely and directly proportional, respectively, to the electrolyte's temperature. This is true for all the nano-pore electrodes. However, the highest induced surface charge densities, inside and outside the pore, are obtained for the slit-pore electrode, followed by the cylindrical and spherical nano-pore electrodes.

Lastly, the differential capacitance is observed to have some fascinating properties. Firstly, it was found that the differential capacitance is inversely proportional to the temperature, and that this factor has the least overall impact on the differential capacitance. Hence, in Figs. 5.1 and 5.2 the differential capacitance is plotted as a three dimensional surface, where its value depends on the electrode's radius and electrolyte's molar concentration. The difference between Figs. 5.1 and 5.2 lies in the range of values of both the electrode's radii and electrolyte's molar concentration. In Fig. 5.1 the electrode's radii ranges from 5 Å and 80 Å and the electrolyte's molar concentration achieves values up to 0.5 M, whereas Fig. 5.2 electrode's radii ranges from 5 Å and 15 Å and its electrolyte's molar concentration achieves values up to 0.1 M. Therefore, from Figs. 5.1 and 5.2 the differential capacitance behavior of the NPE is observed for large and small radii, and large and small concentrations, respectively. Consequently, it is observed that when the nano-pore electrode's radii is increased the differential capacitance follows, specifically the slit-pore achieve the highest differentials capacitances for larger radii. However, for the lowest radius, 5 Å, the spherical pore achieves the highest differential capacitances followed by the cylindrical pore, when low molar concentrations are used. Therefore, the differential capacitance is highly influenced by the electrolyte's molar concentration and the electrode's size.

Moreover, from the comparison between the linear and non-linear differential capacitances for solid electrodes, it is found that the linear case is a good approximation of the non-linear one for low electrolyte's molar concentrations.

The main objective of this thesis was to understand the structure of the electrical double layer, to achieve high differential capacitances. As a first main result, for this purpose, we found that the highest possible differential capacitance depends on the specific area ($m^2kg^{-1}$) of the electrode. Clearly,

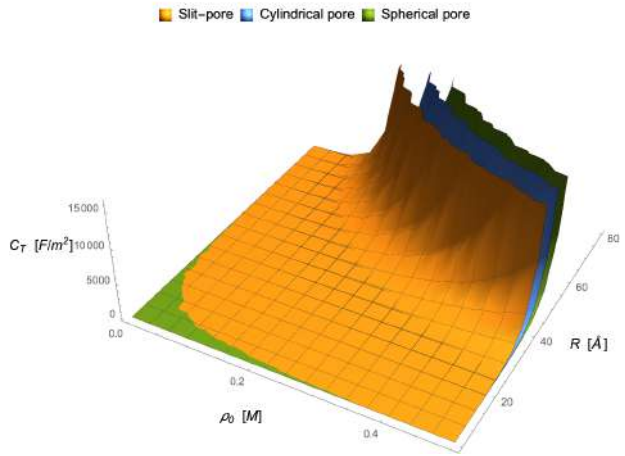


(a) View 1.

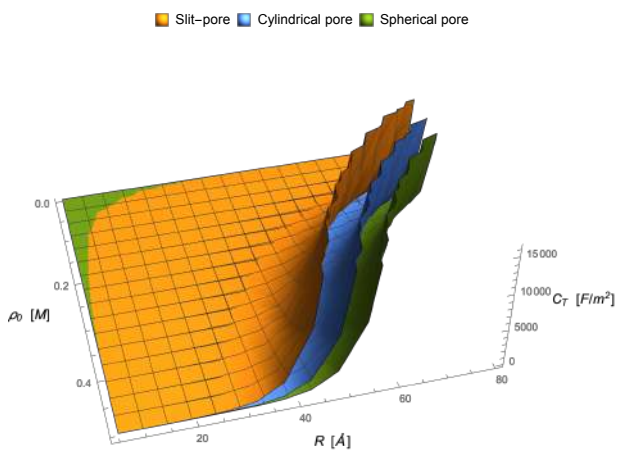


(b) View 2.

Figure 5.1: The differential capacitances, $C_T$, of different nano-pore electrodes, from electrode's radii of 5 Å and 80 Å and an electrolyte's molar concentration up to 0.5 M, in 3D. The electrolyte's temperature is set to 298.15 K and the pore's width to 5 Å.

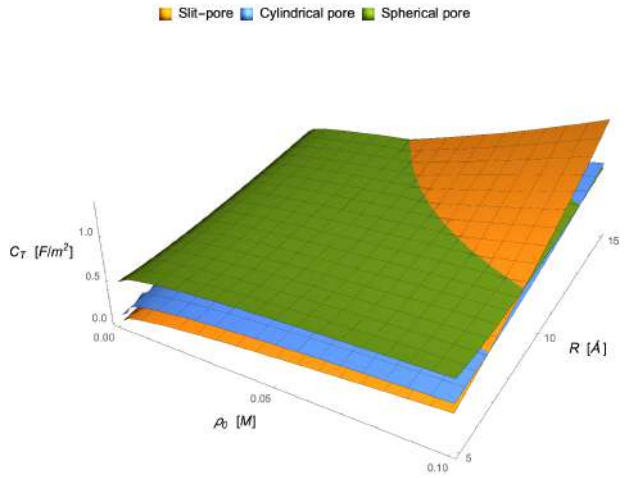


(a) View 1.

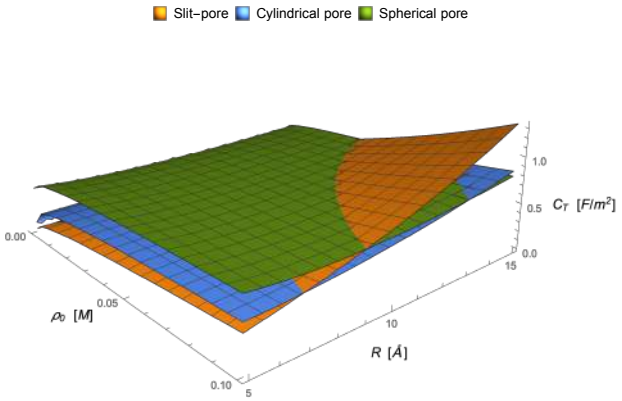


(b) View 2.

Figure 5.2: The differential capacitances, $C_T$, of different nano-pore electrodes, from electrode's radii of 5 Å and 15 Å and an electrolyte's molar concentration up to 0.1 M, in 3D. The electrolyte's temperature is set to 298.15 K and the pore's width to 5 Å.

the smaller the radius of the nano-electrode, the higher the specific area, and hence the higher the differential capacitance. Consequently, the nano-pores are more effective than the solid nano-electrodes; however, the internal radius of the nano-pore should be large enough to allow the electrolyte solution to get into the nano-pore. Therefore, the spherical nano-pore electrode accomplish these requirements. Moreover, such nano-pores could be connected in an electronic array, to increase the voltage and the capacitance, in series and in parallel, respectively, in a possible supercapacitor device.

In conclusion, given the same circumstances, the nano-pore electrodes achieve the highest differential capacitance, in comparison to the solid nano-electrodes; and the spherical and cylindrical topologies favor the capacitance, being of course the spherical nano-pore topology the most effective. Furthermore, the differential capacitance depends on the mean electrostatic potential, which in turns highly

depends on the nano-pore surface charge and on the ionic concentration. In consequence, the higher the molar concentration, the lower the mean electrostatic potential and the higher the differential capacitance. Lastly, even though the temperature has the least impact on the differential capacitance (the higher the temperature, the lower the capacitance), in a large array of nano-pores, closely packed, as components of a supercapacitor device, its temperature during operation will increase, hence decreasing the differential capacitance. Therefore, the temperature must be taken into account to achieve a high differential capacitance.

## 5.3 Future works

It is of interest to obtain the non-linear versions of the Poisson-Boltzmann model with the Stern restriction of the pores and of the remaining solid electrodes. This for comparison purposes, to find now the interval of validity of these non-linear cases. Furthermore, it is of great interest to obtain the HNC/MSA model or Monte Carlo results for any of the pores, both inside and outside. Currently not much works have been done considering the inside and outside pores, which should not be considered separately. As it was observed from our simple model, the inside and outside pores are linked. Furthermore, it would be of interest to find the impact that the pores' width has on the different electric parameters.

# Appendix A

# The single electrical double layer for different solid electrodes

In this appendix, the complete derivations of the single double layer for the different solid electrodes are shown. All of them are obtained by solving the Laplace and Poisson-Boltzmann equations in different coordinate systems. These are solved by assuming that the electric potentials are unidirectional. Therefore, they only depend on one axis, for the Cartesian coordinate system it is taken to be $x$, and for the cylindrical and spherical coordinate systems it is taken to be $r$ axis.

## A.1 The single electrical double layer of a solid planar electrode

The electric potential is obtained from the Poisson-Boltzmann equation with the Stern restriction. The linear and non-linear models share two common factors, the solution in the Helmholtz layer is the same, and the boundary conditions are identical. In the Laplace's interval the boundary conditions are $\psi(0) = \psi_0$ and $\psi(a/2) = \psi_H$, and in the Poisson-Boltzmann's interval $\psi(a/2) = \psi_H$ and $\psi(\infty) = 0$. Furthermore, they also follow Gauss' law. Therefore, the following solution of the Laplace interval is valid for both the p-LPBS and p-nLPBS cases.

From the first interval ($0 \leq x < \frac{a}{2}$) we have that the Laplace equation for a plane electrode is

$$\nabla^2\psi(x) = \frac{\mathrm{d}^2\psi}{\mathrm{d}x^2} = 0$$

The above is an ordinary differential equation which can be easily solved. We integrate both sides and find

$$\frac{\mathrm{d}\psi}{\mathrm{d}x} = C_1$$

From the Gauss' law, when $x = \frac{a}{2}$, we find that the value of our first constant is

$$\frac{\mathrm{d}\psi}{\mathrm{d}x} = -\frac{4\,\pi\,\sigma_M}{\varepsilon}$$

Where $\sigma_M$ is the electrode's surface charge. We integrate a second time and obtain

$$\psi(x) = -\frac{4\,\pi\,\sigma_M}{\varepsilon}\,x + C_2$$

From the boundary condition $\psi(0) = \psi_0$

$$\psi_0 = C_2$$

$$\psi(x) = -\frac{4\,\pi\,\sigma_{_M}}{\varepsilon}\,x + \psi_0$$

Moreover, from the boundary condition $\psi(\frac{a}{2}) = \psi_{_H}$ we have

$$\psi_{_H} = -\frac{4\,\pi\,\sigma_{_M}}{\varepsilon}\,\frac{a}{2} + \psi_0$$

Which means that electric potential between $0 \leq x < \frac{a}{2}$ is

$$\psi(x) = \frac{4\,\pi\,\sigma_{_M}}{\varepsilon}\left(\frac{a}{2} - x\right) + \psi_{_H} \tag{A.1}$$

Equation (A.1) is valid for the p-LPBS and p-nLPBS cases, the difference lies in the value that $\sigma_{_M}$ and $\psi_{_H}$ take for each one.

In the second interval ($x \geq \frac{a}{2}$), we have the Poisson-Boltzmann equation as

$$\nabla^2\psi(x) = \frac{\mathrm{d}^2\psi}{\mathrm{d}x^2} = -\frac{4\,\pi\,\rho_{_{el}}(x)}{\varepsilon} \tag{A.2}$$

Where the electric charge density is given by

$$\rho_{_{el}}(x) = z\,e\,(n_{_+} - n_{_-}) \tag{A.3}$$

where $z$ is the ion valence, $e$ is the electron charge, and $n_{_+}$ and $n_{_-}$ are the average charge concentration of co-ions and counter-ions, and they are given by the Maxwell-Boltzmann theorem

$$\left.\begin{aligned} n_{_-} &= n\exp(z_{_-}e\,\psi(x)/k\,T) \\ n_{_+} &= n\exp(-z_{_+}e\,\psi(x)/k\,T) \end{aligned}\right\} \tag{A.4}$$

$n$ [cm$^{-3}$] is the number of ions away from the surface, and it is given by $n = \rho_0 \times 10^{-3}\,\mathrm{N_A}$, with $\rho_0$ as the molar concentration.

From here forward, the solution of the PB-eq is divided in two different cases; the linear case (p-LPBS), and the non-linear case (p-nLPBS). The common constraint that both approaches use is that a symmetric electrolyte is utilized. The p-LPBS case incorporates another assumption, that the electric potential is very small, such that $z\,e\,\psi(x)/k\,T \ll 1$.

### A.1.1 The solution of the linearized Poisson-Boltzmann equation

For the p-LPBS, we have a symmetric electrolyte ($z_{_+} = z_{_-} = z$) and a very small electric potential, such that $z\,e\,\psi(x)/k\,T \ll 1$, then $\exp(z\,e\,\psi(x)/k\,T)$ is almost equal to $1 + z\,e\,\psi(x)/k\,T$. Therefore, the electric charge density in Eq. (A.3) is

$$\rho_{_{el}}(x) = -\frac{2\,n\,e^2\,z^2}{k\,T}\psi(x)$$

Hence, the PB-eq is

$$\left.\begin{aligned} \frac{\mathrm{d}^2\psi}{\mathrm{d}x^2} = \frac{8\,\pi\,n\,e^2\,z^2}{\varepsilon\,k\,T}\psi(x) &= \kappa^2\,\psi(x) \\ \text{with}\quad \kappa^2 &= \frac{8\,\pi\,n\,e^2\,z^2}{\varepsilon\,k\,T} \end{aligned}\right\} \tag{A.5}$$

In order to simplify the solution, we perform the following changes of variables.

$$y = \frac{z\,e\,\psi}{k\,T}, \quad y_{_H} = \frac{z\,e\,\psi_{_H}}{k\,T}, \quad \kappa^2 = \frac{8\,\pi\,n\,e^2\,z^2}{\varepsilon\,k\,T}, \quad \xi = \kappa\,x \tag{A.6}$$

On one hand, from the change of variable of $y$, one realizes that it is only a function of $\psi(x)$, and that $z\,e/k\,T$ is a constant. Consequently when one derives $y$ with respect of $\xi$, one obtains

$$\frac{\mathrm{d}y}{\mathrm{d}\xi} = \frac{\mathrm{d}}{\mathrm{d}\xi}\left(\frac{z\,e\,\psi}{k\,T}\right) = \frac{z\,e}{k\,T}\frac{\mathrm{d}\psi}{\mathrm{d}\xi}$$

$$\frac{\mathrm{d}^2y}{\mathrm{d}\xi^2} = \frac{\mathrm{d}}{\mathrm{d}\xi}\left(\frac{\mathrm{d}y}{\mathrm{d}\xi}\right) = \frac{\mathrm{d}}{\mathrm{d}\xi}\left(\frac{z\,e}{k\,T}\frac{\mathrm{d}\psi}{\mathrm{d}\xi}\right) = \frac{z\,e}{k\,T}\frac{\mathrm{d}^2\psi}{\mathrm{d}\xi^2}$$

On the other hand, the change of variable of $x$ is more straightforward, the derivative of $x$ with respect of $\xi$ is $\frac{\mathrm{d}x}{\mathrm{d}\xi} = \frac{1}{\kappa}$. Through the chain rule, one finds

$$\frac{\mathrm{d}\psi}{\mathrm{d}\xi} = \frac{\mathrm{d}\psi}{\mathrm{d}x}\frac{\mathrm{d}x}{\mathrm{d}\xi} = \frac{\mathrm{d}\psi}{\mathrm{d}x}\frac{1}{\kappa} = \frac{1}{\kappa}\frac{\mathrm{d}\psi}{\mathrm{d}x}$$

$$\frac{\mathrm{d}^2\psi}{\mathrm{d}\xi^2} = \frac{\mathrm{d}}{\mathrm{d}\xi}\left(\frac{\mathrm{d}\psi}{\mathrm{d}\xi}\right) = \frac{\mathrm{d}}{\mathrm{d}x}\left(\frac{\mathrm{d}\psi}{\mathrm{d}\xi}\right)\frac{\mathrm{d}x}{\mathrm{d}\xi} = \frac{\mathrm{d}}{\mathrm{d}x}\left(\frac{1}{\kappa}\frac{\mathrm{d}\psi}{\mathrm{d}x}\right)\frac{\mathrm{d}x}{\mathrm{d}\xi} = \frac{1}{\kappa}\frac{\mathrm{d}^2\psi}{\mathrm{d}x^2}\frac{1}{\kappa} = \frac{1}{\kappa^2}\frac{\mathrm{d}^2\psi}{\mathrm{d}x^2}$$

Consequently, from our change of variables we have

$$\frac{\mathrm{d}^2y}{\mathrm{d}\xi^2} = \frac{z\,e}{k\,T}\frac{1}{\kappa^2}\frac{\mathrm{d}^2\psi}{\mathrm{d}x^2} \tag{A.7}$$

Substituting Eq. (A.5) in Eq. (A.7), and simplifying we obtain

$$\frac{\mathrm{d}^2y}{\mathrm{d}\xi^2} = y \tag{A.8}$$

The solution of this differential equation is achieved through the following steps. We multiply Eq. (A.8) by $\frac{\mathrm{d}y}{\mathrm{d}\xi}$ and integrate

$$\int \frac{\mathrm{d}y}{\mathrm{d}\xi}\frac{\mathrm{d}^2y}{\mathrm{d}\xi^2} = \int y\frac{\mathrm{d}y}{\mathrm{d}\xi}$$

$$\frac{1}{2}\left(\frac{\mathrm{d}y}{\mathrm{d}\xi}\right)^2 = c_1 + \frac{y^2}{2}$$

Introducing the boundary conditions of $y = y' = 0$ for $\xi = \infty$

$$\frac{1}{2}\cdot 0^2 = c_1 + \frac{0^2}{2} \;\longrightarrow\; c_1 = 0$$

$$\left(\frac{\mathrm{d}y}{\mathrm{d}\xi}\right)^2 = y^2$$

Since for positive values of $y$ the derivative $\frac{\mathrm{d}y}{\mathrm{d}\xi}$ is negative, $x$ and $\xi$ are considered positive from the surface towards the bulk of the solution. Hence

$$\frac{\mathrm{d}y}{\mathrm{d}\xi} = -\sqrt{y^2} = -y$$

$$\int \frac{\mathrm{d}y}{y} = -\int \mathrm{d}\xi$$

$$\ln(y) = -\xi + c_2$$

Applying the boundary condition of $y = y_H$ in $\xi = \frac{\kappa\, a}{2}$

$$\ln(y_H) = -\frac{\kappa\, a}{2} + c_2 \;\longrightarrow\; c_2 = \frac{\kappa\, a}{2} + \ln(y_H)$$

$$\ln(y) = -\xi + \frac{\kappa\, a}{2} + \ln(y_H)$$

$$y(\xi) = y_H\, e^{-\xi}\, e^{\kappa\, a/2}$$

Substituting the values of $y$ and $y_H$, we obtain the solution in terms of our original variables.

$$\psi(x) = \psi_H\, e^{\kappa\left(\frac{a}{2} - x\right)}$$

Now we find the relation between $\sigma_M$ and $\psi_H$, in order to leave Eq. (A.1) only in terms of $\psi_H$. The definition of $\sigma_M$ is given by the Gauss' law as

$$\sigma_M = -\int_{a/2}^{\infty} \rho_{el}(x)\, \mathrm{d}x = \frac{\varepsilon}{4\,\pi} \int_{a/2}^{\infty} \frac{\mathrm{d}^2\psi}{\mathrm{d}x^2}\, \mathrm{d}x = -\frac{\varepsilon}{4\,\pi} \left(\frac{\mathrm{d}\psi}{\mathrm{d}x}\right)_{x=\frac{a}{2}} \tag{A.9}$$

Therefore, the derivative of our linearized Poisson-Boltzmann solution is obtained, and substituted in Eq. (A.9)

$$\frac{\mathrm{d}\psi}{\mathrm{d}x} = -\kappa\, \psi_H\, e^{\kappa\left(\frac{a}{2} - x\right)}$$

$$\sigma_M = \frac{\varepsilon\, \kappa\, \psi_H}{4\,\pi}$$

Therefore, the value of $\psi_H$ is

$$\psi_H = \frac{4\,\pi\, \sigma_M}{\varepsilon\, \kappa} \tag{A.10}$$

And consequently, $\psi_0$ is

$$\psi_0 = \psi_H + \frac{4\,\pi\, \sigma_M}{\varepsilon}\, \frac{a}{2} = \frac{4\,\pi\, \sigma_M}{\varepsilon\, \kappa} \left(1 + \frac{\kappa\, a}{2}\right) \tag{A.11}$$

Then, the mean electrostatic potential is given by

$$\psi(x) = \begin{cases} \psi_H\, \left[1 + \kappa(\frac{a}{2} - x)\right] & \text{if } 0 \le x \le \frac{a}{2} \\ \psi_H\, e^{\kappa\left(\frac{a}{2} - x\right)} & \text{if } x \ge \frac{a}{2} \end{cases}$$

Meanwhile, the induced surface charge density is given by

$$\sigma(x) = -\int_{x}^{\infty} \rho_{el}(x)\, \mathrm{d}x = \frac{\varepsilon}{4\,\pi} \int_{x}^{\infty} \frac{\mathrm{d}^2\psi}{\mathrm{d}x^2}\, \mathrm{d}x = -\frac{\varepsilon}{4\,\pi} \left(\frac{\mathrm{d}\psi}{\mathrm{d}x}\right)_{x} \tag{A.12}$$

Hence, substituting the derivative of the mean electrostatic potential in Eq. (A.12), we obtain

$$\sigma(x) = \frac{\varepsilon\, \kappa}{4\,\pi}\, \psi_H\, e^{\kappa\left(\frac{a}{2} - x\right)}$$

This induced surface charge density is only valid for the interval $[x, \infty)$, where $x \ge \frac{a}{2}$. On the other hand, in the interval $0 \le x < \frac{a}{2}$ the induced surface charge density is zero, because of the ion's size restriction, the ions cannot get closer to the surface than half their diameter. Using the relation found in Eq. (A.10) the induced surface charge density can be expressed as

$$\sigma(x) = \begin{cases} 0 & \text{if } 0 \le x < \frac{a}{2} \\ \sigma_M\, e^{\kappa\left(\frac{a}{2} - x\right)} & \text{if } x \ge \frac{a}{2} \end{cases}$$

The co-ion and counter-ion distribution functions in the Laplace interval are equal to zero due to the ion's size restriction. However, in the Poisson-Boltzmann interval the co-ion and counter-ion distribution functions are obtained from the electric potential by

$$g_{+}(x) = \exp\left(-\frac{z\,e\,\psi(x)}{k\,T}\right) \tag{A.13}$$

$$g_{-}(x) = \exp\left(\frac{z\,e\,\psi(x)}{k\,T}\right) \tag{A.14}$$

Hence, simplifying we have

$$g_{+}(x) = \begin{cases} 0 & \text{if } 0 \leq x < \frac{a}{2} \\ \exp\left(-\frac{z\,e}{k\,T}\,\psi_H\,e^{\kappa\,(\frac{a}{2}-x)}\right) & \text{if } x \geq \frac{a}{2} \end{cases}$$

$$g_{-}(x) = \begin{cases} 0 & \text{if } 0 \leq x < \frac{a}{2} \\ \exp\left(\frac{z\,e}{k\,T}\,\psi_H\,e^{\kappa\,(\frac{a}{2}-x)}\right) & \text{if } x \geq \frac{a}{2} \end{cases}$$

The total differential capacitance is calculated as the sum of the differential capacitances in both intervals.

$$\frac{1}{C_T} = \frac{1}{C_{Lap}} + \frac{1}{C_{PB}}$$

Where the subindexes $Lap$ and $PB$ indicate the Laplace and Poisson-Boltzmann intervals, they are defined as

$$\frac{1}{C_{Lap}} = \frac{\mathrm{d}\psi_0}{\mathrm{d}\sigma_M} = \frac{4\,\pi}{\varepsilon\,\kappa}\left(1 + \frac{\kappa\,a}{2}\right)$$

$$\frac{1}{C_{PB}} = \frac{\mathrm{d}\psi_H}{\mathrm{d}\sigma_M} = \frac{4\,\pi}{\varepsilon\,\kappa}$$

So, we find that the total differential capacitance is

$$\frac{1}{C_T} = \frac{4\,\pi}{\varepsilon\,\kappa}\left(1 + \frac{\kappa\,a}{2}\right) + \frac{4\,\pi}{\varepsilon\,\kappa}$$

$$\frac{1}{C_T} = \frac{4\,\pi}{\varepsilon\,\kappa}\left(2 + \frac{\kappa\,a}{2}\right)$$

$$C_T = \left[\frac{4\,\pi}{\varepsilon\,\kappa}\left(2 + \frac{\kappa\,a}{2}\right)\right]^{-1}$$

### A.1.2 The solution of the non-linearized Poisson-Boltzmann equation

Since we are dealing with a symmetric electrolyte the valencies are equal ($z_{+} = z_{-} = z$) and the electric charge is given by Eq. (A.3). Hence,

$$\rho_{el}(x) = -2\,n\,z\,e\,\sinh\left(\frac{z\,e}{k\,T}\psi(x)\right)$$

Therefore, Eq. (A.2) is

$$\frac{\mathrm{d}^2\psi}{\mathrm{d}x^2} = \frac{8\,\pi\,n\,z\,e}{\varepsilon}\sinh\left(\frac{z\,e}{k\,T}\psi(x)\right) \tag{A.15}$$

In order to simplify the solution of the problem, we perform the changes of variables in Eq. (A.6). Therefore, substituting Eq. (A.15) in Eq. (A.7), and simplifying we obtain

$$\frac{\mathrm{d}^2 y}{\mathrm{d}\xi^2} = \sinh(y) \tag{A.16}$$

The solution of this equation is achieved through the next steps. We first rewrite the hyperbolic sine in Eq. (A.16) on its exponential form and afterwards we multiply it by $\frac{\mathrm{d}y}{\mathrm{d}\xi}$ and integrate

$$2\frac{\mathrm{d}^2 y}{\mathrm{d}\xi^2} = e^{y} - e^{-y}$$

$$\int 2\,\frac{\mathrm{d}^2 y}{\mathrm{d}\xi^2}\,\frac{\mathrm{d}y}{\mathrm{d}\xi} = \int \left(e^{y} - e^{-y}\right)\,\frac{\mathrm{d}y}{\mathrm{d}\xi}$$

$$\left(\frac{\mathrm{d}y}{\mathrm{d}\xi}\right)^2 = e^{y} - (-1)\,e^{-y} + c_1$$

$$\left(\frac{\mathrm{d}y}{\mathrm{d}\xi}\right)^2 = e^{y} + e^{-y} + c_1$$

Introducing the boundary condition of $y = y' = 0$ for $\xi = \infty$

$$(0)^2 = e^{0} + e^{-0} + c_1 \Longrightarrow c_1 = -2$$

$$\left(\frac{\mathrm{d}y}{\mathrm{d}\xi}\right)^2 = e^{y} + e^{-y} - 2$$

Since for positive values of $y$ the derivative $\frac{\mathrm{d}y}{\mathrm{d}\xi}$ is negative, $x$ and $\xi$ are considered positive from the surface towards the bulk of the solution. Therefore

$$\frac{\mathrm{d}y}{\mathrm{d}\xi} = -\sqrt{e^{y} + e^{-y} - 2}$$

Now, since the hyperbolic cosine is equal to $\frac{\exp(y)+\exp(-y)}{2}$, the above is

$$\frac{\mathrm{d}y}{\mathrm{d}\xi} = -\sqrt{2\,\cosh(y) - 2} = -\sqrt{2\,\left[\cosh(y) - 1\right]}$$

Moreover, from the relation between $\sinh(u)$ and $\cosh(u)$, $\sinh^2(u) = \frac{1}{2}\left[\cosh(2u) - 1\right]$, the above is rewritten as

$$\frac{\mathrm{d}y}{\mathrm{d}\xi} = -\sqrt{2\,\left[2\,\sinh^2\!\left(\frac{y}{2}\right)\right]} = -2\,\sinh\!\left(\frac{y}{2}\right) \tag{A.17}$$

Once again, we rewrite the hyperbolic sinus in Eq. (A.17) on its exponential form and perform the change of variable, $a = e^{y/2}$, with $\mathrm{d}a = \frac{1}{2}\,e^{y/2}\,\mathrm{d}y$, and with some manipulation

$$\frac{\mathrm{d}y}{\mathrm{d}\xi} = -\left(e^{y/2} - e^{-y/2}\right)$$

$$\frac{\mathrm{d}y}{e^{y/2} - e^{-y/2}} = -\,\mathrm{d}\xi$$

$$\frac{\mathrm{d}y}{e^{y/2} - e^{-y/2}} = \frac{2\,\mathrm{d}a}{e^{y/2}\left(e^{y/2} - e^{-y/2}\right)} = \frac{2\,\mathrm{d}a}{(e^{y/2})^2 - 1} = \frac{2\,\mathrm{d}a}{a^2 - 1}$$

$$\frac{2\,\mathrm{d}a}{a^2-1} = \frac{A}{a+1} + \frac{B}{a-1} = \frac{A\,a - A + B\,a + B}{a^2-1}$$

$$\left.\begin{aligned}(A+B)\,a &= 0\\ -A+B &= \mathrm{d}a\end{aligned}\right\} \quad \begin{aligned}A &= -\mathrm{d}a\\ B &= \mathrm{d}a\end{aligned}$$

$$\int\left(\frac{\mathrm{d}a}{a-1} - \frac{\mathrm{d}a}{a+1}\right) = \int -\mathrm{d}\xi$$

$$\ln(a-1) - \ln(a+1) = -\xi + c_2$$

$$\ln\left(\frac{e^{y/2}-1}{e^{y/2}+1}\right) = -\xi + c_2$$

Applying the boundary condition of $y = y_H$ in $\xi = \frac{\kappa\,a}{2}$

$$\ln\left(\frac{e^{y_H/2}-1}{e^{y_H/2}+1}\right) = -\frac{\kappa\,a}{2} + c_2 \;\longrightarrow\; c_2 = \frac{\kappa\,a}{2} + \ln\left(\frac{e^{y_H/2}-1}{e^{y_H/2}+1}\right)$$

Hence the solution of Eq. (A.15) in terms of our change of variables is

$$\ln\left(\frac{e^{y/2}-1}{e^{y/2}+1}\right) = -\xi + \frac{\kappa\,a}{2} + \ln\left(\frac{e^{y_H/2}-1}{e^{y_H/2}+1}\right)$$

In order to leave this equation in terms of our original variables, we first clear our equation in terms of $y$ and afterwards we make the change of variables.

$$\frac{e^{y/2}-1}{e^{y/2}+1} = \frac{e^{y_H/2}-1}{e^{y_H/2}+1}\,e^{-\xi}\,e^{\kappa\,a/2}$$

$$1 - \frac{2}{e^{y/2}+1} = \frac{e^{y_H/2}-1}{e^{y_H/2}+1}\,e^{-\xi}\,e^{\kappa\,a/2}$$

$$1 - \frac{e^{y_H/2}-1}{e^{y_H/2}+1}\,e^{-\xi}\,e^{\kappa\,a/2} = \frac{2}{e^{y/2}+1}$$

$$\left(e^{y/2}+1\right)\left[1 - \frac{e^{y_H/2}-1}{e^{y_H/2}+1}\,e^{-\xi}\,e^{\kappa\,a/2}\right] = 2$$

$$e^{y/2}\left[1 - \frac{e^{y_H/2}-1}{e^{y_H/2}+1}\,e^{-\xi}\,e^{\kappa\,a/2}\right] = 2 - 1 + \frac{e^{y_H/2}-1}{e^{y_H/2}+1}\,e^{-\xi}\,e^{\kappa\,a/2}$$

$$e^{y/2}\left[\left(e^{y_H/2}+1\right) - \left(e^{y_H/2}-1\right)\,e^{-\xi}\,e^{\kappa\,a/2}\right] = \left(e^{y_H/2}+1\right) + \left(e^{y_H/2}-1\right)\,e^{-\xi}\,e^{\kappa\,a/2}$$

$$e^{y/2} = \frac{\left(e^{y_H/2}+1\right) + \left(e^{y_H/2}-1\right)\,e^{-\xi}\,e^{\kappa\,a/2}}{\left(e^{y_H/2}+1\right) - \left(e^{y_H/2}-1\right)\,e^{-\xi}\,e^{\kappa\,a/2}}$$

$$y = 2\ln\left(\frac{\left(e^{y_H/2}+1\right) + \left(e^{y_H/2}-1\right)\,e^{-\xi}\,e^{\kappa\,a/2}}{\left(e^{y_H/2}+1\right) - \left(e^{y_H/2}-1\right)\,e^{-\xi}\,e^{\kappa\,a/2}}\right)$$

$$\psi(x) = \frac{2\,k\,T}{z\,e}\ln\left(\frac{\left(\exp\left(\frac{z\,e}{k\,T}\,\frac{\psi_H}{2}\right)+1\right) + \left(\exp\left(\frac{z\,e}{k\,T}\,\frac{\psi_H}{2}\right)-1\right)\,e^{\kappa\left(\frac{a}{2}-x\right)}}{\left(\exp\left(\frac{z\,e}{k\,T}\,\frac{\psi_H}{2}\right)+1\right) - \left(\exp\left(\frac{z\,e}{k\,T}\,\frac{\psi_H}{2}\right)-1\right)\,e^{\kappa\left(\frac{a}{2}-x\right)}}\right)$$

Now we find the relation between $\sigma_M$ and $\psi_H$, from Eq. (A.9). Therefore, the derivative of our p-nLPBS solution must be obtained. To do so we perform three changes of variables in order to simplify the derivation, and for clearness we use $A^+ = \exp\left(\frac{z\,e}{k\,T}\,\frac{\psi_H}{2}\right) + 1$ and $A^- = \exp\left(\frac{z\,e}{k\,T}\,\frac{\psi_H}{2}\right) - 1$.

$$\psi(x) = \frac{2\,k\,T}{z\,e}\,\ln(u)$$

$$\frac{\mathrm{d}\psi}{\mathrm{d}x} = \frac{2\,k\,T}{z\,e}\frac{1}{u}\frac{\mathrm{d}u}{\mathrm{d}x}$$

$$u = \frac{v}{w} = \frac{A^+ + A^-\,e^{\kappa\left(\frac{a}{2}-x\right)}}{A^+ - A^-\,e^{\kappa\left(\frac{a}{2}-x\right)}}$$

$$\frac{\mathrm{d}}{\mathrm{d}x}\left(\frac{v}{w}\right) = \frac{w\,(\mathrm{d}v\,/\,\mathrm{d}x) - v\,(\mathrm{d}w\,/\,\mathrm{d}x)}{w^2}$$

$$\frac{\mathrm{d}v}{\mathrm{d}x} = -\kappa\,A^-\,e^{\kappa\left(\frac{a}{2}-x\right)}$$

$$\frac{\mathrm{d}w}{\mathrm{d}x} = \kappa\,A^-\,e^{\kappa\left(\frac{a}{2}-x\right)}$$

$$\frac{\mathrm{d}u}{\mathrm{d}x} = -\frac{\kappa\,A^-\,e^{\kappa\left(\frac{a}{2}-x\right)}\left[A^+ - A^-\,e^{\kappa\left(\frac{a}{2}-x\right)}\right] + \kappa\,A^-\,e^{\kappa\left(\frac{a}{2}-x\right)}\left[A^+ + A^-\,e^{\kappa\left(\frac{a}{2}-x\right)}\right]}{\left[A^+ - A^-\,e^{\kappa\left(\frac{a}{2}-x\right)}\right]^2}$$

$$\frac{\mathrm{d}u}{\mathrm{d}x} = -\frac{\kappa\,A^-\,e^{\kappa\left(\frac{a}{2}-x\right)}\,[2\,A^+]}{\left[A^+ - A^-\,e^{\kappa\left(\frac{a}{2}-x\right)}\right]^2} = -\frac{2\,\kappa\,A^+\,A^-\,e^{\kappa\left(\frac{a}{2}-x\right)}}{\left[A^+ - A^-\,e^{\kappa\left(\frac{a}{2}-x\right)}\right]^2}$$

$$\frac{\mathrm{d}\psi}{\mathrm{d}x} = -\frac{2\,k\,T}{z\,e}\left(\frac{A^+ - A^-\,e^{\kappa\left(\frac{a}{2}-x\right)}}{A^+ + A^-\,e^{\kappa\left(\frac{a}{2}-x\right)}}\right)\frac{2\,\kappa\,A^+\,A^-\,e^{\kappa\left(\frac{a}{2}-x\right)}}{\left[A^+ - A^-\,e^{\kappa\left(\frac{a}{2}-x\right)}\right]^2}$$

$$\frac{\mathrm{d}\psi}{\mathrm{d}x} = -\frac{4\,\kappa\,k\,T}{z\,e}\frac{A^+\,A^-\,e^{\kappa\left(\frac{a}{2}-x\right)}}{\left(A^+ + A^-\,e^{\kappa\left(\frac{a}{2}-x\right)}\right)\left(A^+ - A^-\,e^{\kappa\left(\frac{a}{2}-x\right)}\right)}$$

Substituting this derivative in Eq. (A.9) we obtain

$$\sigma_M = \frac{\varepsilon}{4\,\pi}\frac{4\,\kappa\,k\,T}{z\,e}\frac{A^+\,A^-}{(A^+ + A^-)\,(A^+ - A^-)}$$

$$\sigma_M = \frac{\varepsilon\,\kappa\,k\,T}{\pi\,z\,e}\frac{A^+\,A^-}{\left((A^+)^2 - (A^-)^2\right)}$$

$$\sigma_M = \frac{\varepsilon\,\kappa\,k\,T}{\pi\,z\,e}\frac{\left(\exp\left(\frac{z\,e}{k\,T}\,\frac{\psi_H}{2}\right)+1\right)\left(\exp\left(\frac{z\,e}{k\,T}\,\frac{\psi_H}{2}\right)-1\right)}{\left(\left(\exp\left(\frac{z\,e}{k\,T}\,\frac{\psi_H}{2}\right)+1\right)^2 - \left(\exp\left(\frac{z\,e}{k\,T}\,\frac{\psi_H}{2}\right)-1\right)^2\right)}$$

For clearness, we now use the change of variable, $y_H$

$$\sigma_M = \frac{\varepsilon\,\kappa\,k\,T}{\pi\,z\,e}\frac{\left(e^{y_H/2}+1\right)\left(e^{y_H/2}-1\right)}{\left(\left(e^{y_H/2}+1\right)^2 - \left(e^{y_H/2}-1\right)^2\right)}$$

$$\sigma_M = \frac{\varepsilon\,\kappa\,k\,T}{\pi\,z\,e}\,\frac{e^{y_H}-1}{\left(e^{y_H}+2\,e^{y_H/2}+1-\left(e^{y_H}-2\,e^{y_H/2}+1\right)\right)}$$

$$\sigma_M = \frac{\varepsilon\,\kappa\,k\,T}{\pi\,z\,e}\,\frac{e^{y_H}-1}{4\,e^{y_H/2}}$$

$$\sigma_M = \frac{\varepsilon\,\kappa\,k\,T}{2\,\pi\,z\,e}\,\frac{e^{y_H/2}-e^{-y_H/2}}{2}$$

$$\sigma_M = \frac{\varepsilon\,\kappa\,k\,T}{2\,\pi\,z\,e}\,\sinh\left(\frac{z\,e\,\psi_H}{2\,k\,T}\right)$$

Therefore, the value of $\psi_H$ is

$$\psi_H = \frac{2\,k\,T}{z\,e}\,\sinh^{-1}\left(\frac{2\,\pi\,z\,e\,\sigma_M}{\varepsilon\,\kappa\,k\,T}\right) \tag{A.18}$$

And consequently, $\psi_0$ is

$$\psi_0 = \psi_H + \frac{4\,\pi\,\sigma_M}{\varepsilon}\,\frac{a}{2} = \frac{2\,k\,T}{z\,e}\,\sinh^{-1}\left(\frac{2\,\pi\,z\,e\,\sigma_M}{\varepsilon\,\kappa\,k\,T}\right) + \frac{4\,\pi\,\sigma_M}{\varepsilon}\,\frac{a}{2} \tag{A.19}$$

Then, the electric potential is given by

$$\psi(x) = \begin{cases} \frac{2\,\kappa\,k\,T}{z\,e}\,\sinh\left(\frac{z\,e\,\psi_H}{2\,k\,T}\right)\left(\frac{a}{2}-x\right)+\psi_H & \text{if } 0 \le x \le \frac{a}{2} \\ \frac{2\,k\,T}{z\,e}\,\ln\left(\frac{\left(\exp\left(\frac{z\,e}{k\,T}\,\frac{\psi_H}{2}\right)+1\right)+\left(\exp\left(\frac{z\,e}{k\,T}\,\frac{\psi_H}{2}\right)-1\right)\,e^{\kappa\left(\frac{a}{2}-x\right)}}{\left(\exp\left(\frac{z\,e}{k\,T}\,\frac{\psi_H}{2}\right)+1\right)-\left(\exp\left(\frac{z\,e}{k\,T}\,\frac{\psi_H}{2}\right)-1\right)\,e^{\kappa\left(\frac{a}{2}-x\right)}}\right) & \text{if } x \ge \frac{a}{2} \end{cases}$$

Meanwhile, the induced surface charge density is obtained by substituting the derivative of the electric potential in Eq. (A.12) and simplifying

$$\sigma(x) = \frac{\varepsilon\,\kappa\,k\,T}{\pi\,z\,e}\,\frac{\left(\exp\left(\frac{z\,e}{k\,T}\,\psi_H\right)-1\right)\,e^{\kappa\left(\frac{a}{2}-x\right)}}{\left(\exp\left(\frac{z\,e}{k\,T}\,\frac{\psi_H}{2}\right)+1\right)^2-\left[\left(\exp\left(\frac{z\,e}{k\,T}\,\frac{\psi_H}{2}\right)-1\right)\,e^{\kappa\left(\frac{a}{2}-x\right)}\right]^2}$$

This induced surface charge density is only valid for the interval $[x,\infty)$, where $x \ge \frac{a}{2}$; whereas, for the interval $0 \le x < \frac{a}{2}$ the induced surface charge density is zero, because of the ion's size restriction, the ions cannot get closer to the surface than half their diameter. Hence, the induced surface charge density is

$$\sigma(x) = \begin{cases} 0 & \text{if } 0 \le x < \frac{a}{2} \\ \frac{\varepsilon\,\kappa\,k\,T}{\pi\,z\,e}\,\frac{\left(\exp\left(\frac{z\,e}{k\,T}\,\psi_H\right)-1\right)\,e^{\kappa\left(\frac{a}{2}-x\right)}}{\left(\exp\left(\frac{z\,e}{k\,T}\,\frac{\psi_H}{2}\right)+1\right)^2-\left[\left(\exp\left(\frac{z\,e}{k\,T}\,\frac{\psi_H}{2}\right)-1\right)\,e^{\kappa\left(\frac{a}{2}-x\right)}\right]^2} & \text{if } x \ge \frac{a}{2} \end{cases}$$

With the electric potential in the Poisson-Boltzmann interval one obtains the co-ion and counter-ion distribution functions by Eqs. (A.13) and (A.14). Whereas, for the Laplace interval, because of the ion's size restriction the co-ion and counter-ion distribution functions are equal to zero. Hence, we find

$$g_+(x) = \begin{cases} 0 & \text{if } 0 \le x < \frac{a}{2} \\ \left[\frac{\left(\exp\left(\frac{z\,e}{k\,T}\,\frac{\psi_H}{2}\right)+1\right)+\left(\exp\left(\frac{z\,e}{k\,T}\,\frac{\psi_H}{2}\right)-1\right)\,e^{\kappa\left(\frac{a}{2}-x\right)}}{\left(\exp\left(\frac{z\,e}{k\,T}\,\frac{\psi_H}{2}\right)+1\right)-\left(\exp\left(\frac{z\,e}{k\,T}\,\frac{\psi_H}{2}\right)-1\right)\,e^{\kappa\left(\frac{a}{2}-x\right)}}\right]^{-2} & \text{if } x \ge \frac{a}{2} \end{cases}$$

$$g_{-}(x) = \begin{cases} 0 & \text{if } 0 \leq x < \frac{a}{2} \\ \left[ \frac{\left(\exp\left(\frac{z\,e}{k\,T}\,\frac{\psi_H}{2}\right)+1\right)+\left(\exp\left(\frac{z\,e}{k\,T}\,\frac{\psi_H}{2}\right)-1\right)e^{\kappa\left(\frac{a}{2}-x\right)}}{\left(\exp\left(\frac{z\,e}{k\,T}\,\frac{\psi_H}{2}\right)+1\right)-\left(\exp\left(\frac{z\,e}{k\,T}\,\frac{\psi_H}{2}\right)-1\right)e^{\kappa\left(\frac{a}{2}-x\right)}} \right]^2 & \text{if } x \geq \frac{a}{2} \end{cases}$$

Meanwhile, the total differential capacitance is calculated as the sum of the differential capacitances in both intervals.

$$\frac{1}{C_T} = \frac{1}{C_{Lap}} + \frac{1}{C_{PB}}$$

The subindexes *Lap* and *PB* indicate the Laplace and Poisson-Boltzmann intervals, they are defined as

$$\frac{1}{C_{Lap}} = \frac{\mathrm{d}\psi_0}{\mathrm{d}\sigma_M} = \frac{4\,\pi}{\varepsilon\,\kappa}\frac{\left(1+\frac{\kappa\,a}{2}\right)}{\sqrt{1+\left(\frac{2\,\pi\,z\,e\,\sigma_M}{\varepsilon\,\kappa\,k\,T}\right)^2}}$$

$$\frac{1}{C_{PB}} = \frac{\mathrm{d}\psi_H}{\mathrm{d}\sigma_M} = \frac{4\,\pi}{\varepsilon\,\kappa}\frac{1}{\sqrt{1+\left(\frac{2\,\pi\,z\,e\,\sigma_M}{\varepsilon\,\kappa\,k\,T}\right)^2}}$$

So, we find that the total differential capacitance is

$$\frac{1}{C_T} = \frac{4\,\pi}{\varepsilon\,\kappa}\frac{\left(1+\frac{\kappa\,a}{2}\right)}{\sqrt{1+\left(\frac{2\,\pi\,z\,e\,\sigma_M}{\varepsilon\,\kappa\,k\,T}\right)^2}} + \frac{4\,\pi}{\varepsilon\,\kappa}\frac{1}{\sqrt{1+\left(\frac{2\,\pi\,z\,e\,\sigma_M}{\varepsilon\,\kappa\,k\,T}\right)^2}}$$

$$\frac{1}{C_T} = \frac{4\,\pi}{\varepsilon\,\kappa}\frac{\left(2+\frac{\kappa\,a}{2}\right)}{\sqrt{1+\left(\frac{2\,\pi\,z\,e\,\sigma_M}{\varepsilon\,\kappa\,k\,T}\right)^2}}$$

$$C_T = \left[\frac{4\,\pi}{\varepsilon\,\kappa}\frac{\left(2+\frac{\kappa\,a}{2}\right)}{\sqrt{1+\left(\frac{2\,\pi\,z\,e\,\sigma_M}{\varepsilon\,\kappa\,k\,T}\right)^2}}\right]^{-1}$$

## A.2 The solution of the linearized Poisson-Boltzmann equation for a solid cylindrical electrode

For a cylindrical electrode, the Laplacian is given by

$$\nabla^2 \equiv \frac{1}{r}\frac{\partial}{\partial r}\left(r\frac{\partial}{\partial r}\right) + \frac{1}{r^2}\left(\frac{\partial^2}{\partial\theta^2}\right) + \frac{\partial^2}{\partial z^2}$$

For the solution of the EDL in a solid cylindrical electrode, one starts from the assumption that the electric potential, $\psi$, only depends on the radius. Hence, the Laplace equation for the cylindrical electrode is

$$\nabla^2\psi = \frac{1}{r}\frac{\partial}{\partial r}\left(r\frac{\partial\psi}{\partial r}\right) = \frac{\mathrm{d}^2\psi}{\mathrm{d}r^2} + \frac{1}{r}\frac{\mathrm{d}\psi}{\mathrm{d}r} = 0$$

The above is an ordinary differential equation and is solved easily by the change of variables of $\varphi(r) = \frac{\mathrm{d}\psi}{\mathrm{d}r}$. We rewrite the Laplace equation in terms of our new variable $\varphi(r)$ and integrate

$$\frac{\mathrm{d}\varphi}{\mathrm{d}r} + \frac{\varphi(r)}{r} = 0$$

$$\frac{\mathrm{d}\varphi}{\mathrm{d}r} = -\frac{\varphi(r)}{r}$$

$$\int \frac{\mathrm{d}\varphi}{\varphi} = -\int \frac{\mathrm{d}r}{r}$$
$$\ln(\varphi(r)) = -\ln(r) + C_1$$
$$\varphi(r) = \frac{C_1}{r}$$

Substituting our change of variable $\varphi(r) = \frac{\mathrm{d}\psi}{\mathrm{d}r}$ and from the Gauss' law in $r = R + \frac{a}{2}$, we find the value of the first constant

$$\frac{\mathrm{d}\psi}{\mathrm{d}r} = \frac{C_1}{r} = -\frac{4\,\pi\,\sigma_M}{\varepsilon} \longrightarrow C_1 = -\frac{4\,\pi\,\sigma_M}{\varepsilon}\,r$$
$$\frac{\mathrm{d}\psi}{\mathrm{d}r} = -\frac{4\,\pi\,\sigma_M}{\varepsilon}$$
$$\psi(r) = -\frac{4\,\pi\,\sigma_M}{\varepsilon}\,r + C_2$$

From our boundary condition $\psi(R) = \psi_R$

$$\psi(R) = -\frac{4\,\pi\,\sigma_M}{\varepsilon}\,R + C_2 = \psi_R \longrightarrow C_2 = \psi_R + \frac{4\,\pi\,\sigma_M}{\varepsilon}\,R$$
$$\psi(r) = \psi_R + \frac{4\,\pi\,\sigma_M}{\varepsilon}\,(R - r)$$

Meanwhile from the boundary condition, $\psi(R + \frac{a}{2}) = \psi_H$, we have

$$\psi\left(R + \frac{a}{2}\right) = \psi_R - \frac{4\,\pi\,\sigma_M}{\varepsilon}\,\frac{a}{2} = \psi_H \longrightarrow \psi_R = \psi_H + \frac{4\,\pi\,\sigma_M}{\varepsilon}\,\frac{a}{2}$$

Hence, our solution for the Laplace interval in terms of $\psi_H$ is

$$\psi(r) = \psi_H + \frac{4\,\pi\,\sigma_M}{\varepsilon}\,\left(R + \frac{a}{2} - r\right)$$

Meanwhile, for the PB interval, we have that the electric charge density is the same as the p-LPBS equation, given by

$$\rho_{el}(r) = -\frac{2\,n\,e^2\,z^2}{k\,T}\psi(r)$$

Therefore, the c-LPBS given by Eq. (A.2), is

$$\left.\begin{aligned} \frac{\mathrm{d}^2\psi}{\mathrm{d}r^2} + \frac{1}{r}\frac{\mathrm{d}\psi}{\mathrm{d}r} = \frac{8\,\pi\,n\,e^2\,z^2}{\varepsilon\,k\,T}\psi(r) = \kappa^2\,\psi(r) \\ \text{with} \quad \kappa^2 = \frac{8\,\pi\,n\,e^2\,z^2}{\varepsilon\,k\,T} \end{aligned}\right\} \tag{A.20}$$

Rewriting Eq. (A.20) one gets

$$\frac{\mathrm{d}^2\psi}{\mathrm{d}r^2} + \frac{1}{r}\frac{\mathrm{d}\psi}{\mathrm{d}r} - \kappa^2\,\psi(r) = 0 \tag{A.21}$$

Equation (A.21) is a modified Bessel equation of order zero. In order to solve it, we take the modified Bessel equation of $v$ order from Bowman [83], which is

$$x^2\frac{\mathrm{d}^2u}{\mathrm{d}x^2} + x\frac{\mathrm{d}u}{\mathrm{d}x} - \left(x^2 + v^2\right)u = 0 \tag{A.22}$$

Defining that $v = 0$, $u = \psi(r)$ and $x = \kappa\, r$, which implies that $r = \frac{x}{\kappa}$ and $\frac{\mathrm{d}r}{\mathrm{d}x} = \frac{1}{\kappa}$. With these changes of variables in Eq. (A.22), and applying the chain rule

$$\frac{\mathrm{d}u}{\mathrm{d}x} = \frac{\mathrm{d}u}{\mathrm{d}r}\frac{\mathrm{d}r}{\mathrm{d}x} = \frac{1}{\kappa}\frac{\mathrm{d}u}{\mathrm{d}r}$$

$$\frac{\mathrm{d}^2u}{\mathrm{d}x^2} = \frac{\mathrm{d}}{\mathrm{d}x}\left(\frac{\mathrm{d}u}{\mathrm{d}x}\right) = \frac{\mathrm{d}}{\mathrm{d}r}\left(\frac{1}{\kappa}\frac{\mathrm{d}u}{\mathrm{d}r}\right)\frac{\mathrm{d}r}{\mathrm{d}x} = \frac{1}{\kappa}\frac{\mathrm{d}^2u}{\mathrm{d}r^2}\frac{1}{\kappa} = \frac{1}{\kappa^2}\frac{\mathrm{d}^2u}{\mathrm{d}r^2}$$

Hence, from the changes of variables, Eq. (A.22) becomes

$$(\kappa r)^2\,\frac{1}{\kappa^2}\frac{\mathrm{d}^2\psi}{\mathrm{d}r^2} + (\kappa r)\,\frac{1}{\kappa}\frac{\mathrm{d}\psi}{\mathrm{d}r} - \left[(\kappa r)^2 + 0^2\right]\psi(r) = 0$$

$$r^2\frac{\mathrm{d}^2\psi}{\mathrm{d}r^2} + r\frac{\mathrm{d}\psi}{\mathrm{d}r} - (\kappa r)^2\,\psi(r) = 0 \tag{A.23}$$

When Eqs. (A.21) and (A.23) are compared it is realized that they are equivalent. Therefore, it is recognized that Eq. (A.21) is the modified Bessel equation of zero order. In order to solve this equation it is assumed that there exists a solution in the form of a power series, such as

$$\psi(r) = \sum_{n=0}^{\infty} a_n\, r^{n+s} \tag{A.24}$$

To find the values of the constants, one must obtain the derivatives of Eq. (A.24) and substitute them in Eq. (A.23)

$$\frac{\mathrm{d}\psi}{\mathrm{d}r} = \sum_{n=0}^{\infty} a_n(n+s)\, r^{n+s-1}$$

$$\frac{\mathrm{d}^2\psi}{\mathrm{d}r^2} = \sum_{n=0}^{\infty} a_n(n+s)(n+s-1)\, r^{n+s-2}$$

$$\sum_{n=0}^{\infty} a_n(n+s)(n+s-1)\, r^{n+s} + \sum_{n=0}^{\infty} a_n(n+s)\, r^{n+s} - \kappa^2\sum_{n=0}^{\infty} a_n\, r^{n+s+2} = 0$$

Simplifying

$$\sum_{n=0}^{\infty} a_n(n+s)^2\, r^{n+s} - \kappa^2\sum_{n=0}^{\infty} a_n\, r^{n+s+2} = 0 \tag{A.25}$$

In order for Eq. (A.25) to be a solution of Eq. (A.21) it is needed that each power series of $r$ is equal to zero. Then

$$a_0\, s^2 = 0 \tag{A.26}$$

$$a_1(s+1)^2 = 0 \tag{A.27}$$

$$a_n(s+n)^2 - \kappa^2\, a_{n-2} = 0 \qquad (n \geq 2) \tag{A.28}$$

Since $a_0 \neq 0$, it is found from Eq. (A.26) that $s^2 = 0$. Therefore, there are two equal solutions $s = +0, -0$. If $s = 0$, it is seen that the only way that Eq. (A.26) is true, is if $a_1 = 0$. Hence, from the recurrence relation in Eq. (A.28) it is seen that all the odd constants are defined by $a_1$. Therefore, a new recurrence relation is made for only the even constants, which are different from 0,

$$a_{2n} = \frac{\kappa^2\, a_{n-2}}{(s+2)^2} \qquad (n \geq 1) \tag{A.29}$$

Substituting Eq. (A.29) in Eq. (A.24), one gets

$$\psi(r) = a_0 r^s \left[1 + \sum_{n=1}^{\infty} \frac{\kappa^{2\,n}}{(s+2)^2(s+4)^2 \cdots (s+2\,n)^2}\, r^{2\,n}\right]$$

a) For $s = +0$

$$\psi_{+0}(r) = a_0 \left[1 + \sum_{n=1}^{\infty} \frac{\kappa^{2\,n}}{2^2 \cdot 4^2 \cdot \cdots \cdot (2\,n)^2}\, r^{2\,n}\right]$$

$$\psi_{+0}(r) = a_0 \left[1 + \sum_{n=1}^{\infty} \frac{\kappa^{2\,n}}{2^{2\,n}(n!)^2}\, r^{2\,n}\right]$$

$$\psi_{+0}(r) = a_0 \sum_{n=0}^{\infty} \frac{1}{(n!)^2} \left(\frac{\kappa\, r}{2}\right)^{2\,n} \tag{A.30}$$

Equation (A.30) is equal to the modified Bessel equation of zero order [84], such as

$$\psi_{+0}(r) = I_{+0}(x) = \sum_{n=0}^{\infty} \frac{1}{(n!)^2} \left(\frac{x}{2}\right)^{2\,n} \quad \text{with} \quad x = \kappa\, r \tag{A.31}$$

b) For $s = -0$

$$\psi_{-0}(r) = a_0 \left[1 + \sum_{n=1}^{\infty} \frac{\kappa^{2\,n}}{2^2 \cdot 4^2 \cdot \cdots \cdot (2\,n)^2}\, r^{2\,n}\right]$$

$$\psi_{-0}(r) = a_0 \left[1 + \sum_{n=1}^{\infty} \frac{\kappa^{2\,n}}{2^{2\,n}(n!)^2}\, r^{2\,n}\right]$$

$$\psi_{-0}(r) = a_0 \sum_{n=0}^{\infty} \frac{1}{(n!)^2} \left(\frac{\kappa\, r}{2}\right)^{2\,n} \tag{A.32}$$

Equation (A.32) is the modified Bessel equation of minus zero order, such as

$$\psi_{-0}(r) = I_{-0}(x) = \sum_{n=0}^{\infty} \frac{1}{(n!)^2} \left(\frac{x}{2}\right)^{2\,n} \quad \text{with} \quad x = \kappa\, r \tag{A.33}$$

From the cases a) and b) it is observed that

$$I_{+0}(x) = I_{-0}(x)$$

This is due to the fact that zero is an even number, and hence the relation $I_{+n}(x) = I_{-n}(x)$ [85] applies, when $n$ is an even number. Therefore, the second solution of Eq. (A.21) is defined by [85]

$$K_0(x) = \frac{\pi}{2}\, \frac{I_{-0}(x) - I_{+0}(x)}{\sin(0 \cdot \pi)}$$

Since 0 is an even number, the modified Bessel function of second order is indeterminate in $\frac{0}{0}$. To avoid, said indetermination, the limit when $n$ tends to 0 is used

$$K_0(x) = \lim_{n \to 0} K_n(x) = \lim_{n \to 0} \frac{\pi}{2}\, \frac{I_{-n}(x) - I_{+n}(x)}{\sin(n\,\pi)} \tag{A.34}$$

The L'Hôpital rule is apllied to Eq. (A.34). Moreover, it is recognised that $\sin(n\,\pi) = 0$ and $\cos(n\,\pi) = (-1)^n$, then

$$K_0(x) = \frac{\pi}{2}\,\frac{\left[\frac{\partial}{\partial n} I_{-n}(x) - \frac{\partial}{\partial n} I_{+n}(x)\right]_{n=0}}{\pi\,[\cos(n\,\pi)]_{n=0}}$$

$$K_0(x) = \frac{(-1)^0}{2}\,\left[\frac{\partial}{\partial n} I_{-n}(x) - \frac{\partial}{\partial n} I_{+n}(x)\right]_{n=0}$$

$$K_0(x) = \frac{1}{2}\,\left[\frac{\partial}{\partial n} I_{-n}(x) - \frac{\partial}{\partial n} I_{+n}(x)\right]_{n=0} \tag{A.35}$$

Now, whether $K_0(x)$ is a solution of Eq. (A.21) and whether it is an independent solution of $I_0(x)$ is verified. Firstly, it is verified if $I_0(x)$ is indeed the solution of the modified Bessel equation of zero order.

$$I_0(x) = \sum_{n=0}^{\infty} \frac{x^{2\,n}}{2^{2\,n}(n!)^2} \quad \text{with} \quad x = \kappa\, r$$

$$\frac{\mathrm{d}I_0}{\mathrm{d}x} = \sum_{n=0}^{\infty} \frac{2\,n\,x^{2\,n-1}}{2^{2\,n}(n!)^2}$$

$$\frac{\mathrm{d}^2 I_0}{\mathrm{d}x^2} = \sum_{n=0}^{\infty} \frac{2\,n\,(2\,n-1)\,x^{2\,n-2}}{2^{2\,n}(n!)^2}$$

Substituting $I_0(x)$ and its derivatives in Eq. (A.22) to verify if it is or not a solution.

$$\sum_{n=0}^{\infty} \frac{2\,n\,(2\,n-1)x^{2\,n}}{2^{2\,n}(n!)^2} + \sum_{n=0}^{\infty} \frac{2\,n\,x^{2\,n}}{2^{2\,n}(n!)^2} - \sum_{n=0}^{\infty} \frac{x^{2\,n+2}}{2^{2\,n}(n!)^2} = 0$$

$$\sum_{n=0}^{\infty} \frac{4\,n^2\,x^{2\,n}}{2^{2\,n}(n!)^2} - \sum_{n=0}^{\infty} \frac{2\,n\,x^{2\,n}}{2^{2\,n}(n!)^2} + \sum_{n=0}^{\infty} \frac{2\,n\,x^{2\,n}}{2^{2\,n}(n!)^2} - \sum_{n=0}^{\infty} \frac{x^{2\,n+2}}{2^{2\,n}(n!)^2} = 0$$

$$\sum_{n=0}^{\infty} \frac{4\,n^2 x^{2\,n}}{2^{2\,n}(n!)^2} - \sum_{n=0}^{\infty} \frac{x^{2\,n+2}}{2^{2\,n}(n!)^2} = 0$$

The change of variable $k = n - 1$ is performed in the left series, and since the factorial is not defined for negative values, the first term when $k = n - 1$ is considered to be zero. Hence

$$\sum_{k=0}^{\infty} \frac{x^{2\,k+2}}{2^{2\,k}(k!)^2} - \sum_{n=0}^{\infty} \frac{x^{2n+2}}{2^{2\,n}(n!)^2} = 0$$

Therefore, it has been proved that

$$x^2 \frac{\mathrm{d}^2 I_0}{\mathrm{d}x^2} + x \frac{\mathrm{d}I_0}{\mathrm{d}x} - x^2\, I_0 = 0$$

which is equivalent to

$$\left[x^2 \frac{\mathrm{d}^2 I_n}{\mathrm{d}x^2} + x \frac{\mathrm{d}I_n}{\mathrm{d}x} - x^2\, I_n = 0\right]_{n=0} \tag{A.36}$$

Since $I_{+n}(x) = I_{-n}(x)$, $I_{-0}(x)$ satisfies Eq. (A.22), such as

$$\left[x^2 \frac{\mathrm{d}^2 I_{-n}}{\mathrm{d}x^2} + x \frac{\mathrm{d}I_{-n}}{\mathrm{d}x} - x^2 I_{-n} = 0\right]_{n=0} \tag{A.37}$$

Differentiating Eq. (A.36) and Eq. (A.37) with respect of $n$, one gets

$$x^2\frac{\mathrm{d}^2}{\mathrm{d}x^2}\left(\frac{\partial I_n}{\partial n}\right)+x\frac{\mathrm{d}}{\mathrm{d}x}\left(\frac{\partial I_n}{\partial n}\right)-x^2\frac{\partial I_n}{\partial n}=0 \tag{A.38}$$

$$x^2\frac{\mathrm{d}^2}{\mathrm{d}x^2}\left(\frac{\partial I_{-n}}{\partial n}\right)+x\frac{\mathrm{d}}{\mathrm{d}x}\left(\frac{\partial I_{-n}}{\partial n}\right)-x^2\frac{\partial I_{-n}}{\partial n}=0 \tag{A.39}$$

Substrating Eq. (A.38) from Eq. (A.39) one finds

$$x^2\frac{\mathrm{d}^2}{\mathrm{d}x^2}\left(\frac{\partial I_{-n}}{\partial n}-\frac{\partial I_n}{\partial n}\right)+x\frac{\mathrm{d}}{\mathrm{d}x}\left(\frac{\partial I_{-n}}{\partial n}-\frac{\partial I_n}{\partial n}\right)-x^2\left(\frac{\partial I_{-n}}{\partial n}-\frac{\partial I_n}{\partial n}\right)=0 \tag{A.40}$$

Multiplying Eq. (A.40) by $\frac{1}{2}$ and evaluating for $n=0$

$$x^2\frac{\mathrm{d}^2}{\mathrm{d}x^2}K_0(x)+x\frac{\mathrm{d}}{\mathrm{d}x}K_0(x)-x^2K_0(x)=0 \tag{A.41}$$

Therefore, it has been proven that $K_0(x)=K_0(\kappa\, r)$ is indeed the second solution of Eq. (A.21) and that it is independent of $I_0(\kappa\, r)$. Hence, the solution of Eq. (A.21) is

$$\psi(r)=c_1I_0(\kappa\, r)+c_2K_0(\kappa\, r) \tag{A.42}$$

Applying the boundary conditions $\psi(R+\frac{a}{2})=\psi_H$ and $\psi(\infty)=0$

$$c_1I_0\left(\kappa\left(R+\frac{a}{2}\right)\right)+c_2K_0\left(\kappa\left(R+\frac{a}{2}\right)\right)=\psi_H \tag{A.43}$$

$$\lim_{M\to\infty}\left[c_1\, I_0(\kappa\, M)+c_2\, K_0(\kappa\, M)\right]=0 \tag{A.44}$$

$c_2$ is cleared from Eq. (A.43) and introduced in Eq. (A.44)

$$c_2=\frac{\psi_H-c_1\, I_0\left(\kappa\left(R+\frac{a}{2}\right)\right)}{K_0\left(\kappa\left(R+\frac{a}{2}\right)\right)}$$

$$\lim_{M\to\infty}\left[c_1\, I_0(\kappa\, M)+\frac{\psi_H-c_1I_0\left(\kappa\left(R+\frac{a}{2}\right)\right)}{K_0\left(\kappa\left(R+\frac{a}{2}\right)\right)}\, K_0(\kappa\, M)\right]=0$$

$$\lim_{M\to\infty}\left[c_1\, I_0(\kappa\, M)+\frac{K_0(\kappa\, M)}{K_0\left(\kappa\left(R+\frac{a}{2}\right)\right)}\psi_H-c_1\frac{K_0(\kappa\, M)\, I_0\left(\kappa\left(R+\frac{a}{2}\right)\right)}{K_0\left(\kappa\left(R+\frac{a}{2}\right)\right)}\right]=0$$

Clearing for $c_1$

$$c_1=\frac{-\frac{K_0(\kappa\, M)}{K_0\left(\kappa\left(R+\frac{a}{2}\right)\right)}\psi_H}{I_0(\kappa\, M)-\frac{K_0(\kappa\, M)\, I_0\left(\kappa\left(R+\frac{a}{2}\right)\right)}{K_0\left(\kappa\left(R+\frac{a}{2}\right)\right)}} \tag{A.45}$$

In Fig. A.1 the functions $I_0(x)$ and $K_0(x)$ are plotted. From this figure it is seen that $\lim_{M\to\infty}K_0(\kappa\, M)=0$ and $\lim_{M\to\infty}I_0(\kappa\, M)=\infty$. Hence, evaluating the limit of Eq. (A.45)

$$c_1=\frac{-\frac{0}{K_0\left(\kappa\left(R+\frac{a}{2}\right)\right)}\,\psi_H}{\infty-\frac{0\cdot I_0\left(\kappa\left(R+\frac{a}{2}\right)\right)}{K_0\left(\kappa\left(R+\frac{a}{2}\right)\right)}}=\frac{0}{\infty-0}=\frac{0}{\infty}=0$$

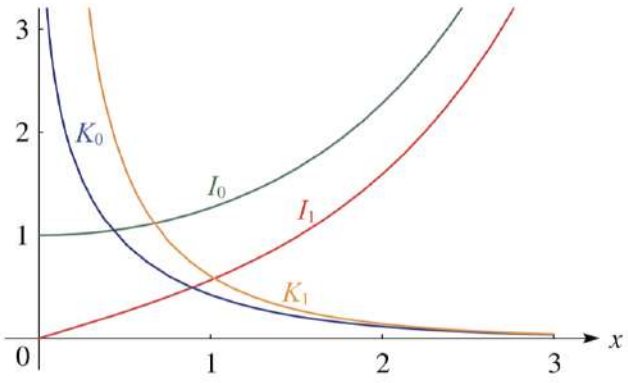


Figure A.1: $I_0(x)$, $I_1(x)$, $K_0(x)$ y $K_1(x)$ for $0 \leq x \leq 3$. Taken from NIST Handbook of Mathematical Functions [84].

Hence, substituting the value of $c_1$ in Eq. (A.43), $c_2$ is found as

$$0 \cdot I_0\left(\kappa\left(R+\frac{a}{2}\right)\right) + c_2\, K_0\left(\kappa\left(R+\frac{a}{2}\right)\right) = \psi_H \;\longrightarrow\; c_2 = \frac{\psi_H}{K_0\left(\kappa\left(R+\frac{a}{2}\right)\right)}$$

Hence, substituting our constants in Eq. (A.42), we found the solution of the electric potential in the Poisson-Boltzmann interval is

$$\psi(r) = \frac{K_0(\kappa\, r)}{K_0\left(\kappa\left(R+\frac{a}{2}\right)\right)}\,\psi_H \tag{A.46}$$

Now we find the relation between $\sigma_M$ and $\psi_H$. The definition of $\sigma_M$ is similar to Eq. (A.9), though the inferior limit of integration is now $R+\frac{a}{2}$. Since, we are working with Bessel equations, we will use the relation $K_n'(x) = \frac{n}{x} - K_{n+1}$ [85]. Hence, Eq. (A.9) for the cylindrical electrode is

$$\begin{aligned}\sigma_M = -\frac{1}{R+\frac{a}{2}}\int_{R+\frac{a}{2}}^{\infty}\rho_{el}(r)\, r\,\mathrm{d}r = \frac{1}{R+\frac{a}{2}}\frac{\varepsilon}{4\,\pi}\int_{R+\frac{a}{2}}^{\infty}\frac{1}{r}\frac{\mathrm{d}}{\mathrm{d}r}\left(r\frac{\mathrm{d}\psi}{\mathrm{d}r}\right)r\,\mathrm{d}r \\ = -\frac{\varepsilon}{4\,\pi}\left(\frac{\mathrm{d}\psi}{\mathrm{d}r}\right)_{r=R+\frac{a}{2}}\end{aligned} \tag{A.47}$$

$$\frac{\mathrm{d}\psi}{\mathrm{d}r} = \frac{\kappa\, K_0'(\kappa\, r)}{K_0\left(\kappa\left(R+\frac{a}{2}\right)\right)}\,\psi_H$$

$$\frac{\mathrm{d}\psi}{\mathrm{d}r} = -\frac{\kappa\, K_1(\kappa\, r)}{K_0\left(\kappa\left(R+\frac{a}{2}\right)\right)}\,\psi_H$$

$$\sigma_M = \frac{\varepsilon\,\kappa}{4\,\pi}\,\frac{K_1\left(\kappa\left(R+\frac{a}{2}\right)\right)}{K_0\left(\kappa\left(R+\frac{a}{2}\right)\right)}\,\psi_H$$

Consequently, $\psi_H$ is

$$\psi_H = \frac{4\,\pi}{\varepsilon\,\kappa}\,\frac{K_0\left(\kappa\left(R+\frac{a}{2}\right)\right)}{K_1\left(\kappa\left(R+\frac{a}{2}\right)\right)}\,\sigma_M \tag{A.48}$$

Hence, $\psi_R$ is

$$\psi_R = \frac{4\,\pi\,\sigma_M}{\varepsilon\,\kappa}\left(\frac{\kappa\, a}{2} + \frac{K_0\left(\kappa\left(R+\frac{a}{2}\right)\right)}{K_1\left(\kappa\left(R+\frac{a}{2}\right)\right)}\right) \tag{A.49}$$

Then, the electric potential is given by

$$\psi(r) = \begin{cases} \psi_H \left[ 1 + \kappa \frac{K_1\left(\kappa\left(R+\frac{a}{2}\right)\right)}{K_0\left(\kappa\left(R+\frac{a}{2}\right)\right)} \left(R + \frac{a}{2} - r\right) \right] & \text{if } R \leq r \leq R + \frac{a}{2} \\ \frac{K_0(\kappa\, r)}{K_0\left(\kappa\left(R+\frac{a}{2}\right)\right)} \psi_H & \text{if } r \geq R + \frac{a}{2} \end{cases}$$

Meanwhile, the induced surface charge density, $\sigma(r)$, which was given by Eq. (A.12) for a plane electrode, is the same for the cylindrical electrode, but on cylindrical coordinates. Then, the surface charge density for the cylindrical electrode is

$$\sigma(r) = -\frac{1}{r}\int_r^\infty \rho_{el}(t)\, t\, \mathrm{d}t = \frac{1}{r}\frac{\varepsilon}{4\,\pi}\int_r^\infty \frac{1}{t}\frac{\mathrm{d}}{\mathrm{d}t}\left(t\frac{\mathrm{d}\psi}{\mathrm{d}t}\right) t\, \mathrm{d}t = -\frac{\varepsilon}{4\,\pi}\left(\frac{\mathrm{d}\psi}{\mathrm{d}r}\right)_r \tag{A.50}$$

$$\sigma(r) = \frac{\varepsilon\,\kappa}{4\,\pi}\frac{K_1(\kappa\, r)}{K_0\left(\kappa\left(R+\frac{a}{2}\right)\right)}\psi_H$$

This induced surface charge density is only valid for the interval $[r, \infty)$, where $r \geq R + \frac{a}{2}$. On the other hand, in the interval $R \leq r < R + \frac{a}{2}$ the surface charge density is zero, because of the ion size restriction, the ions cannot get closer to the surface than half their diameter.

$$\sigma(r) = \begin{cases} 0 & \text{if } R \leq r < R + \frac{a}{2} \\ \frac{\varepsilon\,\kappa}{4\,\pi}\frac{K_1(\kappa\, r)}{K_0\left(\kappa\left(R+\frac{a}{2}\right)\right)}\psi_H & \text{if } r \geq R + \frac{a}{2} \end{cases}$$

Now, the co-ion and counter-ion distribution functions are obtained. For the Laplace interval both distribution functions are equal to zero due to the ion's size restriction. Whereas, in the Poisson-Boltzmann interval the co-ion and counter-ion distribution functions are given by Eqs. (A.13) and (A.14). Hence, we have

$$g_+(r) = \begin{cases} 0 & \text{if } R \leq r < R + \frac{a}{2} \\ \exp\left(-\frac{z\,e}{k\,T}\frac{K_0(\kappa\, r)}{K_0\left(\kappa\left(R+\frac{a}{2}\right)\right)}\psi_H\right) & \text{if } r \geq R + \frac{a}{2} \end{cases}$$

$$g_-(r) = \begin{cases} 0 & \text{if } R \leq r < R + \frac{a}{2} \\ \exp\left(\frac{z\,e}{k\,T}\frac{K_0(\kappa\, r)}{K_0\left(\kappa\left(R+\frac{a}{2}\right)\right)}\psi_H\right) & \text{if } r \geq R + \frac{a}{2} \end{cases}$$

Meanwhile, the total differential capacitance is calculated as the sum of the differential capacitances in both intervals.

$$\frac{1}{C_T} = \frac{1}{C_{Lap}} + \frac{1}{C_{PB}}$$

Where the subindexes $Lap$ and $PB$ indicate the interval of Laplace and Poisson-Boltzmann, they are defined as

$$\frac{1}{C_{Lap}} = \frac{\mathrm{d}\psi_R}{\mathrm{d}\sigma_M} = \frac{4\,\pi}{\varepsilon\,\kappa}\left(\frac{K_0\left(\kappa\left(R+\frac{a}{2}\right)\right)}{K_1\left(\kappa\left(R+\frac{a}{2}\right)\right)} + \frac{\kappa\, a}{2}\right)$$

$$\frac{1}{C_{PB}} = \frac{\mathrm{d}\psi_H}{\mathrm{d}\sigma_M} = \frac{4\,\pi}{\varepsilon\,\kappa}\frac{K_0\left(\kappa\left(R+\frac{a}{2}\right)\right)}{K_1\left(\kappa\left(R+\frac{a}{2}\right)\right)}$$

So, we find that the total differential capacitance is

$$\frac{1}{C_T} = \frac{4\,\pi}{\varepsilon\,\kappa}\left(\frac{2\,K_0\left(\kappa\left(R+\frac{a}{2}\right)\right)}{K_1\left(\kappa\left(R+\frac{a}{2}\right)\right)} + \frac{\kappa\, a}{2}\right)$$

$$C_T = \left[\frac{4\,\pi}{\varepsilon\,\kappa}\left(\frac{2\,K_0\left(\kappa\left(R+\frac{a}{2}\right)\right)}{K_1\left(\kappa\left(R+\frac{a}{2}\right)\right)} + \frac{\kappa\, a}{2}\right)\right]^{-1}$$

## A.3 The solution of the linearized Poisson-Boltzmann equation for a solid spherical electrode

For a spherical electrode, the Laplacian is given by

$$\nabla^2 \equiv \frac{1}{r^2}\frac{\partial}{\partial r}\left(r^2\frac{\partial}{\partial r}\right) + \frac{1}{r^2\sin^2(\phi)}\frac{\partial^2}{\partial\theta^2} + \frac{1}{r^2\sin(\phi)}\frac{\partial}{\partial\phi}\left(\sin(\phi)\frac{\partial}{\partial\phi}\right)$$

In order to solve the electrical double layer in a spherical electrode, one starts from the assumption that the electric potential, $\psi$, only depends on the radius. Hence, the Laplace equation for the spherical electrode is

$$\nabla^2\psi = \frac{1}{r^2}\frac{\partial}{\partial r}\left(r^2\frac{\partial\psi}{\partial r}\right) = \frac{\mathrm{d}^2\psi}{\mathrm{d}r^2} + \frac{2}{r}\frac{\mathrm{d}\psi}{\mathrm{d}r} = 0$$

The above is an ordinary differential equation and is solved easily by reduction of order by the change of variable $\psi = \frac{\varphi}{r}$. We rewrite the Laplace equation in terms of our new variable, $\varphi$, we obtain the derivatives of $\psi$ in terms of $\varphi$ by the following steps

$$\frac{\mathrm{d}\psi}{\mathrm{d}r} = \frac{r\,\frac{\mathrm{d}\varphi}{\mathrm{d}r} - \varphi}{r^2} = \frac{1}{r}\frac{\mathrm{d}\varphi}{\mathrm{d}r} - \frac{1}{r^2}\,\varphi$$

$$\frac{\mathrm{d}^2\psi}{\mathrm{d}r^2} = \frac{r\,\frac{\mathrm{d}^2\varphi}{\mathrm{d}r^2} - \frac{\mathrm{d}\varphi}{\mathrm{d}r}}{r^2} - \frac{r^2\,\frac{\mathrm{d}\varphi}{\mathrm{d}r} - 2\,r\,\varphi}{r^4} = \frac{1}{r}\frac{\mathrm{d}^2\varphi}{\mathrm{d}r^2} - \frac{2}{r^2}\frac{\mathrm{d}\varphi}{\mathrm{d}r} + \frac{2}{r^3}\,\varphi$$

Substituting this values in the original equation and simplifying

$$\frac{1}{r}\frac{\mathrm{d}^2\varphi}{\mathrm{d}r^2} - \frac{2}{r^2}\frac{\mathrm{d}\varphi}{\mathrm{d}r} + \frac{2}{r^3}\,\varphi + \frac{2}{r^2}\frac{\mathrm{d}\varphi}{\mathrm{d}r} - \frac{2}{r^3}\,\varphi = \frac{1}{r}\frac{\mathrm{d}^2\varphi}{\mathrm{d}r^2} = 0$$

Now, this equation is easily solved by multiplying it by $r$ and integrating on both sides

$$\frac{\mathrm{d}\varphi}{\mathrm{d}r} = C_1 \;\longrightarrow\; \varphi(r) = C_1\,r + C_2$$

Substituting this result in our original variable, we obtain

$$\psi(r) = C_1 + \frac{C_2}{r}$$

From the Gauss' law in $r = R + \frac{a}{2}$, and obtaining the derivative of the above we find the value of our first constant

$$\frac{\mathrm{d}\psi}{\mathrm{d}r} = -\frac{1}{r^2}\,C_2 = -\frac{4\,\pi\,\sigma_M}{\varepsilon} \;\longrightarrow\; C_2 = \frac{4\,\pi\,\sigma_M}{\varepsilon}\,r^2$$

$$\frac{\mathrm{d}\psi}{\mathrm{d}r} = -\frac{4\,\pi\,\sigma_M}{\varepsilon}$$

$$\psi(r) = C_1 - \frac{4\,\pi\,\sigma_M}{\varepsilon}\,r$$

From our boundary condition, $\psi(R) = \psi_R$, we have

$$\psi(R) = C_1 - \frac{4\,\pi\,\sigma_M}{\varepsilon}\,R = \psi_R \;\longrightarrow\; C_1 = \psi_R + \frac{4\,\pi\,\sigma_M}{\varepsilon}\,R$$

$$\psi(r) = \psi_R + \frac{4\,\pi\,\sigma_M}{\varepsilon}\,(R - r)$$

Meanwhile, from the boundary condition, $\psi(R+\frac{a}{2})=\psi_H$, it is found

$$\psi\left(R+\frac{a}{2}\right)=\psi_R-\frac{4\,\pi\,\sigma_M}{\varepsilon}\,\frac{a}{2}=\psi_H\;\longrightarrow\;\psi_R=\psi_H+\frac{4\,\pi\,\sigma_M}{\varepsilon}\,\frac{a}{2}$$

Hence, our solution for the Laplace interval in terms of $\psi_H$ is

$$\psi(r)=\psi_H+\frac{4\,\pi\,\sigma_M}{\varepsilon}\,\left(R+\frac{a}{2}-r\right)$$

Meanwhile, for the PB interval, we have that the electric charge density is the same as the p-LPBS equation, given by

$$\rho_{el}(r)=-\frac{2\,n\,e^2\,z^2}{k\,T}\psi(r)$$

Therefore, the s-LPBS is given by Eq. (A.2), namely

$$\left.\begin{aligned}\frac{\mathrm{d}^2\psi}{\mathrm{d}r^2}+\frac{2}{r}\,\frac{\mathrm{d}\psi}{\mathrm{d}r}=\frac{8\,\pi\,n\,e^2\,z^2}{\varepsilon\,k\,T}\psi(r)=\kappa^2\,\psi(r)\\ \text{with}\;\;\kappa^2=\frac{8\,\pi\,n\,e^2\,z^2}{\varepsilon\,k\,T}\end{aligned}\right\}\tag{A.51}$$

Rewriting Eq. (A.51) one gets

$$\frac{\mathrm{d}^2\psi}{\mathrm{d}r^2}+\frac{2}{r}\frac{\mathrm{d}\psi}{\mathrm{d}r}-\kappa^2\,\psi(r)=0\tag{A.52}$$

From Eq. (A.52), one realizes that this differential equation is of the form $\frac{\mathrm{d}^2\psi}{\mathrm{d}r^2}+f(r)\,\frac{\mathrm{d}\psi}{\mathrm{d}r}+\psi(r)\,g(r)=F(r)$. Hence, it can be solved by reduction of order, applying the substitution $\psi(r)=\exp\!\Big(-\int\frac{f(r)}{2}\,\mathrm{d}r\Big)v(r)$, which is equivalent to $\psi(r)=\mu(r)v(r)$. Therefore, one obtains

$$\mu(r)=\exp\!\left(-\int\frac{f(r)}{2}\,\mathrm{d}r\right)=\exp\!\left(-\int\frac{2/r}{2}\,\mathrm{d}r\right)=\exp\!\left(-\int\frac{\mathrm{d}r}{r}\right)$$

$$\mu(r)=\exp[-\ln(r)]=\exp\!\left[\ln\!\left(\frac{1}{r}\right)\right]=\frac{1}{r}$$

The derivatives of $\mu(r)$ are obtained

$$\mu=\frac{1}{r}\qquad\frac{\mathrm{d}\mu}{\mathrm{d}r}=-\frac{1}{r^2}\qquad\frac{\mathrm{d}^2\mu}{\mathrm{d}r^2}=\frac{2}{r^3}\tag{A.53}$$

Now that $\mu(r)$ is obtained as well as its derivatives, one obtains the derivative of $\psi(r)$

$$\psi(r)=\mu(r)\,v(r)\qquad\frac{\mathrm{d}\psi}{\mathrm{d}r}=\mu\frac{\mathrm{d}v}{\mathrm{d}r}+v\frac{\mathrm{d}\mu}{\mathrm{d}r}\qquad\frac{\mathrm{d}^2\psi}{\mathrm{d}r^2}=\mu\frac{\mathrm{d}^2v}{\mathrm{d}r^2}+2\frac{\mathrm{d}\mu}{\mathrm{d}r}\frac{\mathrm{d}v}{\mathrm{d}r}+v\frac{\mathrm{d}^2\mu}{\mathrm{d}r^2}\tag{A.54}$$

The relations in Eqs. (A.53) and (A.54) are used in Eq. (A.52), and one finds

$$\left(\frac{1}{r}\frac{\mathrm{d}^2v}{\mathrm{d}r^2}-\frac{2}{r^2}\frac{\mathrm{d}v}{\mathrm{d}r}+\frac{2}{r^3}v\right)+\frac{2}{r}\left(\frac{1}{r}\frac{\mathrm{d}v}{\mathrm{d}r}-\frac{1}{r^2}v\right)-\kappa^2\left(\frac{v}{r}\right)=0$$

$$\frac{1}{r}\frac{\mathrm{d}^2v}{\mathrm{d}r^2}-\kappa^2\left(\frac{v}{r}\right)=0\;\longrightarrow\;\frac{\mathrm{d}^2v}{\mathrm{d}r^2}-\kappa^2v=0\tag{A.55}$$

Now, assuming that there is a solution of $v$ in the form of $v(r) = e^{\lambda r}$ for a constant $\lambda$, the derivatives of $v(r)$ are $\frac{\mathrm{d}v}{\mathrm{d}r} = \lambda\, e^{\lambda r}$ and $\frac{\mathrm{d}^2 v}{\mathrm{d}r^2} = \lambda^2\, e^{\lambda r}$. Substituting them in Eq. (A.55), one gets

$$\lambda^2\, e^{\lambda r} - \kappa^2\, e^{\lambda r} = 0 \quad \longrightarrow \quad \lambda = \pm\,\kappa$$

$$v(r) = c_1\, e^{\kappa r} + c_2\, e^{-\kappa r}$$

From $\mu(r)$ and $v(r)$ one obtains $\psi(r)$

$$\psi(r) = \frac{c_1\, e^{\kappa r} + c_2\, e^{-\kappa r}}{r} \tag{A.56}$$

In order to find the values of the constants in Eq. (A.56), one applies the boundary condition $\psi(\infty) = 0$

$$0 = \frac{c_1\, e^{\kappa \infty} + c_2\, \cancelto{0}{e^{-\kappa \infty}}}{\infty} = \frac{c_1\, e^{\kappa \infty}}{\infty} \quad \longrightarrow \quad c_1 = 0$$

Therefore, substituting $c_1$ in Eq. (A.56) and using the next boundary condition, $\psi\left(R + \frac{a}{2}\right) = \psi_H$, one finds the value of $c_2$

$$\psi_H = \frac{c_2\, e^{-\kappa\left(R+\frac{a}{2}\right)}}{R + \frac{a}{2}} \;\longrightarrow\; c_2 = \left(R + \frac{a}{2}\right) \psi_H\, e^{\kappa\left(R+\frac{a}{2}\right)}$$

Therefore, the solution of the electric potential for the Poisson Boltzmann interval is

$$\psi(r) = \frac{R + \frac{a}{2}}{r}\, \psi_H\, e^{\kappa\left(R+\frac{a}{2}-r\right)} \tag{A.57}$$

Now we find the relation between $\sigma_M$ and $\psi_H$. The definition of $\sigma_M$ is the same as Eq. (A.47), then

$$\begin{aligned} \sigma_M = -\frac{1}{\left(R+\frac{a}{2}\right)^2} \int_{R+\frac{a}{2}}^{\infty} \rho_{el}(r)\, r^2\, \mathrm{d}r = \frac{1}{\left(R+\frac{a}{2}\right)^2} \frac{\varepsilon}{4\,\pi} \int_{R+\frac{a}{2}}^{\infty} \frac{1}{r^2} \frac{\mathrm{d}}{\mathrm{d}r}\left(r^2 \frac{\mathrm{d}\psi}{\mathrm{d}r}\right) r^2\, \mathrm{d}r \\ = -\frac{\varepsilon}{4\,\pi} \left(\frac{\mathrm{d}\psi}{\mathrm{d}r}\right)_{r=R+\frac{a}{2}} \end{aligned} \tag{A.58}$$

$$\frac{\mathrm{d}\psi}{\mathrm{d}r} = -\frac{R+\frac{a}{2}}{r}\, \kappa\, \psi_H\, e^{\kappa\left(R+\frac{a}{2}-r\right)} - \frac{R+\frac{a}{2}}{r^2}\, \psi_H\, e^{\kappa\left(R+\frac{a}{2}-r\right)}$$

$$\frac{\mathrm{d}\psi}{\mathrm{d}r} = -\psi_H \left(R + \frac{a}{2}\right) \frac{(1+\kappa\, r)}{r^2}\, e^{\kappa\left(R+\frac{a}{2}-r\right)}$$

$$\sigma_M = \frac{\varepsilon}{4\,\pi} \frac{\psi_H \left[1 + \kappa\, \left(R+\frac{a}{2}\right)\right]}{R+\frac{a}{2}}$$

$$\sigma_M = \frac{\varepsilon}{4\,\pi} \left(\kappa + \frac{1}{R+\frac{a}{2}}\right) \psi_H$$

Consequently, $\psi_H$ is

$$\psi_H = \frac{4\,\pi\,\sigma_M}{\varepsilon} \left(\frac{R+\frac{a}{2}}{1+\kappa\, \left(R+\frac{a}{2}\right)}\right) \tag{A.59}$$

And therefore, $\psi_R$ is

$$\psi_R = \frac{4\,\pi\,\sigma_M}{\varepsilon} \left(\frac{R+\frac{a}{2}}{1+\kappa\, \left(R+\frac{a}{2}\right)} + \frac{a}{2}\right) \tag{A.60}$$

Then, the electric potential is given by

$$\psi(r) = \begin{cases} \psi_H \left[1 + \left(\kappa + \frac{1}{R+\frac{a}{2}}\right)\left(R + \frac{a}{2} - r\right)\right] & \text{if } R \leq r \leq R + \frac{a}{2} \\ \frac{R+\frac{a}{2}}{r}\,\psi_H\, e^{\kappa\left(R+\frac{a}{2}-r\right)} & \text{if } r \geq R + \frac{a}{2} \end{cases}$$

Meanwhile, the induced surface charge density $\sigma(r)$ given by Eq. (A.50) for the cylindrical electrode, is the same for the spherical electrode.

$$\sigma(r) = -\frac{1}{r^2}\int_r^\infty \rho_{el}(t)\, t^2\, \mathrm{d}t = \frac{1}{r^2}\frac{\varepsilon}{4\,\pi}\int_r^\infty \frac{1}{t^2}\frac{\mathrm{d}}{\mathrm{d}t}\left(t^2\frac{\mathrm{d}\psi}{\mathrm{d}t}\right)t^2\,\mathrm{d}t = -\frac{\varepsilon}{4\,\pi}\left(\frac{\mathrm{d}\psi}{\mathrm{d}r}\right)_r \tag{A.61}$$

$$\sigma(r) = \frac{\varepsilon\,\psi_H}{4\,\pi}\left(R + \frac{a}{2}\right)\frac{(1+\kappa\, r)}{r^2}\, e^{\kappa\left(R+\frac{a}{2}-r\right)}$$

This induced surface charge density is only valid for the interval $[r, \infty)$, where $r \geq R + \frac{a}{2}$. On the other hand, in the interval $R \leq r < R + \frac{a}{2}$ the surface charge density is zero, because of the ion's size restriction, the ions cannot get closer to the induced surface than half their diameter.

$$\sigma(r) = \begin{cases} 0 & \text{if } R \leq r < R + \frac{a}{2} \\ \frac{\varepsilon\,\psi_H}{4\,\pi}\left(R + \frac{a}{2}\right)\frac{(1+\kappa\, r)}{r^2}\, e^{\kappa\left(R+\frac{a}{2}-r\right)} & \text{if } r \geq R + \frac{a}{2} \end{cases}$$

Now, the co-ion and counter-ion distribution functions are obtained. For the Laplace interval both distributions are equal to zero due to the ion's size restriction. Whereas, in the Poisson-Boltzmann interval the co-ion and counter-ion distribution functions are given by Eqs. (A.13) and (A.14). Hence, we have

$$g_+(r) = \begin{cases} 0 & \text{if } R \leq r < R + \frac{a}{2} \\ \exp\left(-\frac{z\,e}{k\,T}\,\psi_H\,\frac{R+\frac{a}{2}}{r}\, e^{\kappa\left(R+\frac{a}{2}-r\right)}\right) & \text{if } r \geq R + \frac{a}{2} \end{cases}$$

$$g_-(r) = \begin{cases} 0 & \text{if } R \leq r < R + \frac{a}{2} \\ \exp\left(\frac{z\,e}{k\,T}\,\psi_H\,\frac{R+\frac{a}{2}}{r}\, e^{\kappa\left(R+\frac{a}{2}-r\right)}\right) & \text{if } r \geq R + \frac{a}{2} \end{cases}$$

Meanwhile, the total differential capacitance is calculated as the sum of the differential capacitances in both intervals.

$$\frac{1}{C_T} = \frac{1}{C_{Lap}} + \frac{1}{C_{PB}}$$

Where the subindexes $Lap$ and $PB$ indicate the interval of Laplace and Poisson-Boltzmann, they are defined as

$$\frac{1}{C_{Lap}} = \frac{\mathrm{d}\psi_R}{\mathrm{d}\sigma_M} = \frac{4\,\pi}{\varepsilon}\left(\frac{R + \frac{a}{2}}{1 + \kappa\,\left(R + \frac{a}{2}\right)} + \frac{a}{2}\right)$$

$$\frac{1}{C_{PB}} = \frac{\mathrm{d}\psi_H}{\mathrm{d}\sigma_M} = \frac{4\,\pi}{\varepsilon}\left(\frac{R + \frac{a}{2}}{1 + \kappa\,\left(R + \frac{a}{2}\right)}\right)$$

So, we find that the total differential capacitance is

$$\frac{1}{C_T} = \frac{4\,\pi}{\varepsilon}\left(\frac{2\left(R + \frac{a}{2}\right)}{1 + \kappa\,\left(R + \frac{a}{2}\right)} + \frac{a}{2}\right)$$

$$C_T = \left[\frac{4\,\pi}{\varepsilon}\left(\frac{2\left(R + \frac{a}{2}\right)}{1 + \kappa\,\left(R + \frac{a}{2}\right)} + \frac{a}{2}\right)\right]^{-1}$$

# Appendix B

# Computer programs: Mathematica

Within the Mathematica program (Version 12.0.0.0), two subprograms, i.e. Mathematica Notebooks, were created. In the first program "SEDL.nb" the lineal Poisson-Boltzmann equation is solved for the single electrical double layer for solid electrodes. Meanwhile, in the second program "SNCsEDL.nb", with this equation, the electric double layer is calculated for the different pores. In both programs the solutions are obtained in CGS and MKS units, and the initials of their geometry (P for the plane, C for the cylinder, and S for the sphere) are used to differentiate between each one. In order to be as brief as possible, for space concerns, our notebooks only displays the functions used to plot and obtained our different electric parameters. If the reader is interested in having the full version of this notebooks, where the user can easily plot and obtain the values of our different electric parameters feel free to contact the author at adsic@ier.unam.mx.

# The single electrical double layer for solid electrodes

## Preamble

In this program we solve the linearized single electrical double layer for a solid planar (P), cylindrical (C), and spherical (S) electrodes in two system unit CGS (C) and MKS (M). The non-linear solution of the planar electrode (NP) is performed as well. In order, to distinguish between a mean electrostatic potential, $\psi$, from one geometry to the other (as for any other electric parameter), the initials of the geometry and the system unit will be used. Hence, $\psi$NPM is the non-linearized mean electrostatic potential of a solid planar electrode in MKS units, whereas $\psi$CC is the linearized mean electrostatic potential of a solid cylindrical electrode in CGS units.
The first step is to clear all our variables, and to define the constants used throughout this notebook, their units are commented for clarity.

In[•]:=
```
ClearAll["Global`*"]
kM = 1.38064852 × 10^-23 (*J/K*);
kC = 1.38064852 × 10^-16 (*ergs/K*);
ϵ0 = 8.85418781761 × 10^-12 (*C^2/N m^2||F/m||C/V m*);
ϵ = 78.5;
ϵR = ϵ ϵ0 (*C^2/N m^2||F/m||C/Vm*);
c = 2.99792458 × 10^8 (*m/s*);
z = 1;
eM = 1.60217733 × 10^-19 (*C*);
eC = 10 c × eM (*esu||Fr||statC*);
NA = 6.022140857 × 10^23 (*mol^-1*);
a = 4.25 (*Å*);
```

Now, a list of values of our variables is defined

In[•]:=
```
CHARGEDEN = {0.001, 0.002, 0.005, 0.01} (*C/m^2*);
CONCENTRATIONS = {0.001, 0.01, 0.1, 0.5} (*M*);
TEMPERATURES = {278.15, 298.15, 308.15, 328.15} (*K*);
RADIUS = {5, 30, 80, 500} (*Å*) ;
```

Furthermore, the molar concentration and the debye length are defined. This functions are independent of the geometry used.

```
In[•]:= nC[ρ0_] := ρ0 × 10^-3 NA (*cm^-3*);
        nM[ρ0_] := ρ0 × 10^3 NA (*m^-3*);
        κC[ρ0_, T_] := Sqrt[8 π nC[ρ0] eC^2 z^2 / (ϵ kC T)] (*cm^-1*);
        κM[ρ0_, T_] := Sqrt[2 nM[ρ0] eM^2 z^2 / (ϵR kM T)] (*m^-1*);
```

# The mean electrostatic potential

Now, the mean electrostatic potential in the SEDL is calculated for the different geometries. Firstly, the mean electrostatic potential at the distance of closest approach, $\psi$h or $\psi$r, are defined from our set and unset variables. Moreover, for the non-linear case of the solid planar electrode the variable "Z" is define for simplicity. After defining their respective $\psi$h, $\psi$r, and Z, the mean electrostatic potential is defined in two intervals.

```
In[•]:= ψhPC[ρ0_, T_, σm_] := (4 π (10 c)/10^4 σm) / (ϵ κC[ρ0, T]) (*statV*);
        ψhPM[ρ0_, T_, σm_] := 1000 σm / (ϵR κM[ρ0, T]) (*mV*);
        ψhNPC[ρ0_, T_, σm_] := (2 kC T)/(z eC) ArcSinh[(2 π z eC (10 c)/10^4 σm) / (ϵ κC[ρ0, T] kC T)] (*statV*);
        ψhNPM[ρ0_, T_, σm_] := 1000 (2 kM T)/(z eM) ArcSinh[(z eM σm) / (2 ϵR κM[ρ0, T] kM T)] (*mV*);
        ZC[ρ0_, T_, σm_] := (z eC ψhNPC[ρ0, T, σm]) / (2 kC T);
        ZM[ρ0_, T_, σm_] := (z eM (ψhNPM[ρ0,T,σm])/1000) / (2 kM T);
        ψhCC[ρ0_, T_, σm_, R_] :=
          (4 π (10 c)/10^4 σm) / (ϵ κC[ρ0, T]) BesselK[0, κC[ρ0, T] (R + a/2) × 10^-8] / BesselK[1, κC[ρ0, T] (R + a/2) × 10^-8] (*statV*);
        ψhCM[ρ0_, T_, σm_, R_] := 1000 σm / (ϵR κM[ρ0, T]) BesselK[0, κM[ρ0, T] (R + a/2) × 10^-10] / BesselK[1, κM[ρ0, T] (R + a/2) × 10^-10]
          (*mV*);
        ψrCC[ρ0_, T_, σm_, R_] := ψhCC[ρ0, T, σm, R]
          (1 + BesselK[1, κC[ρ0, T] (R + a/2) × 10^-8] / BesselK[0, κC[ρ0, T] (R + a/2) × 10^-8] κC[ρ0, T] a/2 × 10^-8) (*statV*);
```

```
ψrCM[ρ0_, T_, σm_, R_] := ψhCM[ρ0, T, σm, R]
    (1 + BesselK[1, κM[ρ0, T] (R + a/2) × 10^-10] / BesselK[0, κM[ρ0, T] (R + a/2) × 10^-10] κM[ρ0, T] a/2 × 10^-10) (*mV*);

ψhSC[ρ0_, T_, σm_, R_] := (4 π 10 c/10^4 σm)/ϵ (κC[ρ0, T] + 1/((R + a/2) 10^-8))^-1 (*statV*);

ψhSM[ρ0_, T_, σm_, R_] := 1000 σm/(ϵR) (κM[ρ0, T] + 1/((R + a/2) 10^-10))^-1 (*mV*);

ψrSC[ρ0_, T_, σm_, R_] :=
  ψhSC[ρ0, T, σm, R] (1 + (κC[ρ0, T] + 1/((R + a/2) 10^-8)) (a/2 × 10^-8)) (*statV*);

ψrSM[ρ0_, T_, σm_, R_] := ψhSM[ρ0, T, σm, R]
    (1 + (κM[ρ0, T] + 1/((R + a/2) 10^-10)) (a/2 × 10^-10)) (*mV*);

ψPC[ρ0_, T_, σm_, x_] := Piecewise[
   {{ψhPC[ρ0, T, σm] (1 + κC[ρ0, T] (a/2 - x) × 10^-8), 0 ≤ x < a/2},
{ψhPC[ρ0, T, σm] Exp[κC[ρ0, T] (a/2 - x) × 10^-8], x ≥ a/2}}] (*statV*);

ψPM[ρ0_, T_, σm_, x_] :=
  Piecewise[{{ψhPM[ρ0, T, σm] (1 + κM[ρ0, T] (a/2 - x) × 10^-10), 0 ≤ x < a/2},
{ψhPM[ρ0, T, σm] Exp[κM[ρ0, T] (a/2 - x) × 10^-10], x ≥ a/2}}] (*mV*);

ψNPC[ρ0_, T_, σm_, x_] :=
  Piecewise[{{(4 π 10 c/10^4 σm)/ϵ (a/2 - x) × 10^-8 + ψhNPC[ρ0, T, σm], 0 ≤ x < a/2},
{2 kC T/(z eC) Log[
      (Exp[ZC[ρ0, T, σm]] + 1 + (Exp[ZC[ρ0, T, σm]] - 1) Exp[κC[ρ0, T] (a/2 - x) × 10^-8])/
       (Exp[ZC[ρ0, T, σm]] + 1 - (Exp[ZC[ρ0, T, σm]] - 1) Exp[κC[ρ0, T] (a/2 - x) × 10^-8])]
      , x ≥ a/2}}] (*statV*);

ψNPM[ρ0_, T_, σm_, x_] :=
 Piecewise[{{1000 σm/(ϵR) (a/2 - x) × 10^-10 + ψhNPM[ρ0, T, σm] , 0 ≤ x < a/2},
{1000 2 kM T/(z eM) Log[
```

```
        Exp[ZM[ρ0, T, σm]] + 1 + (Exp[ZM[ρ0, T, σm]] - 1) Exp[κM[ρ0, T] (a/2 - x) × 10^-10]
       ------------------------------------------------------------------------------------]
        Exp[ZM[ρ0, T, σm]] + 1 - (Exp[ZM[ρ0, T, σm]] - 1) Exp[κM[ρ0, T] (a/2 - x) × 10^-10]

       , x ≥ a/2}}]

ψCC[ρ0_, T_, σm_, R_, r_] := Piecewise[{{{ψhCC[ρ0, T, σm, R]

       (1 + BesselK[1, κC[ρ0, T] (R + a/2) × 10^-8] / BesselK[0, κC[ρ0, T] (R + a/2) × 10^-8] κC[ρ0, T] (R + a/2 - r) 10^-8),

       R ≤ r < R + a/2}, {BesselK[0, κC[ρ0, T] r × 10^-8] / BesselK[0, κC[ρ0, T] (R + a/2) × 10^-8] ψhCC[ρ0, T, σm, R],

       r ≥ R + a/2}}] (*statV*);

ψCM[ρ0_, T_, σm_, R_, r_] := Piecewise[{{{ψhCM[ρ0, T, σm, R]

       (1 + BesselK[1, κM[ρ0, T] (R + a/2) × 10^-10] / BesselK[0, κM[ρ0, T] (R + a/2) × 10^-10] κM[ρ0, T] (R + a/2 - r) 10^-10),

       R ≤ r < R + a/2}, {BesselK[0, κM[ρ0, T] r × 10^-10] / BesselK[0, κM[ρ0, T] (R + a/2) × 10^-10] ψhCM[ρ0, T, σm, R],

       r ≥ R + a/2}}] (*mV*);

ψSC[ρ0_, T_, σm_, R_, r_] := Piecewise[

    {{ψhSC[ρ0, T, σm, R] (1 + (κC[ρ0, T] + 1 / ((R + a/2) 10^-8)) (R + a/2 - r) 10^-8), R ≤ r < R + a/2},

     {(R + a/2) / r ψhSC[ρ0, T, σm, R] Exp[κC[ρ0, T] (R + a/2 - r) 10^-8],

      r ≥ R + a/2}}] (*statV*);

ψSM[ρ0_, T_, σm_, R_, r_] := Piecewise[{{{ψhSM[ρ0, T, σm, R]

       (1 + (κM[ρ0, T] + 1 / ((R + a/2) 10^-10)) (R + a/2 - r) 10^-10), R ≤ r < R + a/2},

       {(R + a/2) / r ψhSM[ρ0, T, σm, R] Exp[κM[ρ0, T] (R + a/2 - r) 10^-10], r ≥ R + a/2}}] (*mV*);
```

# The induced surface charge density

Now, with the help of $\psi$h, $\psi$r, and Z, the induced surface charge density is defined for the different geometries. Once again, as for $\psi$(r), the induced surface charge density is divided in two intervals.

```
σPC[ρ0_, T_, σm_, x_] := Piecewise[
    {{0, 0 ≤ x < a/2}, {ϵ κC[ρ0, T]/(4 π) ψhPC[ρ0, T, σm] Exp[κC[ρ0, T] (a/2 - x) × 10^-8],
      x ≥ a/2}}] (*esu/cm^2*);
σPM[ρ0_, T_, σm_, x_] := Piecewise[{{0, 0 ≤ x < a/2}, {ϵR κM[ρ0, T]
       ψhPM[ρ0, T, σm]/1000 Exp[κM[ρ0, T] (a/2 - x) × 10^-10], x ≥ a/2}}] (*C/m^2*);
σNPC[ρ0_, T_, σm_, x_] := Piecewise[{{0, 0 ≤ x < a/2},
     {ϵ κC[ρ0, T] kC T/(π z eC) (((Exp[2 ZC[ρ0, T, σm]] - 1) Exp[κC[ρ0, T] (a/2 - x) × 10^-8])/
        ((Exp[ZC[ρ0, T, σm]] + 1)^2 - ((Exp[ZC[ρ0, T, σm]] - 1)
           Exp[κC[ρ0, T] (a/2 - x) × 10^-8])^2)), x ≥ a/2}}] (*esu/cm^2*);
σNPM[ρ0_, T_, σm_, x_] := Piecewise[{{0, 0 ≤ x < a/2},
     {4 ϵR κM[ρ0, T] kM T/(z eM) (((Exp[2 ZM[ρ0, T, σm]] - 1) Exp[κM[ρ0, T] (a/2 - x) × 10^-10])/
        ((Exp[ZM[ρ0, T, σm]] + 1)^2 - ((Exp[ZM[ρ0, T, σm]] - 1)
           Exp[κM[ρ0, T] (a/2 - x) × 10^-10])^2)), x ≥ a/2}}] (*C/m^2*);
σCC[ρ0_, T_, σm_, R_, r_] := Piecewise[{{0, R ≤ r < R + a/2},
     {ϵ κC[ρ0, T]/(4 π) BesselK[1, κC[ρ0, T] r × 10^-8]/BesselK[0, κC[ρ0, T] (R + a/2) 10^-8] ψhCC[ρ0, T, σm, R],
      r ≥ R + a/2}}] (*esu/cm^2*);
σCM[ρ0_, T_, σm_, R_, r_] := Piecewise[{{0, R ≤ r < R + a/2},
     {ϵR κM[ρ0, T] BesselK[1, κM[ρ0, T] r × 10^-10]/BesselK[0, κM[ρ0, T] (R + a/2) 10^-10] ψhCM[ρ0, T, σm, R]/1000,
      r ≥ R + a/2}}] (*C/m^2*);
σSC[ρ0_, T_, σm_, R_, r_] := Piecewise[{{0, R ≤ r < R + a/2},
     {ϵ/(4 π) ((1 + κC[ρ0, T] r × 10^-8)/(r × 10^-8)) (R + a/2)/r ψhSC[ρ0, T, σm, R]
```

$$\text{Exp}\left[\kappa C[\rho 0, T]\ \left(R+\frac{a}{2}-r\right) 10^{-8}\right], r \geq R+\frac{a}{2}\}\}\Big]\ (*\text{esu}/\text{cm}^2*);$$

$$\sigma SM[\rho 0\_, T\_, \sigma m\_, R\_, r\_] := \text{Piecewise}\Big[\Big\{\Big\{0, R \leq r < R+\frac{a}{2}\Big\},$$

$$\Big\{\epsilon R\left(\frac{1+\kappa M[\rho 0, T]\ r \times 10^{-10}}{r \times 10^{-10}}\right) \frac{\psi hSM[\rho 0, T, \sigma m, R]}{1000}\ \frac{\left(R+\frac{a}{2}\right)}{r}$$

$$\text{Exp}\left[\kappa M[\rho 0, T]\ \left(R+\frac{a}{2}-r\right) 10^{-10}\right], r \geq R+\frac{a}{2}\}\}\Big]\ (*C/m^2*);$$

# The concentration profiles

Now, the co-ion (p) and counter-ion (n) distribution functions are defined for the different geometries.

In[•]:=
```
gpP[ρ0_, T_, σm_, x_] := Piecewise[{{0, 0 ≤ x < a/2},
    {Exp[-(z eM)/(kM T) ψhPM[ρ0, T, σm]/1000 Exp[κM[ρ0, T] (a/2 - x) × 10^-10]], x ≥ a/2}}] ;
gnP[ρ0_, T_, σm_, x_] := Piecewise[{{0, 0 ≤ x < a/2},
    {Exp[(z eM)/(kM T) ψhPM[ρ0, T, σm]/1000 Exp[κM[ρ0, T] (a/2 - x) × 10^-10]], x ≥ a/2}}] ;
gpNP[ρ0_, T_, σm_, x_] := Piecewise[{{0, 0 ≤ x < a/2},
    {Exp[-2 Log[(Exp[ZM[ρ0, T, σm]] + 1 + (Exp[ZM[ρ0, T, σm]] - 1)
          Exp[κM[ρ0, T] (a/2 - x) × 10^-10])/(Exp[ZM[ρ0, T, σm]] + 1 -
          (Exp[ZM[ρ0, T, σm]] - 1) Exp[κM[ρ0, T] (a/2 - x) × 10^-10])]], x ≥ a/2}}] ;
gnNP[ρ0_, T_, σm_, x_] := Piecewise[{{0, 0 ≤ x < a/2},
    {Exp[2 Log[(Exp[ZM[ρ0, T, σm]] + 1 + (Exp[ZM[ρ0, T, σm]] - 1)
          Exp[κM[ρ0, T] (a/2 - x) × 10^-10])/(Exp[ZM[ρ0, T, σm]] + 1 -
          (Exp[ZM[ρ0, T, σm]] - 1) Exp[κM[ρ0, T] (a/2 - x) × 10^-10])]], x ≥ a/2}}] ;
gpC[ρ0_, T_, σm_, R_, r_] := Piecewise[{{0, R ≤ r < R + a/2}, {Exp[
    -(z eM)/(kM T) ψhCM[ρ0, T, σm, R]/1000 BesselK[0, κM[ρ0, T] r × 10^-10]/BesselK[0, κM[ρ0, T] (R + a/2) × 10^-10]], r ≥ R + a/2}}] ;
gnC[ρ0_, T_, σm_, R_, r_] := Piecewise[{{0, R ≤ r < R + a/2}, {Exp[
    (z eM)/(kM T) ψhCM[ρ0, T, σm, R]/1000 BesselK[0, κM[ρ0, T] r × 10^-10]/BesselK[0, κM[ρ0, T] (R + a/2) × 10^-10]], r ≥ R + a/2}}] ;
gpS[ρ0_, T_, σm_, R_, r_] := Piecewise[{{0, R ≤ r < R + a/2}, {Exp[-(z eM)/(kM T)
    ψhSM[ρ0, T, σm, R]/1000 (R + a/2)/r Exp[κM[ρ0, T] (R + a/2 - r) 10^-10]], r ≥ R + a/2}}] ;
gnS[ρ0_, T_, σm_, R_, r_] := Piecewise[{{0, R ≤ r < R + a/2}, {Exp[
    (z eM)/(kM T) ψhSM[ρ0, T, σm, R]/1000 (R + a/2)/r Exp[κM[ρ0, T] (R + a/2 - r) 10^-10]], r ≥ R + a/2}}] ;
```

# The differential capacitance

Finally, the differential capacitance is obtained for our different geometries.

In[•]:=
```
CdPC[ρ0_, T_] := (4 π (2 + κC[ρ0, T] (a/2 × 10^-8)))/(ϵ κC[ρ0, T]))^-1 (*cm^-1||cm/cm^2*);

CdPM[ρ0_, T_] := (2 + κM[ρ0, T] (a/2 × 10^-10))/(ϵR κM[ρ0, T]))^-1 (*F/m^2*);

CdNPC[ρ0_, T_, σm_] := (4 π)/(ϵ κC[ρ0, T]) (2 + κC[ρ0, T] (a/2 × 10^-8))/Sqrt[1 + ((2 π z eC 10 c/10^4 σm)/(ϵ κC[ρ0,T] kC T))^2])^-1

(*cm^-1||cm/cm^2*);

CdNPM[ρ0_, T_, σm_] := (1/(ϵR κM[ρ0, T]) (2 + κM[ρ0, T] (a/2 × 10^-10))/Sqrt[1 + ((z eM σm)/(2 ϵR κM[ρ0,T] kM T))^2])^-1 (*F/m^2*);

CdCC[ρ0_, T_, R_] :=
 ((4 π)/(ϵ κC[ρ0, T]) (2 BesselK[0, κC[ρ0, T] (R + a/2) × 10^-8]/BesselK[1, κC[ρ0, T] (R + a/2) × 10^-8] + κC[ρ0, T] a/2 × 10^-8))^-1
 (*cm^-1||cm/cm^2*);
CdCM[ρ0_, T_, R_] :=
 ((1/(ϵR κM[ρ0, T]) (2 BesselK[0, κM[ρ0, T] (R + a/2) × 10^-10]/BesselK[1, κM[ρ0, T] (R + a/2) × 10^-10] + κM[ρ0, T] a/2 × 10^-10))^-1 (*F/
 m^2*);

CdSC[ρ0_, T_, R_] := (4 π/ϵ (2 (R + a/2) 10^-8/(1 + κC[ρ0, T] (R + a/2) 10^-8) + a/2 × 10^-8))^-1 (*cm^-1||cm/cm^2*);

CdSM[ρ0_, T_, R_] := (1/(ϵR) (2 (R + a/2) 10^-10/(1 + κM[ρ0, T] (R + a/2) 10^-10) + a/2 × 10^-10))^-1 (*F/m^2*);
```

# The electrical double layer for nano-pore electrodes

## Preamble

In this program we solve the linearized  electrical double layer for nano-pore electrodes of different topologies, such a slit-pore (P), a cylindrical (C), and spherical (S) pores in two system unit CGS (C) and MKS (M). In order, to distinguish the different electric parameters, $\omega$, from the different pore topologies and unit system used their initials are used. Hence, $\psi$PM is the linearized mean electrostatic potential of a slit-pore in MKS units, whereas $\psi$CC is the linearized mean electrostatic potential of a cylindrical pore in CGS units.
The first step is to clear all our variables, and to define the constants used throughout this cell, their units are commented for clarity.

```
In[•]:= ClearAll["Global`*"]
kM = 1.38064852 × 10^-23 (*J/K*);
kC = 1.38064852 × 10^-16 (*ergs/K*);
ϵ0 = 8.85418781761 × 10^-12 (*C^2/N m^2||F/m||C/V m*);
ϵ = 78.5;
ϵR = ϵ ϵ0 (*C^2/N m^2||F/m||C/Vm*);
c = 2.99792458 × 10^8 (*m/s*);
z = 1;
eM = 1.60217733 × 10^-19 (*C*);
eC = 10 c × eM (*esu||Fr||statC*);
NA = 6.022140857 × 10^23 (*mol^-1*);
a = 4.25 (*Å*);
```

Now, a list of values of our variables is defined

```
In[•]:= CHARGEDEN = {0.001, 0.002, 0.005, 0.01} (*C/m^2*);
CONCENTRATIONS = {0.001, 0.01, 0.1, 0.5} (*M*);
TEMPERATURES = {278.15, 298.15, 308.15, 328.15} (*K*);
RADIUS = {5, 30, 80, 200} (*Å*) ;
```

Furthermore, the molar concentration and the debye length are defined. This functions are independent of the topology used.

```
In[•]:= nC[ρ0_] := ρ0 × 10^-3 NA (*cm^-3*);
        nM[ρ0_] := ρ0 × 10^3 NA (*m^-3*);
        κC[ρ0_, T_] := Sqrt[8 π nC[ρ0] eC^2 z^2 / (ϵ kC T)] (*cm^-1*);
        κM[ρ0_, T_] := Sqrt[2 nM[ρ0] eM^2 z^2 / (ϵR kM T)] (*m^-1*);
```

# Constants

For the EDL of a pore, we solve five differential equations of second order with ten boundary conditions. By solving them, we find the values of the different constants for each topology. These constants depend on the molar concentration, $\rho_0$, temperature, T, inner and outer surface charge, $\sigma_I$ and $\sigma_{II}$, the distance between the pores' center and pores' inner surface, t or R, and the pores' width, d. With these constants values we find the solutions of all the electric parameters.

```
c1PC := 0;
c1PM := 0;
c2PC[ρ0_, T_, σI_, σII_, t_, d_] :=
  (((4 π / ϵ) (10 c / 10^4) (σII ((d + a/2) 10^-8 + Coth[κC[ρ0, T] (t - a/2) 10^-8] / κC[ρ0, T]) +
      σI ((a/2) 10^-8 + Coth[κC[ρ0, T] (t - a/2) 10^-8] / κC[ρ0, T])))) /
   (1 + κC[ρ0, T] (d + a) 10^-8 + Coth[κC[ρ0, T] (t - a/2) 10^-8])) Exp[κC[ρ0, T] (t + d + a/2) 10^-8] (*statV*);
c2PM[ρ0_, T_, σI_, σII_, t_, d_] :=
  1000 (((1 / ϵR) (σII ((d + a/2) 10^-10 + Coth[κM[ρ0, T] (t - a/2) 10^-10] / κM[ρ0, T]) +
      σI ((a/2) 10^-10 + Coth[κM[ρ0, T] (t - a/2) 10^-10] / κM[ρ0, T])))) /
   (1 + κM[ρ0, T] (d + a) 10^-10 + Coth[κM[ρ0, T] (t - a/2) 10^-10])) Exp[κM[ρ0, T] (t + d + a/2) 10^-10] (*mV*);
c3PC[ρ0_, T_, σI_, σII_, t_, d_] :=
```

```
  c2PC[ρ0, T, σI, σII, t, d] Exp[-κC[ρ0, T] (t + d + a/2) 10^-8] -
   c4PC[ρ0, T, σI, σII, t, d] (t + d + a/2) 10^-8 (*statV*);
c3PM[ρ0_, T_, σI_, σII_, t_, d_] :=
  c2PM[ρ0, T, σI, σII, t, d] Exp[-κM[ρ0, T] (t + d + a/2) 10^-10] -
   c4PM[ρ0, T, σI, σII, t, d] (t + d + a/2) 10^-10 (*mV*);
c4PC[ρ0_, T_, σI_, σII_, t_, d_] := -c2PC[ρ0, T, σI, σII, t, d] ×
   κC[ρ0, T] Exp[-κC[ρ0, T] (t + d + a/2) 10^-8] (*statV/cm*);
c4PM[ρ0_, T_, σI_, σII_, t_, d_] := -c2PM[ρ0, T, σI, σII, t, d] ×
   κM[ρ0, T] Exp[-κM[ρ0, T] (t + d + a/2) 10^-10] (*mV/m*);
c5PC[ρ0_, T_, σI_, σII_, t_, d_] := c3PC[ρ0, T, σI, σII, t, d] +
   (c4PC[ρ0, T, σI, σII, t, d] - c6PC[ρ0, T, σI, σII, t, d]) (t + d) 10^-8 (*statV*);
c5PM[ρ0_, T_, σI_, σII_, t_, d_] := c3PM[ρ0, T, σI, σII, t, d] +
   (c4PM[ρ0, T, σI, σII, t, d] - c6PM[ρ0, T, σI, σII, t, d]) (t + d) 10^-10 (*mV*);
c6PC[ρ0_, T_, σI_, σII_, t_, d_] := c4PC[ρ0, T, σI, σII, t, d] + 4 π/ϵ 10 c/10^4 σII
(*statV/cm*);
c6PM[ρ0_, T_, σI_, σII_, t_, d_] :=
 c4PM[ρ0, T, σI, σII, t, d] + 1000 1/(ϵR) σII (*mV/m*);
c7PC[ρ0_, T_, σI_, σII_, t_, d_] := c5PC[ρ0, T, σI, σII, t, d] +
  (c6PC[ρ0, T, σI, σII, t, d] - c8PC[ρ0, T, σI, σII, t, d]) (t) 10^-8 (*statV*);
c7PM[ρ0_, T_, σI_, σII_, t_, d_] := c5PM[ρ0, T, σI, σII, t, d] +
  (c6PM[ρ0, T, σI, σII, t, d] - c8PM[ρ0, T, σI, σII, t, d]) (t) 10^-10 (*mV*);
c8PC[ρ0_, T_, σI_, σII_, t_, d_] := c6PC[ρ0, T, σI, σII, t, d] + 4 π/ϵ 10 c/10^4 σI
 (*statV/cm*);
c8PM[ρ0_, T_, σI_, σII_, t_, d_] := c6PM[ρ0, T, σI, σII, t, d] + 1000 1/(ϵR) σI
 (*mV/m*);
c9PC[ρ0_, T_, σI_, σII_, t_, d_] := c8PC[ρ0, T, σI, σII, t, d] / (2 κC[ρ0, T] Sinh[κC[ρ0, T] (t - a/2) 10^-8])
 (*statV*);
c9PM[ρ0_, T_, σI_, σII_, t_, d_] := c8PM[ρ0, T, σI, σII, t, d] / (2 κM[ρ0, T] Sinh[κM[ρ0, T] (t - a/2) 10^-10])
 (*mV*);
c10PC[ρ0_, T_, σI_, σII_, t_, d_] := c9PC[ρ0, T, σI, σII, t, d](*statV*);
c10PM[ρ0_, T_, σI_, σII_, t_ , d_] := c9PM[ρ0, T, σI, σII, t, d](*mV*);
```

```
c1CC := 0 ;
c1CM := 0 ;
c2CC[ρ0_, T_, σI_, σII_, R_, d_] := ((((4 π)/ϵ) (10 c)/10^4 (σII ((R + d) 10^-8) (Log[(R - a/2)/(R + d)] -
                BesselI[0, κC[ρ0, T] (R - a/2) 10^-8]/(κC[ρ0, T] (R - a/2) 10^-8 BesselI[1, κC[ρ0, T] (R - a/2) 10^-8])) + σI (R 10^-8)
            (Log[(R - a/2)/R] - BesselI[0, κC[ρ0, T] (R - a/2) 10^-8]/(κC[ρ0, T] (R - a/2) 10^-8 BesselI[1, κC[ρ0, T] (R - a/2) 10^-8])))))/
        (κC[ρ0, T] (R + d + a/2) 10^-8 BesselK[1, κC[ρ0, T] (R + d + a/2) 10^-8]
            (Log[(R - a/2)/(R + d + a/2)] - BesselI[0, κC[ρ0, T] (R - a/2) 10^-8]/(κC[ρ0, T] (R - a/2) 10^-8 BesselI[1, κC[ρ0, T] (R - a/2) 10^-8])) -
            BesselK[0, κC[ρ0, T] (R + d + a/2) 10^-8])) (*statV*);
c2CM[ρ0_, T_, σI_, σII_, R_, d_] := 1000 ((((1/(ϵR)) (σII ((R + d) 10^-10)
                (Log[(R - a/2)/(R + d)] - BesselI[0, κM[ρ0, T] (R - a/2) 10^-10]/(κM[ρ0, T] (R - a/2) 10^-10 BesselI[1, κM[ρ0, T] (R - a/2) 10^-10])) +
            σI (R 10^-10) (Log[(R - a/2)/R] -
                BesselI[0, κM[ρ0, T] (R - a/2) 10^-10]/(κM[ρ0, T] (R - a/2) 10^-10 BesselI[1, κM[ρ0, T] (R - a/2) 10^-10])))))/
        (κM[ρ0, T] (R + d + a/2) 10^-10 BesselK[1, κM[ρ0, T] (R + d + a/2) 10^-10]
            (Log[(R - a/2)/(R + d + a/2)] - BesselI[0, κM[ρ0, T] (R - a/2) 10^-10]/(κM[ρ0, T] (R - a/2) 10^-10 BesselI[1, κM[ρ0, T] (R - a/2) 10^-10])) -
            BesselK[0, κM[ρ0, T] (R + d + a/2) 10^-10])) (*mV*);
c3CC[ρ0_, T_, σI_, σII_, R_, d_] := c2CC[ρ0, T, σI, σII, R, d]
    BesselK[0, κC[ρ0, T] (R + d + a/2) 10^-8] -
  c4CC[ρ0, T, σI, σII, R, d] Log[(R + d + a/2) 10^-8] (*statV*);
```

```
c3CM[ρ0_, T_, σI_, σII_, R_, d_] :=
  c2CM[ρ0, T, σI, σII, R, d] BesselK[0, κM[ρ0, T] (R + d + a/2) 10^-10] -
   c4CM[ρ0, T, σI, σII, R, d] Log[(R + d + a/2) 10^-10] (*mV*);
c4CC[ρ0_, T_, σI_, σII_, R_, d_] := -c2CC[ρ0, T, σI, σII, R, d] × κC[ρ0, T]
   (R + d + a/2) 10^-8 BesselK[1, κC[ρ0, T] (R + d + a/2) 10^-8] (*statV/cm*);
c4CM[ρ0_, T_, σI_, σII_, R_, d_] := -c2CM[ρ0, T, σI, σII, R, d] × κM[ρ0, T]
   (R + d + a/2) 10^-10 BesselK[1, κM[ρ0, T] (R + d + a/2) 10^-10] (*mV/m*);
c5CC[ρ0_, T_, σI_, σII_, R_, d_] := c3CC[ρ0, T, σI, σII, R, d] +
   (c4CC[ρ0, T, σI, σII, R, d] - c6CC[ρ0, T, σI, σII, R, d])
    Log[(R + d) 10^-8] (*statV*);
c5CM[ρ0_, T_, σI_, σII_, R_, d_] := c3CM[ρ0, T, σI, σII, R, d] +
   (c4CM[ρ0, T, σI, σII, R, d] - c6CM[ρ0, T, σI, σII, R, d])
    Log[(R + d) 10^-10] (*mV*);
c6CC[ρ0_, T_, σI_, σII_, R_, d_] := c4CC[ρ0, T, σI, σII, R, d] +
   4 π/ϵ 10 c/10^4 σII (R + d) 10^-8 (*statV/cm*);
c6CM[ρ0_, T_, σI_, σII_, R_, d_] := c4CM[ρ0, T, σI, σII, R, d] +
   1000 1/(ϵR) σII (R + d) 10^-10 (*mV/m*);
c7CC[ρ0_, T_, σI_, σII_, R_, d_] := c5CC[ρ0, T, σI, σII, R, d] +
   (c6CC[ρ0, T, σI, σII, R, d] - c8CC[ρ0, T, σI, σII, R, d])
    Log[(R) 10^-8] (*statV*);
c7CM[ρ0_, T_, σI_, σII_, R_, d_] := c5CM[ρ0, T, σI, σII, R, d] +
   (c6CM[ρ0, T, σI, σII, R, d] - c8CM[ρ0, T, σI, σII, R, d]) Log[(R) 10^-10] (*mV*);
c8CC[ρ0_, T_, σI_, σII_, R_, d_] := c6CC[ρ0, T, σI, σII, R, d] + 4 π/ϵ 10 c/10^4 σI (R) 10^-8
 (*statV/cm*);
c8CM[ρ0_, T_, σI_, σII_, R_, d_] := c6CM[ρ0, T, σI, σII, R, d] + 1000 1/(ϵR) σI (R) 10^-10
 (*mV/m*);
c9CC[ρ0_, T_, σI_, σII_, R_, d_] :=
  c8CC[ρ0, T, σI, σII, R, d] / (κC[ρ0, T] (R - a/2) 10^-8 BesselI[1, κC[ρ0, T] (R - a/2) 10^-8]) (*statV*);
c9CM[ρ0_, T_, σI_, σII_, R_, d_] :=
  c8CM[ρ0, T, σI, σII, R, d] / (κM[ρ0, T] (R - a/2) 10^-10 BesselI[1, κM[ρ0, T] (R - a/2) 10^-10]) (*mV*);
c10CC := 0;
c10CM := 0;
c1SC := 0 ;
```

```
c1SM := 0 ;
c2SC[ρ0_, T_, σI_, σII_, R_, d_] :=
  (((4 π)/(ϵ κC[ρ0]) (10 c)/10^4 (σI (R 10^-10) (Tanh[κC[ρ0, T] (R - a/2) 10^-8] + κC[ρ0, T] a/2 10^-8) +
        σII ((R + d) 10^-8) (Tanh[κC[ρ0, T] (R - a/2) 10^-8] + κC[ρ0, T] (d + a/2) 10^-8)))/
    (Tanh[κC[ρ0, T] (R - a/2) 10^-8] + κC[ρ0, T] (d + a) 10^-8 + 1))
   Exp[κC[ρ0, T] (R + d + a/2) 10^-8] (*statV*cm*);
c2SM[ρ0_, T_, σI_, σII_, R_, d_] := 1000 (((1/(ϵR κM[ρ0, T]
      (σI (R 10^-10) (Tanh[κM[ρ0, T] (R - a/2) 10^-10] + κM[ρ0, T] a/2 10^-10) + σII
        ((R + d) 10^-10) (Tanh[κM[ρ0, T] (R - a/2) 10^-10] + κM[ρ0, T] (d + a/2) 10^-10)))/
    (Tanh[κM[ρ0, T] (R - a/2) 10^-10] + κM[ρ0, T] (d + a) 10^-10 + 1))
   Exp[κM[ρ0, T] (R + d + a/2) 10^-10] (*mV*m*);
c3SC[ρ0_, T_, σI_, σII_, R_, d_] := 1/((R + d + a/2) 10^-8)
   (c2SC[ρ0, T, σI, σII, R, d] Exp[-κC[ρ0, T] (R + d + a/2) 10^-8] -
     c4SC[ρ0, T, σI, σII, R, d]) (*statV*);
c3SM[ρ0_, T_, σI_, σII_, R_, d_] := 1/((R + d + a/2) 10^-10)
   (c2SM[ρ0, T, σI, σII, R, d] Exp[-κM[ρ0, T] (R + d + a/2) 10^-10] -
     c4SM[ρ0, T, σI, σII, R, d]) (*mV*);
c4SC[ρ0_, T_, σI_, σII_, R_, d_] := c2SC[ρ0, T, σI, σII, R, d]
   Exp[-κC[ρ0, T] (R + d + a/2) 10^-8] (κC[ρ0, T] (R + d + a/2) 10^-8 + 1) (*statV*cm*);
c4SM[ρ0_, T_, σI_, σII_, R_, d_] := c2SM[ρ0, T, σI, σII, R, d]
   Exp[-κM[ρ0, T] (R + d + a/2) 10^-10] (κM[ρ0, T] (R + d + a/2) 10^-10 + 1) (*mV*m*);
c5SC[ρ0_, T_, σI_, σII_, R_, d_] := c3SC[ρ0, T, σI, σII, R, d] +
   (c4SC[ρ0, T, σI, σII, R, d] - c6SC[ρ0, T, σI, σII, R, d])/((R + d) 10^-8) (*statV*);
c5SM[ρ0_, T_, σI_, σII_, R_, d_] := c3SM[ρ0, T, σI, σII, R, d] +
```

```
    (c4SM[ρ0, T, σI, σII, R, d] - c6SM[ρ0, T, σI, σII, R, d]) / ((R + d) 10^-10) (*mV*);
c6SC[ρ0_, T_, σI_, σII_, R_, d_] := c4SC[ρ0, T, σI, σII, R, d] -
    (4 π / ϵ) (10 c / 10^4) σII ((R + d) 10^-8)^2 (*statV*cm*);
c6SM[ρ0_, T_, σI_, σII_, R_, d_] := c4SM[ρ0, T, σI, σII, R, d] -
    1000 (1 / (ϵR)) σII ((R + d) 10^-10)^2 (*mV*m*);
c7SC[ρ0_, T_, σI_, σII_, R_, d_] := c5SC[ρ0, T, σI, σII, R, d] +
    (c6SC[ρ0, T, σI, σII, R, d] - c8SC[ρ0, T, σI, σII, R, d]) / ((R) 10^-8) (*statV*);
c7SM[ρ0_, T_, σI_, σII_, R_, d_] := c5SM[ρ0, T, σI, σII, R, d] +
    (c6SM[ρ0, T, σI, σII, R, d] - c8SM[ρ0, T, σI, σII, R, d]) / ((R) 10^-10) (*mV*);
c8SC[ρ0_, T_, σI_, σII_, R_, d_] := c6SC[ρ0, T, σI, σII, R, d] -
    (4 π / ϵ) (10 c / 10^4) σI ((R) 10^-8)^2 (*statV*cm*);
c8SM[ρ0_, T_, σI_, σII_, R_, d_] := c6SM[ρ0, T, σI, σII, R, d] -
    1000 (1 / (ϵR)) σI ((R) 10^-10)^2 (*mV*m*);
c9SC[ρ0_, T_, σI_, σII_, R_, d_] :=
  - c8SC[ρ0, T, σI, σII, R, d] / (2 (κC[ρ0, T] (R - a/2) 10^-8 Cosh[κC[ρ0, T] (R - a/2) 10^-8] - Sinh[κC[ρ0, T] (R - a/2) 10^-8]))
  (*statV*cm*);
c9SM[ρ0_, T_, σI_, σII_, R_, d_] :=
  - (c8SM[ρ0, T, σI, σII, R, d] / (2 (κM[ρ0, T] (R - a/2) 10^-10 Cosh[
          κM[ρ0, T] (R - a/2) 10^-10] - Sinh[κM[ρ0, T] (R - a/2) 10^-10])))) (*mV*m*);
c10SC[ρ0_, T_, σI_, σII_, R_, d_] := -c9SC[ρ0, T, σI, σII, R , d] (*statV*cm*);
c10SM[ρ0_, T_, σI_, σII_, R_, d_] := -c9SM[ρ0, T, σI, σII, R , d] (*mV*m*);
```

# The mean electrostatic potential

Now, with our constants, we define the mean electrostatic potential in five intervals for each topology as

```
In[•]:= ψPC[ρ0_, T_, σI_, σII_, t_, d_, x_] :=
  Piecewise[{{{2 c9PC [ρ0, T, σI, σII, t, d] Cosh[κC[ρ0, T] (x) 10^-8], 0 ≤ x ≤ t - a/2},
    {c7PC[ρ0, T, σI, σII, t, d] + c8PC[ρ0, T, σI, σII, t, d] (x) 10^-8, t - a/2 < x ≤ t},
    {c5PC[ρ0, T, σI, σII, t, d] + c6PC[ρ0, T, σI, σII, t, d] (x) 10^-8, t ≤ x ≤ t + d},
```

```
    {c3PC[ρ0, T, σI, σII, t, d] + c4PC[ρ0, T, σI, σII, t, d] (x) 10^-8,
     t + d ≤ x < t + d + a/2}, {c1PC Exp[κC[ρ0, T] (x) 10^-8] + c2PC[ρ0, T, σI, σII, t, d]
       Exp[-κC[ρ0, T] (x) 10^-8], x ≥ t + d + a/2}}] (*statV*);
ψPM[ρ0_, T_, σI_, σII_, t_, d_, x_] := Piecewise[
  {{2 c9PM[ρ0, T, σI, σII, t, d] Cosh[κM[ρ0, T] (x) 10^-10], 0 ≤ x ≤ t - a/2},
   {c7PM[ρ0, T, σI, σII, t, d] + c8PM[ρ0, T, σI, σII, t, d] (x) 10^-10, t - a/2 < x ≤ t},
   {c5PM[ρ0, T, σI, σII, t, d] + c6PM[ρ0, T, σI, σII, t, d] (x) 10^-10, t ≤ x ≤ t + d},
   {c3PM[ρ0, T, σI, σII, t, d] + c4PM[ρ0, T, σI, σII, t, d] (x) 10^-10,
    t + d ≤ x < t + d + a/2}, {c1PM Exp[κM[ρ0, T] (x) 10^-10] +
     c2PM[ρ0, T, σI, σII, t, d] Exp[-κM[ρ0, T] (x) 10^-10], x ≥ t + d + a/2}}] (*mV*);
ψCC[ρ0_, T_, σI_, σII_, R_, d_, r_] := Piecewise[
  {{c9CC [ρ0, T, σI, σII, R, d] BesselI[0, κC[ρ0, T] (r) 10^-8] +
     c10CC BesselK[0, κC[ρ0, T] (r) 10^-8], 0 ≤ r ≤ R - a/2},
   {c7CC[ρ0, T, σI, σII, R, d] + c8CC[ρ0, T, σI, σII, R, d] Log[(r) 10^-8],
    R - a/2 < r ≤ R}, {c5CC[ρ0, T, σI, σII, R, d] +
     c6CC[ρ0, T, σI, σII, R, d] Log[(r) 10^-8], R ≤ r ≤ R + d},
   {c3CC[ρ0, T, σI, σII, R, d] + c4CC[ρ0, T, σI, σII, R, d] Log[(r) 10^-8],
    R + d ≤ r < R + d + a/2},
   {c1CC BesselI[0, κC[ρ0, T] (r) 10^-8] + c2CC[ρ0, T, σI, σII, R, d]
       BesselK[0, κC[ρ0, T] (r) 10^-8], r ≥ R + d + a/2}}] (*statV*);
ψCM[ρ0_, T_, σI_, σII_, R_, d_, r_] := Piecewise[
  {{c9CM[ρ0, T, σI, σII, R, d] BesselI[0, κM[ρ0, T] (r) 10^-10] +
     c10CM BesselK[0, κM[ρ0, T] (r) 10^-10], 0 ≤ r ≤ R - a/2},
   {c7CM[ρ0, T, σI, σII, R, d] + c8CM[ρ0, T, σI, σII, R, d] Log[(r) 10^-10],
    R - a/2 < r ≤ R}, {c5CM[ρ0, T, σI, σII, R, d] +
     c6CM[ρ0, T, σI, σII, R, d] Log[(r) 10^-10], R ≤ r ≤ R + d},
   {c3CM[ρ0, σI, σII, R, d] + c4CM[ρ0, σI, σII, R, d] Log[(r) 10^-10],
    R + d ≤ r < R + d + a/2},
```

```
    {c1CM BesselI[0, κM[ρ0, T] (r) 10^-10] + c2CM[ρ0, T, σI, σII, R, d]
       BesselK[0, κM[ρ0, T] (r) 10^-10], r ≥ R + d + a/2}}] (*mV*);
ψSC[ρ0_, T_, σI_, σII_, R_, d_, r_] := Piecewise[
  {{1/((r) 10^-8) (c9SC[ρ0, T, σI, σII, R, d] Exp[κC[ρ0, T] (r) 10^-8] +
      c10SC[ρ0, T, σI, σII, R, d] Exp[-κC[ρ0, T] (r) 10^-8]), 0 ≤ r ≤ R - a/2},
   {c7SC[ρ0, T, σI, σII, R, d] + c8SC[ρ0, T, σI, σII, R, d]/((r) 10^-8), R - a/2 < r ≤ R},
   {c5SC[ρ0, T, σI, σII, R, d] + c6SC[ρ0, T, σI, σII, R, d]/((r) 10^-8), R ≤ r ≤ R + d},
   {c3SC[ρ0, T, σI, σII, R, d] + c4SC[ρ0, T, σI, σII, R, d]/((r) 10^-8), R + d ≤ r < R + d + a/2},
   {1/((r) 10^-8) (c1SC Exp[κC[ρ0, T] (r) 10^-8] + c2SC[ρ0, T, σI, σII, R, d]
       Exp[-κC[ρ0, T] (r) 10^-8]), r ≥ R + d + a/2}}] (*statV*);
ψSM[ρ0_, T_, σI_, σII_, R_, d_, r_] := Piecewise[
  {{1/((r) 10^-10) (c9SM[ρ0, T, σI, σII, R, d] Exp[κM[ρ0, T] (r) 10^-10] +
      c10SM[ρ0, T, σI, σII, R, d] Exp[-κM[ρ0, T] (r) 10^-10]), 0 ≤ r ≤ R - a/2},
   {c7SM[ρ0, T, σI, σII, R, d] + c8SM[ρ0, T, σI, σII, R, d]/((r) 10^-10), R - a/2 < r ≤ R},
   {c5SM[ρ0, T, σI, σII, R, d] + c6SM[ρ0, T, σI, σII, R, d]/((r) 10^-10), R ≤ r ≤ R + d},
   {c3SM[ρ0, T, σI, σII, R, d] + c4SM[ρ0, T, σI, σII, R, d]/((r) 10^-10), R + d ≤ r < R + d + a/2},
   {1/((r) 10^-10) (c1SM Exp[κM[ρ0, T] (r) 10^-10] + c2SM[ρ0, T, σI, σII, R, d]
       Exp[-κM[ρ0, T] (r) 10^-10]), r ≥ R + d + a/2}}] (*mV*);
```

# The induced surface charge density

Again, with our constants, we define the induced surface charge density in three intervals, for each topology as

```
σPC[ρ0_, T_, σI_, σII_, t_, d_, x_] :=
  Piecewise[{{{{(10 c/10^4 (σI + σII) - (κC[ρ0, T] 10 c/10^4
```

$$\left(\sigma II\left(\left(d+\frac{a}{2}\right)10^{-8}+\frac{\text{Coth}\left[\kappa C[\rho 0,T]\left(t-\frac{a}{2}\right)10^{-8}\right]}{\kappa C[\rho 0,T]}\right)+\sigma I\right.$$
$$\left.\left(\left(\frac{a}{2}\right)10^{-8}+\frac{\text{Coth}\left[\kappa C[\rho 0,T]\left(t-\frac{a}{2}\right)10^{-8}\right]}{\kappa C[\rho 0,T]}\right)\right)\Big/$$
$$\left(1+\kappa C[\rho 0,T]\,(d+a)\,10^{-8}+\text{Coth}\left[\kappa C[\rho 0,T]\left(t-\frac{a}{2}\right)10^{-8}\right]\right)\Big/$$
$$\text{Sinh}\left[\kappa C[\rho 0,T]\left(t-\frac{a}{2}\right)10^{-8}\right]\text{Sinh}\left[\kappa C[\rho 0,T]\,(x)\,10^{-8}\right],$$
$$0\le x\le t-\frac{a}{2}\Big\},\ \Big\{0,\ t-\frac{a}{2}<x\le t+d+\frac{a}{2}\Big\},$$
$$\Big\{\frac{\epsilon\,\kappa C[\rho 0,T]}{4\pi}\left(c1PC\,\text{Exp}\left[\kappa C[\rho 0,T]\,(x)\,10^{-8}\right]+c2PC[\rho 0,T,\sigma I,\sigma II,t,d]\right.$$
$$\left.\text{Exp}\left[-\kappa C[\rho 0,T]\,(x)\,10^{-8}\right]\right),\ x\ge t+d+\frac{a}{2}\Big\}\Big\}\Big](*\text{esu/cm}^2*);$$
$$\sigma PM[\rho 0\_,T\_,\sigma I\_,\sigma II\_,t\_,d\_,x\_]:=\text{Piecewise}\Big[$$
$$\left\{\left\{\left(\frac{(\sigma I+\sigma II)-\frac{\left(\kappa M[\rho 0,T]\left(\sigma II\left(\left(d+\frac{a}{2}\right)10^{-10}+\frac{\text{Coth}\left[\kappa M[\rho 0,T]\left(t-\frac{a}{2}\right)10^{-10}\right]}{\kappa M[\rho 0,T]}\right)+\sigma I\left(\left(\frac{a}{2}\right)10^{-10}+\frac{\text{Coth}\left[\kappa M[\rho 0,T]\left(t-\frac{a}{2}\right)10^{-10}\right]}{\kappa M[\rho 0,T]}\right)\right)\right)}{\left(1+\kappa M[\rho 0,T]\,(d+a)\,10^{-10}+\text{Coth}\left[\kappa M[\rho 0,T]\left(t-\frac{a}{2}\right)10^{-10}\right]\right)}}{\text{Sinh}\left[\kappa M[\rho 0,T]\left(t-\frac{a}{2}\right)10^{-10}\right]}\right)\right.$$
$$\text{Sinh}\left[\kappa M[\rho 0,T]\,(x)\,10^{-10}\right],\ 0\le x\le t-\frac{a}{2}\Big\},\ \Big\{0,\ t-\frac{a}{2}<x<t+d+\frac{a}{2}\Big\},$$
$$\Big\{\frac{\epsilon R\,\kappa M[\rho 0,T]}{1000}\left(c1PM\,\text{Exp}\left[\kappa M[\rho 0,T]\,(x)\,10^{-10}\right]+c2PM[\rho 0,T,\sigma I,\sigma II,t,d]\right.$$
$$\left.\text{Exp}\left[-\kappa M[\rho 0,T]\,(x)\,10^{-10}\right]\right),\ x\ge t+d+\frac{a}{2}\Big\}\Big\}\Big](*\text{C/m}^2*);$$
$$\sigma CC[\rho 0\_,T\_,\sigma I\_,\sigma II\_,R\_,d\_,r\_]:=\text{Piecewise}\Big[$$
$$\Big\{\Big\{\frac{\epsilon\,\kappa C[\rho 0,T]}{4\pi}\,c9CC\,[\rho 0,T,\sigma I,\sigma II,R,d]\,\text{BesselI}\left[1,\kappa C[\rho 0,T]\,(r)\,10^{-8}\right],$$
$$0\le r\le R-\frac{a}{2}\Big\},\ \Big\{0,\ R-\frac{a}{2}<r<R+d+\frac{a}{2}\Big\},\ \Big\{\frac{\epsilon\,\kappa C[\rho 0,T]}{4\pi}\,c2CC[\rho 0,T,\sigma I,\sigma II,R,d]$$
$$\text{BesselK}\left[1,\kappa C[\rho 0,T]\,(r)\,10^{-8}\right],\ r\ge R+d+\frac{a}{2}\Big\}\Big\}\Big](*\text{esu/cm}^2*);$$
$$\sigma CM[\rho 0\_,T\_,\sigma I\_,\sigma II\_,R\_,d\_,r\_]:=\text{Piecewise}\Big[$$
$$\Big\{\Big\{\epsilon R\,\kappa M[\rho 0,T]\,\frac{c9CM\,[\rho 0,T,\sigma I,\sigma II,R,d]}{1000}\,\text{BesselI}\left[1,\kappa M[\rho 0,T]\,(r)\,10^{-10}\right],$$
$$0\le r\le R-\frac{a}{2}\Big\},\ \Big\{0,\ R-\frac{a}{2}<r<R+d+\frac{a}{2}\Big\},$$

```
    {ϵR κM[ρ0, T] c2CM[ρ0, T, σI, σII, R, d] / 1000 BesselK[1, κM[ρ0, T] (r) 10^-10],
     r ≥ R + d + a/2}}] (*C/m^2*);
σSC[ρ0_, T_, σI_, σII_, R_, d_, r_] := Piecewise[{{2 ϵ / (4 π) c9SC[ρ0, T, σI, σII, R, d]
     κC[ρ0, T] r 10^-8 Cosh[κC[ρ0, T] r 10^-8] - Sinh[κC[ρ0, T] r 10^-8] / (r 10^-8)^2, 0 ≤ r ≤ R - a/2},
    {0, R - a/2 < r < R + d + a/2}, {ϵ / (4 π) c2SC[ρ0, T, σI, σII, R, d]
     (Exp[-κC[ρ0, T] r 10^-8] (κC[ρ0, T] r 10^-8 + 1)) / (r × 10^-8)^2, r ≥ R + d + a/2}}] (*esu/cm^2*);
σSM[ρ0_, T_, σI_, σII_, R_, d_, r_] := Piecewise[{{2 ϵR c9SM[ρ0, T, σI, σII, R, d] / 1000
     κM[ρ0, T] r 10^-10 Cosh[κM[ρ0, T] r 10^-10] - Sinh[κM[ρ0, T] r 10^-10] / (r 10^-10)^2,
    0 ≤ r ≤ R - a/2}, {0, R - a/2 < r < R + d + a/2}, {ϵR c2SM[ρ0, T, σI, σII, R, d] / 1000
     (Exp[-κM[ρ0, T] r 10^-10] (κM[ρ0, T] r 10^-10 + 1)) / (r × 10^-10)^2, r ≥ R + d + a/2}}] (*C/m^2*);
```

# The density profiles

Finally, with the constants the co-ion (p) and counter-ion (n) distribution functions are defined for the different pore topologies in three intervals.

```
In[•]:= gpP[ρ0_, T_, σI_, σII_, t_, d_, x_] := Piecewise[
    {{Exp[- z eM / kM T 1/1000 (2 c9PM[ρ0, T, σI, σII, t, d] Cosh[κM[ρ0, T] (x) 10^-10])],
     0 ≤ x ≤ t - a/2}, {0, t - a/2 < x < t + d + a/2},
    {Exp[- z eM / kM T 1/1000 (c1PM Exp[κM[ρ0, T] (x) 10^-10] +
          c2PM[ρ0, T, σI, σII, t, d] Exp[-κM[ρ0, T] (x) 10^-10])], x ≥ t + d + a/2}}] ;
gnP[ρ0_, T_, σI_, σII_, t_, d_, x_] := Piecewise[
    {{Exp[z eM / kM T 1/1000 (2 c9PM[ρ0, T, σI, σII, t, d] Cosh[κM[ρ0, T] (x) 10^-10])],
     0 ≤ x ≤ t - a/2}, {0, t - a/2 < x < t + d + a/2},
```

```
    {Exp[ z eM / kM T  1 / 1000 (c1PM Exp[κM[ρ0, T] (x) 10^-10] +
          c2PM[ρ0, T, σI, σII, t, d] Exp[-κM[ρ0, T] (x) 10^-10])], x ≥ t + d + a/2}}] ;
gpC[ρ0_, T_, σI_, σII_, R_, d_, r_] := Piecewise[
   {{Exp[- z eM / kM T  1 / 1000 (c9CM[ρ0, T, σI, σII, R, d] BesselI[0, κM[ρ0, T] (r) 10^-10] +
         c10CM BesselK[0, κM[ρ0, T] (r) 10^-10])],
     0 ≤ r ≤ R - a/2}, {0, R - a/2 < r < R + d + a/2}, {Exp[- z eM / kM T  1 / 1000
      (c1CM BesselI[0, κM[ρ0, T] (r) 10^-10] + c2CM[ρ0, T, σI, σII, R, d]
        BesselK[0, κM[ρ0, T] (r) 10^-10])], r ≥ R + d + a/2}}] ;
gnC[ρ0_, T_, σI_, σII_, R_, d_, r_] := Piecewise[
   {{Exp[ z eM / kM T  1 / 1000 (c9CM[ρ0, T, σI, σII, R, d] BesselI[0, κM[ρ0, T] (r) 10^-10] +
         c10CM BesselK[0, κM[ρ0, T] (r) 10^-10])],
     0 ≤ r ≤ R - a/2}, {0, R - a/2 < r < R + d + a/2},
    {Exp[ z eM / kM T  1 / 1000 (c1CM BesselI[0, κM[ρ0, T] (r) 10^-10] + c2CM[ρ0, T, σI, σII, R, d]
        BesselK[0, κM[ρ0, T] (r) 10^-10])], r ≥ R + d + a/2}}] ;
gpS[ρ0_, T_, σI_, σII_, R_, d_, r_] := Piecewise[
   {{Exp[- z eM / kM T  1 / 1000 (1 / (r) 10^-10 (c9SM[ρ0, T, σI, σII, R, d] Exp[κM[ρ0, T] (r) 10^-10] +
          c10SM[ρ0, T, σI, σII, R, d] Exp[-κM[ρ0, T] (r) 10^-10]))],
     0 ≤ r ≤ R - a/2}, {0, R - a/2 < r < R + d + a/2}, {Exp[- z eM / kM T  1 / 1000
      (1 / (r) 10^-10 (c1SM Exp[κM[ρ0, T] (r) 10^-10] + c2SM[ρ0, T, σI, σII, R, d]
          Exp[-κM[ρ0, T] (r) 10^-10] ))], r ≥ R + d + a/2}}] ;
gnS[ρ0_, T_, σI_, σII_, R_, d_, r_] := Piecewise[
   {{Exp[ z eM / kM T  1 / 1000 (1 / (r) 10^-10 (c9SM[ρ0, T, σI, σII, R, d] Exp[κM[ρ0, T] (r) 10^-10] +
          c10SM[ρ0, T, σI, σII, R, d] Exp[-κM[ρ0, T] (r) 10^-10]))],
     0 ≤ r ≤ R - a/2}, {0, R - a/2 < r < R + d + a/2}, {Exp[ z eM / kM T  1 / 1000
```

```
( 1/((r) 10^-10) (c1SM Exp[κM[ρ0, T] (r) 10^-10] +
      c2SM[ρ0, T, σI, σII, R, d] Exp[-κM[ρ0, T] (r) 10^-10] )), r ≥ R + d + a/2}}];
```

# The differential capacitance

Finally, the differential capacitance is obtained for our different pores by

```
In[•]:= CdPC[ρ0_, T_, t_, d_] :=
          (D[Limit[ψPC[ρ0, T, σ, σ, t, d, x], x → 0, Direction → "FromAbove"], σ])^-1
         (*cm^-1||cm/cm^2*);
        CdPM[ρ0_, T_, t_, d_] :=
          (D[Limit[ψPM[ρ0, T, σ, σ, t, d, x], x → 0, Direction → "FromAbove"]/1000, σ])^-1 (*F/
          m^2*);
        CdCC[ρ0_, T_, R_, d_] :=
          (D[Limit[ψCC[ρ0, T, σ, σ, R, d, r], r → 0, Direction → "FromAbove"], σ])^-1
         (*cm^-1||cm/cm^2*);
        CdCM[ρ0_, T_, R_, d_] :=
          (D[Limit[ψCM[ρ0, T, σ, σ, R, d, r], r → 0, Direction → "FromAbove"]/1000, σ])^-1 (*F/
          m^2*);
        CdSC[ρ0_, T_, R_, d_] :=
          (D[Limit[ψSC[ρ0, T, σ, σ, R, d, r], r → 0, Direction → "FromAbove"], σ])^-1
         (*cm^-1||cm/cm^2*);
        CdSM[ρ0_, T_, R_, d_] :=
          (D[Limit[ψSM[ρ0, T, σ, σ, R, d, r], r → 0, Direction → "FromAbove"]/1000, σ])^-1 (*F/
          m^2*);
```

# Bibliography


[1] E. J. W. Verwey and K. F. Niessen. XL. The electrical double layer at the interface of two liquids. *Phil. Mag. S. 7*, 28(189):435–446, 1939.

[2] E. J. W. Verwey and J. Th. G. Overbeek. *Theory of the Stability of Lyophobic Colloids*. Elsevier, Netherlands, 1948.

[3] P. Sharma and T. S. Bhatti. A review on electrochemical double-layer capacitors. *Energy Convers. Manag.*, 51(12):2901–2912, 2010.

[4] R. Kötz and M. Carlen. Principles and applications of electrochemical capacitors. *Electrochim. Acta*, 45(15-16):2483–2498, 2000.

[5] M. Endo, T. Takeda, Y. J. Kim, K. Koshiba, and K. Ishii. High Power Electric Double Layer Capacitor (EDLC's); from Operating Principle to Pore Size Control in Advanced Activated Carbons. *Carbon Lett.*, 1(3&4):117–128, 2001.

[6] P. Kurzweil. History: Electrochemical Capacitors. In J. Garche and C. K. Dyer, editors, *Encyclopedia of Electrochemical Power Sources*. Elsevier, Germany, 2009.

[7] J. Yan, Q. Wang, T. Wei, and Z. Fan. Recent Advances in Design and Fabrication of Electrochemical Supercapacitors with High Energy Densities. *Adv. Energy Mater.*, 4(4):1300816(1)–1300816(43), 2014.

[8] Z. S. Iro, C. Subramani, and S. S. Dash. A Brief Review on Electrode Materials for Supercapacitor. *Int. J. Electrochem. Sci.*, 11(12):10628–10643, 2016.

[9] A. González, E. Goikolea, J. A. Barrena, and R. Mysyk. Review on supercapacitors: Technologies and materials. *Renew. Sust. Energ. Rev.*, 58:1189–1206, 2016.

[10] L. L. Zhang and X. S. Zhao. Carbon-based materials as supercapcitor electrodes. *Chem. Soc. Rev.*, 38(9):2520–2531, 2009.

[11] P. Simon and Y. Gogotsi. Materials for electrochemical capacitors. *Nat. Mater.*, 7(11):845–854, 2008.

[12] Z. Wu, L. Li, J. M. Yan, and X. B. Zhang. Materials Design and System Construction for Conventional and New-Concept Supercapacitors. *Adv. Sci.*, 4(6):1600382(1)–1600382(48), 2017.

[13] H. M. Coromina, B. Adeniran, R. Mokaya, and D. A. Walsh. Bridging the performance gap between electric double-layer capacitors and batteries with high-energy/high-power carbon nanotube-based. *J. Mater. Chem. A*, 4(38):14586–14594, 2016.

[14] C. Liu, Z. Yu, D. Neff, A. Zhamu, and B. Z. Jang. Graphene-Based Supercapacitor with an Ultrahigh Energy Density. *NANO Lett.*, 10(12):4863–4868, 2010.

[15] Q. Ke and J. Wang. Graphene-based materials for supercapacitor electrodes – A review. *J. Materiomics*, 2(1):37–54, 2016.

[16] A. Peigney, C. Lauren, E. Flahaut, R. R. Bacsa, and A. Rousset. Specific surface area of carbon nanotubes and bundles of carbon nanotubes. *Carbon*, 39(4):507–514, 2001.

[17] U. K. Sur. Graphene: A Rising Star on the Horizon of Materials Science. *Int. J. Electrochem.*, 2012:237689(1)–237689(12), 2012.

[18] T. Y. Kim, G. Jung, S. Yoo, K. S. Suh, and R. S. Ruoff. Activated Graphene-Based Carbons as Supercapacitor Electrodes with Macro- and Mesopores. *ACS Nano*, 7(8):6899–6905, 2013.

[19] Y. Chen, X. Zhang, D. Zhang, P. Yu, and Y. Ma. High performance supercapacitors based on reduced graphene oxide in aqueous and ionic liquid electrolytes. *Carbon*, 49(2):573–580, 2011.

[20] C. Zhong, Y. Deng, W. Hu, J. Qiao, L. Zhang, and J. Zhang. A review of electrolyte materials and compositions for electrochemical supercapacitors. *Chem. Soc. Rev.*, 44(21):7484–7539, 2015.

[21] F. Béguin, V. Presser, A. Balducci, and E. Frackowiak. Carbons and Electrolytes for Advanced Supercapacitors carbons and electrolytes for advanced supercapacitors. *Adv. Mater.*, 26(14):2219–2251, 2014.

[22] P. Kurzweil. Electrochemical Double-Layer Capacitors. In J. Garche and C. K. Dyer, editors, *Encyclopedia of Electrochemical Power Sources*. Elsevier, Germany, 2009.

[23] S. Shahzad, A. Shah, E. Kowsari, F. J. Iftikhar, A. Nawab, B. Piro, M. S. Akhter, U. A. Rana, and Y. Zou. Ionic Liquids as Environmentally Benign Electrolytes for High-Performance Supercapacitors. *Global Challenges*, 3(1):1800023(1)–1800023(17), 2019.

[24] J. Vatamanu and D. Bedrov. Capacitive Energy Storage: Current and Future Challenges. *J. Phys. Chem. Lett.*, 6(18):3594–3609, 2015.

[25] F. Zheng, Y. Li, and X. Wang. Study on effects of applied current and voltage on the ageing of supercapacitors. *Electrochim. Acta*, 276:343–351, 2018.

[26] T. Pandolfo, V. Ruiz, S.i Sivakkumar, and J. Nerkar. General Properties of Electrochemical Capacitors. In F. Béguin and E. Frackowiak, editors, *Supercapacitors: Materials, Systems, and Applications*. John Wiley & Sons, Ltd, Singapore, 2013.

[27] T. Christen and M. W. Carlen. Theory of Ragone plots. *J. Power Sources*, 91(2):210–216, 2010.

[28] A. G. Pandolfo and A. F. Hollenkamp. Carbon properties and their role in supercapaictors. *J. Power Sources*, 157(1):11–27, 2006.

[29] J. R. Miller and P. Simon. Electrochemical Capacitors for Energy Management. *Science*, 321(5889):651–652, 2008.

[30] D. C. Grahame. The Electrical Double Layer and the Theory of Electrocapillarity. *Chem. Rev.*, 41(3):441–501, 1947.

[31] H. Helmholtz. Studien über electrische grenzschichten. *Ann. d. Phy. u. Chem.*, 243(7):337–382, 1879.

[32] M. Gouy. Sur la Constitution de la Charge Électrique a la Surface d'un Électrolyte. *J. Phys. T. Ap.*, 9(1):457–468, 1910.

[33] D. L. Chapman. LI. A contribution to the theory of electrocapillarity. *Phil. Mag. S. 6*, 25(148):475–481, 1913.

[34] O. Stern-Hamburg. Zur theorie der elektrolytischen doppelschicht. *Z. Elektrochem.*, 30(21-22):508–516, 1924.

[35] M. Lozada-Cassou. A new method of deriving electrical double layer equations from electrolyte theories. *J. Chem. Phys.*, 75(3):1412–1421, 1981.

[36] M. Lozada-Cassou. Fluids Between Walls and in Pores. In D. Henderson, editor, *Fundamentals of Inhomogeneous Fluids*, chapter 8, pages 303–361. Marcel Dekker, New York, 1992.

[37] R. Kjellander and D. J. Mitchel. An exact but linear and Poisson—Boltzmann-like theory for electrolytes and colloid dispersions in the primitive modelboltzmann-like theory for electrolytes and colloid dispersions in the primitive model. *Chem. Phys. Lett.*, 200(1):76–82, 1992.

[38] D. M. Zuckerman, M. E. Fisher, and S. Bekiranov. Asymmetric primitive-model electrolytes: Debye-Hückel theory, criticality, and energy bounds. *Phys. Rev. E*, 64(1):011206(1)–011206(13), 2001.

[39] H. M. Manzanilla-Granados, F. Jiménez-Ángeles, and M. Lozada-Cassou. The ζ-potential for a concentrated colloidal dispersion: The colloidal primitive model vs. the cell model. *Colloids Surf. A: Physicochem. Eng. Asp.*, 376(1):59–66, 2011.

[40] H. M. Manzanilla-Granados, F. Jiménez-Ángeles, and M. Lozada-Cassou. Polarity Inversion of ζ-Potential in Concentrated Colloidal Dispersions. *J. Phys. Chem. B*, 115(42):12094–12097, 2011.

[41] H. M. Manzanilla-Granados and M. Lozada-Cassou. Modified Colloidal Primitive Model as a Homogeneous Surface Charge Distribution: ζ-Potential. *J. Phys. Chem. B*, 117(39):11812–11829, 2013.

[42] A. González-Calderón, E. González-Tovar, and M. Lozada-Cassou. Very long-range attractive and repulsive forces in model colloidal dispersions. *Eur. Phys. J. Spec. Top.*, 227(15):2375–2390, 2019.

[43] G. Ordiozola and M. Lozada-Cassou. Equivalence between particles and fields: A general statistical mechanics theory for short and long range many-body forces. *Fortschr. Phys.*, 65(6-8):1600072(1)–1600072(21), 2017.

[44] H. L. Friedman. *A Course in Statistical Mechanics*. Prentice-Hall, Inc., United States of America, 1985.

[45] S. L. Carnie, D. Y. C. Chan, D. J. Mitchell, and B. W. Ninham. The structure of electrolytes at charged surfaces: The primitive model. *J. Chem. Phys.*, 74(2):1472–1478, 1981.

[46] M. Lozada-Cassou, R. Saavedra-Barrera, and D. Henderson. The application of the hypernetted chain approximation to the electrical double layer: Comparison with monte carlo results for symmetric salts. *J. Chem. Phys.*, 77(10):5150–5156, 1982.

[47] M. Lozada-Cassou. Hypernetted Chain Theory for the Distribution of Ions around a Cylindrical Electrode. *J. Phys. Chem.*, 87(19):3729–3732, 1983.

[48] M. Lozada-Cassou. The force between two planar electrical double layers. *J. Chem. Phys.*, 80(7):3344–3349, 1984.

[49] K. Hiroike. Ornastein-Zernike Relation for a Fluid Mixture with Direct Correlation Functions of Finite Range. *J. Phys. Soc. Jpn.*, 27(6):1415–1421, 1969.

[50] L. Blum. Mean spherical model for asymmetric electrolytes I. Method of solution. *Mol. Phys.*, 30(5):1529–1535, 1975.

[51] K. Hiroike. Supplement to Blum's theory for asymmetric electrolytes. *Mol. Phys.*, 33(4):1195–1198, 1977.

[52] L. Mier y Terán, A. H. Falls, L. E. Scriven, and H. T. Davis. Structure and thermodynamics of stable, metastable, and unstable fluid – efficient numerical method for solving the equations of equilbrium fluid physics. In J. V. Sengers, editor, *Proceedings of the Eighth Symposioum on Thermophysical Properties*, volume I. American Society of Mechanical Engineers, New York, 1982.

[53] L. Mier y Terán, E. Díaz-Herrera, and M. Lozada-Cassou. Temperature Dependence of the Primitive-Model Double Layer Differential Capacitance: A Hypernetted Chain/Mean Spherical Approximation Calculation. *J. Phys. Chem.*, 92(22):6408–6413, 1988.

[54] M. J. Grimson and G. Rickayzen. Solvation forces in charged fluids. *Mol. Phys.*, 44(4):817–840, 1981.

[55] P. Attard. Electrolytes and the Electric Double Layer. In I. Prigogine and S. A. Rice, editors, *Advances in Chemical Physics, Volume XCII*, pages 1–159, Australia, 1996. John Wiley & Sons, Inc.

[56] L. Belloni. Colloidal interactions. *J. Phys.: Condens. Matter*, 12(46):R549–R587, 2000.

[57] H. Greberg and R. Kjellander. Charge inversion in electric double layers and effects of different sizes for counterions and coions. *J. Chem. Phys.*, 108(7):2940–2953, 1998.

[58] G. I. Guerrero-García, E. González-Tovar, M. Lozada-Cassou, and F. de J. Guevara-Rodríguez. The electrical double layer for a fully asymmetric electrolyte around a spherical colloid: An integral equation study. *J. Chem. Phys.*, 123(3):034703(1)–034703(20), 2005.

[59] G. I. Guerrero-García, E. González-Tovar, M. Chávez-Páez, and M. Lozada-Cassou. Overcharging and charge reversal in the electrical double layer around the point of zero charge. *J. Chem. Phys.*, 132(5):054903(1)–054903(19), 2010.

[60] F. Jiménez-Ángeles and M. Lozada-Cassou. A Model Macroion Solution Next to a Charged Wall: Overcharging, Charge Reversal, and Charge Inversion by Macroions. *J. Phys. Chem. B*, 108(22):7286–7296, 2004.

[61] F. Jiménez-Ángeles and M. Lozada-Cassou. Simple Model for Semipermeable Membrane: Donnan Equilibrium. *J. Phys. Chem. B*, 108(5):1719–1730, 2004.

[62] M. Lozada-Cassou and E. Díaz-Herrera. Three point extension for hypernetted chain and other integral equation theories: Numerical results. *J. Chem. Phys.*, 92(2):1386–1398, 1990.

[63] J. M. Hammersley and D. C. Handscomb. *Monte Carlo Methods.* Methuen Young Books, Great Britain, 1964.

[64] D. N. Card and J. P. Valleau. Monte Carlo Study of the Thermodynamics of Electrolyte Solutions. *J. Chem. Phys.*, 52(12):6232–6240, 1970.

[65] D. Henderson, M. Lozada-Cassou, and L. Blum. The application of the HNC/MSA approximation to bulk electrolytes. *J. Chem. Phys.*, 79(6):3055–3057, 1983.

[66] G.M. Torrie and J. P. Valleau. A Monte Carlo study of an electrical double layer. *Chem. Phys. Lett.*, 65(2):343–346, 1979.

[67] G. M. Torrie and J. P. Valleau. Electrical double layers. I. Monte Carlo study of a uniformly charged surface. *J. Chem. Phys.*, 73(11):5807–5816, 1980.

[68] L. Degrève, M. Lozada-Cassou, E. Sànchez, and E. González-Tovar. Monte Carlo simulation for a symmetrical electrolyte next to a charged spherical colloid particle. *J. Chem. Phys.*, 98(11):8905–8909, 1993.

[69] L. Degrève and M. Lozada-Cassou. Monte Carlo and HNC/MSA results for an asymmetrical electrolyte in an external electric field of spherical geometry. *Mol. Phys.*, 86(4):759–768, 1995.

[70] D. Bratko and V. Vlachy. Distribution of counterions in the double layer around a cylindrical polyion. *Chem. Phys. Lett.*, 90(6):434–438, 1982.

[71] M. Le Bret and B. H. Zimm. Monte Carlo Determination of the Distribution of Ions About a Cylindrical Polyelectrolyte. *Biopolymers*, 23(2):271–285, 1984.

[72] T. Goel, C. N. Patra, S. K. Ghosh, and T. Mukherjee. Structure of cylindrical electric double layers: A systematic study by Monte Carlo simulations and density functional theory. *J. Chem. Phys.*, 129(15):154906(1)–154906(12), 2008.

[73] E. González-Tovar, M. Lozada-Cassou, L. B. Bhuiyan, and C. W. Outhwaite. Comparison of zeta potentials and structure for statistical mechanical theories of a model cylindrical double layer. *J. Mol. Liq.*, 270:157–167, 2018.

[74] K. D. Joshi. *Introduction to General Topology.* Wiley Eastern limited, India, 1983.

[75] C. Nash and S. Sen. *Topology and Geometry for Physicists.* Academic Press, Inc., Great Britain, third edition, 1987.

[76] D. A. McQuarrie. *Statistical Mechanics.* Harper & Row, New York, 1976.

[77] E. González-Tovar, M. Lozada-Cassou, and D. Henderson. Hypernetted chain approximation for the distribution of ions around a cylindrical electrode. II. Numerical solution for a model cylindrical polyelectrolyte. *J. Chem. Phys.*, 83(1):361–372, 1985.

[78] E. González-Tovar and M. Lozada-Cassou. The Spherical Double Layer: A Hypernetted Chain Mean Spherical Approximation Calculation for a Model Spherical Colloid Particle. *J. Phys. Chem.*, 93(9):3761–3768, 1989.

[79] G. E. Aguilar-Pineda, F. Jiménez-Ángeles, J. Yu, and M. Lozada-Cassou. Van der Waals-Like Isotherms in a Confined Electrolyte by Spherical and Cylindrical Nanopores. *J. Phys. Chem. B*, 111(8):2033–2044, 2007.

[80] J. Yu, L. Degrève, and M. Lozada-Cassou. Charge Separation in Confined Charge Fluids. *Phys. Rev. Lett.*, 79(19):3656–3659, 1997.

[81] W. Olivares, B. Sulbarán, and M. Lozada-Cassou. Static and transport propoerties of symmetric and asymmetric electrolytes in micropores at fixed surface potential. *J. Chem. Phys.*, 103(18):8179–8188, 1995.

[82] W. Olivares-Rivas, B. Sulbarán-Maldonado, and M. Lozada-Cassou. Effect of the ionic charge on the transport properties of electrolytes through narrow pores. *J. Mol. Struc-TEOCHEM*, 304(2):121–127, 1994.

[83] F. Bowman. *Introduction to Bessel Functions.* Dover Publication Inc., New York, 1958.

[84] F. W. J. Olver, D. W. Lozier, R. F. Boisvert, and C. W. Clark, editors. *NIST Handbook of Mathematical Functions.* Cambridge University Press, United States of America, 2010.

[85] W. W. Bell. *Special Functions for Scientists and Engineers.* D. Van Nostrand Company, Ltd, Great Britain, 1968.